INTERNATIONAL SOIL AND WATER CONSERVATION RESEARCH (ISWCR)

Volume 7, No. 2, June 2019

CONTENTS

Available online at www.sciencedirect.com

ScienceDirect

ISSN 2095-6339

9 772095 633197 06>

International Soil and Water Conservation Research (ISWCR) Vol. 7 (2019) 109–202

ISSN 2095-6339
CN 10-1107/P

International Soil and Water Conservation Research

Volume 7, No. 2, June 2019

国际水土保持研究

United Nations Educational, Scientific and Cultural Organization

International Research and Training Center on Erosion and Sedimentation

CHINA WATER & POWER PRESS

IWHR

The *International Soil and Water Conservation Research (ISWCR)* is the official journal of World Association of Soil and Water Conservation (WASWAC), which is a non-governmental, non-profit organization. The mission of WASWAC is to promote the wise use of management practices, to improve and safeguard the quality of land and water resources. The Journal is co-owned by the International Research and Training Center on Erosion and Sedimentation, China Water & Power Press, and China Institute of Water Resources and Hydropower Research.

United Nations Educational, Scientific and Cultural Organization

International Research and Training Center on Erosion and Sedimentation

20 Chegongzhuang West Road
IRTCES Building 401-514
Beijing 100048, China
+86 10 68766413
irtces@iwhr.com
www.irtces.org

The International Research and Training Center on Erosion and Sedimentation (IRTCES) was jointly set up by the Government of China and UNESCO. It aims at the promotion of international exchange of knowledge and cooperation in the studies of erosion and sedimentation.

CHINA WATER & POWER PRESS

Building D, No. 1, South Yuyuantan Road,
Beijing 100038, China
+86 10 68545912
zt@waterpub.com.cn
http://www.waterpub.com.cn

China Water & Power Press (CWPP) is affiliated to the Ministry of Water Resources of China, which takes leadership of science and technology publishing in China.

A-1 Fuxing Road,
Beijing100038, China
+86 10 68781650
dic@iwhr.com
http://www.iwhr.com

China Institute of Water Resources and Hydropower Research is the largest and most comprehensive research institute in the field of water resources and hydropower in China.

Publishing services provided by Elsevier B.V. on behalf of KeAi

International Soil and Water Conservation Research (ISWCR)

Editorial Board

International Soil and Water Conservation Research (ISWCR)

Volume 7, Number 2, June 2019

International Research and Training Center on Erosion and Sedimentation and China Water and Power Press

AIMS AND SCOPE

The ***International Soil and Water Conservation Research*** (*ISWCR*), *the official journal of World Association of Soil and Water Conservation* (*WASWAC*) *www.waswac.org*, is a multidisciplinary journal of soil and water conservation research, practice, policy, and perspectives. It aims to disseminate new knowledge and promote the practice of **soil and water conservation.**

The scope of ***International Soil and Water Conservation Research*** includes research, strategies, and technologies for prediction, prevention, and protection of soil and water resources. It deals with identification, characterization, and modeling; dynamic monitoring and evaluation; assessment and management of conservation practice and creation and implementation of quality standards.

Examples of appropriate topical areas include (but are not limited to):

- ∑ Soil erosion and its control
- ∑ Watershed management
- ∑ Water resources assessment and management
- ∑ Nonpoint-source pollution
- ∑ Conservation models, tools, and technologies
- ∑ Conservation agricultural
- ∑ Soil health resources, indicators, assessment, and management
- ∑ Land degradation
- ∑ Sedimentation
- ∑ Sustainable development
- ∑ Literature review on topics related soil and water conservation research

Peer review under responsibility of IRTCES and CWPP.

INTERNATIONAL SOIL AND WATER CONSERVATION RESEARCH (ISWCR)

Volume 7, No. 2, June 2019

CONTENTS

International Soil and Water Conservation Research 7 (2019) 109–118

Contents lists available at ScienceDirect

International Soil and Water Conservation Research

journal homepage: www.elsevier.com/locate/iswcr

Original Research Article

Persistence in tillage decisions: Aggregate data analysis

Dat Q. Tran [a, b, *], Lyubov A. Kurkalova [c, d]

[a] University of Arkansas at Fayetteville, AR 72701, Department of Agricultural Economics and Agribusiness, USA
[b] Can Tho University, Department of Hydraulic Engineering, Vietnam
[c] 1601 E. Market St., Greensboro, NC, 27411, North Carolina A&T State University, Department of Economics, USA
[d] 1601 E. Market St., Greensboro, NC, 27411, North Carolina A&T State University, Department of Energy and Environmental Systems, USA

ARTICLE INFO

Article history:
Received 22 August 2018
Received in revised form
3 March 2019
Accepted 20 March 2019
Available online 23 March 2019

Keywords:
Aggregate data
Continuous conservation tillage
Markov chain model
Crop rotations
Highly erodible land

ABSTRACT

The Emission Gap Report 2013 from the United Nations Environment Program showed that adopting conservation tillage such as no-till, as an alternative to conventional tillage, contributes significantly to climate change mitigation through carbon sequestration. However, substantial amounts of soil carbon are lost when farmers interrupt continuous use of conservation tillage with conventional tillage. Conservation tillage is spreading, but little is known about the behavioral persistence in tillage decisions. To address the gap in the literature, we estimate county-specific Markov models of tillage-crop choices, and use the predicted probabilities of alternative two- and three-year tillage rotations to evaluate spatial variation and temporal persistence in conservation tillage adoption for the state of Iowa (U.S). We find that the county-average probabilities of continuous conservation tillage range between 0.133 and 0.295, and vary significantly among crop rotations. We also find a statistically strong positive effect of the incidence of the highly erodible land on the county-average use of continuous conservation tillage. Our results underscore the importance of dynamic modeling for understanding behavioral persistence in tillage decisions, and the interdependence between farmers' crop and tillage rotations.

1. Introduction

Conservation tillage (CT) has been a subject of considerable research because, when compared to conventional tillage (VT), it provides numerous environmental benefits and could play a major role in climate change mitigation (Knowler & Bradshaw, 2007; Mangalassery et al., 2014; Prokopy, Floress, Klotthor-Weinkauf, & Baumgart-Getz, 2008; UNEP, 2013; Wade & Claassen, 2017). While both CT and VT are umbrella terms encompassing multiple tillage systems, the delineations used in the U.S. most commonly follow the ones by the Conservation Technology Information Center (CTIC), which defines CT (VT) as any tillage system that leaves at least 30% (less than 30%) of the soil covered with crop residue after planting. Under these definitions, CT encompasses no-till/strip-till, mulch-till and ridge-till, and VT - reduced-till and/or intensive-till with involvement of moldboard plowing and/or multiple tillage trips (CTIC, 2018).

Controlled experiments conducted under a wide range of soil and climatic conditions show that continuous CT (CCT), i.e., CT used continuously over a number of years, contributes to protection of soil from erosion, enhances beneficial microbial activity, and sequesters carbon, when compared to continuous conventional tillage (CVT), i.e., VT practiced continuously over the same number of years (Busari, Kukal, Kaur, Bhatt, & Dulazi, 2015; Lal, 2004, 2014; Sainju, Senwo, Nyakatawa, Tazisong, & Reddy, 2008; Uri, 2001). Alternating CT (ACT), i.e., the practice under which CT is alternated with VT in some years, has received less attention in the literature. Nevertheless, it has been shown that the many environmental benefits of CT are lost with the reversal back to VT even for a single year (Conant, Easter, Paustian, Swan, & Williams, 2007; Grace et al., 2011; Six et al., 2004). Specifically, climate change mitigation benefits of CT and its most stringent version, no-till (NT), are fully realized only when the practices are used continuously over a period of years, as CCT or continuous NT (CNT) (Grandy, Robertson, & Thelen, 2006; USDA-NRCS, 2015; VandenBygaart, 2016).

Because of the associated environmental benefits, CCT use has been promoted by multiple U.S. agricultural conservation programs (Bowman, Wallander, & Lynch, 2016; Claassen, Cattaneo, & Johansson, 2008; Duriancik et al., 2008; USDA-NRCS, 2015). Although the planning, monitoring, and evaluation of such conservation programs requires historical data on land use and CT

* Corresponding author. University of Arkansas at Fayetteville, AR 72701, Department of Agricultural Economics and Agribusiness, USA
E-mail addresses: datquoct@uark.edu (D.Q. Tran), lakurkal@ncat.edu (L.A. Kurkalova).

https://doi.org/10.1016/j.iswcr.2019.03.002

Abbreviations

CT	conservation tillage
VT	conventional tillage
ACT	alternating conservation tillage
CCT	continuous conservation tillage
CVT	continuous conventional tillage
CC and CCC	corn after corn and corn after corn after corn rotations, respectively
CS	corn after soybeans or soybeans after corn rotations
CCS	corn after corn after soybeans
CSC	corn after soybeans after corn
SCC	soybeans after corn after corn
SCS	soybeans after corn after soybeans
HEL	highly erodible land

(Gallant, Sadinski, Roth, & Rewa, 2011; Jackson-Smith, Halling, de la Hoz, McEvoy, & Horsburgh, 2010; Lobb, Huffman, & Reicosky, 2007; Osmond et al., 2012; Tomer et al., 2014), the spatial patterns of CCT, CVT and ACT remain poorly understood. Prokopy et al. (2008) reviewed 25 years of literature focused on the adoption of conservation practices and concluded that much of the literature on tillage adoption utilizes cross-sectional data and use static approaches. Therefore, little is known about persistence in tillage decisions. Similarly, Claassen and Ribaudo (2016) noted that disadoption is an issue for conservation programs and only a few studies have examined the persistence of cropland conservation practices. Most recently, Dayer, Lutter, Sesser, Hickey, and Gardali (2017) meta-analysis of private landowner conservation behavior argued that persistence in the adoption of easily reversible conservation practices should not be assumed to be the outcome, and that empirical research to examine whether and why landowners continue with conservation practices is urgently needed.

Identification of tillage data through remote sensing remain challenging (Zheng, Campbell, Serbin, & Galbraith, 2014; Sharma et al., 2016; Bégué et al., 2018), and the known tillage dynamics estimates come from field-level surveys. The surveys conducted in selected regions of the U.S. Corn Belt showed that NT was commonly alternated with other tillage practices in the 1990s (Hill, 1998, 2001; Napier & Tucker, 2001) and in 2004–2007 (USDA-NRCS, 2012). More recently, a national survey of famers growing corn, soybeans and wheat in the U.S. in 2009 and 2010 found that out of 622 farmers surveyed in the Corn Belt, which includes Illinois, Indiana, Iowa, Missouri, and Ohio, some 55% used CT on all crops in both years, 14% used VT on all crops in both years, and the remaining part of the sample used ACT (Andrews, Clawson, Gramig, & Raymond, 2013).

Exclusive reliance on farmer surveys for understanding of the spatial patterns of CCT, CVT, and ACT has several downsides. The high cost of conducting the surveys often results in relatively small samples, which limit the ability to make statistically reliable inferences. The detailed survey results could be inaccessible to researchers because of confidentiality concerns, resulting in the availability of the tillage time pattern estimates aggregated to the state or even multi-state regions only.[1] Finally, the tillage persistence patterns discerned from survey-based studies conducted in specific regions and on specific cropping patterns are not immediately transferable to other regions and/or cropping patterns because no explanation of the spatial variation in observed rates of CCT or ACT has been attempted (Knowler & Bradshaw, 2007; Knowler, Bradshaw, & Holmes, 2014; Prokopy et al., 2008; Baumgart-Getz, Prokopy, & Floress, 2012).

To address the need for alternative approaches to quantification of persistence in tillage decisions, our study evaluates the use of CCT and ACT using an explicitly dynamic Markov chain approach. Unlike static models, such as logistic regression, that focus on one-time choice, Markov chain is a probabilistic model that describes sequential processes - in our case, sequential choices of tillage. The method relies not on farmer surveys, but on time-ordered spatially aggregated data (Kurkalova & Tran, 2017; Lee, Judge, & Takayama, 1965).

A variety of past studies on the use of CT provided useful insights about the factors that are likely to affect the tillage adoption decisions (Knowler & Bradshaw, 2007; Prokopy et al., 2008; Baumgart-Getz at al., 2012; Knowler et al., 2014; Carlisle, 2016; Adusumilli & Wang, 2018); however, most of previous tillage studies used static models to study tillage decisions (Wallander, Bowman, Beeson, & Claassen, 2018). The use of the CT has been shown to vary by crops (Ding, Schoengold, & Tadesse, 2009; Horowitz, Ebel, & Ueda, 2010). The link between CT use and cropping sequences (crop rotations) has been suggested (Choi & Sohngen, 2010; Hill, 1998; Lewandrowski et al., 2004; Robertson et al., 2014; Torre Ugarte, Hellwinckel, & Larson, 2004), but barely explored. This is most likely because the majority of CT use studies used a static (one year at a time) as opposed to a dynamic (year to year transitions) settings, and tended to focus on analyzing the differences between one-year CT adopters versus one-year CT non-adopters (Claassen & Ribaudo, 2016; Wallander et al., 2018). To preview the results of our analysis, we show that in fact, the time patters of farmers' tillage and crop choices are highly interrelated.

We also gain insights into the relation between CCT and ACT, and soil erodibility. CT is the conservation practice that is used most widely among the practices aimed at combatting soil erosion on actively cropped Iowa land (Secchi et al., 2007; USDA-NRCS, 2012). Recent analysis of field-level, 2010 corn and 2012 soybean U.S. national survey found that designation of land as highly erodible land (HEL) increases the probability of NT alternated with other tillage practices and, to a greater extent, the probability of CNT (Wade & Claassen, 2017). To the best of our knowledge, our study is the first one to employ a dynamic framework to analyze the use of CCT.

The study has three interrelated objectives: to evaluate the spatial variability of CCT and ACT across the 99 counties, to analyze whether the variation in tillage dynamics is related to crop rotations, and to test whether the variability in CT persistence could be explained by a spatial variability in soil erodibility for a major U.S. crop production region, state of Iowa. The resulting improved understanding of both (a) the extent of CCT and ACT and (b) the factors associated with their spatial variability is likely to be helpful in improving the assessment of the environmental effects of alternative tillage systems.

2. Data and methods

The analysis involves two major steps. In step one, we estimate the matrices describing the transitions among alternative tillage-crop choices for each of the 99 counties in Iowa, and calculate the county-specific probabilities of CCT and ACT. To reveal the spatial pattern of CT persistence, we map the probabilities. In the step two, we study how CCT and ACT probabilities vary with crop rotations

[1] For example, the Agricultural Resource Management Survey (ARMS) estimate of NT adoption for corn following corn in Iowa is statistically unreliable due to a low sample size (USDA-ERS, 2018). Likewise, the National Resources Inventory-Conservation Effects Assessment Project (NRI-CEAP) estimates of CNT are based on a low sample size and currently available only for a limited sets of geographic regions, each encompassing multiple states (Horowitz et al., 2010).

and soil erodibility in the study area. The following subsections detail the study area, statistical model, data, computation of CCT and ACT probabilities, and the measurement of the dependency between the estimated probabilities of alternative tillage rotations, crop rotations, and soil erodibility.

2.1. Study area

Our study is conducted for the state of Iowa (U.S), where row cropping is dominated by two crops, corn and soybeans, the combined share of which in Iowa harvested cropland was 91, 92, 93, and 94 percent in 1992, 1997, 2002, and 2007, respectively (USDA, 2019). The two crops are usually alternated in consecutive years i.e., corn after corn, corn after soybeans and soybeans after corn (Plourde, Pijanowski, & Pekin, 2013; Sahajpal, Zhang, Izaurralde, Gelfand, & Hurtt, 2014; Secchi, Kurkalova, Gassman, & Hart, 2011; Stern, Doraiswamy, & Raymond, 2012). While many possible delineations of tillage systems exist (CTIC, 2018), we focus on the two commonly considered alternatives, CT and VT.

2.2. Markov chain model of tillage-crop choices

The first-order, Markov chain model of tillage-crop choices starts with the assumption that all cropland in a given county k in year t is allocated to one of four mutually exclusive tillage-crop uses: 1 (CT corn), 2 (VT corn), 3 (CT soybeans), and 4 (VT soybeans) (Howard, 1971; Kurkalova & Tran, 2017; Lee et al., 1965). The model postulates that present year tillage-crop choices depend on previous year decisions and the probabilities of transition. Specifically, let p_{ijk} be the probability of tillage-crop choice j in the current year following tillage-crop use i in the year before in county k, where $i, j = 1, \ldots 4$; $k = 1, \ldots, K$, and $K = 99$ is the total number of counties considered. Then s_{jk}^{t+1}, the proportion of the county k's land in tillage-crop j in year $t+1$, is equal

$$s_{jk}^{t+1} = \sum_{i=1}^{4} p_{ijk} s_{ik}^{t} + \varepsilon_{jk}^{t+1}, \quad j = 1, \ldots, 4; \quad k = 1, \ldots, K, \tag{1}$$

where s_{ik}^{t} is the proportion of the county k's land in tillage-crop i in year t (previous year), ε_{jk}^{t+1} is a random error, and $\sum_{j=1}^{4} p_{ijk} = 1, \quad i = 1, \ldots 4; \quad k = 1, \ldots, K$.

Because of the multiple diseases associated with planting soybeans after soybeans under Iowa soil and climatic conditions (Mueller, Robertson, Sisson, & Tylka, 2010), the practice is very rare in the state and the corresponding probabilities, p_{ijk}, $i,j = 3,4$, are postulated to be zero. The remaining probabilities of tillage-crop choices can be estimated using the restricted least squares (RLS) method if four or more years of the land proportion data are available (Kurkalova & Tran, 2017).

2.3. Data

We estimate models (1), one for each Iowa county, using the data on the proportions of land in the four tillage-crop uses that come from the National Crop Residue Management (CRM) survey by CTIC (CTIC, 2018). As a complete, county-level, national coverage survey, CRM has been the backbone of numerous studies of alternative tillage systems (Ding et al., 2009; Ogle et al., 2010; Baker, 2011; Panagopoulos et al., 2015, 2017). The CRM records are based on a combination of county conservation experts' opinions and the roadside transect method that requires visual assessment of tillage systems while driving a set course through the county. The accuracy of the data has been regarded adequate (Baker, 2011; Gassman, Secchi, Jha, & Kurkalova, 2006). The periodicity of the survey was reduced from every year (1989–1998) to every other year (1998–2004), and the later data were collected only for selected counties in selected states (2006–2008) (CTIC, 2018). Fig. 1 shows the summary of the data.

We estimate the county-specific models (1) using the six year of data, t = 1992, …,1997, leaving 1998, 2000, 2002 and 2004 for out-of-sample evaluation of model performance. We chose the 1992 to 1997 period for estimation because it is the longest time span for which the data fluctuate annually without a significant increasing or decreasing trend – the fluctuations consistent with the stationary Markov model (Lee et al., 1965). Note that although annual data are available 1989–1991, they do not display the zigzag pattern consistent with the model, and in consequence are not used for model estimation. Also of note is the fact that the six-year time span of the data is sufficient for estimating a four-state Markov model (Lee et al., 1965).

To investigate whether the use of continuous and/or alternating CT is affected by soil erodibility, we focus on the HEL. USDA Natural Resource Conservation Service (NRCS) classifies cropland as HEL if the potential of a soil to erode, considering the physical and chemical properties of the soil and climatic conditions where it is located, is eight times or more the rate at which the soil can sustain productivity (USDA/NRCS, 2002). To match the spatial resolution of

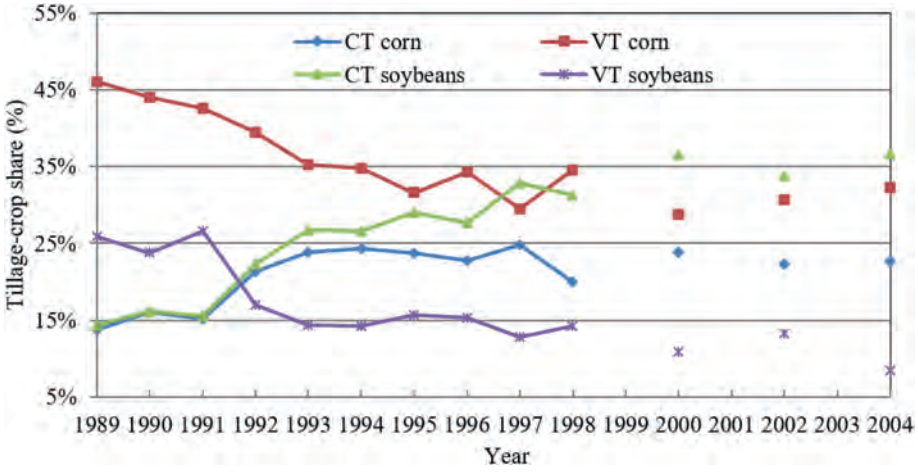

Fig. 1. Shares of alternative tillage-crop areas in the combined corn and soybeans total area, Iowa. Source: CTIC data (CTIC, 2018). CT = conservation tillage and VT = conventional tillage.

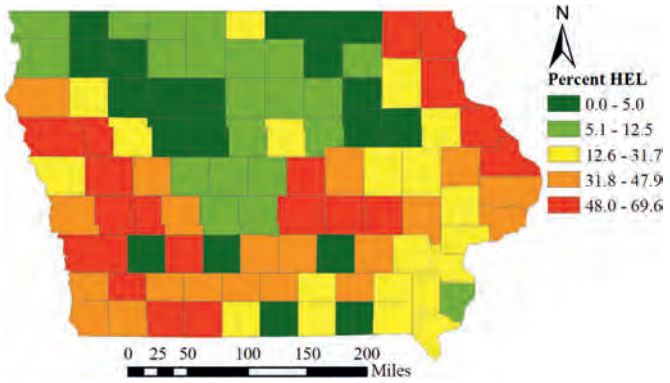

Fig. 2. Percentage of cropland classified as highly erodible land (HEL code of 1, highly erodible), by county, Iowa.

CRM, which is reported at the county level, we use the county k average percentage of cropland designated as HEL, HEL_k, as a measure of county-average soil erodibility.

The data for the HEL acreage come from the Iowa Soil Properties and Interpretations Database (ISPAID) version 7.1 (ISU, 2004), in which the HEL code has three possible values: 1, if a given map unit if highly erodible, 2, if the map unit is potentially highly erodible, and 3, if the map unit is not highly erodible. + the HEL code value of 1 only. Following previous crop production studies that use county-level data (Claassen et al., 2017; Ding et al., 2009; Zimmermann & Heckelei, 2012), we calculate HEL_k as the percentage of the county's cropland with the HEL code value of 1 in the total county's cropland. Fig. 2 shows the spatial variation of the county-average percentage of cropland classified as HEL, HEL_k, k = 1, …,99, on the map of Iowa.

2.4. Extent of CCT and ACT

Once the models (1) are estimated, we test several hypotheses about the extent of CCT and ACT. In line with the most common crop rotations in Iowa, which are either biannual or triannual, corn-soybeans, continuous corn, and corn-corn-soybeans (Plourde et al., 2013; Sahajpal et al., 2014; Secchi et al., 2009, 2011), we focus on two- and three-year tillage rotations.

We use the estimates of the transition probabilities in model (1) to estimate the probabilities of (or shares of cropland in) alternative tillage and crop rotations. When only two years of tillage-crop choices are considered, the probability of CCT in any given year is the probability that tillage is CT in both the current and the previous years, i.e., the sum of the probabilities of CT corn after CT corn, CT corn after CT soybeans, and CT soybeans after CT corn. The probabilities of CCT are computed for all the five two-year sequences within the time period of our data, i.e., for 1992–93, 1993–94, 1994–95, 1995–96, 1996–97; we use the five-year average as a single, county-level measure of the extent of two-year CCT, $P_{k,CCT-2}$:

$$P_{k,CCT-2} = \frac{1}{5}\sum_{t=1992}^{1996}\left(p_{11k}s_{1k}^t + p_{31k}s_{3k}^t + p_{13k}s_{1k}^t\right) \quad (2)$$

The computation of the three-year probabilities of CCT follows the same logic as for the two-year counterparts, except we average over the four three-year sequences within the time period of our data, i.e., for 1992–94, 1993–95, 1994–96, and 1995–97:

$$P_{k,CCT-3} = \frac{1}{4}\sum_{t=1992}^{1995}\left(p_{11k}p_{11k}s_{1k}^t + p_{11k}p_{13k}s_{1k}^t + p_{13k}p_{31k}s_{1k}^t + p_{31k}p_{13k}s_{3k}^t + p_{31k}p_{11k}s_{3k}^t\right). \quad (3)$$

The average probabilities of two- (three-) year ACT, $P_{k,ACT-2}$ ($P_{k,ACT-3}$), are computed similarly; they are detailed in the Appendix.

In addition to the unconditional probabilities of alternative tillage rotations, we compute the probabilities conditional on alternative crop rotations. Specifically, the probability of county k, two-year CCT on land that is in continuous corn (corn after corn), CC, rotation is measured as the five-year average of the probability of CCT conditional on CC rotation, $P_{k,CCT-2|CC}$. Similarly, the extent of county k, two-year CCT on land that is in corn-soybeans rotation (corn after soybeans or soybeans after corn), CS, is measured as the five-year average of the probability of CCT conditional on CS, $P_{k,CCT-2|CS}$ (Howard, 1971):

$$P_{k,CCT-2|CC} = \frac{1}{5}\sum_{t=1992}^{1996}\left(\frac{p_{11k}s_{1k}^t}{p_{11k}s_{1k}^t + p_{21k}s_{2k}^t + p_{12k}s_{1k}^t + p_{22k}s_{2k}^t}\right)$$
$$P_{k,CCT-2|CS} = \frac{1}{5}\sum_{t=1992}^{1996}\left(\frac{p_{31k}s_{3k}^t + p_{13k}s_{1k}^t}{p_{31k}s_{3k}^t + p_{41k}s_{4k}^t + p_{32k}s_{3k}^t + p_{42k}s_{4k}^t + p_{13k}s_{1k}^t + p_{23k}s_{2k}^t + p_{14k}s_{1k}^t + p_{24k}s_{2k}^t}\right) \quad (4)$$

For the sake of brevity, the formulas for the five-year-average conditional probabilities of two-year ACT conditional on CC rotation, $P_{k,ACT-2|CC}$; and ACT conditional on CS, $P_{k,ACT-2|CS}$, are provided in the Appendix. The Appendix also details the four-year-average probabilities of three-year CCT and ACT, conditional on three years of corn, CCC ($P_{k,CCT-3|CCC}$ and $P_{k,ACT-3|CCC}$); two years of corn in a three-year cropping pattern, CCS/CSC/SCC ($P_{k,CCT-3|CCS}$ and $P_{k,ACT-3|CCS}$); and one year of corn in a three-year cropping pattern, SCS ($P_{k,CCT-3|SCS}$ and $P_{k,ACT-3|SCS}$).

We use the probabilities of alternative tillage rotations conditional on crop rotations to test the following hypotheses:

H1. The probability of CCT differs between crop rotations.

H2. The probability of ACT differs between crop rotations.

We test each hypothesis using both the two- and the three-year estimates. To test hypothesis H1 with the two-year estimates, we use the analysis of variance (ANOVA) F-test (Casella & Berger, 2002) to test the null hypothesis of equal means for $\overline{P}_{CCT-2|CC}$ and $\overline{P}_{CCT-2|CS}$. Here and throughout the rest of the paper the "bar" over notation means that the estimate is averaged over county

estimates, i.e., for example, $\overline{P}_{CCT-2|CC} = \sum_k P_{k,CCT-2|CC}/K$. If the F-test rejects the null hypothesis, we conclude that the probabilities of a two-year CCT differ between crop rotations.

For the three-year estimates, we begin with the ANOVA to test the null hypothesis of equal means for $\overline{P}_{k,CCT-3|CCC}$, $\overline{P}_{k,CCT-3|CCS \text{ or } CSC \text{ or } SCC}$ and $\overline{P}_{k,CCT-3|SCS}$. If we cannot reject this null hypothesis, we conclude that the three-year probability of CCT does not differ by crop rotation. If we reject this null hypothesis, we follow with the Fisher's Least Significant Difference (LSD) test (Schlotzhauer & Littell, 1997) to identify the conditional probabilities that are different from the rest of the group. Hypothesis H2 is tested following similar procedures.

Finally, we use the unconditional probabilities of alternative tillage rotations to test the following hypotheses:

H3. The greater the percentage of land classified as HEL the greater the use of CCT.

H4. The greater the percentage of land classified as HEL the greater the use of ACT.

As with the hypotheses H1 and H2, we use both two- and three-year probabilities to ascertain the effect of HEL on CCT and ACT. To test hypothesis H3, we fit a simple linear regression of the probability of CCT ($P_{k,CCT-2}$ or $P_{k,CCT-3}$) on HEL_k, $k = 1, \ldots, 99$. If the estimated slope coefficient is positive and statistically different from zero, then we conclude that the data support the hypothesis. Hypothesis H4 is tested similarly, with the probability of CCT replaced by the probability of ACT.

3. Results and discussion

3.1. Estimated models and probabilities of alternative tillage rotations

The results of estimating the 99 county-specific models (1) are summarized in Table 1.

Evaluation of fit of the county-specific models (1) is based on the comparison of the observed versus predicted tillage-crop shares. The Mean Absolute Error (MAE), calculated as the year- and county-specific average of the difference between observed and estimated tillage-crop shares, is relatively small. The in-sample MAEs are less than 5% for the majority of counties (92 out of 99), and no county has the MAE greater than 10%. The out-of-sample model prediction are likewise reasonable: the average MAE is equal 6, 9, 8 and 9 percent with standard deviation of 4, 5, 4 and 4 percent for 1998, 2000, 2002 and 2004, respectively. Another measure of model fit, the estimated coefficients of correlation between the observed shares and simulated shares, also suggests that the model fits well with the data (Table 2).

The average probability of adopting CT when prior tillage decision was CT ranges from 0.098 to 0.51. When farmers use CT on soybeans, they more often than not rotate the practice with VT: only 44% of CT soybean fields remain in CT the next year. In contrast, more than 60% of the fields remain in CT the year after using CT on corn (Table 1). We also find that the use of ACT is widespread in Iowa: for two-year tillage-crop sequences, the average probability of being ACT is almost equal to the sum of the average probabilities of CVT and CCT, whereas on average 70% hectares are in ACT for three-year tillage-crop sequences, an increase by 21% after one year (Fig. 3).

We find that CT and VT are practiced continuously to approximately the same extent: the acreage-weighted average probabilities of CCT and CVT are equal 0.269 vs. 0.242 after two years, and 0.161 and 0.139 after three years (Fig. 3). The same consistency shows in the comparison across counties. The counties with the higher VT rates tend to have higher two- and three-year CVT rates: the coefficients of determination between average VT rate and the average probabilities of two- and three-year CVT are 0.400 and 0.294. Similarly, the coefficients of determination between average CT rate and the average probabilities of two- and three-year CCT are 0.416 (Fig. 4a) and 0.305 (Fig. 4b). However, it must be noted that

Table 2
Estimated correlation between the observed and simulated shares.

Year	Tillage-crop share			
	CT corn	VT corn	CT soybeans	VT soybeans
1993	0.824	0.875	0.796	0.769
1994	0.783	0.802	0.781	0.653
1995	0.828	0.810	0.808	0.850
1996	0.836	0.813	0.819	0.857
1997	0.836	0.743	0.687	0.725

Note: *p*-values are smaller than 0.0001 for all correlation coefficients. CT = conservation tillage and VT = conventional tillage.

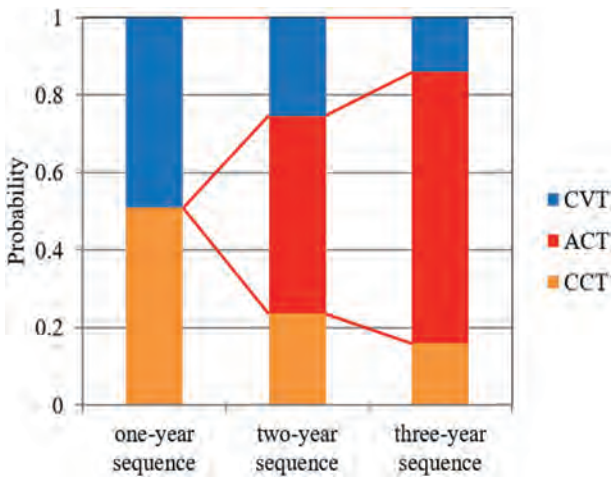

Fig. 3. Estimated average probability of continuous conservation tillage (CCT), continuous conventional tillage (CVT) and alternating conservation tillage (ACT). The one-year sequence is the county- and 1992–1997 average of the observed data. The average two-year probabilities are $\overline{P}_{CCT-2}$, $\overline{P}_{ACT-2}$, and $\overline{P}_{CVT-2} = 1 - \overline{P}_{CCT-2} - \overline{P}_{ACT-2}$; and the average three-year probabilities are $\overline{P}_{CCT-3}$, $\overline{P}_{ACT-3}$, and $\overline{P}_{CVT-3} = 1 - \overline{P}_{CCT-3} - \overline{P}_{ACT-3}$, for CCT, ACT, and CVT, respectively.

Table 1
Estimated average probabilities $\overline{p}_{ij}$ with the corresponding standard errors.

Previous year tillage-crop choice	Current year tillage-crop choice			
	CT corn	VT corn	CT soybeans	VT soybeans
CT corn	0.098 ± 0.017	0.125 ± 0.017	0.510 ± 0.031	0.267 ± 0.028
VT corn	0.120 ± 0.016	0.149 ± 0.020	0.475 ± 0.023	0.256 ± 0.019
CT soybeans	0.440 ± 0.029	0.560 ± 0.029	0	0
VT soybeans	0.397 ± 0.038	0.603 ± 0.038	0	0

Notes: The probabilities of transition from soybeans to soybeans were postulated to be zero. CT = conservation tillage and VT = conventional tillage.

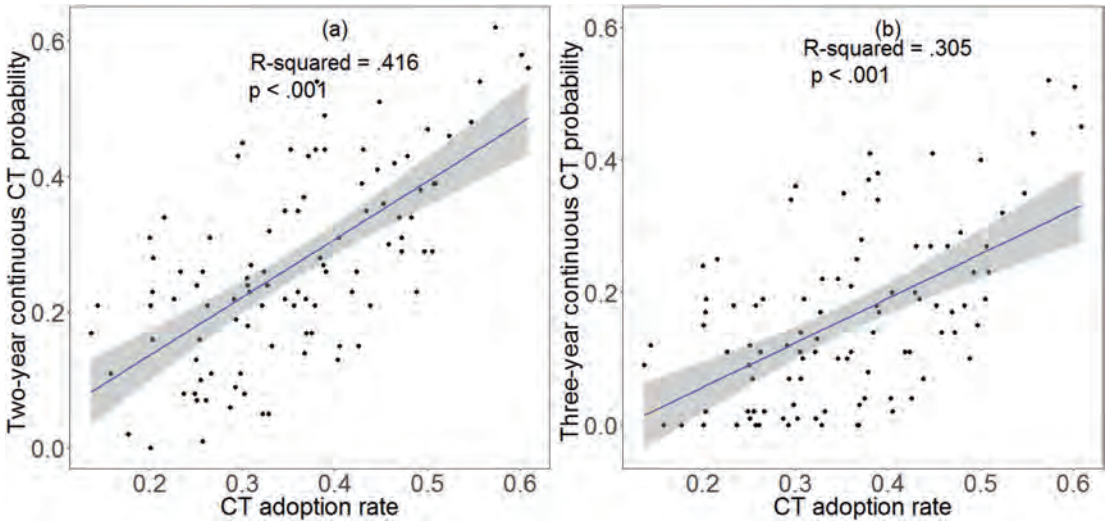

Fig. 4. Average probability of continuous conservation tillage (CCT) for two-year cropping sequence (Fig. 4a) and three-year cropping sequence (Fig. 4b) as a function of conservation tillage (CT) adoption rate. Scatterplots of two and three-year CCT by CT adoption rate are overlaid with the fit lines, 95% confidence bands are shaded.

the coefficients of determination are notably less than one. These findings imply that neither one-year rate of CT is an accurate measure of the CCT, nor one-year rate of VT is an accurate measure of the CVT.

In addition, our findings support to the concerns in the recent literature that argue that the CT's contribution to climate change mitigation is likely to be overstated because a sizable portion of CT is not in this practice permanently (Powlson et al., 2014; VandenBygaart, 2016). A noteworthy extension of our work would be a revision of the estimates of the current rate of carbon sequestration in the Iowa and/or U.S. Midwest agricultural soils taking into consideration the degree and the spatial patterns of the persistence in tillage decisions.

3.2. Hypotheses testing: CCT and crop rotations

The transition matrices estimated suggest that the choices of tillage and crop rotations are indeed bundled, i.e., the tillage time patterns differ significantly between crop rotations. On average, the probability of CT corn following CT corn is just 0.098, compared to 0.440 and 0.510 for the CT corn after CT soybeans and CT soybeans after CT corn, respectively (Table 1). The null hypothesis of the three mean probabilities being equal, $\overline{p}_{11} = \overline{p}_{13} = \overline{p}_{31}$ was rejected because the ANOVA F-test resulted in a p-value of less than 0.0001. The between-crop rotation difference is statistically strong: using the Fisher's LSD test at a 5% level of significance, we failed to reject the hypothesis $\overline{p}_{13} = \overline{p}_{31}$ and rejected the hypotheses of $\overline{p}_{11} = \overline{p}_{13}$ and $\overline{p}_{11} = \overline{p}_{31}$. These findings support hypothesis H1; they imply that land in continuous corn is less likely to be in CCT that the land in corn-soybean rotation.

The same general conclusion about the tight connections between CCT and crop rotations emerges from the comparison of the probabilities of CCT conditional on crop rotations (Table 3a and Table 3b). For two-year rotations, we find a strong support to hypothesis H1, because the average probabilities of CCT are statistically different between the two rotations considered, continuous corn and corn-soybeans. When three-year rotations considered, the support for hypothesis H1 is not as strong because two of the three considered probabilities are not statistically different. Nevertheless, we find that the average probabilities of CCT are lower for corn-heavy three-year rotations (continuous corn and corn-corn-soybeans) than rotations with only one year of corn.

Table 3a
Estimated average probabilities of two-year tillage rotations conditional on two-year crop rotation.

Rotation	Tillage-crop choice	
	CCT	ACT
CC	0.171 [a]	0.481 [c]
CS	0.295 [b]	0.504 [c]

Note: Within-column means followed by the same letter are not significantly different using Fisher's LSD at a 5% significance. We exclude estimated probabilities of nine counties since the probability of corn after corn is equal zero. CC = corn after corn rotation, CS = corn after soybeans and soybeans after corn rotations, CCT = continuous conservation tillage, and ACT = alternating conservation tillage.

Table 3b
Estimated average probabilities of three-year tillage rotations conditional on three-year crop rotation.

Rotation	Tillage-crop choice	
	CCT	ACT
CCC	0.151 [a]	0.525[c]
CCS/CSC/SCC	0.133 [a]	0.739 [d]
SCS	0.212 [b]	0.710 [d]

Note: Within-column, means followed by the same letter are not significantly different using Fisher's LSD at a 5% significance. We exclude estimated probabilities of nine counties since the probability of corn after corn after corn is equal zero. CCC = corn after corn after corn rotation, CCS = corn after corn after soybeans rotation, CSC = corn after soybeans after corn rotation, SCC = soybeans after corn after corn rotation, and SCS = soybeans after corn after soybeans rotation.

Unlike for CCT, our estimation results suggest only weak interactions between ACT and crop rotations (Table 4). Hypothesis H2 is rejected when two-year rotations are considered, and is weakly supported when three-year rotations are considered. We find that the probability of ACT is lower for the continuous corn when compared to the three-year rotations that include soybeans.

To our knowledge, this is the first study that quantifies the interdependence of farmers' choices of crop and tillage rotations in a major U.S. crop production region, Iowa. We find that the crop rotations associated with greater incidence of corn are associated with lower use of CCT, and possibly, with lower use of ACT. These results are important for two reasons. First, these findings may help explain the inconsistent statistical significance of the impact of crop

Table 4
Summary of hypotheses testing.

Hypothesis	Transition matrix estimates	Two-year probabilities	Three-year probabilities
H1 - supported	The probability of transition from CT to CT is higher for corn-soybeans rotation than for continuous corn	CCT use is lower on continuous corn than on corn-soybeans rotation	CCT use is lower for rotations with two or three years of corn versus rotations with only one year of corn
H2 - supported partially	N/A	No statistical evidence that ACT use differs between continuous corn and corn-soybeans rotation	ACT use is lower on continuous corn versus rotations that include soybeans
H3 - supported	N/A	HEL status increases the probability of CCT	HEL status increases the probability of CCT
H4 - rejected	N/A	HEL is not a significant predictor of ACT use	HEL is not a significant predictor of ACT use

Note: N/A means not applicable. CCT = continuous conservation tillage, ACT = alternating conservation tillage and HEL = highly erodible land.

rotations on the CT use noted in previous research. For example, Fuglie (1999) found an insignificant effect of crop rotation on CT adoption, but the results of Wu and Babcock (1998) and Torre Ugarte et al. (2004) implied that rotating crops positively affects the use of CT. However, these previous studies employed a static framework that dealt with a one-year CT use only. Our findings imply that a dynamic framework is imperative when assessing and explaining CT use.

Second, the recent past has seen an increase in continuous corn at the expense of corn-soybean rotation throughout the U.S. Midwest (Plourde et al., 2013; Stern et al., 2012). If the connections between crop and tillage rotations that we have quantified using the 1992–2004 data hold for later years, then the shift toward corn monoculture has also affected tillage intensity. An important topic for future research is then to analyze the environmental implications of this combined change in rotations and tillage intensity.

3.3. Hypotheses testing: CCT and HEL

The estimated slope coefficient from the regression of $P_{k,CCT-2}$ on HEL_k is 0.0019 with the p-value of 0.006, and that of $P_{k,CCT-3}$ on HEL_k is 0.0013 with the p-value of 0.036. These estimates provide a strong support to the hypothesis H3. Indeed, the spatial distribution of the average probability of three-year CCT (Fig. 5) is reasonably similar to the spatial distribution of the percentage of cropland in HEL (Fig. 2). However, we find no statistically significant impact of HEL_k on $P_{k,ACT-2}$ or $P_{k,ACT-3}$, thus rejecting hypothesis H4.

While previous studies acknowledged the possible relationship between CT adoption and HEL, they commonly utilized static frameworks (e.g., Logit model) and cross-sectional data, and in consequence, did not analyze the potential link between the persistence of CT use and HEL. A study of Wade and Claassen (2017) is an exception. Using a unique, four-year panel coming from farmers' survey, ARMS data, Wade and Claassen (2017) found that HEL designation could be the single important factor influencing the use of continuous no-till by the U.S. corn and soybean producers. Unfortunately, such ideal data to study CT persistence in large geographic regions, i.e., panel farmer survey (or remote sensing) data on tillage systems, is presently technologically challenging and/or expensive to collect (Sharma et al., 2016; Bégué et al., 2018). In the absence of the ideal tillage data, the method we use offers a viable alternative, complementing approach that relies on only aggregate, county-average, time ordered data.

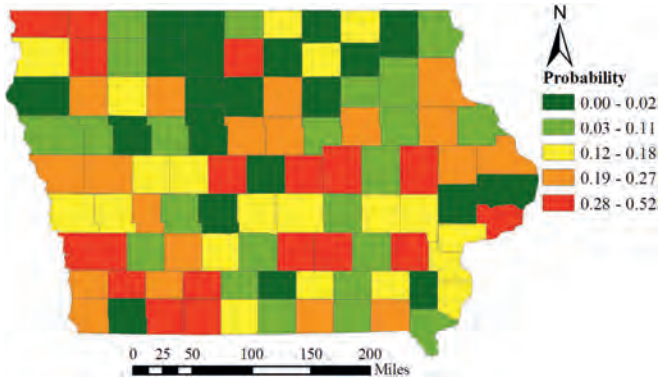

Fig. 5. Average probability of three-year continuous conservation tillage (CCT), by county, Iowa.

The statistically strong positive effect of HEL on the use of CCT and no effect of HEL on the use of ACT that we find could contribute to resolving another inconsistency in previous research. As the soil erosion prevention contribution of CT is well recognized by farmers (Andrews et al., 2013; Cooper, 1997; Fuglie, 1999; Perry, Moschini, & Hennessy, 2016; Tomer, Moorman, James, Hadish, & Rossi, 2008), researchers have been puzzled on why a wider use of CT on the land that is prone to erosion did not always show as statistically significant (Knowler & Bradshaw, 2007; Lambert, Sullivan, Claassen, & Foreman, 2007; Ding et al., 2009). The inability to find the differences in CT use on HEL vs. non-HEL land in these studies has been attributed to small sample size, the insufficient incentives provided by the conservation compliance, the policy that penalizes for intensive farming on HEL (Claassen et al., 2017), and/or insufficient monitoring of conservation compliance. Our findings about the differentiated impact of HEL on the use of CCT versus ACT contribute to this discussion by pointing to another possible explanation: the impact of HEL on CT use varies depending on whether the practice is used continuously or intermittently.

4. Conclusions

Most of previous tillage adoption research used static models to study tillage decisions (Wallander et al., 2018). Our study contributes to closing the gap in the understanding of the dynamics of tillage decisions in a major U.S. crop production region, Iowa. County-specific Markov chain models of tillage-crop transitions were estimated using the 1992–1997 CTIC data, with a good out-of-sample performance on the data through 2004. We showed that the probabilities of two- and three-year CCT and ACT are related to crop rotations, and the county-average use of CCT and ACT are affected by soil erodibility as measured by the county-average HEL proportion. We also find that there is a weak correlation between the use of CCT and CT adoption rate. This result implies that relying on conservation practices adoption rates to evaluate the success of conservation efforts might be misleading; an increase in adoption rates might be associated with increase in intermittent conservation practices rather than continuous conservation practices.

The better understanding of the persistence in tillage decisions could help refine the assessments of environmental ramifications from crop production and guide agri-environmental policies in the

U.S. Midwest, where corn and soybean commonly dominate crop production (USDA-NRCS, 2012). If data on other conservation practices of comparable time and spatial resolution become available, investigating how alternative crop-tillage rotations are related to the use of other conservation practices could further refine such assessments.[2]

The approach used in the study is not envisioned as a replacement for using field survey data to study the relationship between soil erodibility and the persistence in CT. Rather, our approach should be viewed as a complementary tool for an assessment of the relationship when multiple-year tillage survey data, which track the same fields over time, are not available.

Acknowledgements

This research was partially funded by the U.S Department of Agriculture (USDA) National Institute of Food and Agriculture (NIFA), award No. 2016-67024-24755. The funding source has no involvement in the study design, data collection and analysis, or any other aspects of the research or paper publication. The views expressed in this article are those of the authors and do not necessarily reflect the views or policies of the USDA.

Appendix. Details on computation of the probabilities of alternative crop and tillage rotations

Unconditional probabilities

The average probability of two-year ACT, $P_{k,ACT-2}$: $P_{k,ACT-2} = 1 - P_{k,CCT-2} - P_{k,CVT-2}$,

where $P_{k,CCT-2}$ is given in (2), and the average probability of two-year CVT,$P_{k,CVT-2}$, is given by

$$P_{k,CVT-2} = \frac{1}{5}\sum_{t=1992}^{1996}\left(p_{22k}s_{2k}^{t} + p_{42k}s_{4k}^{t} + p_{24k}s_{2k}^{t}\right).$$

The average probability of three-year ACT, $P_{k,ACT-3}$: $P_{k,ACT-3} = 1 - P_{k,CCT-3} - P_{k,CVT-3}$, where $P_{k,CCT-3}$ is given in (3), and the average probability of three-year CVT,$P_{k,CVT-3}$, is given by

$$P_{k,CVT-3} = \frac{1}{4}\sum_{t=1992}^{1995}\left(p_{22k}p_{22k}s_{2k}^{t} + p_{22k}p_{24k}s_{2k}^{t} + p_{24k}p_{42k}s_{2k}^{t} + p_{42k}p_{22k}s_{4k}^{t} + p_{42k}p_{24k}s_{4k}^{t}\right).$$

Conditional probabilities

Two-year conditional probabilities

The average probabilities of two-year ACT conditional on alternative rotations:

$$P_{k,ACT-2|CC} = \frac{1}{5}\sum_{t=1992}^{1996}\left(\frac{p_{21k}s_{2k}^{t} + p_{12k}s_{1k}^{t}}{p_{11k}s_{1k}^{t} + p_{21k}s_{2k}^{t} + p_{12k}s_{1k}^{t} + p_{22k}s_{2k}^{t}}\right),$$

$$P_{k,ACT-2|CS} = \frac{1}{5}\sum_{t=1992}^{1996}\left(\frac{p_{41k}s_{4k}^{t} + p_{32k}s_{3k}^{t} + p_{23k}s_{2k}^{t} + p_{14k}s_{1k}^{t}}{p_{31k}s_{3k}^{t} + p_{41k}s_{4k}^{t} + p_{32k}s_{3k}^{t} + p_{42k}s_{4k}^{t} + p_{13k}s_{1k}^{t} + p_{23k}s_{2k}^{t} + p_{14k}s_{1k}^{t} + p_{24k}s_{2k}^{t}}\right).$$

Three-year conditional probabilities

The average probabilities of three-year CCT conditional on alternative crop rotations:

$$P_{k,CCT|CCC} = \frac{1}{4}\sum_{t=1992}^{1995}\left(\frac{p_{11k}p_{11k}s_{1k}^{t}}{P(CCC_k^t)}\right), \text{ where}$$

$$P\left(CCC_k^t\right) = p_{11k}p_{11k}s_{1k}^{t} + p_{11k}p_{21k}s_{2k}^{t} + p_{21k}p_{12k}s_{1k}^{t} + p_{21k}p_{22k}s_{2k}^{t} + p_{12k}p_{11k}s_{1k}^{t} + p_{12k}p_{21k}s_{2k}^{t} + p_{22k}p_{12k}s_{1k}^{t} + p_{22k}p_{22k}s_{2k}^{t}. \quad (A.1)$$

$$P_{k,CCT\ CCS\ \text{or}\ CCS\ \text{or}\ SCC} = \frac{1}{4}\sum_{t=1992}^{1995}\left(\frac{p_{11k}p_{31k}s_{3k}^{t} + p_{31k}p_{13k}s_{1k}^{t} + p_{13k}p_{11k}s_{1k}^{t}}{P(CCS_k^t)}\right),$$

where

$$\begin{aligned} P\left(CCS_k^t\right) = {} & p_{11k}p_{31k}s_{3k}^{t} + p_{11k}p_{41k}s_{4k}^{t} + p_{21k}p_{32k}s_{3k}^{t} \\ & + p_{21k}p_{42k}s_{4k}^{t} + p_{31k}p_{13k}s_{1k}^{t} + p_{31k}p_{23k}s_{2k}^{t} \\ & + p_{41k}p_{14k}s_{1k}^{t} + p_{41k}p_{24k}s_{2k}^{t} + p_{12k}p_{31k}s_{3k}^{t} \\ & + p_{12k}p_{41k}s_{4k}^{t} + p_{22k}p_{32k}s_{3k}^{t} + p_{22k}p_{42k}s_{4k}^{t} \\ & + p_{32k}p_{13k}s_{1k}^{t} + p_{32k}p_{23k}s_{2k}^{t} + p_{42k}p_{14k}s_{1k}^{t} \\ & + p_{42k}p_{24k}s_{2k}^{t} + p_{13k}p_{11k}s_{1k}^{t} + p_{13k}p_{21k}s_{2k}^{t} \\ & + p_{23k}p_{12k}s_{1k}^{t} + p_{23k}p_{22k}s_{2k}^{t} + p_{14k}p_{11k}s_{1k}^{t} \\ & + p_{14k}p_{21k}s_{2k}^{t} + p_{24k}p_{12k}s_{1k}^{t} + p_{24k}p_{22k}s_{2k}^{t}. \end{aligned} \quad (A.2)$$

$$P_{k,CCT|SCS} = \frac{1}{4}\sum_{t=1992}^{1995}\left(\frac{p_{13k}p_{31k}s_{3k}^{t}}{P(SCS_k^t)}\right), \text{ where}$$

$$P\left(SCS_k^t\right) = p_{13k}p_{31k}s_{3k}^{t} + p_{13k}p_{41k}s_{4k}^{t} + p_{23k}p_{32k}s_{3k}^{t} + p_{23k}p_{42k}s_{4k}^{t} + p_{14k}p_{31k}s_{3k}^{t} + p_{14k}p_{41k}s_{4k}^{t} + p_{24k}p_{32k}s_{3k}^{t} + p_{24k}p_{42k}s_{4k}^{t}. \quad (A.3)$$

The average probabilities of three-year ACT conditional on alternative crop rotations:

$$P_{k,ACT|CCC} = \frac{1}{4}\sum_{t=1992}^{1995}\left(\frac{P(ACT_k^t \cap CCC_k^t)}{P(CCC_k^t)}\right), \text{ where } P(CCC_k^t) \text{is given in (A.1), and}$$

$$P\left(ACT_k^t \cap CCC_k^t\right) = p_{11k}p_{21k}s_{2k}^{t} + p_{21k}p_{12k}s_{1k}^{t} + p_{21k}p_{22k}s_{2k}^{t} + p_{12k}p_{11k}s_{1k}^{t} + p_{12k}p_{21k}s_{2k}^{t} + p_{22k}p_{12k}s_{1k}^{t}.$$

$$P_{k,ACT|CCS} = \frac{1}{4}\sum_{t=1992}^{1995}\left(\frac{P(ACT_k^t \cap CCS_k^t)}{P(CCS_k^t)}\right), \text{ where } P(CCS_k^t) \text{is given in}$$

[2] We thank an anonymous reviewer for making this point.

(A.2), and

$$P\left(ACT_k^t \cap CCS_k^t\right) = p_{11k}p_{41k}s_{4k}^t + p_{21k}p_{32k}s_{3k}^t + p_{21k}p_{42k}s_{4k}^t + p_{31k}p_{23k}s_{2k}^t + p_{41k}p_{14k}s_{1k}^t + p_{41k}p_{24k}s_{2k}^t + p_{12k}p_{31k}s_{3k}^t + p_{12k}p_{41k}s_{4k}^t + p_{22k}p_{32k}s_{3k}^t + p_{32k}p_{13k}s_{1k}^t + p_{32k}p_{23k}s_{2k}^t + p_{42k}p_{14k}s_{1k}^t + p_{13k}p_{21k}s_{2k}^t + p_{23k}p_{12k}s_{1k}^t + p_{23k}p_{22k}s_{2k}^t + p_{14k}p_{11k}s_{1k}^t + p_{14k}p_{21k}s_{2k}^t + p_{24k}p_{12k}s_{1k}^t.$$

$P_{k,ACT|SCS} = \frac{1}{4}\sum_{t=1992}^{1995}\left(\frac{P(ACT_k^t \cap SCS_k^t)}{P(SCS_k^t)}\right)$, where $P(SCS_k^t)$is given in (A.3), and

$$P\left(ACT_k^t \cap SCS_k^t\right) = p_{13k}p_{41k}s_{4k}^t + p_{23k}p_{32k}s_{3k}^t + p_{23k}p_{42k}s_{4k}^t + p_{14k}p_{31k}s_{3k}^t + p_{14k}p_{41k}s_{4k}^t + p_{24k}p_{32k}s_{3k}^t.$$

References

Adusumilli, N., & Wang, H. (2018). Analysis of soil management and water conservation practices adoption among crop and pasture farmers in humid-south of the United States. *International Soil and Water Conservation Research, 6*(2), 79–86. https://doi.org/10.1016/j.iswcr.2017.12.005.

Andrews, A. C., Clawson, R. A., Gramig, B. M., & Raymond, L. (2013). Why do farmers adopt conservation tillage? An experimental investigation of framing effects. *Journal of Soil and Water Conservation, 68*(6), 501–511.

Baker, N. T. (2011). *Tillage practices in the conterminous United States*, 1989-2004-Datasets Aggregated by Watershed (2327-638X) https://pubs.usgs.gov/ds/ds573/. (Accessed 6 December 2016).

Baumgart-Getz, A., Prokopy, L. S., & Floress, K. (2012). Why farmers adopt best management practice in the United States: A meta-analysis of the adoption literature. *Journal of Environmental Management, 96*(1), 17–25.

Bégué, A., Arvor, D., Bellon, B., Betbeder, J., Abelleyra, D. d., Ferraz, R.,P. D., et al. (2018). Remote sensing and cropping practices: A review. *Remote Sensing, 10*(99), 1–32. https://doi.org/10.3390/rs10010099.

Bowman, M., Wallander, S., & Lynch, L. (2016). *An economic perspective on soil health*. Amber Waves, 1_9A.

Busari, M. A., Kukal, S. S., Kaur, A., Bhatt, R., & Dulazi, A. A. (2015). Conservation tillage impacts on soil, crop and the environment. *International Soil and Water Conservation Research, 3*(2), 119–129. https://doi.org/10.1016/j.iswcr.2015.05.002.

Carlisle, L. (2016). Factors influencing farmer adoption of soil health practices in the United States: A narrative review. *Agroecology and Sustainable Food Systems, 40*(6), 583–613. https://doi.org/10.1080/21683565.2016.1156596.

Casella, G., & Berger, R. L. (2002). *Statistical inference* (2nd ed.). California: Thomson Learning.

Choi, S. W., & Sohngen, B. (2010). The optimal choice of residue management, crop rotations, and cost of carbon sequestration: Empirical results in the midwest US. *Climatic Change, 99*(1), 279–294.

Claassen, R., Bowman, M., Breneman, V., Wade, T., Williams, R., Fooks, J., … Loesch, C. (2017). *Conservation compliance: How farmer incentives are changing in the crop insurance era*. Retrieved from https://www.ers.usda.gov/publications/pub-details/?pubid=84456.

Claassen, R., Cattaneo, A., & Johansson, R. (2008). Cost-effective design of agri-environmental payment programs: U.S. Experience in theory and practice. *Ecological Economics, 65*(4), 737–752.

Claassen, R., & Ribaudo, M. (2016). Cost-effective conservation programs for sustaining environmental quality. *Choices, 31*(3), 1–12.

Conant, R. T., Easter, M., Paustian, K., Swan, A., & Williams, S. (2007). Impacts of periodic tillage on soil C stocks: A synthesis. *Soil and Tillage Research, 95*(1), 1–10.

Conservation Tillage Information Center (CTIC). (2018). *Tillage survey*. http://www.ctic.purdue.edu/CRM/. (Accessed 10 January 2018).

Cooper, J. (1997). Combining actual and contingent behavior data to model farmer adoption of water quality protection practices. *Agricultural and Resource Economics, 22*(1), 30–43.

Dayer, A. A., Lutter, S. H., Sesser, K. A., Hickey, C. M., & Gardali, T. (2017). Private landowner conservation behavior following participation in voluntary incentive programs: Recommendations to facilitate behavioral persistence. *Conservation Letters, 11*(2), 1–11. https://doi.org/10.1111/conl.12394.

Ding, Y., Schoengold, K., & Tadesse, T. (2009). The impact of weather extremes on agricultural production methods: Does drought increase adoption of conservation tillage practices? *Journal of Agricultural and Resource Economics, 34*(3), 395–411.

Duriancik, L. F., Bucks, D., Dobrowolski, J. P., Drewes, T., Eckles, S. D., Jolley, L., et al. (2008). The first five years of the conservation effects assessment Project. *Journal of Soil and Water Conservation, 63*(6), 185A–197A.

Fuglie, K. O. (1999). Conservation tillage and pesticide use in the Corn Belt. *Journal of Agricultural & Applied Economics, 31*(01), 133–148.

Gallant, A. L., Sadinski, W., Roth, M. F., & Rewa, C. A. (2011). Changes in historical Iowa land cover as context for assessing the environmental benefits of current and future conservation efforts on agricultural lands. *Journal of Soil and Water Conservation, 66*(3), 67A–77A.

Gassman, P. W., Secchi, S., Jha, M., & Kurkalova, L. A. (2006). Upper Mississippi river basin modeling system part 1: SWAT input data requirements and issues. In Y. P. Singh, & Y. Jun Xu (Eds.), *Coastal hydrology and processes* (pp. 03–115). Colorado: Water Resources Publications, LLC.

Grace, P. R., Robertson, P., Millar, N., Colunga-Garcia, M., Basso, B., Gage, S. H., et al. (2011). The contribution of maize cropping in the midwest USA to global warming: A regional estimate. *Agricultural Systems, 104*(3), 292–296. https://doi.org/10.1016/j.agsy.2010.09.001.

Grandy, A. S., Robertson, G. P., & Thelen, K. D. (2006). Do productivity and environmental trade-offs justify periodically cultivating no-till cropping systems? *Agronomy Journal, 98*(6), 1377–1383. https://doi.org/10.2134/agronj2006.0137.

Hill, P. R. (1998). Use of rotational tillage for corn and soybean production in the eastern corn belt. *Journal of Production Agriculture, 11*(1), 125–128.

Hill, P. R. (2001). Use of continuous no-till and rotational tillage systems in the central and northern Corn Belt. *Journal of Soil and Water Conservation, 56*(4), 286–290.

Horowitz, J., Ebel, R., & Ueda, K. (2010). *No-till farming is a growing practice*. Economic Information Bulletin Number 70. Washington: USDA https://www.ers.usda.gov/publications/pub-details/?pubid=44515. (Accessed 7 December 2017).

Howard, R. A. (1971). *Dynamic probabilistic systems*. New York: Wiley.

Iowa State University (ISU). (2004). *Soil survey & digital soil data: ISPAID version 7.1*. http://www.extension.iastate.edu/soils/ispaid.

Jackson-Smith, D. B., Halling, M., de la Hoz, E., McEvoy, J. P., & Horsburgh, J. S. (2010). Measuring conservation program best management practice implementation and maintenance at the watershed scale. *Journal of Soil and Water Conservation, 65*(6), 413–423. https://doi.org/10.2489/jswc.65.6.413.

Knowler, D., & Bradshaw, B. (2007). Farmers' adoption of conservation agriculture: A review and synthesis of recent research. *Food Policy, 32*(1), 25–48.

Knowler, D., Bradshaw, B., & Holmes, E. (2014). Conservation agriculture: Farmer adoption and policy issues. In P. B. Thompson, & D. M. Kaplan (Eds.), *Encyclopedia of Food and agricultural ethics* (pp. 1–10). Netherlands: Springer.

Kurkalova, L. A., & Tran, D. Q. (2017). Is the use of no-till continuous or rotational? Quantifying tillage dynamics from time-ordered spatially aggregated data. *Journal of Soil and Water Conservation, 72*(2), 131–138. https://doi.org/10.2489/jswc.72.2.131.

Lal, R. (2004). Soil carbon sequestration impacts on global climate change and food security. *Science, 304*(5677), 1623–1627.

Lal, R. (2014). Soil conservation and ecosystem services. *International Soil and Water Conservation Research, 2*(3), 36–47. https://doi.org/10.1016/S2095-6339(15)30021-6.

Lambert, D. M., Sullivan, P., Claassen, R., & Foreman, L. (2007). Profiles of US farm households adopting conservation-compatible practices. *Land Use Policy, 24*(1), 72–88.

Lee, T. C., Judge, G. G., & Takayama, T. (1965). On estimating the transition probabilities of a Markov process. *Journal of Farm Economics, 47*(3), 742–762.

Lewandrowski, J., Peters, M., Jones, C., House, R., Sperow, M., Eve, M., et al. (2004). *Economics of sequestering carbon in the US agricultural sector*. Technical Bulletin Number 1090, USDA ERS http://extension.agron.iastate.edu/soilmgmt/Publications/EconSeqCarbon.pdf.

Lobb, D. A., Huffman, E., & Reicosky, D. C. (2007). Importance of information on tillage practices in the modelling of environmental processes and in the use of environmental indicators. *Journal of Environmental Management, 82*(3),

377–387. https://doi.org/10.1016/j.jenvman.2006.04.019.
Mangalassery, S., Sjögersten, S., Sparkes, D. L., Sturrock, C. J., Craigon, J., & Mooney, S. J. (2014). To what extent can zero tillage lead to a reduction in greenhouse gas emissions from temperate soils? *Scientific Reports, 4*, 4586. https://doi.org/10.1038/srep04586.
Mueller, D., Robertson, A., Sisson, A., & Tylka, G. (2010). *Soybean diseases*. Iowa State University Extension, publication CSI-0004.
Napier, T.,L., & Tucker, M. (2001). Use of soil and water protection practices among farmers in three midwest watersheds. *Environmental Management, 27*(2), 269–279.
Ogle, S. M., Breidt, F.,J., Easter, M., Williams, S., Killian, K., & Paustian, K. (2010). Scale and uncertainty in modeled soil organic carbon stock changes for US croplands using a process-based model. *Global Change Biology, 16*(2), 810–822. https://doi.org/10.1111/j.1365-2486.2009.01951.x.
Osmond, D., Meals, D., Hoag, D., Arabi, M., Luloff, A., Jennings, G., et al. (2012). Improving conservation practices programming to protect water quality in agricultural watersheds: Lessons learned from the national Institute of food and agriculture–conservation effects assessment Project. *Journal of Soil and Water Conservation, 67*(5), 122A–127A. https://doi.org/10.2489/jswc.67.5.122A.
Panagopoulos, Y., Gassman, P. W., Jha, M. K., Kling, C. L., Campbell, T., Srinivasan, R., et al. (2015). A refined regional modeling approach for the Corn Belt – experiences and recommendations for large-scale integrated modeling. *Journal of Hydrology, 524*, 348–366. https://doi.org/10.1016/j.jhydrol.2015.02.039.
Panagopoulos, Y., Gassman, P. W., Kling, C. L., Cibin, R., & Chaubey, I. (2017). Water quality assessment of large-scale bioenergy cropping scenarios for the upper Mississippi and Ohio-Tennessee river basins. *JAWRA Journal of the American Water Resources Association, 53*(6), 1355–1367. https://doi.org/10.1111/1752-1688.12594.
Perry, E. D., Moschini, G., & Hennessy, D. A. (2016). Testing for complementarity: Glyphosate tolerant soybeans and conservation tillage. *American Journal of Agricultural Economics, 98*(3), 765–784. https://doi.org/10.1093/ajae/aaw001.
Plourde, J. D., Pijanowski, B. C., & Pekin, B. K. (2013). Evidence for increased monoculture cropping in the Central United States. *Agriculture, Ecosystems & Environment, 165*, 50–59. https://doi.org/10.1016/j.agee.2012.11.011.
Powlson, D. S., Stirling, C. M., Jat, M. L., Gerard, B. G., Palm, C. A., Sanchez, P. A., et al. (2014). Limited potential of no-till agriculture for climate change mitigation. *Nature Climate Change, 4*(8), 678–683. https://doi.org/10.1038/nclimate2292.
Prokopy, L. S., Floress, K., Klotthor-Weinkauf, D., & Baumgart-Getz, A. (2008). Determinants of agricultural best management practice adoption: Evidence from the literature. *Journal of Soil and Water Conservation, 63*(5), 300–311.
Robertson, P. G., Gross, K. L., Hamilton, S. K., Landis, D. A., Schmidt, T. M., Snapp, S. S., et al. (2014). Farming for ecosystem services: An ecological approach to production agriculture. *BioScience, 64*(5), 404–415. https://doi.org/10.1093/biosci/biu037.
Sahajpal, R., Zhang, X., Izaurralde, R. C., Gelfand, I., & Hurtt, G. C. (2014). Identifying representative crop rotation patterns and grassland loss in the US Western Corn Belt. *Computers and Electronics in Agriculture, 108*, 173–182. https://doi.org/10.1016/j.compag.2014.08.005.
Sainju, U. M., Senwo, Z. N., Nyakatawa, E. Z., Tazisong, I. A., & Reddy, K. C. (2008). Soil carbon and nitrogen sequestration as affected by long-term tillage, cropping systems, and nitrogen fertilizer sources. *Agriculture, Ecosystems & Environment, 127*(3–4), 234–240. https://doi.org/10.1016/j.agee.2008.04.006.
Schlotzhauer, S. D., & Littell, R. C. (1997). *SAS system for elementary statistical analysis* (2nd ed.). Cary (NC): SAS Institute, Inc.
Secchi, S., Gassman, P. W., Jha, M., Kurkalova, L. A., Feng, H., Campbell, T., et al. (2007). The cost of clean water: Assessing agricultural pollution reduction at the watershed scale. *Journal of Soil and Water Conservation, 62*(1), 10–21.
Secchi, S., Gassman, P. W., Williams, J. R., & Babcock, B. A. (2009). Corn-based ethanol production and environmental quality: A case of Iowa and the conservation reserve program. *Environmental Management, 44*(4), 732–744. https://doi.org/10.1007/s00267-009-9365-x.
Secchi, S., Kurkalova, L., Gassman, P. W., & Hart, C. (2011). Land use change in a biofuels hotspot: The case of Iowa. *Biomass and Bioenergy, 35*(6), 2391–2400. https://doi.org/10.1016/j.biombioe.2010.08.047. USA.
Sharma, V., Irmak, S., Kilic, A., Sharma, V., Gilley, J. E., Meyer, G. E., et al. (2016). Quantification and mapping of surface residue cover and tillage practices for maize and soybean fields in south central Nebraska-USA using Landsat imagery. *T ASABE, 59*(3), 925–939. https://doi.org/10.13031/trans.59.11489.
Six, J., Ogle, S. M., Jay, B. F., Conant, R. T., Mosier, A. R., & Paustian, K. (2004). The potential to mitigate global warming with no-tillage management is only realized when practised in the long term. *Global Change Biology, 10*(2), 155–160. https://doi.org/10.1111/j.1529-8817.2003.00730.x.
Stern, A. J., Doraiswamy, P. C., & Raymond, H. J. E. (2012). Changes of crop rotation in Iowa determined from the United States Department of Agriculture, National Agricultural Statistics Service cropland data layer product. *Journal of Applied Remote Sensing, 6*(1), 063590. https://doi.org/10.1117/1.jrs.6.063590, 063590.
Tomer, M. D., Moorman, T. B., James, D. E., Hadish, G., & Rossi, C. G. (2008). Assessment of the Iowa river's south fork watershed: Part 2. Conservation practices. *Journal of Soil and Water Conservation, 63*(6), 371–379. https://doi.org/10.2489/jswc.63.6.371.
Tomer, M. D., Sadler, E. J., Lizotte, R. E., Bryant, R. B., Potter, T. L., Moore, M. T., et al. (2014). A decade of conservation effects assessment research by the USDA Agricultural Research Service: Progress overview and future outlook. *Journal of Soil and Water Conservation, 69*(5), 365–373. https://doi.org/10.2489/jswc.69.5.365.
Torre Ugarte, D. G. D. L., Hellwinckel, C. M., & Larson, J. A. (2004). Enhancing agriculture's potential to sequester carbon: A framework to estimate incentive levels for reduced tillage. *Environmental Management, 33*(1), S229–S237. https://doi.org/10.1007/s00267-003-9133-2.
UNEP. (2013). *The Emissions Gap Report 2013 A UNEP Synthesis Report*.
Uri, N. D. (2001). The potential impact of conservation practices in US agriculture on global climate change. *Agroecology and Sustainable Food Systems, 18*(1), 109–131. https://doi.org/10.1300/J064v18n01_09.
U.S. Department of Agriculture, Natural Resources Conservation Service (USDA-NRCS). (2002). *Farm Bill 2002 highly erodible land & wetland conservation compliance*. https://prod.nrcs.usda.gov/Internet/FSE_DOCUMENTS/nrcs143_007707.pdf. (Accessed 12 May 2017).
U.S. Department of Agriculture, Natural Resources Conservation Service (USDA-NRCS). (2012). *Assessment of the effects of conservation practices on cultivated cropland in the Upper Mississippi River Basin*. Washington, DC https://www.nrcs.usda.gov/Internet/FSE_DOCUMENTS/stelprdb1042093.pdf.
U.S. Department of Agriculture, Natural Resources Conservation Service (USDA-NRCS). (2015). *Soil health literature summary – effects of conservation practices on soil properties in areas of cropland*. https://www.nrcs.usda.gov/wps/portal/nrcs/detailfull/soils/health/?cid=stelprdb1257753. (Accessed 5 January 2018).
U.S. Department of Agriculture- National AgricultuStatistical Service (USDA-NASS). (2019). *Census of agriculture*. February 2019 https://www.nass.usda.gov/Quick_Stats/.
U.S. Department of Agriculture–Economic Research Service (USDA-ERS). (2018). *Tailored reports: Crop production practices*. https://data.ers.usda.gov/reports.aspx?ID=17883#Pe3788618d83047a98245ed80997d743b_8_65iT0R0T0R0x0. (Accessed 5 January 2018).
VandenBygaart, A. J. (2016). The myth that no-till can mitigate global climate change. *Agriculture, Ecosystems & Environment, 216*, 98–99. https://doi.org/10.1016/j.agee.2015.09.013.
Wade, T., & Claassen, R. (2017). Modeling no-till adoption by corn and soybean producers: Insights into sustained adoption. *Journal of Agricultural & Applied Economics, 49*(2), 186–210. https://doi.org/10.1017/aae.2016.48.
Wallander, S., Bowman, M., Beeson, P., & Claassen, R. (2018). *Farmers and habits: The challenge of identifying the sources of persistence in tillage decisions*. Invited paper presented at the 2018. Philadelphia, PA: ASSA Annual Meeting. January 05-07.
Wu, J., & Babcock, B. A. (1998). The choice of tillage, rotation, and soil testing practices: Economic and environmental implications. *American Journal of Agricultural Economics, 80*(3), 494–511. https://doi.org/10.2307/1244552.
Zheng, B., Campbell, J., Serbin, G., & Galbraith, J. (2014). Remote sensing of crop residue and tillage practices: Present capabilities and future prospects. *Soil and Tillage Research, 138*(0), 26–34.
Zimmermann, A., & Heckelei, T. (2012). Structural change of european dairy farms – a cross-regional analysis. *Journal of Agricultural Economics, 63*(3), 576–603. https://doi.org/10.1111/j.1477-9552.2012.00355.x.

International Soil and Water Conservation Research 7 (2019) 119–129

Contents lists available at ScienceDirect

International Soil and Water Conservation Research

journal homepage: www.elsevier.com/locate/iswcr

Original Research Article

Suspended sediment load prediction using non-dominated sorting genetic algorithm II

Mahmoudreza Tabatabaei *, Amin Salehpour Jam, Seyed Ahmad Hosseini

Soil Conservation and Watershed Management Research Institute, Agricultural Research, Education and Extension Organization (AREEO), Tehran, Iran

ARTICLE INFO

Article history:
Received 24 June 2018
Received in revised form
27 November 2018
Accepted 30 January 2019
Available online 31 January 2019

Keywords:
Clustering
Neural network
Non-dominated sorting genetic algorithm II (NSGA-II)
Sediment rating curve
Self-organizing map

ABSTRACT

Awareness of suspended sediment load (SSL) and its continuous monitoring plays an important role in soil erosion studies and watershed management. Despite the common use of the conventional model of the sediment rating curve (SRC) and the methods proposed to correct it, the results of this model are still not sufficiently accurate. In this study, in order to increase the efficiency of SRC model, a multi-objective optimization approach is proposed using the Non-dominated Sorting Genetic Algorithm II (NSGA-II) algorithm. The instantaneous flow discharge and SSL data from the Ramian hydrometric station on the Ghorichay River, Iran are used as a case study. In the first part of the study, using self-organizing map (SOM), an unsupervised artificial neural network, the data were clustered and classified as two homogeneous groups as 70% and 30% for use in calibration and evaluation of SRC models, respectively. In the second part of the study, two different groups of SRC model comprised of conventional SRC models and optimized models (single and multi-objective optimization algorithms) were extracted from calibration data set and their performance was evaluated. The comparative analysis of the results revealed that the optimal SRC model achieved through NSGA-II algorithm was superior to the SRC models in the daily SSL estimation for the data used in this study. Given that the use of the SRC model is common, the proposed model in this study can increase the efficiency of this regression model.

1. Introduction

Estimating the SSL is very crucial for water resource quantitative and qualitative research (Buyukyildiz & Kumcu, 2017; Salehpour Jam et al., 2017; Sarkar, Sharma, & Singh, 2017; Tayfur, 2012; Vercruysse, Grabowski, & Rickson, 2017). Considering the restrictions of time, cost etc., the SSL is typically predicted indirectly by SRC model. The standard SRC model is the power regression equation, which is firstly calibrated via taking logarithm of variables corresponding to sediment and flow discharge and formulating a linear regression, and lastly, the linear regression coefficients to be computed with the error least square technique. Once the SSL is computed, the achieved amounts should be back-transformed (an anti-log must be taken) in order to be utilized. Investigations have revealed that the remaining distribution (error values) is not normal, and the average distribution is higher than zero (Kao, Lee, & Milliman, 2005). In other words, when calculating model coefficients, a bias is created and cause the expected amount of SSL become smaller than its observational corresponding values (Ferguson, 1986). This problem is most clear in flood discharges and leads to more errors. To correct the bias caused from the logarithmic transformation, diverse types of correction factors have been proposed for instance the minimum variance unbiased estimator (MVUE or CF1) (Cohn, Delong, Gilroy, Hirsch, & Wells, 1989), non-parametric smearing estimator (CF2) (Duan, 1983), the maximum probability estimation (Ferguson, 1986), Food and Agriculture Organization (FAO) correction factor (Jones, Berney, Carr, & Barrett, 1981) and other approaches (Jansson, 1996; Miller, 1984). All approaches aim to improve the values that are computed via SRC model. However, these correction factors sometimes lead to another bias in the form of an overestimation in addition to generating the findings with the similar data differently (Kao et al., 2005). Recent years, the application of computational intelligence approaches in calibration and estimation of environmental variables like SSL and modeling the complex hydrological procedures, including rainfall-runoff has been quickly increasing (Buyukyildiz & Kumcu, 2017; Chau & Jiang, 2002; Chen & Chau, 2016; Fotovatikhah et al., 2018; Olyaie, Banejad, Chau, & Melesse, 2015; Taormina & Chau, 2015; Wang, Xu, Chau, & Lei, 2014; Wu & Chau, 2011). Because of the drawbacks related to gradient based algorithms (converge to optimum sets of model factors), use of meta-heuristic or evolutionary algorithms in calibrating hydrologic models has been also enhanced

* Corresponding author.
E-mail address: tabatabaei@scwmri.ac.ir (M. Tabatabaei).

Peer review under responsibility of International Research and Training Center on Erosion and Sedimentation and China Water and Power Press.

https://doi.org/10.1016/j.iswcr.2019.01.004

(Bekele & Nicklow, 2007). However, evolutionary algorithms have been essentially proved to carry out well on difficult optimization problems including nonlinear, non-convex, and noisy functions (Schwefel, 1995). Kisi, Keshavarzi, Shiri, Zounemat-Kermani, and Omran (2017) utilized particle swarm optimization (PSO) and differential evolution (DE) algorithms for training artificial neural networks (ANNs) (ANN-PSO and ANN-DE) for modeling qualitative parameters corresponding to groundwater, i.e., SAR and SO4. In other researches performed with Altunkaynak (2009), MohammadRezapour, Nour Jou, and Zeynali (2016) and Tabatabaei and Salehpour Jam (2017), the optimization of relations between flow and sediment discharge was performed with genetic and PSO algorithms. The mentioned evolutionary algorithms are single-objective, and optimization of the flow discharge and SSL relationship is accomplished only by minimizing an objective function (error function). The comparison of the findings of models presented that the results of SRC models optimized using evolutionary algorithms were better comparing to those of the conventional SRC models. In general, in most cases in automatic calibration, processes have focused mostly on applying a single overall objective function (e.g. mean square error (MSE)) for measuring the goodness-of-fit related to the calibrated model (Madsen, 2000). Yapo, Gupta, and Sorooshian (1998) showed that the main attention of these approaches is on choosing and searching the values of model factors, which minimize the distance between observed and simulated data. Considering only one objective function is not sufficient for simulation of all aspects of a system (Madsen, 2000). In this regard, Nash and Sutcliffe (1970) presented the Nash-Sutcliffe efficiency (NSE), which is the most common index (Gupta, Kling, Yilmaz, & Martinez, 2009). In spite of the popularity of the NSE, it has several disadvantages (Gupta et al., 2009; Moriasi et al., 2007).

The NSE has excellent sensitivity to peak flow values since it utilizes squared errors that result in less sensitivity of the hydrologic models to simulate small flows (Criss & Winston, 2008). There is a same condition to other objective functions including root mean square error (RMSE) and MSE, which minimize the residuals square. Mean absolute error (MAE) is less sensitive to large values of flow and more sensitive to smaller flow values in comparison with NSE and RMSE and expresses model efficiency more consistently (Muleta, 2011). Based on Muleta (2011), accuracy of multi-objective calibrations can be improved by selecting one objective function from each group (e.g. MAE, which is sensitive to small flows and NSE or RMSE that are sensitive to large flows). In this regard, the multi-objective optimization algorithm of NSGA-II was introduced by Srinivas and Deb (1994) that is a newer version of NSGA and can be utilized in the automatic calibrations. For example, Choudhury and Sil (2010) employed NSGA to simulate water discharge and SSL in the Mississippi River Basin, USA. Achieved findings showed that a model with multiple objectives improved model performance.

In Iran, due to the lack of facilities and financial constraints, continuous measurements and monitoring flow discharge and sediment loads of rivers at hydrometric stations are not possible, so providing a suitable method that can estimate the amount of suspended load is very important. Therefore, the main objectives of this study are (1) to optimize the coefficients of SRC model by employing different objective functions, and (2) to compare and evaluate the results of the optimized SRC model with other conventional SRC models.

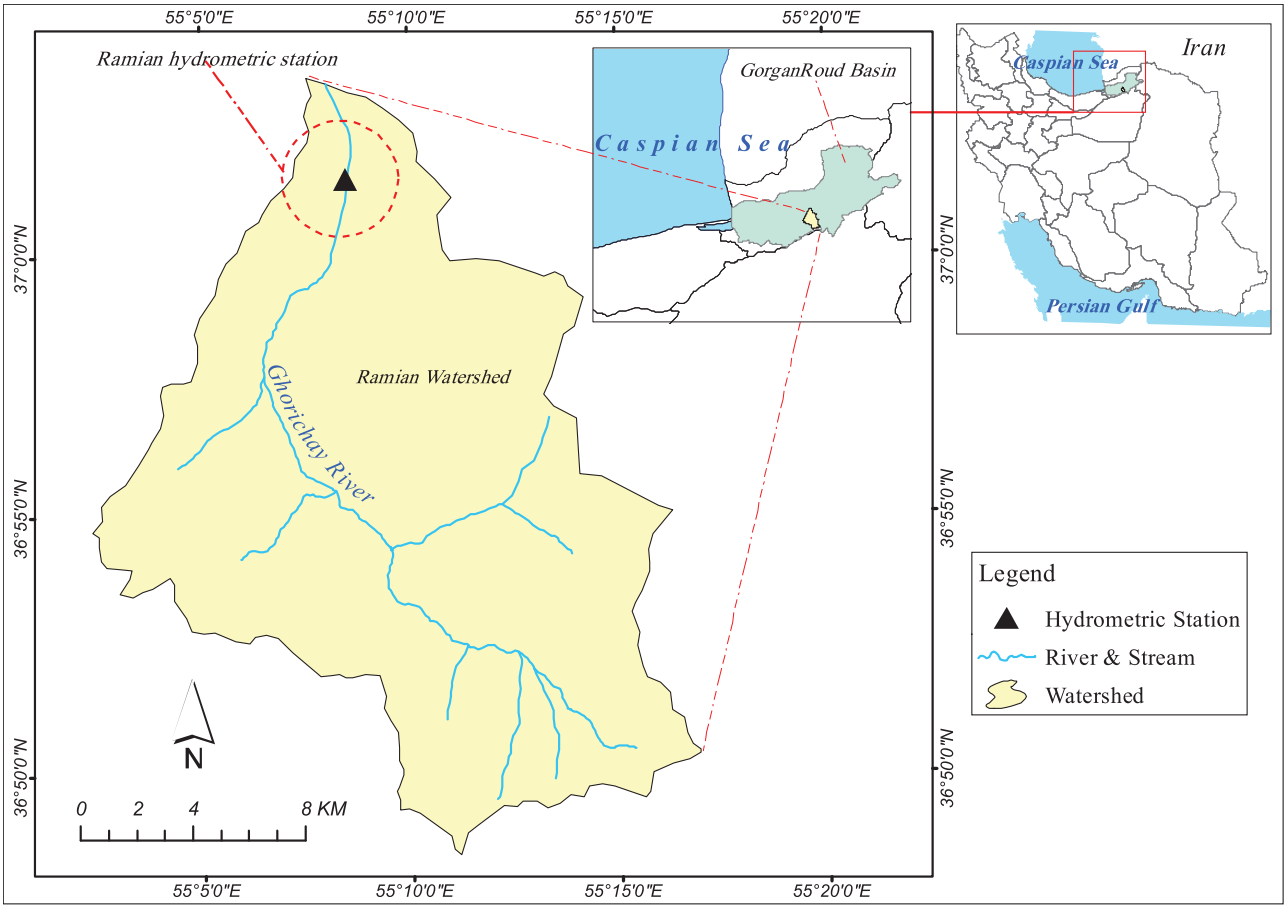

Fig. 1. The location of Ramian watershed and Ramian Hydrometric Station.

2. Materials and methods

2.1. Study area

Ramian watershed (55°02′-55°15′ E and 36°48′- 37°02′ N) which is one of the sub-basins of GorganRoud basin has an area of 30345 ha and located in the Golestan province in Iran (Fig. 1).

It has a main river (Ghorichay River) of 33 km long and an average elevation of 1189 m above sea level. The river crosses a different height altitude along the way, so that its upstream area is quite mountainous and is more forested in terms of land use, but the surrounding areas are almost flat and allocated to agricultural lands. The study area has a humid to semi-humid climate based on the method of De-Martonne and its soil texture is silt-loam. In Table 1, some of the physiographic and land use characteristics of the Ramian watershed are presented.

2.2. Data

The data utilized in current study includes 410 information records of hydrometric data corresponding to instantaneous flow and sediment discharge in the Ramian hydrometric station over 1966–2012 (46 years). At this station, sampling of SSL is carried out by USDH-48 instrument once or twice a month and at the same time as the flow discharge is measured. Sampling is done in shallow flow depth manually by a person. In times of flooding, the sampling of the flow discharge is done more. The statistical factors of the data set are presented in Table 2.

As can be observed in the Table 2, the SSL has a high variation coefficient and skewness. Moreover, the variation between its minimum and maximum is also high. Totally, the findings of the extracted statistical data showed that there is a difficulty of SSL modeling in the Ramian hydrometric station.

2.3. Sediment Rating Curve (SRC) models and bias correction factors

The SRC model is a power regression relationship between flow discharge and SSL and can be used to estimate the amount of SSL from flow discharge. The SRC model is based on Eq. (1) and the least square technique (Ulke, Tayfur, & Ozkul, 2009):

$$SSL_{(t)} = aQ_{(t)}^{b} \quad (1)$$

Where, $Q_{(t)}$ represents the daily average flow discharge (m^3/s), $SSL_{(t)}$ refers to the SSL (ton/day), and a and b represent the constant coefficients of the regression equation.

In this equation, suspended sediment concentration (SSC) (mg/l) can be used instead of SSL.

In Eq. (1), the values of a and b are determined from a linear regression relationship between (log SSL) and (log Q). In order to use the estimated SSL values, it is necessary to convert these values from logarithmic space to an arithmetic space. This conversion causes a bias and therefore, the estimated SSL is less than its actual value. In order to reduce the log-transformations bias, various correction factors (CFs) have been suggested so far, and some of them have been used in this study.

Table 1
Ramian watershed area characteristics.

Physiographic/Land use characteristics	values
Area (ha)	30345
Main stream length (km)	33
Mean slope (%)	35.7
Minimum elevation (m)	127
Maximum elevation (m)	2774
Mean elevation (m)	1189
Forest (%)	57.67
Rangeland (%)	10.21
Agriculture (%)	32.12

Table 2
Statistical characteristics of data.

Data Set	Data Type	$\bar{X}$ [a]	S_x [b]	X_{max} [c]	X_{min} [d]	C_{sx} [e]	C_v [f]
Whole data	Flow Discharge (m^3/s)	1.53	2.29	13.46	0.002	2.57	1.49
	SSL[g] (ton/day)	384.12	1491.76	14166.47	0.001	6.51	3.88

[a] Mean of data.
[b] Standard deviation of data.
[c] Maximum of data.
[d] Minimum of data.
[e] Skewness coefficient of data.
[f] Variation coefficient of data.
[g] Suspended sediment load.

2.3.1. Bias correction factors (CFs)

The general form of using the CFs is the following equation:

$$SSL_{(t)} = CF.\, aQ_{(t)}^{b} \quad (2)$$

Where, $SSL_{(t)}$ and $Q_{(t)}$ are the variables, a and b are the coefficients used in Eq. (1), and CF is a correction factor. There are three CFs are presented in this study:

FAO

The FAO correction factor proposed by Jones et al. (1981) is used to modify the estimated values of SRC model (Eq. (1)) in arid and semi-arid regions.

$$FAO = \frac{\bar{Qs}}{\bar{Qw}^{b}} \quad (3)$$

Where, $\bar{Qs}$ is mean sediment discharge (mg/l or ton/day); $\bar{Qw}$ is mean flow discharge (m3/s); and b is the parameter used in the SRC model (Eq. (1)).

Finally, a coefficient (in Eq. (1)) is replaced with FAO correction factor.

QMLE

The quasi-maximum likelihood estimator (QMLE or CF1 correction factor) is a parametric method (Ferguson, 1986) which is based on the following equation:

$$CF1 = e^{2.65\sigma^2} \quad (4)$$

Where, e is the exponential function and σ is the standard error of linear log-regression of Eq. (1).

Smearing

Smearing correction factor (CF2) is a nonparametric method and is based on Eq. (5) (Duan, 1983):

$$CF2 = \sum_{i=1}^{n} \frac{1}{n} 10^{e_i} \quad (5)$$

Where, n is the sample size; and e_i is the error term, or the residual, for each sample:

$$e_i = \log Qs_i - \left(a + b \log Qw_i\right) \quad (6)$$

Where, a and b are the coefficients of linear log-regression of Eq. (1).

Another valuable technique for making an SRC model is the

"mean load within discharge classes" SRC. This technique is also on the basis of Eq. (1), with the difference that the technique utilizes the mean sediment load within the flow discharge classes (Jansson, 1996).

In the present study, in order to facilitate the comparison of the models, the name of models is abbreviated and they are listed in the order, including SRC, SRC-FAO, SRC-CF1, SRC-CF2, and SRC-MeanLoad. In addition to the conventional SRC models mentioned above, the multi-objective optimization algorithm has also been used to improve the performance of SRC model which are referred in the following:

2.4. Optimization of the coefficients the SRC model using Multi-objective optimization

2.4.1. Multi-objective optimization

If the optimization problem deals with multiple objective functions, the procedure of finding one or more optimum solution is named multi-objective optimization. In such case, it is nearly difficult to obtain a solution that optimizes all the objectives and efforts should be to achieve a set of solutions (Pareto set) with relative optimum for all goals (Deb, 2001). In the Pareto optimum set, as none of the answers dominate each other, moving from one point (the solution) to another point, one objective function becomes better and the other one is worse (Yee, Ray, & Rangaiah, 2003).

2.4.2. Non-Dominated Sorting Genetic Algorithm II (NSGA-II)

NSGA-II, which is a newer version of NSGA (Srinivas & Deb, 1994), is the multi-objective evolutionary optimization algorithm utilized in a large number of disciplines including the development of the automatic calibration routine (Bekele & Nicklow, 2007). The algorithm utilizes a quick and non-dominating sorting technique for distinguishing solutions based on the concept of Pareto dominance and optimality (Veldhuizen & Lamont, 2000), The NSGA-II algorithm is recognized as an algorithm based on population. It begins with the random generation of the parent population (Pt), which includes potential solutions (in current research, the coefficients of a and b in Eq. (1)) for a problem. Next, by applying a binary tournament selection operator, a population set corresponding to that generation will be selected for participating at the crossover and mutation operations. On the part of chosen population, the crossover and on the rest mutation occur and a population of offspring and mutants are generated (Qt). In the following, the population is combined with the main population (Rt). The members of the recently generated population are firstly set in terms of rank and ascending. The rank value is a fitness value computed in terms of Pareto dominance and equal to the non-domination Level. As an example, rank 1, matches the best level of non-domination Level, rank 2, for the next best level and so on. Based on the rank value of all solutions, that solution is assigned to diverse fronts. Consequently, the first front includes solutions, which dominate the rest of front solutions. Members of the population with the similar rank are arranged in descending order in terms of Crowding-Distance (Deb, Pratap, Agarwal, & Meyarivan, 2002) (Fig. 2 and Eqs. (7)–(9)).

$$d_i^1 = \frac{f_1(x_{i+1}) - f_1(x_{i-1})}{f_1^{max} - f_1^{min}} \tag{7}$$

$$d_i^2 = \frac{f_2(x_{i+1}) - f_2(x_{i-1})}{f_2^{max} - f_2^{min}} \tag{8}$$

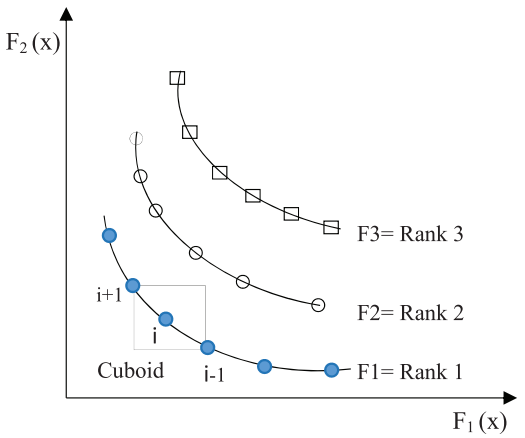

Fig. 2. Computation of crowding distance. The marked points with colored circles show the solutions of the identical non-dominated front.

$$d_i = d_i^1 + d_i^2 \tag{9}$$

Where, d_i^1 and d_i^2 represent the crowding-distance values corresponding to the ith solution (a and b coefficients in Eq. 1) for the first and second objective functions (f1, f2) respectively; f1 (xi+1) and f2(xi+1) refer to the first and the second objective function values for the (i + 1)th solution and f1(xi-1), and f2(xi-1) represent the first and second objective function values for the (i-1) th solution, respectively; f_1^{min}, f_1^{max} , f_2^{min} and f_2^{max} represent the least and highest population values for the first and second objective functions, respectively.

The outcome is that the population members are ranked mainly in rank, and secondly in terms of the crowding distance. Consequently, equal to the number of main populations (Pt), members from the top of the arranged list are chosen, and the other populations are discarded. This cycle is repeated to meet the desired conditions.

2.4.3. Calibration objective functions

According to the earlier literature review, functions including RMSE, MSE, and NSE when are applying as objective function tends to provide a stronger emphasis on fitting model for greater or values of peak output. However, in comparison with the RMSE, an objective function that uses the log-transformation of the observed and simulated outputs, rather than their original values (LOGE) emphasizes on the fitting model for the lower output values (Bekele & Nicklow, 2007):

$$LOGE = \sqrt{\frac{1}{N} \times \sum_{J=1}^{N} \left(Log\left(\frac{O_j}{S_j}\right)\right)^2} \tag{10}$$

Where Oj and Sj are found and simulated SSL, respectively, and N refers to the total number of data.

In current study, multi-objective function was made by choosing one objective function from each group (NSE or RMSE to emphasize on high SSL and MAE or LOGE to emphasize on low SSL), Eqs. (10)–(12) and (14):

$$RMSE = \sqrt{\frac{1}{N} \times \sum_{J=1}^{N} (O_j - S_j)^2} \tag{11}$$

$$MAE = \frac{\sum_{J=1}^{N} \left|(O_j - S_j)\right|}{N} \tag{12}$$

$$NSE = 1 - \frac{\sum_{J=1}^{N}(O_j - S_j)^2}{\sum_{J=1}^{N}(O_j - \bar{O}_j)^2} \quad (13)$$

In Eq. (13), $\bar{O}_j$ represents the average of experimental SSL of calibration data set. The NSE amounts are in the range of negative infinity to 1, where 1 represents a perfect model. It should be mentioned that if this equation is used as an objective function, only its fractional part (number 1 and minus) is utilized and the model tries for minimizing it (Eq. (14)). Consequently, by minimizing this section, the value of NSE results in the highest values, which is one.

$$NS\_objfun = \frac{\sum_{J=1}^{N}(O_j - S_j)^2}{\sum_{J=1}^{N}(O_j - \bar{O}_j)^2} \quad (14)$$

2.4.4. Calibration scenarios in genetic algorithms

In current study, the optimization procedures are formulated as a single objective function (the first scenario, SRC-GA-I) and multi-objective (the second scenario, SRC-GA-II) involving objective functions showed in Eqs. ((10)–(12) and (14)). The decision variables (a and b coefficients in Eq. (1)) to be calibrated and a vector of these decision variables shows a specific solution for the calibration problem. The calibration outcomes of all models are then assessed on the basis of the evaluation criteria (described in the following section) and the optimal model is shown with the best optimization.

2.5. Preparing homogenous data for the model calibration and evaluation

To create robust SRC models, the calibration data should be representative data of the statistical period for creating robust SRC models. Furthermore, to assess the models, the test data set should be as same as the set of calibration data (in terms of statistical parameters) and have the similar distribution. Therefore, the approaches of SOM clustering and proportional allocation were utilized for clustering data and for sampling the clusters, respectively, to provide two homogenous data groups containing calibration and test data sets. The optimum number of clusters was identified with Davies-Bouldin validity index. For statistical analyzing the clustering outcomes, in addition to comparing the statistical parameters, the similarity of data distribution (in both calibration and test data sets) was studied through Two-Sample Kolmogorov-Smirnov Test (KS). All these phases are summarized in the following:

2.5.1. Data clustering using self-organizing map (SOM) neural network

Clustering data is an appropriate technique to analyze statistical data in which same data are categorized into diverse clusters in such way that the samples in every cluster are as same as one another but diverse from samples of other clusters (Yar Kiani, 2009). The SOM is an unsupervised artificial neural network (ANN) showed by Kohonen (1982) and is a strong technique for clustering data. In general, learning the SOM network will be performed for clustering input data from a greater dimensional space onto a lower dimensional discrete network (typically two-dimensional (2D)) corresponding to neurons in an output layer. A complete explanation of the SOM procedure was suggested by Kohonen (1982).

2.5.2. Cluster validity index (Determining the optimal number of clusters)

Most indices assessing the quality of clustering utilize the distance criterion for computing intra-cluster compactness and intra-cluster separation (May, Maier, & Dandy, 2010). Davies-Bouldin index in used in current study because of its proper efficiency to determine the optimal number of clusters. It computes average similarity between two most similar clusters (Yar Kiani, 2009). The lower computed value corresponding to the index enhances the quality of clustering.

2.5.3. Cluster sampling method

To generate two homogenous data sets that are as same as probable (calibration and test data sets), the proportional allocation technique was utilized to sample the clusters. In this technique, the number of samples varies with the dimension of the cluster, as the dimension of a cluster enhances, the number of samples enhances too, and vice versa (May et al., 2010). In the current study, 80% of the data were utilized to make the calibration set, and the rest of data (20%) were utilized to create the test sets.

2.5.4. Statistical analysis of the data obtained from clustering

Besides comparing statistical data (mean, standard deviation, skewness, etc.), the nonparametric two-sample Kolmogorov-Smirnov (K-S) test, was utilized for testing and comparing homogeneity and the similarity of the data in calibration and test data sets. The KS test was done at error level of 1% ($\alpha = 1\%$).

2.6. Evaluating and comparing the model efficiency

The number of criteria by which the performance of the models is measured is very diverse. It should be noted that the use of a single criterion can not reflect the different characteristics of the model. Therefore, it is necessary to use several different criteria to evaluate the models performance. In this study, to assess the findings obtained from several models (SRC, SRC-CF1, SRC-CF2, SRC-FAO, SRC-Mean-Load, SRC-GA-I and SRC-GA-II) and to compare them, the criteria of RMSE, NSE, MAE (Eqs. (11)–(13)), coefficient of determination (R^2) (Eq. (15)) and percent bias (PBIAS) (Eq. (16)) have been used. In this regard, the RMSE and MAE measure large and low error values, respectively. The NSE criterion acts like RMSE, but it is non-dimensional. The R^2 measures the degree of linear relationship between two variables relative to each other. In this regard, a model can have a high R^2, but its estimated values are very different from reality. Therefore, it is better to use it along with other model evaluation criteria.

$$R^2 = \left[\frac{\sum_{I=1}^{N}(O_j - \bar{O}_j) \times (S_j - \bar{S}_j)}{\sqrt{\sum_{I=1}^{N}(O_j - \bar{O}_j)^2 \times \sum_{I=1}^{N}(S_j - \bar{S}_j)^2}} \right]^2 \quad (15)$$

In the Eq. (15), $\bar{S}_j$ is the mean of estimated SSL of the test data set.

The PBIAS measures the average tendency of the simulated data to be larger or smaller than their observed counterparts (Gupta, Sorooshian, & Yapo, 1999). The optimal value of PBIAS is 0.0, with low-magnitude values indicating accurate model simulation. Positive values indicate model underestimation bias, whereas negative values indicate overestimation bias (Gupta et al., 1999). PBIAS is calculated with Eq. (16):

$$PBIAS = \left[\frac{\sum_{I=1}^{N}(O_j - S_j)}{\sum_{I=1}^{N} O_j} * 100 \right] \quad (16)$$

Where, PBIAS is the deviation of the evaluated data, expressed as a percentage.

2.7. Software used to implement statistical analysis and model optimization

In this study, MATLAB R2015b software was utilized for implementing NSGA-II algorithm, clustering the data, and computing the clusters validity index. The statistical analysis corresponding to data was performed using MATLAB software.

3. Results and discussion

3.1. Results of data clustering

Using SOM clustering technique and Davies-Bouldin cluster validity index the optimum number of clusters was obtained as 6 clusters (Fig. 3). The findings of statistical parameters and K-S test are showed in Tables 3 and 4.

In Table 4, h letter refers to a statistic for K-S test in MATLAB software and when h = 0, it means that the null hypothesis is not rejected (which is two variables are from the similar continuous distribution) at the significance level of α (α is the desired significance level, e.g. 0.01). The K-S test presented that the distribution of the related data in both data sets was same (proof of H0 hypothesis of the K-S test). Moreover, these findings are graphically revealed in Fig. 4.

3.2. Results of optimization and modeling

Among the objective functions (LOGE, RMSE, MAE and NS_objfun) used to optimize the SRC-GA-I and SRC-GA-II models, the RMSE for SRC-GA-I model and LOGE and NS_objfun for SRC-GA-II model were selected as the best objective functions, respectively. Fig. 5 represents the Pareto optimum fronts in calibration phase. The figure shows considerable tradeoffs between LOGE and NS_objfun to find optimum parameter set (a and b coefficients in Eq. (1)) that results good results in estimating SSL in calibration process.

In Fig. 6, the fitness of various models of SRC to observational data in calibration data set has been showed. As can be seen, GA models show better fitness than other models.

In this figure some of the data are far from the regression line. This problem can be due to the following reasons: a) climate change, seasonal variability and vegetation changes in watersheds with rain or snow-rain regimes cause the amount of sediment yield and streamflow of watersheds varies considerably over different time periods. In this regard, flow discharges with the same values, but with different origins (due to melting processes or heavy rainstorms) can contain very different suspended sediment concentration (SSC) values. In other words, in the data set on a hydrometric station, there are data recorded with the same flow discharge but with different SSC values. b) At the scale of the flow hydrograph, the amount of sediment recorded in a given discharge at the start of the ascending limb varies with the amount of sediment in the same discharge in the falling limb (hysteresis loops) (Rodríguez-Blanco, Taboada-Castro, Palleiro, & Taboada-Castro, 2010; Sadeghi et al., 2008). The reason is that most portable suspended sediment is displaced by peak discharge. Therefore, in the falling limb of hydrograph, its value decreases. c) The occurrence of consequent floods reduces the SSC of the river, which may result in different SSC in the same flow discharges. d) The discharge-sediment data set recorded at the hydrometric stations may belong to different wet, dry, and normal periods of the watershed, in which case the samples with the same discharge can contain different amount of sediments. e) The spatial distribution of precipitation is one of the important factors affecting the amount of erosion and sediment yield of the watershed. Due to the differences in soil type, land use, slope and other factors, the occurrence of storms with different spatial distribution causes different runoff and sediment rates in the watersheds. In this regard, for example, the core of the rainfall in a rainstorm may be concentrated in the forest and then in the next storms on the plowed slopes, in which case the amount of sediment produced will be very different (Johnson, 1996).

Table 5 shows the findings of evaluating different models of SRC using test data set.

With test data set, the results indicate that GA models (SRC-GA-I and SRC-GA-II) are more favorable than the conventional SRC, SRC-MeanLoad and SRC models corrected using the correction factors (SRC-CF1, SRC-CF2, SRC-FAO). The SRC-GA-II model has the smallest RMSE (669.13 t/day) and MAE (209.39 t/day) and the highest NSE (0.83) and R^2 (0.84) among the SRC models. Additionally, the comparison between the SRC-GA-I and SRC-GA-II models indicate that the performance of the SRC-GA-II model is relatively better than the SRC-GA-I model. After the GA models, the SRC-MeanLoad model has better performance than the SRC, SRC-CF1, SRC-CF2 and SRC-FAO models. The SRC-FAO model has the least amount of RMSE and more NSE in comparing with the models of SRC, SRC-CF1 and SRC-CF2. However, its MAE is higher than the mentioned models. This means that this model estimates high sediment values better than the moderate and low values.

Table 3
Statistical parameters of the variables used in calibration and test data sets.

Model Variables & Data Set			Statistical Parameters			
Flow Discharge (m^3/s)	$\bar{X}$[a]	S_x[b]	X_{max}[c]	X_{min}[d]	C_{sx}[e]	C_v[f]
Calibration Set	1.494	2.239	13.460	0.002	2.737	149.819
Test Set	1.626	2.403	12.740	0.002	2.533	147.760
Suspended Sediment Load (ton/day)						
Calibration Set	374.625	1423.476	12902.797	0.001	6.212	379.973
Test Set	406.269	1646.056	14166.472	0.007	6.832	405.165

[a] Mean of data.
[b] Standard deviation of data.
[c] Maximum of data.
[d] Minimum of data.
[e] Skewness coefficient of data.
[f] Variation coefficient of data.

Table 4
Results of two-sample Kolmogorov-Smirnov test of the data.

Model Variables	Data Sets	P-values[a]	D_c[a]	h[b]
Flow Discharge (m^3/s)	Calibration & Test	0.9621	0.053**	0
Suspended Sediment Load (ton/day)	Calibration & Test	0.98	0.049**	0

** significant at the error level (α) = 1%.
[a] test statistic.
[b] Hypothesis test result in MATLAB.

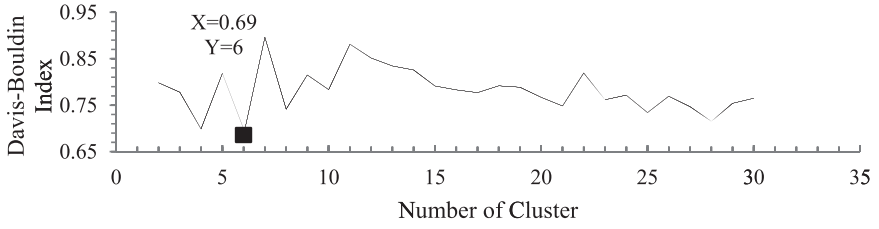

Fig. 3. The optimal cluster numbers using SOM clustering and Davies-Bouldin validity index.

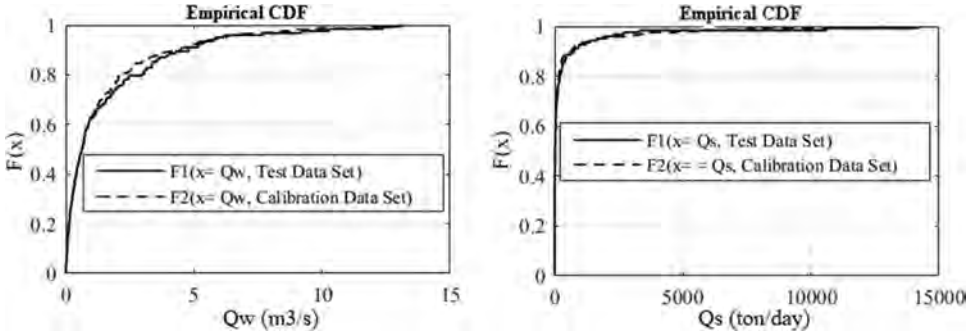

Fig. 4. Comparing the flow discharge distribution (Q_w) and suspended sediment load (Q_s) in the calibration and test data sets using K-S test. CDF is cumulative distribution function.

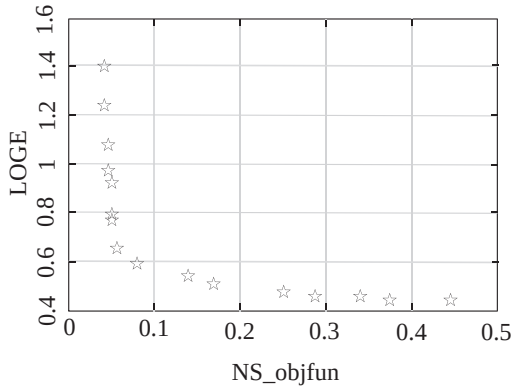

Fig. 5. Pareto optimal front showing Nash-Sutcliffe objective function (NS_objfun) versus logarithmic objective function (LOGE).

Further details on this item are provided later on. Although the SRC-CF1 and SRC-CF2 models have a relatively similar performance, they are, however, superior to the SRC model. Fig. 7 shows scatter plots and findings achieved from simulation of observational suspended sediment discharge corresponding to the test data set of various models.

As can be seen from the figure, the values of the slope, y-intercept and R^2 of the fit line of the SRC-GA-II model (0.89, 63.33 and 0.83, respectively) are better comparing to the corresponding values of the fit lines of the rest of the models. In order to better understand, a logarithmic scale of scatter plots of Fig. 7 is shown in Fig. 8. As shown in Fig. 8, the estimated SSL values of the SRC-FAO model are often higher than the 45° line, in other words, this model overestimates the SSL values much more than their actual values. The FAO correction factor (in the SRC-FAO model) is more affected by flood discharges, and large data in the data set will result in a very large coefficient (200 value in the FAO equation).

Table 5
Results of evaluating various models with test data set.

Performance criteria					
Model Name	Equation	RMSE[a] (ton/day)	MAE[b] (ton/day)	NSE[c]	R^{2d}
SRC[e]	Q_s[f] $= 41.4835Q_w^{1.5538}$	1384.68	289.43	0.29	0.69
SRC-CF[g]1	$Q_s = 94.7814Q_w^{1.5538}$	1070.13	303.36	0.57	0.69
SRC-CF2	$Q_s = 95.7520Q_w^{1.5538}$	1065.64	304.12	0.58	0.69
SRC-FAO[h]	$Q_s = 200.6796Q_w^{1.5538}$	1021.72	452.92	0.61	0.69
SRC-MeanLoad	$Q_s = 100.9007Q_w^{1.6381}$	945.58	311.08	0.67	0.71
SRC-GA[i]-I	$Q_s = 26.71993Q_w^{2.31}$	726.83	238.04	0.8	0.81
SRC-GA-II	$\mathbf{Q_s = 13.4246Q_w^{2.6546}}$	**669.13**	**209.39**	**0.83**	**0.84**

[a] Root mean square error.
[b] Mean absolute error.
[c] Nash-Sutcliffe efficiency.
[d] Coefficient of determination.
[e] Sediment rating curve.
[f] Suspended sediment load (discharge).
[g] Correction factor.
[h] Food and Agriculture Organization.
[i] Genetic algorithm.

Therefore, it is recommended that this coefficient is used for extrapolation and for estimating the sediment of flood events. This result is consistent with the results of Jones et al. (1981).

In addition to evaluating and comparing the performance of the various SRC models in the estimation of daily SSL (as mentioned above), the total estimated SSL amounts for the test data set are prepared in Table 6. This issue is important in management of dams' reservoirs.

The SRC-GA-II, SRC-GA-I, SRC-MeanLoad and SRC-FAO models estimate the observed total SSL of 49971 t as 52290.8, 50346.5, 53468 and 91963.8 t with an overestimation of

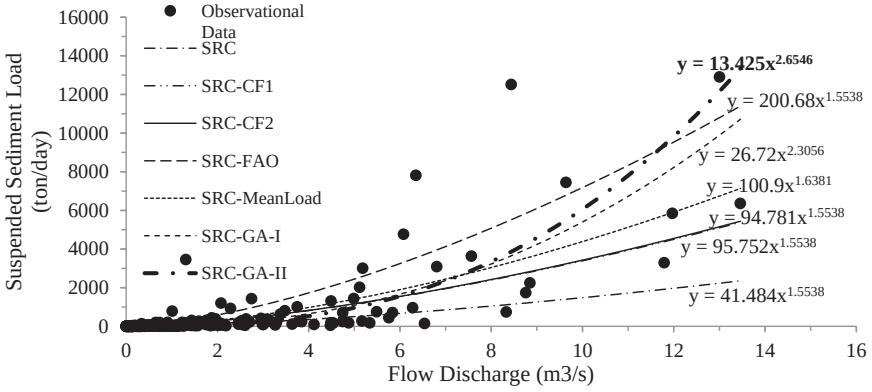

Fig. 6. Fitness of various SRC models to the observational data (calibration data set).

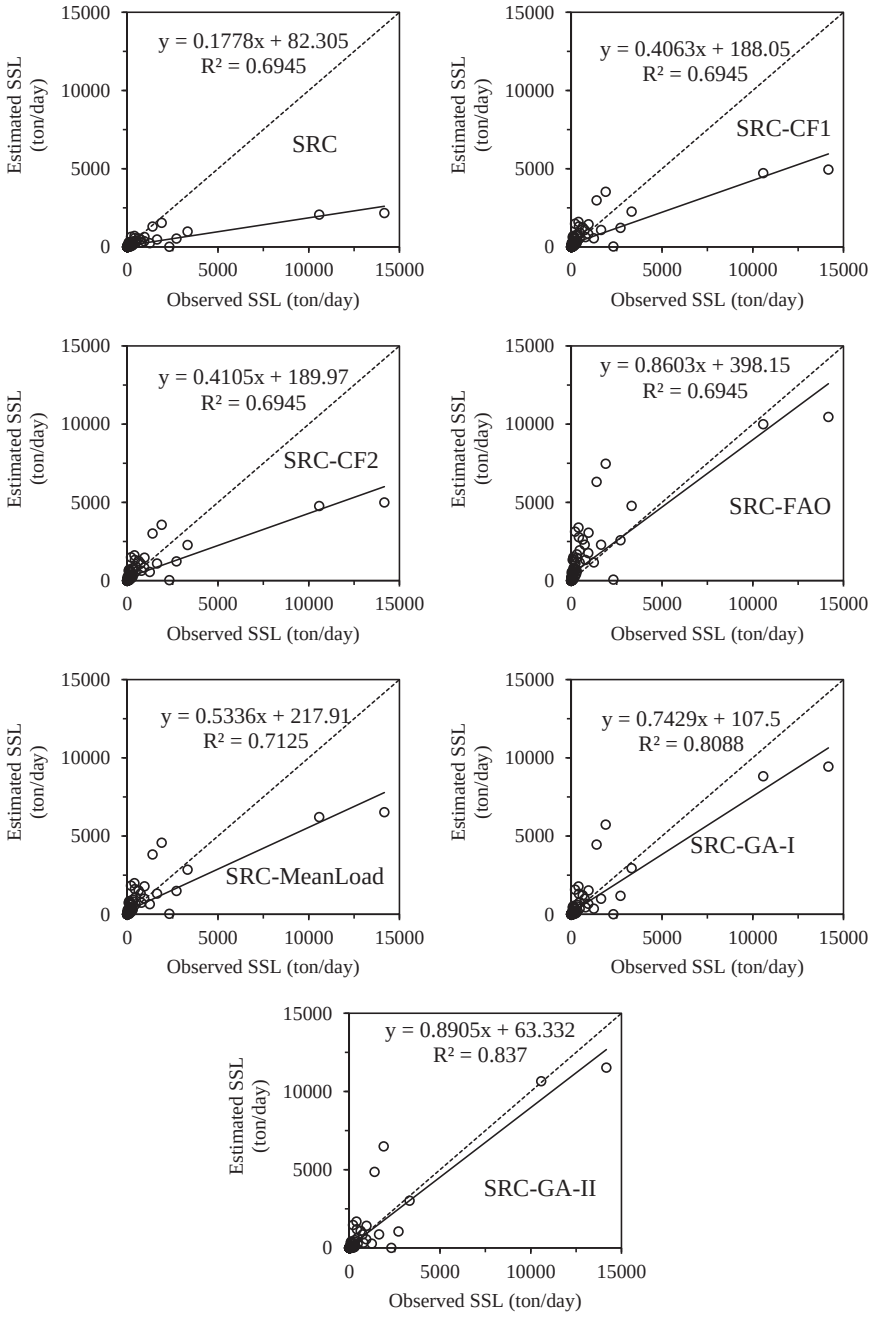

Fig. 7. Scatter plots of observed and estimated SSL by different SRC models for the test data set.

− 0.8%, − 4.6%, − 7% and − 84%, respectively. However, models SRC-CF2 and SRC-CF1 and SRC estimate the total observed SSL as 43879.5, 43434.7 and 19010.3 t respectively, with an underestimation of 12.2%, 13.1% and 62%, respectively. Totally, the SRC-GA-II and SRC-FAO models with the lowest (less than 1%) and highest (more than 80%) amount of relative error are the best and worst models in estimating total SSL, respectively.

The findings of current study about use of evolutionary algorithms are corresponding with studies performed by Altunkaynak (2009), MohammadRezapour et al. (2016) and Swain and Sahoo (2017). Also, like the results of Muleta (2011), the simultaneous application of two objective functions in the multi-objective model (SRC-GA-II) resulted in the best model's performance.

4. Conclusions

In this study, daily SSL of Ramian watershed was estimated by various corrected and optimized SRC models. In this regard, given the existing log-transformation bias in SRC model, two general approaches were taken into consideration. In the first approach, the SRC model was used in the form of a linear (SRC), "mean load within discharge classes" (SRC-MeanLoad), and corrected by bias correction factors (SRC-CF1, SRC-CF2, SRC-FAO). In the second approach, the coefficients of SRC model were optimized by evolutionary algorithms (SRC-GA-I and SRC-GA-II single and multi-objective genetic algorithms (GAs), respectively). The results obtained from the comparison of the efficiency of various SRC models showed that the SRC-GA-II model in which the NSGA-II has

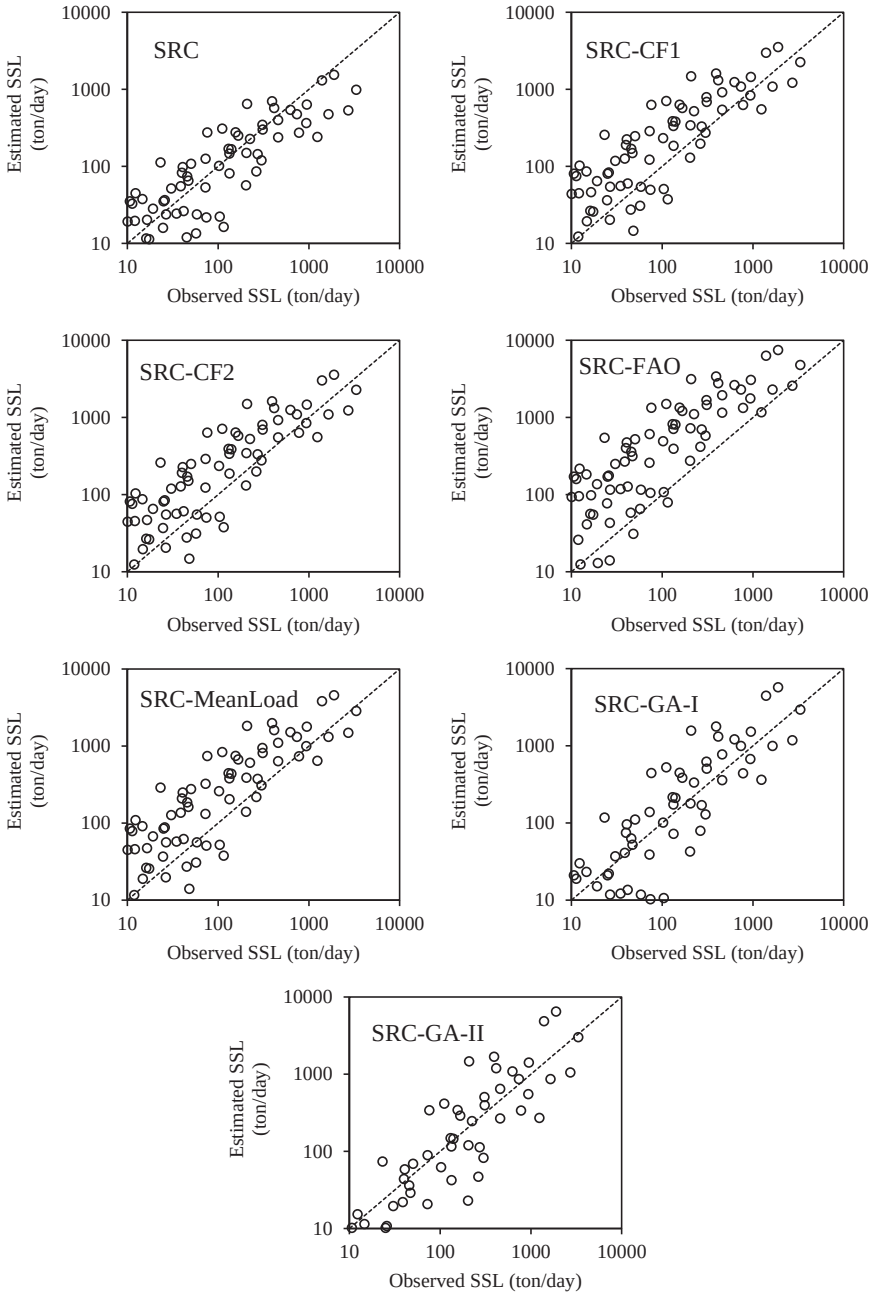

Fig. 8. Logarithmic scatter plots of observed and estimated SSL by different SRC models for the test data set.

Table 6
Total SSL estimated by different SRC models for the test data set.

	Observed	SRC[a]	SRC-CF[b]1	SRC-CF2	SRC-FAO[c]	SRC-MeanLoad	SRC-GA[d]-I	SRC-GA-II
Estimate (ton)	49971.0	19010.3	43434.7	43879.5	91963.8	53468.0	50346.5	52290.8
PBIAS (%)		62.0	13.1	12.2	− 84.0	− 7.0	− 4.6	− 0.8

[a] Sediment rating curve.
[b] Correction factor.
[c] Food and Agriculture Organization.
[d] Genetic algorithm.

been used, has better efficiency than the other models. In this regard, in automated calibration phase, the sensitivity of the SRC-GA-II model to the different objective functions (LOGE, RMSE, MAE and NS_objfun) was assessed and LOGE and NS_objfun were selected as the best objective functions.

Data division and data clustering prior modeling was also taken into account and emphasized in the current study. Generally, to increase the generalizability of data-driven models, the samples utilized in calibration of models should be representative data of the total statistical period. Furthermore, to evaluate the performance of models properly, the test data set should be similar to calibration data set. This is a main problem and the major challenge in modeling, as the failure to apply same homogenous data in calibration and test data sets may greatly impact the results of modeling. In this respect, the SOM neural network clustering technique was utilized for data division and providing same uniform data sets (calibration and test data sets).

In sum, what was emphasized in this study was how to optimize the coefficients of the SRC model using the modern algorithms. Despite the impact of these algorithms on improving the performance of models, the inappropriate quality and quantity of the discharge-sediment time series recorded at the hydrometric stations have a lot of effects on the accuracy of the results obtained from the models, which should be considered. Therefore, it is necessary to pay attention to the following points: a) The data set recorded at hydrometric stations is often related to the base flows of rivers and are less related to flood conditions, and since most of the SSL of the rivers is carried by flood discharge, so the SRC model cannot be a good representative model for estimation of SSL in low and high flows. b) In the SRC model, there is just one predictor variable that is the flow discharge. In this regard, Rodríguez-Blanco et al. (2010) indicated that only 19% of the variance of suspended sediment discharge can be explained by flow discharge. Therefore, in addition to flow discharge, it is necessary to use the other effective watershed variables in estimating the SSL of rivers.

Totally, the relationships between water quality parameters and physical, geochemical and biological processes between watershed resources (soil, vegetation cover, geology, land use, etc.), meteorological variables (temperature, precipitation, melting, etc.), the hydrological variable of the river (flow discharge), as well as human activities, are often very complex, non-deterministic and non-linear in a way that makes it impossible to comprehend them completely. The result is that in such a situation, it is important to use methods that can understand the complexity of relationships between basin variables and allow accurate estimation of SSL. Therefore, using soft computing methods, such as artificial neural networks, Neuro-fuzzy, etc. is suggested to respond to this need.

Acknowledgements

This study was founded by Soil Conservation and Watershed Management Research Institute (SCWMRI) (Project No. 0-29-29-94128). The authors would like to acknowledge the staff of SCWMRI and the honorable reviewers, which helped us to improve the quality of the article.

References

Altunkaynak, A. (2009). Sediment load prediction by genetic algorithms. *Advances in Engineering Software*, *40*(9), 928–934.

Bekele, E. G., & Nicklow, J. W. (2007). Multi-objective automatic calibration of SWAT using NSGA-II. *Journal of Hydrology*, *341*(3–4), 165–176.

Buyukyildiz, M., & Kumcu, S. Y. (2017). An estimation of the suspended sediment load using adaptive network based fuzzy inference system, support vector machine and artificial neural network Models. *Water Resources Management*, *31*(4), 1343–1359.

Chau, K. W., & Jiang, Y. W. (2002). Three-dimensional pollutant transport model for the Pearl River Estuary. *Water Research*, *36*(8), 2029–2039.

Chen, X. Y., & Chau, K. W. (2016). A hybrid double feedforward neural network for suspended sediment load estimation. *Water Resources Management*, *30*(7), 2179–2194.

Choudhury, P., & Sil, B. S. (2010). Integrated water and sediment flow simulation and forecasting models for river reaches. *Journal of Hydrology*, *385*(1–4), 313–322.

Cohn, T. A., Delong, L. L., Gilroy, E. J., Hirsch, R. M., & Wells, D. K. (1989). Estimating constituent loads. *Water Resources Research*, *25*(5), 937–942.

Criss, R. E., & Winston, W. E. (2008). Do Nash values have value? Discussion and alternate proposals. *Hydrological Processes: An International Journal*, *22*(14), 2723–2725.

Deb, K. (2001). *Multi-objective optimization using evolutionary algorithms*. Chichester: Wiley.

Deb, K., Pratap, A., Agarwal, S., & Meyarivan, T. A. M. T. (2002). A fast and elitist multiobjective genetic algorithm: NSGA-II. *IEEE Transactions on Evolutionary Computation*, *6*(2), 182–197.

Duan, N. (1983). Smearing estimate: A nonparametric retransformation method. *Journal of the American Statistical Association*, *78*(383), 605–610.

Ferguson, R. I. (1986). River loads underestimated by rating curves. *Water Resources Research*, *22*(1), 74–76.

Fotovatikhah, F., Herrera, M., Shamshirband, S., Chau, K. W., Faizollahzadeh Ardabili, S., & Piran, M. J. (2018). Survey of computational intelligence as basis to big flood management: Challenges, research directions and future work. *Engineering Applications of Computational Fluid Mechanics*, *12*(1), 411–437.

Gupta, H. V., Sorooshian, S., & Yapo, P. O. (1999). Status of automatic calibration for hydrologic models: Comparison with multilevel expert calibration. *Journal of Hydrologic Engineering*, *4*(2), 135–143.

Gupta, H. V., Kling, H., Yilmaz, K. K., & Martinez, G. F. (2009). Decomposition of the mean squared error and NSE performance criteria: Implications for improving hydrological modelling. *Journal of Hydrology*, *377*(1–2), 80–91.

Jansson, M. B. (1996). Estimating a sediment rating curve of the Reventazon river at Palomo using logged mean loads within discharge classes. *Journal of Hydrology*, *183*(3), 227–241.

Jones, K. R., Berney, O., Carr, D. P., & Barrett, E. C. (1981). Arid zone hydrology for agricultural development. *FAO Irrigation and Drainage Paper*(37).

Kao, S. J., Lee, T. Y., & Milliman, J. D. (2005). Calculating highly fluctuated suspended sediment fluxes from mountainous rivers in Taiwan. *Terrestrial Atmospheric and Oceanic Sciences*, *16*(3), 653.

Kisi, O., Keshavarzi, A., Shiri, J., Zounemat-Kermani, M., & Omran, E. S. E. (2017). Groundwater quality modeling using neuro-particle swarm optimization and neuro-differential evolution techniques. *Hydrology Research*, *48*(6), 1508–1519.

Kohonen, T. (1982). Analysis of a simple self-organizing process. *Biological Cybernetics*, *44*(2), 135–140.

Madsen, H. (2000). Automatic calibration of a conceptual rainfall–runoff model using multiple objectives. *Journal of Hydrology*, *235*(3–4), 276–288.

May, R. J., Maier, H. R., & Dandy, G. C. (2010). Data splitting for artificial neural networks using SOM-based stratified sampling. *Neural Networks*, *23*(2), 283–294.

Miller, D. M. (1984). Reducing transformation bias in curve fitting. *The American Statistician*, *38*(2), 124–126.

MohammadRezapour, O., Nour Jou, P., & Zeynali, M. J. (2016). Compression of genetic algorithm and particle swarm algorithm models for Optimizing coefficients of sediment rating curve in the estimation of suspended sediment in Sistan River (case study: Kohak station). *The Iranian Society of Irrigation & Water Engineering*, *6*, 76–89.

Moriasi, D. N., Arnold, J. G., Van Liew, M. W., Bingner, R. L., Harmel, R. D., & Veith, T. L. (2007). Model evaluation guidelines for systematic quantification of accuracy in watershed simulations. *Transactions of the ASABE*, *50*(3), 885–900.

Muleta, M. K. (2011). Model performance sensitivity to objective function during automated calibrations. *Journal of Hydrologic Engineering*, *17*(6), 756–767.

Nash, J. E., & Sutcliffe, J. V. (1970). River flow forecasting through conceptual models part I—A discussion of principles. *Journal of Hydrology*, *10*(3), 282–290.

Olyaie, E., Banejad, H., Chau, K. W., & Melesse, A. M. (2015). A comparison of various artificial intelligence approaches performance for estimating suspended sediment load of river systems: A case study in United States. *Environmental Monitoring and Assessment*, *187*(4), 189.

Rodríguez-Blanco, M. L., Taboada-Castro, M. M., Palleiro, L., & Taboada-Castro, M. T. (2010). Temporal changes in suspended sediment transport in an Atlantic catchment, NW Spain. *Geomorphology*, *123*(1–2), 181–188.

Sadeghi, S. H. R., Mizuyama, T., Miyata, S., Gomi, T., Kosugi, K., Fukushima, T., & Onda, Y. (2008). Development, evaluation and interpretation of sediment rating curves for a Japanese small mountainous reforested watershed. *Geoderma*, *144*(1–2), 198–211.

Sarkar, A., Sharma, N., & Singh, R. D. (2017). Sediment Runoff Modelling Using ANNs in an Eastern Himalayan Basin, India In: *River System Analysis and Management* (pp. 73–82). Singapore: Springer.

Schwefel, H. P. (1995). *Evolution and optimum seeking. Sixth-generation computer technology series*. New York: Wiley.

Srinivas, N., & Deb, K. (1994). Muiltiobjective optimization using nondominated sorting in genetic algorithms. *Evolutionary Computation*, *2*(3), 221–248.

Swain, R., & Sahoo, B. (2017). Mapping of heavy metal pollution in river water at daily time-scale using spatio-temporal fusion of MODIS-aqua and Landsat satellite imageries. *Journal of Environmental Management*, *192*, 1–14.
Tabatabaei, M., & Salehpour Jam, A. (2017). Optimization of sediment rating curve coefficients using evolutionary algorithms and unsupervised artificial neural network. *Caspian Journal of Environmental Sciences*, *15*(4), 385–399.
Taormina, R., & Chau, K. W. (2015). Data-driven input variable selection for rainfall–runoff modeling using binary-coded particle swarm optimization and Extreme Learning Machines. *Journal of Hydrology*, *529*, 1617–1632.
Tayfur, G. (2012). *Soft computing in water resources engineering: Artificial neural networks, fuzzy logic and genetic algorithms*. Southamton: WIT Press.
Ulke, A., Tayfur, G., & Ozkul, S. (2009). Predicting suspended sediment loads and missing data for Gediz River, Turkey. *Journal of Hydrologic Engineering*, *14*(9), 954–965.
Vercruysse, K., Grabowski, R. C., & Rickson, R. J. (2017). Suspended sediment transport dynamics in rivers: Multi-scale drivers of temporal variation. *Earth-Science Reviews*, *166*, 38–52.
Veldhuizen, D. A. V., & Lamont, G. B. (2000). Multiobjective evolutionary algorithms: Analyzing the state-of-the-art. *Evolutionary Computation*, *8*(2), 125–147.
Wang, W. C., Xu, D. M., Chau, K. W., & Lei, G. J. (2014). Assessment of river water quality based on theory of variable fuzzy sets and fuzzy binary comparison method. *Water Resources Management*, *28*(12), 4183–4200.
Wu, C. L., & Chau, K. W. (2011). Rainfall–runoff modeling using artificial neural network coupled with singular spectrum analysis. *Journal of Hydrology*, *399*(3–4), 394–409.
Yar Kiani, A. (2009). *Intelligent systems*. Tehran: Press Center of Poyesh Andisheh.
Yapo, P. O., Gupta, H. V., & Sorooshian, S. (1998). Multi-objective global optimization for hydrologic models. *Journal of Hydrology*, *204*(1–4), 83–97.
Yee, A. K., Ray, A. K., & Rangaiah, G. P. (2003). Multiobjective optimization of an industrial styrene reactor. *Computers & Chemical Engineering*, *27*(1), 111–130.

International Soil and Water Conservation Research 7 (2019) 130–137

Contents lists available at ScienceDirect

International Soil and Water Conservation Research

journal homepage: www.elsevier.com/locate/iswcr

Original Research Article

Soil loss estimation using rusle model to prioritize erosion control in *KELANI* river basin in Sri Lanka

Cassim Mohamed Fayas [a], Nimal Shantha Abeysingha [a,*], Korotta Gamage Shyamala Nirmanee [a], Dinithi Samaratunga [b], Ananda Mallawatantri [b]

[a] Faculty of Agriculture, Rajarata University of Sri Lanka, Puliyankulama, Anuradhapura, Sri Lanka
[b] International Union for Conservation of Nature, Sri Lanka Office, Colombo, Sri Lanka

ARTICLE INFO

Article history:
Received 4 September 2018
Received in revised form
6 January 2019
Accepted 10 January 2019
Available online 15 January 2019

Keywords:
Kelani river basin
Revised universal soil loss equation
RUSLE
Soil erosion
Soil erosion hazard map
Land degradation

ABSTRACT

Soil erosion contributes negatively to agricultural production, quality of source water for drinking, ecosystem health in land and aquatic environments, and aesthetic value of landscapes. Approaches to understand the spatial variability of erosion severity are important for improving landuse management. This study uses the *Kelani* river basin in Sri Lanka as the study area to assess erosion severity using the Revised Universal Soil Loss Equation (RUSLE) model supported by a GIS system. Erosion severity across the river basin was estimated using RUSLE, a Digital Elevation Model (15 × 15 m), twenty years rainfall data at 14 rain gauge stations across the basin, landuse and land cover, and soil maps and cropping factors. The estimated average annual soil loss in *Kelani* river basin varied from zero to 103.7 t ha-1 yr^{-1}, with a mean annual soil loss estimated at 10.9 t ha^{-1} yr^{-1}. About 70% of the river basin area was identified with low to moderate erosion severity (< 12 t $ha-1$ yr^{-1}) indicating that erosion control measures are urgently needed to ensure a sustainable ecosystem in the *Kelani* river basin, which in turn, is connected with the quality of life of over 5 million people. Use of this severity information developed with RUSLE along with its individual parameters can help to design landuse management practices. This effort can be further refined by analyzing RUSLE results along with *Kelani* river sub-basins level real time erosion estimations as a monitoring measure for conservation practices.

1. Introduction

Soil erosion is a natural phenomenon which causes depletion of soil materials by natural caustic factors such as wind, water, gravity but often accelerated by human activities (Gunawan, Sutjiningsih, Soeryantono, & Sulistioweni, 2013). Erosional losses are connected to ecosystem sustainability and long-term soil quality of productive landscapes due to lowering soil depth, water retention ability, soil organic matter content, plant nutrients and albedo. Erosion led siltation reduces the storage capacity of reservoirs at a rate of about 1% per year (Mahmood, 1987). Worldwide, the average soil erosion in agricultural crop lands are about 30 t ha^{-1} yr^{-1} ranging from 0.5 to 400 t ha^{-1} yr^{-1} (Pimentel, Harvey, & Resosudarmo, 1995). Poor soil quality adds to fertilizer expenses on crop lands while leading to land desertion (Singh & Panda, 2017).

Out of the erosion assessment tools the Universal Soil Loss Equation (USLE) and the Revised Universal Soil Loss Equation (RUSLE) are the most widely used (Udayakumara, Shrestha, Samarakoon, & Schmidt-vogt, 2010). RUSLE uses an empirical approach based on functionalities of the erosion processes. It has been adopted to landscape and watershed scales combined with Geographic Information Systems (GIS) (Das, Paul, Bordoloi, Prakash, & Pankaj, 2018; Prasannakumar, Vijith, Abinod, & Geetha, 2012; Ranzi, Le, & Rulli, 2012; Renard, Foster, Weesies, McCool, & Yoder, 1997; Sharma, 2010; Wijesundara, Abeysingha, & Dissanayake, 2018).

In the tropical Sri Lanka erosional processes are impacting ecosystems and environmental services such as power generation, drinking water sources at off-site locations and overall agricultural productivity contributing negatively to socio-economic development. In addition, climate change induced changes in rainfall intensity and shifts in rainfall patterns also contribute to the erosion potential.

* Correspondence to: Department of Agric. Engineering, Rajarata University of Sri Lanka, Puliyankulama, Anuradhapura, Sri Lanka.
E-mail address: nabeysingha@gmail.com (N.S. Abeysingha).

Peer review under responsibility of International Research and Training Center on Erosion and Sedimentation and China Water and Power Press.

https://doi.org/10.1016/j.iswcr.2019.01.003

Ability to assess erosion potential in a given landscape is important to target resources and manage erosional losses by focusing on key contributory factors. Wijesundara et al. (2018), used RUSLE model to simulate soil erosion in *Kirindi Oya* river basin as one of the first attempts in Sri Lanka. This study is a scaled up approach combined with a GIS interface to estimate soil erosion using the RUSLE model in the *Kelani* river basin, which is more complex, in terms of land use and landscape characteristics. *Kelani* river basin provides a ridge to reef scenario as it originated in the central hills of the country and reach the Indian Ocean by the capital city of Colombo through landscapes under agricultural, industrial and urban land uses. *Kelani* river basin soil erosion is severely impacting the source drinking water quality of millions of people. The *Kelani* river basin located in the wet zone, water erosion is one of the main factors compared to wind related erosion. Hence splash and sheet (interrill), rill, gully erosion and channel flow are the main processes contributing to erosion with climate induced high rainfall intensities (Jayawardena, Dharshika, & Herath, 2017).

Mallawatantri, Rodrigo, and De Silva (2016) assessed the sediment yield of the water passing at a location near *Hanwella* in the *Kelani* river basin. The assessment indicated that at the end of the steeper area, near *Hanwella*, the *Kelani* river records an average sediment loading of about 2350 metric tons, annually. In addition, mid and downstream of the basin is associated with large reservoirs contributing to power generation and drinking water supply such as *Castlereigh*, *Norton*, *Maskeliya*, *Canyon* and *Laxapana* reservoirs where erosion and siltation is a major challenge. In this study, RUSLE model combined with a GIS interface is used to assess the average annual soil loss, and create a soil erosion hazard map to better understand the spatial variability of soil erosion in the entire *Kelani* river basin.

2. Material and methods

2.1. Study area

Kelani river originates in the central hills near Horton Plains National Park and Peak Wilderness Sanctuary. The basin is located in northern latitudes from 6°47–7°05′ and eastern longitudes from 79°52–80°13′ (Kottagoda & Abeysingha, 2017). Approximate extent of the basin is 2292 km^2 (Survey Department of Sri Lanka, 2007). The *Kelani* river is 145 km in length and it originates approximately 2250 m above mean sea level. Its elevation varies from 0 to 2346 m above mean sea level (Fig. 1). *Kelani* river basin includes four administrative districts (*Nuwara–Eliya*, *Kegalle*, *Gampaha*, and *Colombo*) and three provinces (Western, Central and Sabaragamuwa) in the country.

2.2. Data collection

Spatial distribution of the annual average rainfall (Table 1) was computed using the daily rainfall data at fourteen rainfall stations located in and near the *Kelani* river basin (*Aranayaka, Colombo, Deraniyagala, Glencourse, Hanwella, Henarathgoda, Holombuwa, Homagama, Kithulgala, Kosgama, Norwood, Pasyala, Rathnapura, Wagolla*) obtained from the Department of Meteorology and the Natural Resource Management Center in Sri Lanka. Variability of relevant soil properties for the basin was obtained from 'Soils of the wet zone of Sri Lanka' by Mapa, Somasiri, and Nagarajah (1999). Land use and the Digital elevation model (DEM) (15 × 15 m resolution) for the basin were obtained from the Survey Department of Sri Lanka.

2.3. RUSLE model description

Universal Soil Loss equation (USLE) and Revised Universal Soil Loss equation (RUSLE) are two of the most popular and widely used soil erosion models for agricultural watersheds throughout the world (Udayakumara et al., 2010). The RUSLE model was selected for this study due to its demonstrated effectiveness with compared to the USLE model (Renard et al., 1997; Wischmeier & Smith, 1978). In addition, the RUSLE model is flexible in modeling soil erosion in terms its ability to change conditions and parameters and easy to integrate with a GIS for spatial analysis (Wischmeier & Smith, 1965).

The RUSLE (Renard et al., 1997) model can be expressed as Eq. (1);

$$A = R \times K \times LS \times C \times P \quad (1)$$

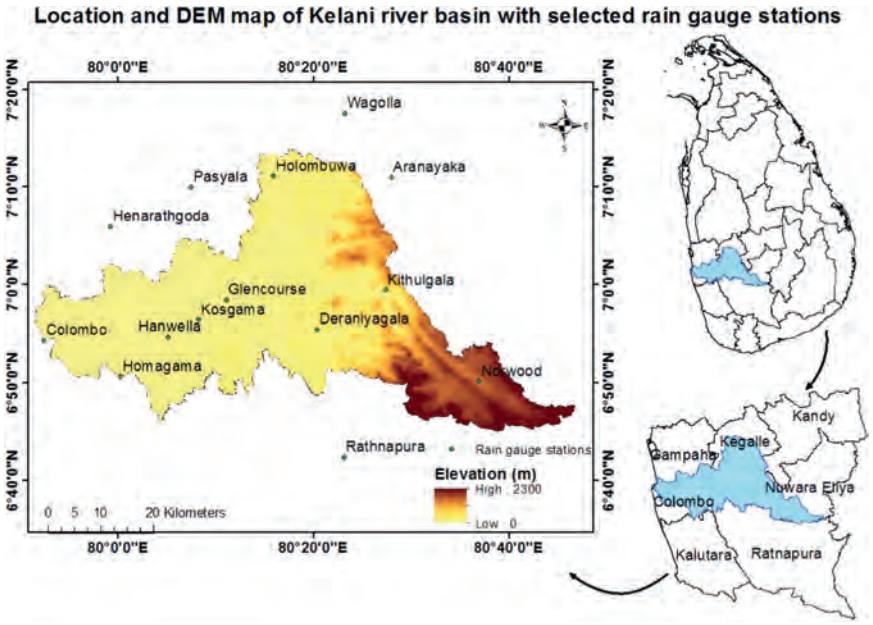

Fig. 1. Geographical location of *Kelani* river basin, spatial distribution of rain gauge stations and its DEM.

Table 1
Detail of the rainfall station in the *Kelani* river basin.

Climate Station	Longitude DD	Latitude DD	Period	Annual rainfall (mm)
Aranayaka	80.4666640	7.1831580	1997–2017	2440
Colombo	79.8720330	6.9050000	1997–2017	2220
Deraniyagala	80.3389720	6.9231190	1997–2017	3749
Glencourse	80.1841670	6.9736110	1997–2017	3577
Hanwella	80.0842110	6.9109390	1997–2017	2916
Henarathgoda	79.9857830	7.0993030	1997–2017	2284
Holombuwa	80.2648060	7.1851670	1997–2017	2993
Homagama	80.0031830	6.8432750	1997–2017	2800
Kithulgala	80.4561110	6.9900000	1997–2017	4235
Kosgama	80.1369280	6.9397170	1997–2017	3100
Norwood	80.6146530	6.8356440	1997–2017	2392
Pasyala	80.1233100	7.1667110	1997–2017	2684
Rathnapura	80.3847330	6.7055750	1997–2017	3840
Wagolla	80.3856970	7.2931420	1997–2017	2014

Where,

A Computed soil loss per unit area per year (t/ha per year)
LS The slope length and steepness factor (dimensionless)
K The soil erodibility factor (t ha MJ^{-1} mm^{-1})
R The rainfall erosivity factor (MJ mm ha^{-1} h^{-1} $year^{-1}$)
C The cover and management factor (dimensionless)
P The support practice factor (dimensionless)

2.3.1. Rainfall erosivity factor (R)

The effect of rainfall intensity on soil erosion is estimated by the rainfall erosivity factor R that explains the effect of raindrop impacts. Therefore R reflects the extent of runoff likely to be associated with the rain (Renard et al., 1997). The modeling of R factor requires continuous precipitation data (Wischmeier & Smith, 1978). Daily rainfall data of 14 rainfall gauging stations for 20 years (1997–2017) duration were used in calculating the R factor along with the rainfall erosivity factor equation developed for Sri Lanka conditions by Premalal (1986).

$$R = (972.75 + 9.95 \times F)/100 \quad (2)$$

R=Rainfall erosivity factor (MJ mm ha^{-1} h^{-1} per year)
F=Average annual rainfall (mm)

Such regression relationships using local environmental conditions have been used in literature where no rainfall intensity data are available (Gelagay & Minale, 2016; Zeng et al., 2017). The same equation has been used by Wijesundara et al. (2018) in *Kirindi oya* river basin and Weerasinghe and Thuraisingham (2015) in *Bibili oya* river basin in Sri Lanka.

We tested Inverse Distance Weighted (IDW) and Kriging methods to interpolate point rainfall data to cover the entire basin using ArcGIS (10.2). The results of cross validation of interpolated data using Geostatistical wizard indicated that IDW provides the least interpolation error (RMSE = 60.54) for rainfall over Kriging method (RMSE = 60.89). Therefore, both annual rainfall variability map and rainfall erosivity factor map for the *Kelani* river basin were generated using IDW interpolation.

2.3.2. Soil erodibility factor (K)

The soil erodibility factor (K) depends on the soil characteristics and the ability of soil or surface material to persist against the erosion. K factor is defined as the rate of soil loss per unit of erosive energy created by the rainfall calculated under a standard condition by a plot of land consist of clean bare soil with slope of 9% and 22.6 m long (Brady & Weil, 2012).

Table 2
Soil erodibility values for soil types in *Kelani* river basin. Source: (Joshua, 1977; Wijesekera & Samarakoon, 2001).

Soil type	(K) Factor values
Red Yellow Podsolic	0.22
Sandy Regosol	0.48
Reddish Brown Earth	0.27
Immature Brown Loams	0.33
Low Humic Gley soils	0.10
Alluvial soils	0.31
Red Yellow Latosol	0.33
Reddish brown Latosol	0.17

Soil map for the *Kelani* river basin was digitized and soil data base were developed based on 'Soils of the wet zone of Sri Lanka' (Mapa et al., 1999). Direct measurement of K factor is considered as the most reliable way of estimation (Romkens et al., 1977). K values for different soil types were determined from the past studies conducted in Sri Lanka as in Table 2 (Joshua, 1977; Wijesekera & Samarakoon, 2001). The K factor raster map was generated for different soil types.

2.3.3. Slope length and steepness factor (LS)

The extent of soil erosion is influenced by the topography of the landscape, mainly the slope length and slope steepness. Slope length and slope gradient were estimated using the Digital Elevation Model (DEM) obtained from the Survey Department of Sri Lanka. DEM was used to develop the fill and flow direction raster map using ArcGIS spatial analysis tool. The slope length factor (Wischmeier & Smith, 1978) was computed using the equation Eq. (3).

$$L = (\lambda/22.1)^{m} \quad (3)$$

where
L=Slope length factor
λ = horizontal projected slope length (m)
m=slope length exponent.
(λ = flow accumulation * cell size)

In this equation, 'm' slope length varies based on slope steepness; m equals 0.5 if the slope is 4.5% or more; 0.4 on slopes of 3–4.5%; 0.3 on slopes of 1–3%; and 0.2 of uniform gradient of less than 1% (Wischmeier & Smith, 1978).

The slope steepness factor was calculated based on the relationship given by McCool et al. (1987). Eqs. (4 and 5).

$$S = 10.8\ sin\alpha + 0.03 \text{ for slope percent } < 9\% \quad (4)$$

$$S = 16.8\ sin\alpha - 0.50 \text{ for slope percent} \geq 9\% \quad (5)$$

Where
S=Slope steepness factor and α = Slope angle in degree

The LS factor layer has been generated by the multiplication of both L and S factors in the raster calculator in ArcGIS.

2.3.4. Cover and Management factor (C)

The effect of the cropping system and crop management practices on the rate of erosion is expressed using the C factor. This factor can be used to compare the relative effect of management strategy on conservation plans (Renard et al., 1997). It also represents the contribution of soil disturbing activities, plant sequence and productivity level, soil cover and subsurface bio-mass on soil erosion. Cover and management factor is important in developing conservation plans.

Landuse and the land cover maps of the *Kelani* river basin obtained from the Survey Department of Sri Lanka were used to

Table 3
C factor and P factor values and % area occupied by different landuse types in *Kelani* river basin. Source: Munasinghe et al. (2001), Prasannakumar et al. (2012), and Senanayake et al. (2013).

Land use	C Factor value	P Factor value	Area (sq; km)	Area (%)
Bare land	1.00	1.00	0.592	0.0255
Built up area	0.73	0.00	5.097	0.2194
Coconut	0.54	0.60	113.709	4.8947
Chena	0.80	0.40	2.434	0.1048
Forest – Open	0.50	0.30	235.694	10.145
Grassland	0.51	1.00	0.002	0.0001
Home Garden	0.51	0.25	581.122	25.015
Marsh/Boggy	0.30	1.00	17.627	0.7588
Other cultivation	0.73	1.00	26.290	1.1317
Paddy	0.43	0.15	180.496	7.7697
Rubber	0.44	0.35	784.699	33.778
Rock	0.10	0.00	16.230	0.6986
Scrub land	0.60	1.00	53.081	2.2849
Stream	0.20	0.00	28.008	1.2056
Tea	0.57	0.35	277.031	11.925
Tank	0.20	0.00	0.971	0.0418
Unclassified	0.00	0.00	0.007	0.0003

create the C factor map using ArcGIS clipping tool. Then the literature-based C factor values were assigned for different landuse and land cover types (Table 3) (Munasinghe, Pushpakumara, Bandara, & Herath, 2001; Senanayake, Munasinghe, & Wickramasinghe, 2013; Wijesundara et al., 2018). Then the C factor raster map with a 15 m resolution was generated for the *Kelani* river basin.

2.3.5. Support and Conservation Practices factor (P)

The soil loss estimates corresponding to a specific support practice in upslope to downslope cultivation can be described as support and conservation practices factor (Renard et al., 1997). The P factor map for the *Kelani* river basin was created based on the landuse and land cover map of the *Kelani* river basin. Literature based P factor values (Table 3) for different land use categories were assigned (Munasinghe et al., 2001; Prasannakumar et al., 2012; Senanayake el al., 2013; Wijesundara et al., 2018) to generate the P factor map.

2.3.6. Soil erosion severity mapping

R,K,C and P maps were in 15 × 15 m pixel size after rasterization of each variable. The DEM was resampled from 5 × 5 m scale to 15 × 15 m pixel size using bilinear method to create LS raster map. Pixel based information developed for individual factors of the RUSLE model were used in the empirical formula ($A = R \times K \times LS \times C \times P$), as described by Renard et al. (1997), to compute the average annual soil loss rate per hectare per year for each pixel in the GIS at 15 m × 15 m, resolution. The estimated pixel level soil loss values were grouped into five soil erosion severity classes (low, moderate, high, very high, and extremely high) based on their value, to form the soil erosion severity map for the *Kelani* river basin.

3. Results and discussion

Soil erosion severity map computed using six RUSLE parameters is helpful in the management and control of erosion in the *Kelani* river basin. The type of interventions and investments to be applied to manage soil erosion can be decided based on the analysis of individual RUSLE model components.

3.1. Rainfall runoff erosivity factor (R)

Studies showed that rainfall is one of the most sensitive factor for soil erosion (Dabral, Baithuri, & Pandey, 2008; Ganasri & Ramesh, 2016). Long term mean annual rainfall over the basin varied from 2220 to 4236 mm (Figs. 2 and 3). R factor map (Fig. 2) indicates that R factor ranges from 232.37 to 431.20 MJ mm ha^{-1} h^{-1} $year^{-1}$ in the *Kelani* river basin with an average of 325.72 MJ mm ha^{-1} h^{-1} $year^{-1}$. R factor follows the variation of mean annual rainfall. Area covering the northern part of the *Kegalle* district, *Kitulgala*, *Rathnapura* and *Kosgama* areas located at the midstream of the basin received comparatively high annual rainfall varying from 3740 to 4235 mm (Fig. 2). As such the susceptibility for soil erosion is higher in the middle portion of the river basin based on the R factor compared to the other parts of the basin. R values recorded in the present study in *Kelani* river basin is higher than those recorded for *Kirindi Oya* river basin (96–347 MJ mm ha^{-1} h^{-1} $year^{-1}$) located in dry zone of the country (Wijesundara et al., 2017), primarily due to lower rainfall. Management practices to reduce the impact of rainfall and sediment control measures can be adopted to Kelani river basin based on the R values.

3.2. Soil erodibility factor (K)

Results indicated that more than 70% of the *Kelani* river basin is covered by Red Yellow Podsolic (RYP) soils. RYP mixed with Low Humic Gley (LHG) soils covered more than 20% of the basin area. Remaining less than 10% of the area is covered by Alluvial soils (AS), Red Yellow Latosol (RYL), Sandy Regosol (SR) and other soils (Fig. 4). K factors assigned for the areas in the *Kelani* river basin (Table 2) ranged from 0.16 to 0.48. The relative susceptibility of different great soil groups is in the order Non Calcic Brown > Red Yellow Latosol > Reddish Brown Earth > Red Yellow Podzolic

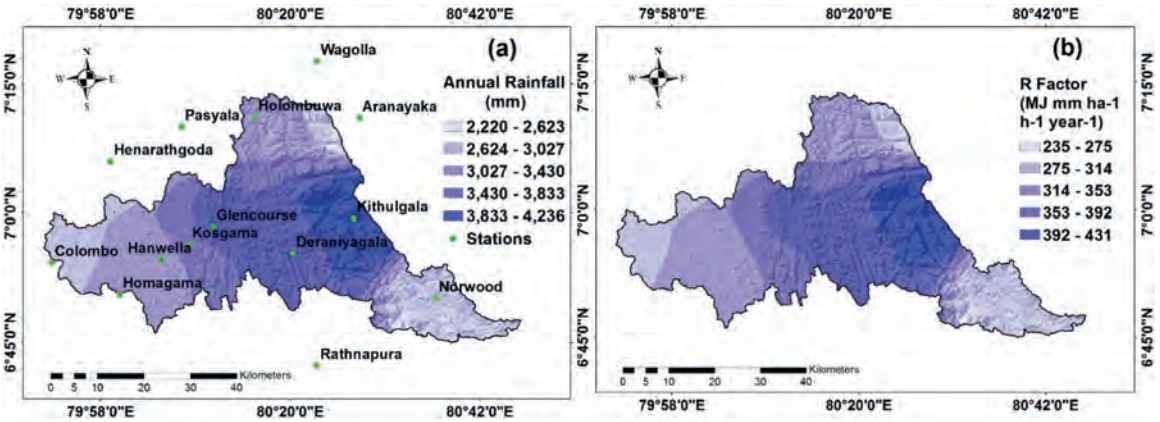

Fig. 2. Mean annual rainfall variability map (a), R factor map (b) of *Kelani* river basin.

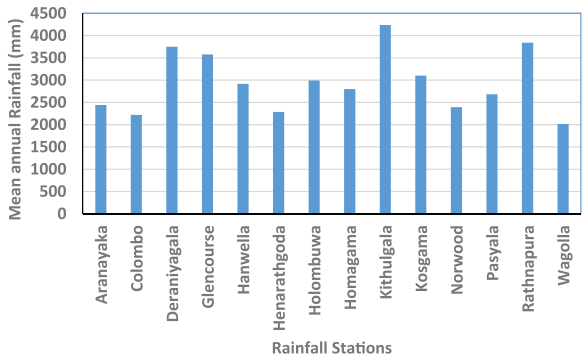

Fig. 3. Mean annual rainfall of different rainfall stations in and closer to *Kelani* river basin.

soils > Reddish Brown Latosolic soils (Joshua, 1997). RYP soils dominated the areas with a K value of 0.22, moderately susceptible to soil erosion. Downstream of the basin is prominently occupied by RYP and LHG associations with K value of 0.22–0.10 and are comparatively less susceptible to erosion. Management factors that improve the soil carbon, cover and conservation efforts could reduce the effective K factor.

3.3. Slope length and Steepness factor (LS)

Kelani river basin includes steep slopes with 25–30% in the eastern parts (Goonatilake, Perera, Silva, Weerakoon, & Mallawatantri, 2016) and the study indicated an average slope steepness was 19.62% (Fig. 5) with midstream and some part of the upstream areas having significantly higher slope steepness. LS values ranged from 0 to 111.41 with mean value of 0.107 (Fig. 5). Therefore, high soil erosion is likely to occur in up and midstream areas than in downstream areas of the basin in terms of the LS factor. In general, most of the areas of the basin is characterized by moderate slopes with moderate LS factor values.

3.4. Cover and Management factor (C)

Land use map (Fig. 6) indicates that *Kelani* river basin consists of different vegetations such as a) forest-open (10%), b) home gardens (25%), c) paddy (7.7%), d) rubber (33%), e) tea (11%) and f) coconut cultivated lands (4%). Those lands occupied about 70% of the basin area with considerable variation in the C factor (Fig. 7). Other than the vegetation, built up (C, 0.73) areas and boggy (C, 0.3) areas are located in the downstream areas of the basin. The C factor value of *Kelani* river basin mostly vary between 0.4 and 0.5 (Fig. 7) due to high cover, therefore, characterized as having low and moderate soil erosion potentials. The areas with high C factor can be changed to enhance infiltration by changing the cropping and surface management.

3.5. Support and conservation practices factor (P)

P factors is ranging from zero for good conservation practices to one for poor conservation practices (Ganasri & Ramesh, 2016). Soil erosion in the *Kelani* river basin is mostly on the higher side with bare lands, grass lands and scrub lands with high P value (Table 3), except for paddy lands where P value is a relatively low, 0.15 (Fig. 7).

3.6. Soil erosion estimation

Soil erosion estimates for the *Kelani* river basin with RUSLE ranged from zero to 103.69 t/ha per year with a mean annual soil loss of 10.88 t/ha per year. According to the Ministry of Environment and Renewable Energy in Sri Lanka (2014) the tolerable soil erosion rate for the upcountry and mid country wet zone is 13.2 and 9.0 t/ha per annum, respectively. Most part of the *Kelani* river basin belongs to the mid country wet zone with estimated soil loss rates between 12 and 25 t/ha per year, exceeding the tolerable soil erosion rates. The mid-stream area of *Kelani* river basin recorded higher erosion rates compared to upstream areas of the basin. Presence of dense forest cover and lower mean annual rainfall in the upstream may contribute to comparatively lower erosion rates. Thomas, Joseph, and Thrivikramji (2018) estimated the soil loss rate in *Muthirapuzha* river basin of southern Western Ghats, India, and their estimated values ranged from zero to 785 t/ha per year which is higher than values recorded in *Kelani* basin. *Muthirapuzha* river is also a monsoon dominated rain receiving basin similar to *Kelani* river basin, however its R factor varies from 337 and 1320 MJ mm ha^{-1} h^{-1} $year^{-1}$ due to higher rainfall which is higher than those of *Kelani* river basin (232.37–431.20 MJ mm ha^{-1} h^{-1} $year^{-1}$).

3.7. Soil erosion severity classes

The average annual soil erosion rates were classified into the five priority classes, namely, 'Slight (0 – 5), Moderate (5 – 12), High (12 – 25), Very high (25 – 60) and Extremely high (> 60) t/ha per year to develop soil erosion severity maps (Figs. 8 and 9). Approximately similar erosion severity classes could be observed in Senanayake et al. (2013) and Sing and Panda (2017).

Approximately 25% percent of *Kelani* river basin was categorized into high soil erosion hazard class (12–25 t ha^{-1} per year) located primarily in *Kegalle* district in the midstream of the basin.

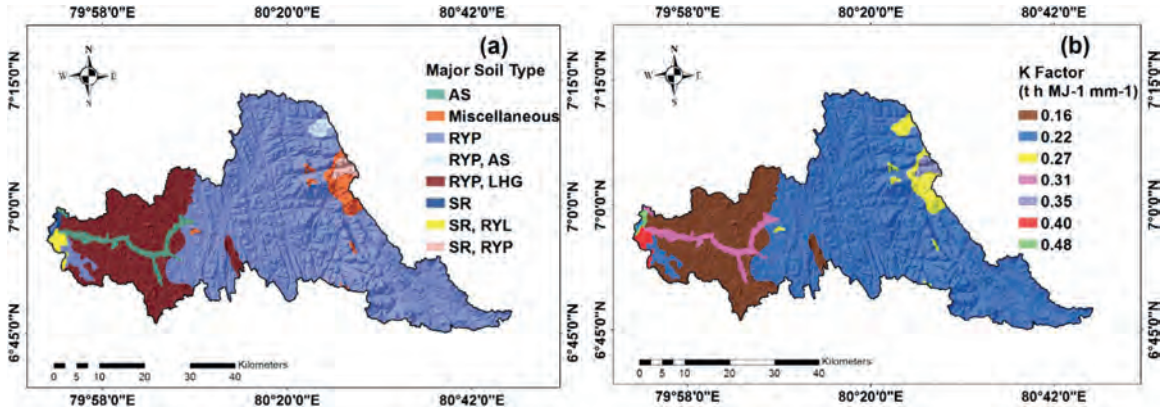

Fig. 4. Major Soil types map of *Kelani* river basin (a) and respective K factor map (b) (AS-Alluvial Soil, RYP-Red Yellow Podsolic, LHG-Low Humic Gley, SR-Sandy Regosol, RYL-Red Yellow Latosol).

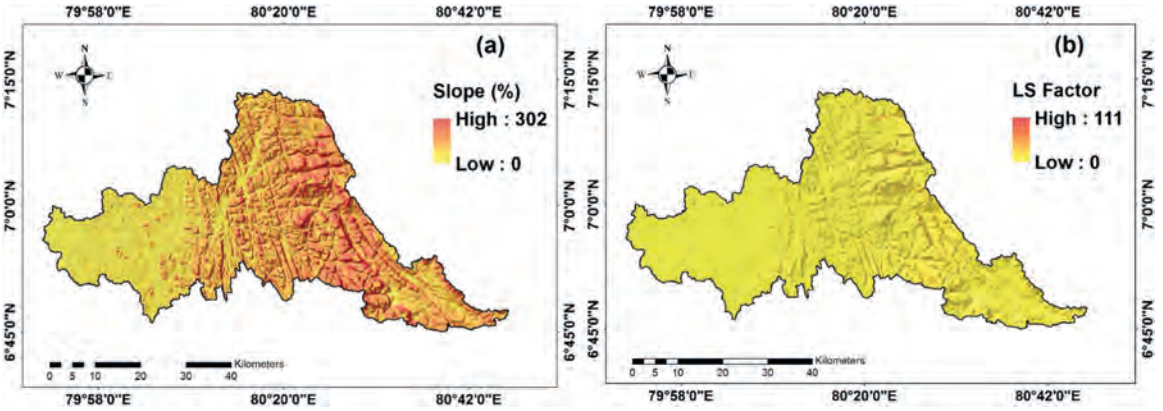

Fig. 5. Slope % map (a) and LS factor map (b) of *Kelani* river basin.

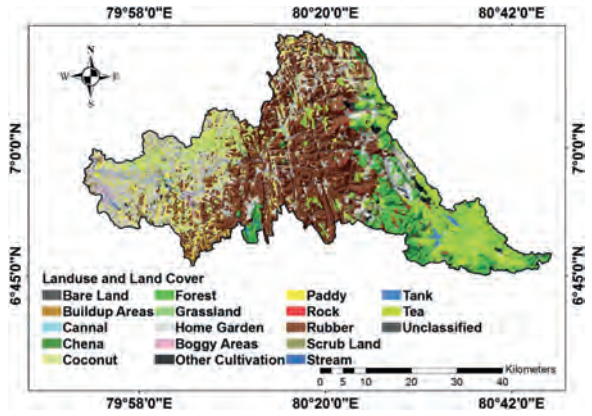

Fig. 6. Landuse and Land cover map of *Kelani* river basin.

This area can be characterized by its higher slopes and high annual rainfall compared to the other areas of the basin. Therefore, higher R and LS factor contributed to the higher erosion estimates in this area.

Based on the RUSLE model estimates, about 70% of the basin area is categorized into low to moderate erosion severity class (< 12 t/ha per year). Lands located in *Nuwaraeliya*, northern part of *Kegalle* district and some parts of *Gampaha* to *Colombo* districts falls into the moderate erosion category.

About 4% of the *Kelani* river basin falls under very high soil erosion hazard class with 25–60 t ha^{-1} yr^{-1} soil erosion. It is irregularly distributed across the basin but prominent in *Kegalle*, *Nuwaraeliya*, *Kandy and Gampaha* districts (Fig. 8). These areas are consisted of bare lands as well as land mostly used for coconut with relatively high P factor and C factor values.

Approximately 1% of the total basin area falls under the extremely vulnerable soil erosion class (> 60 t ha^{-1} yr^{-1}) which is located in *Kithulgala*, *Ampana* areas and in the northern part of *Nuwaraeliya* in the upstream of the basin. Main land use and land cover in this area are bare land and crop lands and lands consisting of considerably higher C factor values (C = 0.73–1) and P factor values (P = 1). Moreover, higher range of annual rainfall (3896 mm to 4228 mm) resulted in higher R values and relatively high elevation (996 m to 1472 m) resulting in higher LS factor contributed to the higher soil loss estimates. Jayasekara, Kadupitiya, and Vitharana (2018) mapped the soil erosion hazard zone of Sri Lanka and indicated that grater soil erosion hazard is recorded upcountry mainly due to higher R and LS factor.

Out of the 20 sub basins of the *Kelani* river basin (Fig. 9) indicated that the lower reaches of *Kehelgamuwa ganga*, upper reaches of *Walihel Oya*, and upper middle *Kelani ganga* are more prone to soil erosion compared to the other sub basins.

Since soil loss rates in most of the basin areas is moderate to low, agronomic soil conservation measures can be applied to manage and control soil erosion. In the upstream arable lands can be converted into agro–forestry systems with mixture of trees and crops so that the soil is covered and protected. Home gardens in the areas also need to be strengthened with more canopy cover. However, for steep areas and very high soil erosion prone areas may need comparatively low cost mechanical structures such as stone terraces, lock and spill drains, drop structures etc. Sloping Agricultural Land Techniques (SALT) is also an option for these high erosion prone areas in mid and upstream basin.

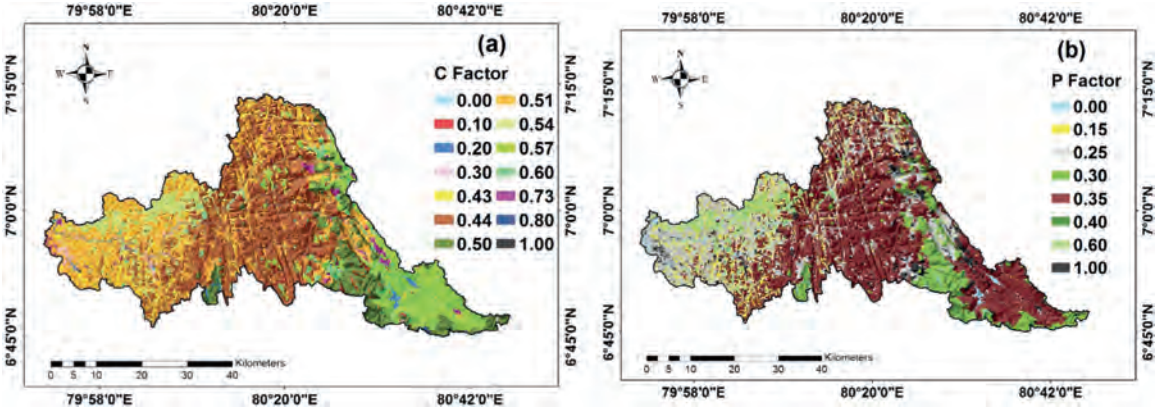

Fig. 7. C factor (a) and P factor (b) maps.

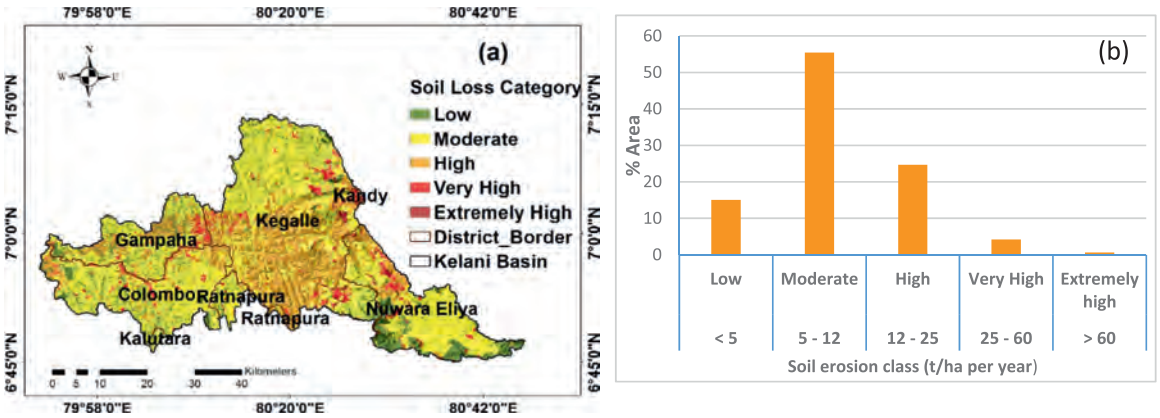

Fig. 8. Soil erosion severity map of *Kelani* river basin with the district boundaries (a) and soil erosion classes and the % of area of the basin under each class (b).

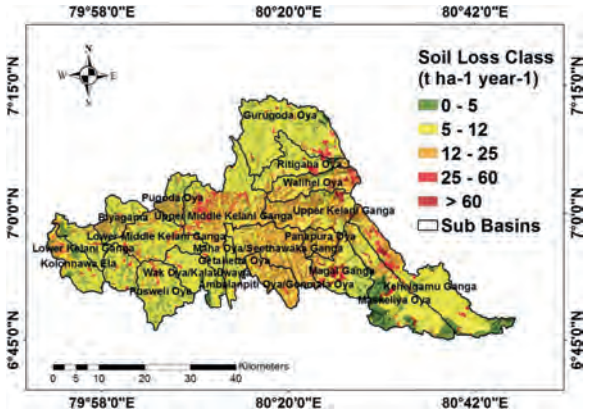

Fig. 9. Soil erosion severity map of *Kelani* river basin with its 20 sub-basins.

3.8. Monitoring erosion processes

The average amount of sediments in main *Kelani* River estimated by Mallawatantri et al. (2016), using measured turbidity and flow data, is about 2350 t ha^{-1} yr^{-1}, at a river location corresponding to a drainage area of 175,000 ha, after draining about 75% of the total basin area, indicating a sediment yield in the river about 0.134 t per ha per annum. The erosion estimates using RUSLE and the sediment load estimate cannot be directly related but provides an idea about the environmental processes related to sediment generation, depositions and transport.

The potential exists to refine the RUSLE model outputs with field measured values in place of literature-based estimates, as conservation practices are in place. This with real time load estimates in the river locations corresponding to the sediment discharges from sub-watersheds can be used to support to improve the erosion control efforts. This refinement requires strengthening the sediment and water quality monitoring programmes to measure daily river flow and periodic sediment data at the confluence points of the sub-watersheds and the main river.

4. Conclusion

A quantitative assessment of soil erosion in *Kelani* river basin using RUSLE equation in a GIS interface successfully provided a set of spatially different management approaches to arrest erosion in the basin. The study divided the *Kelani* river basin into five erosion severity categories; low (< 5 t ha^{-1} yr^{-1}), moderate (5–12 t ha^{-1} yr^{-1}), high (12–25 t ha^{-1} yr^{-1}), very high (25–60 t^{-1} ha^{-1} yr^{-1}), and extremely high (> 60 t^{-1} ha^{-1} yr^{-1}).

This categorization along with individual maps on RUSLE parameters can be used to introduce targeted conservation practices and investments to address erosion across the *Kelani* river basin. The spatial distribution of erosion severity in different sub-basins will help to target resources and monitor the progress at sub-basin levels with sediment loading estimates. Erosion is connected to soil quality, fertility and the quality of source drinking water, among other things.

This study also demonstrated that the GIS systems combined with RUSLE model is a practical and relevant method for assessing spatial variability of soil erosion for effective and efficient sediment and water quality management. The study is useful to formulate ecosystem-based benefit sharing, financing etc., as *Kelani* River basin being a provider of multiple benefits, including drinking, hydropower, agriculture, urban uses etc., Investments needed for erosion controls be paid off by the potential ecosystem benefits based on this type of studies which will help to bring together multiple stakeholders as well as socio-economic sectors.

Conflict of interest

None.

References

Dabral, P. P., Baithuri, N., & Pandey, A. (2008). Soil erosion assessment in a hilly catchment of North Eastern India using USLE, GIS and remote sensing. *Water Resources Management*, *22*(12), 1783–1798.

Das, B., Paul, A., Bordoloi, R., Prakash, O., & Pankaj, T. (2018). Soil erosion risk assessment of hilly terrain through integrated approach of RUSLE and geospatial technology: A case study of Tirap District, Arunachal Pradesh. *Modeling Earth Systems and Environment*, *4*, 37–381. http://dx.doi.org/10.1007/s40808-018-0435-z.

Ganasri, B. P., & Ramesh, H. (2016). Assessment of soil erosion by RUSLE model using remote sensing and GIS - A case study of Nethravathi Basin. *Geoscience Frontiers*, *7*, 953–961.

Gelagay, H. S., & Minale, A. S. (2016). Soil loss estimation using GIS and Remote sensing techniques: Case of Koga watershed, Northwestern Ethiopia. *International Soil and Water Conservation Research*, *4*(2), 126–136.

Goonatilake, S. D. A., Perera, N., Silva, G. D., Weerakoon, D., & Mallawatantri, A. (2016). *Natural resource profile of the Kelani River Basin*. .

Gunawan, G., Sutjiningsih, D., Soeryantono, H., & Sulistioweni, W. (2013). Soil erosion estimation based on GIS and remote sensing for supporting integrated water resources conservation management. *International Journal of Technology*, *4*(2), 147–156.

Jayawardena, S., Dharshika, T., & Herath, R. (2017). Observed trends, future climate change projections and possible impacts for Sri Lanka. *Neela Haritha Climate Change Magazine of Sri Lanka*, *2*, 144–151.

Jayasekara, M. J. P. T.M., Kadupitiya, H. K., & Vitharana, U. W. A. (2018). Mapping of soil erosion hazard zones of Sri Lanka. *Tropical Agricultural Research*, *29*(2), 135–146.

Joshua, W. D. (1977). Soil erosive power of rainfall in the different climatic zones of Sri Lanka. In: Erosion and Solid Matter Transport in Inland Waters, Proceedings

of Symposium Publication, No. 122. IAHSAISH, Paris, pp 51–61.
Kottagoda, S., & Abeysingha, N. S. (2017). Morphometric analysis of watersheds in Kelani river basin for soil and water conservation. *Journal of the National Science Foundation of Sri Lanka*, *45*(3), 273. http://dx.doi.org/10.4038/jnsfsr.v45i3.8192.
Mahmood, K. (1987). Reservoir sedimentation; Impact, extent, and mitigation In: Encyclopedia of Hydrological Sciences. *Encyclopedia of Hydrological Sciences*. http://dx.doi.org/10.1002/0470848944.
Mallawatantri, A., Rodrigo, A., & De Silva, K. (2016). *Medium to long-term multi-stakeholder strategy and action plan for management and conservation of Kelani River Basin* (p. 153) (Available from ⟨https://goo.gl/s7FCWh⟩ Accessed 14 August 2018).
Mapa, R. B., Somasiri, S., & Nagarajah, S. (1999). Soils of the wet zone of Sri Lanka In: *Morphology, characterization and classification*. Sri Lanka: Soil science society.
Munasinghe, M. A. K., Pushpakumara, V., Bandara, T. M. J., & Herath, H. M. B. (2001). Use of information systems for soil erosion hazard assessment of the central province of Sri Lanka. *Annals of Department of Agriculture*, *3*, 148.
Pimentel, D., Harvey, C., Resosudarmo, P., et al. (1995). Environmental and economic costs of soil erosion and conservation benefits. *Science*, *267*(5201), 1117–1123.
Prasannakumar, V., Vijith, H., Abinod, S., & Geetha, N. (2012). Estimation of soil erosion risk within a small mountainous sub-watershed in Kerala, India, using Revised Universal Soil Loss Equation (RUSLE) and geo-information technology. *Geoscience Frontiers*, *3*(2), 209–215. http://dx.doi.org/10.1016/j.gsf.2011.11.003.
Premalal (1986). *Development of an erosivity map for Sri Lanka*. Sri Lanka: Department of Agricultural Engineering, University Peradeniya (A research report submitted for the B.Sc. degree).
Ranzi, R., Le, T. H., & Rulli, M. C. (2012). A RUSLE approach to model suspended sediment load in the Lo river (Vietnam): Effects of reservoirs and land use changes. *Journal of Hydrology*, *422–423*, 17–29. http://dx.doi.org/10.1016/j.jhydrol.2011.12.009.
Renard, K. G., Foster, G. R., Weesies, G. A., McCool, D. K., & Yoder, D. C. (1997). *Predicting soil erosion by water: A guide to conservation planning with revised universal soil loss equation (RUSLE)*. Washington, D.C: United States Department of Agriculture (Agricultural Handbook No. 703).
Romkens, M. J. M., Roth, C. B., & Nelson, D. W. (1997). *Soil Science Society America Journal*, *41*(954).
Senanayake, S. S., Munasinghe, M. A. K., & Wickramasinghe, W. M. A. D.B. (2013). Use of erosion hazard assessments for regional scale crop suitability mapping in the Uva Province. *Annals of the Sri Lanka Department of Agriculture*, *15*, 127–141.
Sharma, A. (2010). Integrating terrain and vegetation indices for identifying potential soil erosion risk area. *Geo-Spatial Information Science*, *13*(3), 201–209. http://dx.doi.org/10.1007/s11806-010-0342-6.
Singh, G., & Panda, R. K. (2017). Grid-cell based assessment of soil erosion potential for identification of critical erosion prone areas using USLE, GIS and remote sensing: A case study in the Kapgari watershed, India. *International Soil and Water Conservation Research*, *5*(3), 202–211.
Thomas, J., Joseph, S., & Thrivikramji, K. P. (2018). Assessment of soil erosion in a monsoon-dominated mountain river basin in India using RUSLE-SDR and AHP. *Hydrological Sciences Journal*, *63*(4), 542–560. http://dx.doi.org/10.1080/02626667.2018.1429614.
Udayakumara, E. P. N., Shrestha, R. P., Samarakoon, L., & Schmidt-vogt, D. (2010). People's perception and socioeconomic determinants of soil erosion: A case study of Samanalawewa watershed. *Sri Lanka International Journal of Sediment Research*, *25*, 323–339.
Weerasinghe, V. P. A., & Thuraisingham, K. (2015). Soil Erosion Study for Bibili Oya Watershed in Kelani River Basin, ArcGIS User Conference (SLAUC-2015), September 15.
Wijesekera, N. T. S., & Samarakoon, L., (2001). Extraction of Parameters and Modelling Soil Erosion using GIS in a GRID Environment, The 22nd Asian Conference in Remote Sensing, National University of Singapore, 5-9 November 2001, pp 34-39.
Wijesundara, N. C., Abeysingha, N. S., & Dissanayake, D. M. S. L.B. (2018). GIS-based soil loss estimation using RUSLE model: A case of Kirindi Oya river basin. *Sri Lanka Modeling Earth Systems and Environment*, *4*(1), 251–262. http://dx.doi.org/10.1007/s40808-018-0419-z.
Wischmeier, W. H., & Smith, D. D. (1965). *Predicting rainfall erosion losses from Cropland East of the Rocky Mountains*. Washington DC: United States Department ofAgriculture (Handbook no. 282).
Wischmeier, W. H., & Smith, D. D. (1978). *Predicting rainfall erosion losses: A guide to conservation planning*. Washington, D.C: United States Department of Agriculture (Agricultural hand book No. 537).
Zeng, C., Wang, S., Bai, X., Li, Y., Tian, Y., Li, Y., & Luo, G. (2017). Soil erosion evolution and spatial correlation analysis in a typical karst geomorphology using RUSLE with GIS. *Solid Earth*, *8*, 721–736.

International Soil and Water Conservation Research 7 (2019) 138–149

Contents lists available at ScienceDirect

International Soil and Water Conservation Research

journal homepage: www.elsevier.com/locate/iswcr

Original Research Article

Accuracy of sedimentgraph modeling from topography map scale and DEM mesh size

Seyed Hamidreza Sadeghi [a,*], Mostafa Moradi Dashtpagerdi [a], Hamidreza Moradi Rekabdarkoolai [a], Jeroen M. Schoorl [b]

[a] Department of Watershed Management Engineering, Faculty of Natural Resources, Tarbiat Modares University, Noor 46417-76489, Mazandaran, Iran
[b] Department of Environmental Sciences, Soil Geography and landscape, Wageningen University and Research, PO Box 47 6700AA Wageningen, The Netherlands

ARTICLE INFO

Article history:
Received 30 October 2018
Received in revised form
6 January 2019
Accepted 10 January 2019
Available online 11 January 2019

Keywords:
Multiscale Modeling
Sedimentgraph variability
Spatial Resolution
Watershed simulation

ABSTRACT

The evaluation of scale effects on modeling performance of sedimentgraphs as the ultimate outputs of the hydrological simulation is vital for adaptive watershed management. The present study therefore analyzed effectability of simulated sedimentgraphs components in association with different topographic maps with various vector scales. The whole procedure was materialized to select the critical scale and cell size for the Galazchai Watershed, Iran. To this end, the stormwise sedimentgraphs were modeled for 23 recorded events using the Clark's Instantaneous Unit Hydrograph (IUH) model stemmed for developing Instantaneous Unit Sedimentgraphs (IUSGs) incorporated with dimensionless sediment concentration distribution (DSCD) based on the vector scales of 1:25000, 1:50000, 1:100000 and 1:250000 and cell sizes of 5, 10, 20 30, 50, 100 and 200 m. Some 644 direct sedimentgraphs (DSGs) were then evaluated based on Relative Errors (REs) for sediment volume, peak sediment, time to peak, base time and the Coefficient of Efficiency (CE). The results confirmed that REs for peak sediment, time to peak and CE were sensitive to cell size. The results further verified that the cell sizes of 5, 20, 30, 50 and 100 m were critical cell sizes in viewpoint of time to peak. In addition, the vector scales of 1:50000 with cell size of 50 m, and 1:100000 with cell sizes of 5 and 10 m were critical vector scales and cell sizes based on RMSE evaluation criterion. It is concluded from the current research that the accuracy of simulation of sedimentgraph was influenced by map scales and mesh sizes.

1. Introduction

Soil erosion related issues are supposed as the most important soil degradation agents worldwide (Amore, Modica, Nearing, & Santoro, 2004). It emphasizes the need to the precise estimation of sediment as the ultimate output of the erosion processes (Sadeghi et al., 2008). Therefore, having the acceptable output of hydrological models to evaluate the sediment components is very important leading to improvement of sound decision-making and planning in association with the integrated watershed management (Sadeghi, Jalili, & Nikkami, 2009; Schmalz et al., 2015; Wu, Li, & Huang, 2008). In addition, the main input of hydrological models is topographic maps with different scales and cell sizes (Wilbanks, 2006). Thus, different vector scales and cell sizes have a significant impact on performance of hydrological models in the estimation of watershed sedimentgraph. Identification of optimal vector scale and cell sizes is therefore essential to achieve the most precise sedimentgraph and to recognize internal relationships among different vector scales and cell sizes and sedimentgraph components (Wu & Qi, 2000).

The critical scale is a scale in which the hydrological models and the resulted equations have the highest performance and were used as a citation (Gentine, Troy, Lintner, & Findell, 2012). Indeed, the critical cell size is defined as a measure in which the optimal cell sizes of the topographic maps of the hydrological model is determined by the highest accuracy. So that accurate calibration and localization of hydrological models (Sadeghi, Gholami, Sharifi, Darvishan, & Homaee, 2015a) helps experts and decision makers recognize the complex effects of scale and cell

* Corresponding author.
E-mail addresses: sadeghi@modares.ac.ir (S.H. Sadeghi), Moradi20000@gmail.com (M. Moradi Dashtpagerdi), hrmoradi@modares.ac.ir (H. Moradi Rekabdarkoolai), jeroen.schoorl@wur.nl (J.M. Schoorl).
Peer review under responsibility of International Research and Training Center on Erosion and Sedimentation and China Water and Power Press.

https://doi.org/10.1016/j.iswcr.2019.01.002

size leading to proper estimation of the watershed outputs (Ayana & Vargheese, 2013; Geng, Burcher, Kroetsch, & Mitchell, 2016; Gurnell et al., 2016; Javernick, Brasington, & Caruso, 2014; Kauffeldt, Wetterhall, Pappenberger, Salamon, & Thielen, 2016; Metz & Tielbörger, 2016; Nelson, Bellugi, & Dietrich, 2014; Ouédraogo, Degré, Debouche, & Lisein, 2014; Shaw, 2015; Silakhori & Ownegh, 2012).

The Instantaneous Unit Sedimentgraph (IUSG) as a resultant of the Clark's Instantaneous Unit Hydrograph (IUH) and sediment concentration values (Kumar & Rastogi, 1987; Rovira & Batalla, 2006; Sadeghi et al., 2008; Saeidi, Sadeghi, & Telvari, 2016, 2017) is an applied approach to simulate the synthetic sedimentgraphs for watersheds with lack of comprehensive data. While, the performance of the Clark's IUH model as one of the most widely used hydrological simulation models (Sadeghi, Mostafazadeh, & Sadoddin, 2015) is also controlled by scale and cell size. Developing the Clark's IUH model (Clark, 1945) is based on lag and route technique and Muskingum method, and influenced by isochrone resulted from time of concentration (TC). On the other hand, the accuracy of TC map is directly influenced by the watershed features including flow length, flow accumulation, flow direction, slope and contributing areas whose accuracies are entirely controlled by scales of topographic maps and mesh sizes. Thus, different cell sizes of the topographic maps result in dissimilar outputs of the Clark's IUH model and eventually lead to various performance of sedimentgraph developments.

Although previous studies focused on effects of different spatiotemporal scales on hydrological models and watershed physiographic characteristics (Azizian & Shokoohi, 2014; Goodchild, 2011; Lemma, Gessesse, Kassa, & Edossa, 2018; Lv, Liao, Zhou, Zhu, & Shen, 2019; Morera et al., 2013; Schneider, 2009; Sherriff et al., 2015), the effect of different scales of topographic maps on the performance of IUSG and sedimentgraph components resulted from critical scale and cell sizes based on storms events has been less addressed. In this matter, Schoorl, Sonneveld, and Veldkamp (2000) evaluated the impacts of DEMs of 1, 3, 9, 27 and 81 m on soil erosion estimation using the LAPSUS model. The results showed increasing cell sizes led to increasing the amount of net erosion. They approved that changes in cell sizes leads to changes in flow routing and consequently changes in sediment rate. In addition, Amore et al. (2004) investigated the scale effect in the Universal Soil Loss Equation (USLE) model, and the physically based model of Water Erosion Prediction Project (WEPP) for soil erosion computation from three Sicilian basins in three different scales in upstream of Ragoleto, Italy. The results showed that variability of two models outputs was dissimilar in different spatially scales. The USLE and WEPP models both estimated sediment volumes in large spatially basins higher than those of small basins. Chaplot (2005) also studied the impact of the cell sizes of the DEM from 20 to 500 m using the Soil and Water Analysis Tool (SWAT) to simulate runoff, sediment, and NO3–N loads in the Walnut Creek watershed, central Iowa, USA. The results demonstrated that the various cells sizes led to different outputs of runoff, sediment, and NO3–N loads. Decreasing the cell size beyond 50 m threshold represented more prediction errors for nitrogen and sediment loads. Teegavarapu, Viswanathan, and Ormsbee (2006) evaluated hydrological parameters in different cell sizes. They confirmed that the DEMs with different cell sizes influence on hydrography components of the delineated watershed and characteristics of the watershed streams. The effect of different DEMs with cell sizes of 30, 90 and 300 m was investigated by Dixon and Earls (2009) using SWAT model on the monthly flow in the Charlie Creek Watershed, Florida, USA. The results approved that different cell sizes were driving force in SWAT model and showing accuracy level of performance of model.

Similarly, Zhang, Wu, Chang, Elliot, and Dun (2009) studied DEMs from the National Elevation Dataset, Shuttle Radar Topography Mission (SRTM), and Light Detection and Ranging (LIDAR) at three resolutions of 4, 10 and 30 m using WEPP model in the Moscow Mountain Region in northern Idaho, USA. The results expressed DEMs with different resolutions and generated sources had different outputs of erosion simulations. Accordingly, 10 m LIDAR DEM had the highest accuracy of watershed seasonal discharge and sediment yield. Tarolli (2014) surveyed challenges and opportunities related to high-resolution topography in earth surface processes. He approved topography maps resulted from different sources represent different results to better understand geomorphic processes. The effect of DEMs cell sizes of 5, 10 and 25 m on flow accumulation threshold value to generate drainage networks in four river basins located in the Andalusia, southern Spain, was studied by Ariza-Villaverde, Jiménez-Hornero, and de Ravé (2015). They reported that with increasing DEM resolution, flow accumulation threshold value increases and consequently more variability occurred for lower drainage densities. Shrestha, Sulis, Simmer, and Kollet (2015) studied the type of DEMs on different soil components and surface flow in the Rur Watershed, Germany. They showed that the cells sizes of 100–200 m had the lowest errors. Likewise, Pawluszek and Borkowski (2017) studied the performance of cell sizes of different DEMs for landslide zoning in south-western Poland. The results verified 5 and 1 m cell sizes had the highest performance for the study purposes. In fact, their study approved that different cell sizes led to variation of slope, stream power index and roughness index and consequently significant difference in research results. Lu et al. (2017) also proved effects of different grid sizes of DEMs on sediment delivery of rill/interrill erosions in the Little Tennessee River of Loudon County, USA. They showed that different mesh sizes effects on to the overall shapes of the observed phenomenon, which in turn led to change in erosion and deposition. Recently, Zhang et al. (2018) reported the effects of soil maps at scales of 1:50000, 1:250000, 1:500000, 1:1000000, 1:4000000 and 1:10000000 on studying soil organic carbon dynamics in eastern China. The results showed different map scales provided different details of soil properties and the range of the relative deviation (1.51 – 7.86%).

Scrutinizing reviewing the literature verifies diversified performances of assessment approaches due to effects of resolution level of the inputs. It clearly authenticates the necessity of more studies to investigate the effects of different cell sizes resulted from various vector scales and cell sizes on the watershed response. The present study was therefore planned to assess the accuracy of sedimentgraph modeling from different topographic source maps of 1:25000, 1:50000, 1:100000 and 1:250000 with the original and re-sized mesh sizes of 5, 10, 20, 30, 50, 100 and 200 m to earn the highest accuracy of storm basis simulated sedimentgraphs through applying IUSG model resulted from the Clark's IUH model and sediment concentration in the Galazchai Watershed, Iran. It was accordingly hypothesized that different map scales with various mesh sizes behaved dissimilarly in estimation of sedimentgraph components. In addition, the combined applications of large scaled maps with high resolution cell sizes may produce reasonable outputs.

2. Materials and methods

2.1. Study area

The current study was formulated to conduct in the well monitored Galazchai Watershed in the Oshnavieh Region, West Azarbaijan Province, Iran (Fig. 1). It incorporates an area of 103 km^2 and extended between 44°56' and 45°35' E and 37°01' and 37°09' N. The elevation varies from 1500 to 3271 m, and the average slope is 32% (Adhami, Sadeghi, & Sheikhmohammady,

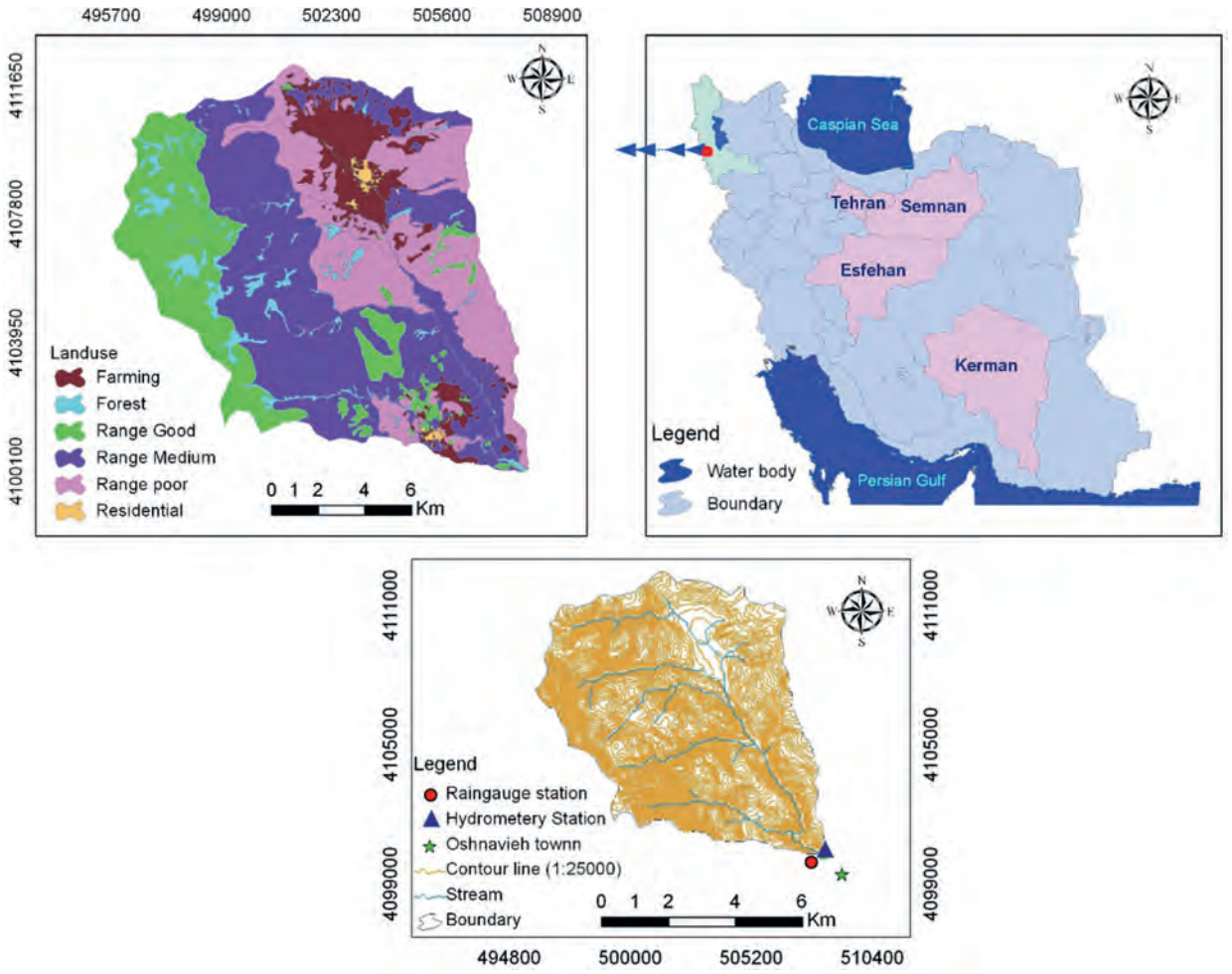

Fig. 1. General location (upper Right), Landuse (upper left) and topography (Bottom) maps of the Galazchai Watershed, Iran.

2018). There is the Oshnavieh rainguage station in output of Galazchaii Watershed and we extracted hyetographs of resulted from this station in same times of recorded flood hydrographs with 0.5 h time intervals. Galazchai Watershed is small steep watershed which in turn led to hydrologic rapid response and then we used Oshnavieh rainguage station data to estimation of total storms rainfall of Galazchai Watershed.

2.2. Data collection and preparation

In the present study, the base contour lines maps with scales of 1:25000, 1:50000, 1:100000 and 1:250000 were acquired from the National Geography Organization of Iran (NGO; http://www.ngo-iran.ir/). The DEM, fill, sink, slope, flow direction, flow length, flow accumulation and TC maps for each topography map were produced in different cell sizes of 5, 10, 20, 30, 50, 100 and 200 m using ArcGIS9.3 and ArcHydro softwares. The maximum available 23 monitored storm events with corresponding measured hydrographs and sedimentgraphs (Mostafazadeh, Sadeghi, & Sadoddin, 2015; Saeidi et al., 2016, 2017) were collected and analyzed to produce IUSGs using the Clark's IUH model and direct sedimentgraphs (DSGs). The detailed characteristics of recorded hyetographs, hydrographs and sedimentgraphs in the Galazchai Watershed, Iran, have been summarized in Table 1. The fixed base method (Agirre, Goñi, López, & Gimena, 2005) was used for converting flood runoff hydrograph (FRH) to direct runoff hydrograph (DRH) and also, volume of direct runoff equaled the total excess rainfall distributed during the storm events using phi-index method and then effective rainfall was calculated. Storage attenuation coefficient (K) was obtained from recession part of observed flood hydrograph of the watershed to represent the storage characteristic of stream channel (Sadeghi, Mostafazadeh, et al., 2015; Subramanya, 2000).

2.3. Runoff modeling

The runoff generation was modeled using the Clark's IUH model based on input discharge variables, TC and K values of IUH as shown in the following equations (Kumar, Chatterjee, Lohani, Kumar, & Singh, 2002; Sadeghi, Mostafazadeh, et al., 2015).

$$\mathbf{I_i = 2.78 * \frac{A_i}{\Delta t_c}} \quad (1)$$

$$\mathbf{Q_2 = \frac{K - 0.5\,\Delta t_c}{K + 0.5 \Delta t_c} Q_1 + I_2 \frac{\Delta t_c}{K + 0.5 \quad \Delta t_c}} \quad (2)$$

$$\mathbf{k = \frac{\Delta t}{\ln\left(\frac{Q_0}{Q_1}\right)}} \quad (3)$$

where, I_i is the input discharge at any time ($m^3\ s^{-1}$), A_i is the area engaged in the runoff generation at the end of the period (km^2), Δt_c is the base time of the IUH (h), Q_2 is the outflow after the time step of t_1 ($m^3\ s^{-1}$), Q_1 is the initial inflow, k is the storage

Table 1
Characteristics of observed hyetographs, hydrographs and sedimentgraphs for the Galazchai Watershed, Iran (adapted from Mostafazadeh et al., 2015; Saeidi et al., 2017).

No.	Storm event	Hyetograph					Hydrograph					Sedimentgraph			
		Total rainfall (mm)	Rainfall duration (h)	Average intensity (mm h^{-1})	Phi-index (mm h^{-1})	Effective rainfall (mm)	Base time (h)	Time to peak (h)	Peak discharge (m3 s^{-1})	Flood volume (m3)	Storage coefficient (h)	Base time (h)	Time to peak (h)	Peak sediment (gr l^{-1})	Sediment volume (ton)
1	Oct. 29, 2011	2.40	3.00	1.70	2.9	2.90	12.00	4.00	1.32	27177.12	5.86	10.50	6.50	0.24	2.14
2	Oct. 30, 2011	13.20	8.00	1.65	3.1	3.10	10.50	6.00	1.07	25234.02	7.7	15.50	3.00	0.10	1.41
3	Nov. 4, 2011	13.60	4.50	0.50	2	2.00	13.00	6.00	0.98	18369.90	8.19	17.00	5.50	0.28	5.09
4	Nov. 5, 2011	4.60	3.00	1.53	1.1	1.10	12.50	5.50	2.28	48077.28	6.15	4.00	3.00	0.05	0.33
5	Nov. 3, 2012	8.30	2.00	4.10	3.3	3.30	10.00	3.00	9.6	132402.40	3.42	18.00	3.00	1.04	116.29
6	Nov. 11, 2012	13.50	2.50	5.40	3.9	3.90	10.00	2.00	7.10	261921.78	4.27	14.00	5.50	0.32	10.07
7	Nov. 12, 2012	8.70	2.00	4.40	2.4	2.40	9.00	2.00	4.00	102260.52	3.5	10.50	1.00	0.05	0.79
8	Nov. 13, 2012	14.70	4.00	3.70	2	2.00	15.00	3.00	3.62	83347.38	4.18	10.50	6.00	0.39	27.10
9	Nov. 14, 2012	2.40	4.00	1.70	1.4	1.40	10.50	3.50	3.26	71523.00	4.47	13.00	3.00	1.06	63.38
10	Nov. 19, 2012	5.20	3.00	4.10	2.3	2.30	7.50	2.50	2.81	41289.84	6.04	12.50	5.50	0.11	1.45
11	Nov. 20,2012	10.30	2.50	1.10	0.5	0.50	6.00	3.00	2.29	22246.57	4.27	18.00	3.50	0.17	8.09
12	Nov. 25, 2012	3.40	3.00	2.60	2.2	2.20	6.00	4.00	2.95	28795.76	7.14	14.50	5.50	0.12	5.82
13	Mar. 10,2013	6.40	2.50	1.40	1.2	1.20	7.00	3.00	3.82	62388.90	5.16	10.50	1.00	0.05	1.40
14	Mar. 17,2013	4.60	5.00	0.90	0.5	0.50	4.00	3.00	1.10	10563.08	4.3	7.00	2.00	0.09	1.42
15	Mar. 30,2013	5.50	6.50	0.85	0.5	0.50	4.50	3.00	1.87	15838.89	6.2	6.00	4.00	0.65	6.02
16	Apr. 13, 2013	15.00	6.0	2.5	1	1.00	16.00	10.50	14.88	587803.66	5.5	16.00	6.50	2.42	467.77
17	Apr. 18, 2013	7.00	8.00	0.85	1.1	1.10	6.00	2.50	6.91	139034.49	3.6	6.00	1.50	0.87	49.24
18	Oct. 19, 2013	5.00	5.50	0.90	1.1	1.10	7.00	3.00	7.09	96159.52	3.3	6.00	2.50	0.35	16.87
19	Oct. 20, 2013	5.50	6.00	0.90	1.5	1.50	5.500	2.00	6.92	121063.92	5.2	5.50	1.50	0.67	36.72
20	Nov. 2, 2013	3.50	4.00	0.80	0.8	0.80	7.50	3.50	2.80	38158.31	7.2	7.50	5.50	0.05	0.66
21	Nov. 16, 2013	4.00	4.50	0.89	0.7	0.70	11.00	5.50	4.05	89051.13	4	6.00	1.50	0.32	6.39
22	Nov. 22, 2013	6.30	4.50	1.33	0.6	0.60	9.00	5.50	4.95	66017.34	3.7	7.00	3.00	0.37	10.01
23	Dec. 13, 2013	8.00	3.00	2.67	0.2	0.20	14.00	8.00	6.18	154178.10	3	4.50	3.00	0.40	4.11
Maximum		15	8.00	5.4	3.9	2.9	16.00	10.50	14.88	587803.66	8.19	18.00	6.50	2.42	467.77
Minimum		2.4	2.00	0.5	0.2	3.1	4.00	2.00	0.98	10563.08	3.00	4.00	1.00	0.05	0.33
Mean		6.3	4.22	1.53	1.2	2	9.28	4.09	4.43	97517.52	5.06	10.43	3.61	0.44	36.63
Coefficient of variations (%)		54.39	41.97	69.53	65.17	124.98	36.53	51.33	73.92	125.12	29.95	44.11	50.64	120.21	267.14

coefficient accomplished from the graphical method due to more application and high effectuation compared to other methods (Chow, Maidment, & Mays, 1988; Sadeghi & Dehghani, 2006), Q_0 is the discharge at the start time ($m^3\ s^{-1}$), Q_t is the discharge after a logarithmic time base of Δt ($m^3\ s^{-1}$).

TC for each segment of isochrones (Δt_c in h) resulted from Time-Area Histograms (TAHs) to simulate the spatial and temporal changes of runoff and consequently sediment (Fang, Cleveland, Garcia, Thompson, & Malla, 2005; Matei, 2012; Sadeghi, Mizuyama, Singh, & Tofighi, 2009; Saghafian, Julien, & Rajaie, 2002; Singh, 1988; Usul & Yilmaz, 2002). TAHs by different topographic maps and the cell sizes based on spatial distributed travel time method for the study area were developed using the kinematic wave time travel equation (Eq. (4)) as spatial distributed travel time method (Froehlich, 2011; Overton & Meadows, 2013; Sadeghi, Mostafazadeh, et al., 2015; Welle & Woodward, 1986).

$$\mathbf{T_C = \frac{6.942}{I^{0.4}} * \left(\frac{n * L}{\sqrt{S}}\right)^{0.6}} \tag{4}$$

where T_C, I, n, L and S are runoff travel time or time of concentration (min), rainfall intensity with two years return period ($5.12\ mm\ h^{-1}$), roughness coefficient, flow length (m) and watershed slope ($m\ m^{-1}$), respectively. For the production of TAHs, TC was obtained from spatial distributed travel time using scales of 1:25000, 1:50000, 1:100000 and 1:250000 and the cell sizes of 5, 10, 20, 30, 50, 100 and 200 m in ArcGIS 9.3. For all the 28 maps resulted from combination of four base scales and seven cell sizes, the isochrones were produced on a pixel basis with 0.5 h time intervals. The sectional areas of each isochrone maps were obtained and the corresponding TAHs as input factor to the Clark's IUH model were used. The produced IUHs based on different TAHs were finally applied for the production of IUH.

2.4. Sediment modeling

Sediment modeling as one of the methods of analysis of suspended sediment load changes was analyzed based on governing concepts on IUSG as a product of multiplying IUH ordinates by sediment concentration proposed by Williams (1978), Kumar and Rastogi (1987) and Sadeghi et al. (2008).

2.4.1. Analysis of sediment concentration

Changes of suspended sediment load in each flood were represented by the dimensionless sediment concentration distribution (DSCD) to obtain the IUSG (Eq. (5)). The sediment concentration at time t was calculated using the concept of the first order kinetic equation (Williams, 1975; Banasik & Walling, 1996; Sadeghi et al., 2009) shown as follows,

$$\mathbf{C_t = exp(-Zt)} \tag{5}$$

Where C_t is the ordinate of DSCD, Z is the sediment routing parameter (h^{-1}) and t is the passed time from the beginning to the end of IUH (h). Sediment routing parameter (Z) shows effectability of temporal and rate of IUSG based on IUH and rainfall feature. The sediment routing parameter (Z) was obtained for each storm using the following equation:

$$\mathbf{Z = -\ln \frac{\left(\frac{qp}{Qp}\right)^{0.56}}{Tp}} \tag{6}$$

where q_p is the peak discharge ($m^3\ s^{-1}$), Q_p is the peak rainfall ($m^3\ s^{-1}$) and Tp is the watershed time to peak (h). According to Eq. (6), the rates of DSCD in association with time could be identified. Indeed, in order to develop IUSG ordinates, IUH and the sediment concentration were used. The following formula was then applied for production of IUSG ordinates (Banasik & Walling, 1996).

$$\mathbf{S_t = \frac{U_t C_t}{\int_0^\infty U_t C_t dt}} \tag{7}$$

where S_t, U_t and C_t were the ordinates of IUSG, IUH and DSCD, respectively.

2.4.2. Development of IUSG

Based on the entire 28 vector scales and cell sizes and all the 23 storm events, some 644 IUSG (23 storm events × 4 vector scales × 7 pixel sizes) were produced using Visual Basic for Applications (VBA) Programming in Excel 2013. IUSGs were subsequently converted to Δt-h unit sedimentgraph (USG) with a time lag of 0.5 h (Ghasemizade & Schirmer, 2013; Lhomme, Bouvier, & Perrin, 2004; Sadeghi et al., 2009; Seong & Lee, 2011). The DSGs were all ordinarily calculated based on direct sediment. Direct sediment was obtained from tested statistical relationships between effective rainfall and observed direct sediment in the Galazchai Watershed.

2.5. Evaluation of model performance

All the simulated components of the sedimentgraph viz. total sediment, peak sediment, time to peak and base time were evaluated. The model performance in the different scales and cell sizes was evaluated using nonlinear generalized gradient algorithm (NGGA) based on each sedimentgraph components, separately. The relative errors (REs) were calculated for total sediment, peak sediment, time to peak and base time using Eq. (8). The coefficient of efficiency (CE) and the root mean squared error (RMSE) (Sadeghi et al., 2009; Sadeghi & Asadi, 2010; Thirel et al., 2015) were also applied using Eqs. (9) and (10), respectively, for the assessment of entire simulated sedimentgrapgh as a whole.

$$\mathbf{RE(\%) = \left|\frac{SG_{Obs(i)} - SG_{Sim(i)}}{SG_{Obs(i)}}\right| \times 100} \tag{8}$$

$$\mathbf{CE = 1 - \frac{\sum_{i=1}^{n}\left(L_{Obs(i)} - L_{Sim(i)}\right)^2}{\sum_{i=1}^{n}\left(L_{Obs(i)} - \bar{L}_{Obs}\right)^2}} \tag{9}$$

$$\mathbf{RMSE = \sqrt{\frac{1}{n}\sum_{i=1}^{n}\left(L_{Sim(i)} - L_{Obs(i)}\right)^2}} \tag{10}$$

where $SG_{Obs(i)}$ and $SG_{Sim(i)}$, respectively show the sediment components (i.e., total sediment (t), peak sediment ($gr\ l^{-1}$), time to peak (h) and base time (h)) of the observed and simulated sedimentgraph. $L_{Obs(i)}$, $L_{Sim(i)}$ and $\bar{L}_{Obs}$ represent observed, simulated and average of sediment load (ton) at time i, respectively, and n is the time horizon in the sedimentgraphs. The higher CE and the smaller RE and RMSE the better performance of the model. The whole calculations were done in the IBM SPSS Statistic 22 software environment.

2.5.1. Clustering model evaluation criteria

To select of the best evaluation criterion among the study evaluation criteria (i.e., RE, CE and RMSE), they were initially clustered using clustering algorithm (Murphy, 2012; Purviya, Tiwari, & Mishra, 2014) using the k-mean algorithm. In this vein, a desired number of points were firstly used as the center of the cluster. The data were then allocated to the nearest cluster center (Han, Pei, & Kamber, 2011; Mishra, Dwivedi, Sarvanan, & Pathak,

2013). Finally, the cluster centers (error of sedimentgraph simulated components) and new clusters were produced based on extraction of the average in each cluster (Huang & Zhang, 2011). Each criterion evaluation were then clustered using the k-mean clustering method based on maximum similarity and minimum distance for the 644 produced DSGs. Finally, the variables with the highest intra-similarity in each individual group and with the least inter-similarity were clustered (Wu & Yang, 2005; Yao et al., 2013; Zong, Jin, Xu, & Pan, 2013). The relationships among datasets were also formulated in an un-supervised learning method using the K-mean method (Vijayalakshmi & Devi, 2012) as shown in Eq. (11).

$$J = \sum_{j=1}^{k} \sum_{i=1}^{n} \|x_i^{(j)} - c_j\|^2 \quad (11)$$

where, $\|\ \|$ and c_j were the distance between points and the center of j^{th} cluster, respectively.

The cluster center with the least value separately represented the optimal cluster with the least error for REs, CE and RMSE evaluation criteria for the entire 644 produced DSGs. Six optimal clusters associated with REs for total sediment, peak sediment, time to peak, base time and CE and RMSE with the highest accuracy of simulated sedimentgraphs were ultimately chosen. The mean error of $< 10\%$ in each optimal cluster was denoted as an acceptable range for simulated sedimentgraph components performance (Cotter, Chaubey, Costello, Soerens, & Nelson, 2003). The simulated sedimentgraphs and respective vector scales and cell sizes of each optimal cluster resulted from evaluated criterion were eventually analyzed and the corresponding critical vector scales and cell sizes were separately introduced. Accordingly, the general code of EjCjSjSGj was programmed for each variable in an individual cluster, respectively denoting storm event number, cell size, vector scale and number of simulated sedimentgraph. Obviously, the codes were different for each individual cluster and evaluation criterion.

2.5.2. Validation of selected clusters

The one-way analysis of variance (ANOVA) was applied in the long run to evaluate the soundness of k-mean algorithm in allocating separated variables among clusters (Giuntoli, Vidal, Prudhomme, & Hannah, 2015; Vlachos, Lin, Keogh, & Gunopulos, 2003). In this method, observations were allocated to different classes in related to an agent variable and the significant difference between classes of parameters was tested based on magnitude of F and significant level (P-value) (Spitzner, Marron, & Essick, 2003). The cluster with the lowest center (i.e., optimal cluster) showed the least error. The simulated sedimentgraphs for the optimal clusters were tested using ANOVA. The maximum frequency of scales and cell sizes in each optimal cluster was designated and the corresponding scale and cell size with the maximum percentage in each optimal cluster was defined as critical scale and cell size in connection with the study evaluation criterion. In addition, one sample *t*-test was also applied to analyze the significant difference in selected critical scale and cell size in each optimal cluster based on available frequency of scale and cell size category (Kim & Ramakrishna, 2005).

2.6. Factor analysis

Since the simulated sedimentgraphs in each optimal cluster belong to REs, CE and RMSE were different, the correlation coefficients of simulated sedimentgraphs were analyzed using principal component analysis (PCA) (Tripathi & Govindaraju, 2008; Singh, Kumar, Purohit, Kothari, & Dashora, 2009). The simulated sedimentgraphs related to evaluation criteria were accordingly reduced to a limited number of variables based on their influence rate that called factors. The impact of principal factors was then assessed through scrutinizing of factors and correlation coefficients for each evaluation criterion (Bro & Smilde, 2014; Adhami & Sadeghi, 2016).

3. Results and discussion

3.1. IUSG model development

About 644 sedimentgraphs were produced for all four vector scales and seven cell sizes associated with 23 storm events using developing TAHs, running the Clark's IUH model and ultimately processing IUSGs. An example of the simulated sedimentgraphs and corresponding detailed characteristics resulted from applying vector scale of 1:50000 and different cell sizes for the storm event of Nov. 14, 20012 have been shown in Fig. 2 and Table 2, respectively.

3.2. Direct sediment and effective rainfall relationship

The established well-fitting statistic relationship between direct sediment and effective rainfall was to develop IUSGs for the Galazchai Watershed as depicted in Eq. (12). According to Eq. (12), statistical linear relationship between observed sediments and effective rainfall showed the best correlation (Williams, 1975 and Sadeghi et al., 2009). Saeidi et al. (2016) also verified high correlation between direct sediment with some rainfall and runoff components in the Galazchai Watershed, Iran.

$$Sy = 28.454\ ER \qquad \left(R^2 = 0.78\right) \quad (12)$$

where Sy is observed total sediment (t) and ER is effective rainfall (mm).

3.3. Results of clusters validation

Table 3 shows the results of ANOVA test for accuracy and performance of k-mean clustering related to simulated sedimentgraphs in optimal clusters belong to REs for total sediment, peak sediment, time to peak, base time and also CE and RMSE (Liu et al., 2016). According to Table 3 and considering p-values of very low and variable magnitudes of F-value, null hypothesis was refused. Therefore, the validity of the classified clusters was confirmed for all REs, CE and RMSE. Besides, for each optimal cluster, the one-sample *t*-test was applied based on REs for total sediment, peak sediment, time to peak, base time as well as CE and RMSE (Xiong, Wu, & Chen, 2009) to test difference among selected critical scales and cell sizes. The detailed results have been given in Table 4.

3.4. Analysis of selected clusters for model evaluation

Six optimal clusters were classified according to the lowest REs for total sediment, peak sediment, time to peak, base time and also CE and RMSE evaluation criteria, separately, whose corresponding results have been shown in Table 5.

According to Table 5, all vector scales viz. 1:25000, 1:50000, 1:100000 and 1:250000 performed similarly in simulation of total sediment, peak sediment, time to peak and base time as well as CE. But the critical scales of 1:50000 and 1:100000 were determined by RMSE evaluation criterion. Whilst, cell sizes had different roles and effects compared to vector scales for sedimentgraphs simulation. So that, critical cell sizes resulted from simulated sedimentgraphs of optimal clusters for total sediment and base time were not unique to a particular cell size. Whenever, cell sizes of 5, 20, 30, 50 and 100 m for time to peak component with a

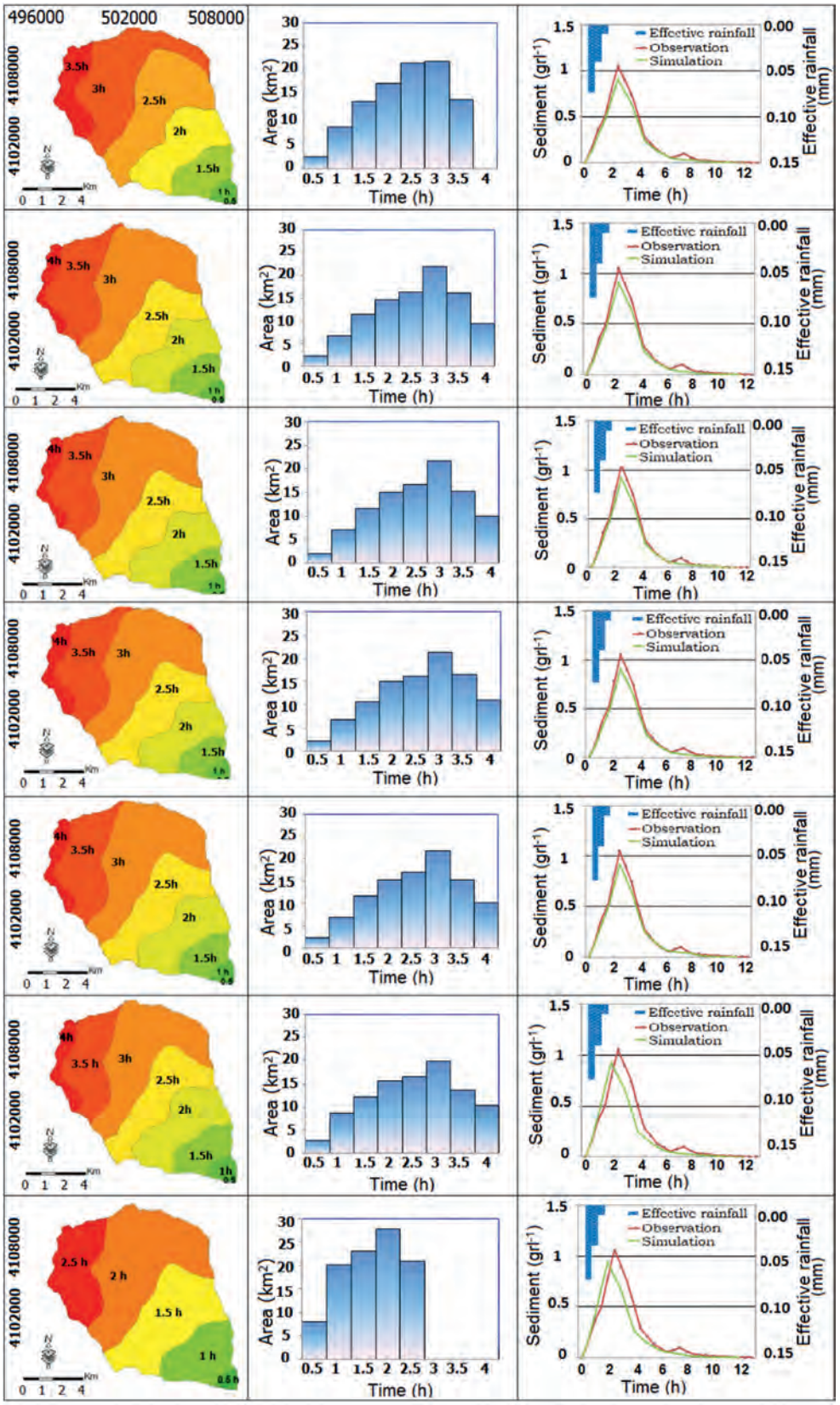

Fig. 2. Isochrone maps with 0.5 h interval for vector scale of 1:50000 and cell sizes of 5, 10, 20, 30, 50, 100 and 200 m (Top to down) in Left column, corresponding time-area histograms (Center), and simulated direct sedimentgraph for Nov. 14, 2012 storm event (Right) for the Galazchai Watershed, Iran.

less sensitivity were found as critical cell sizes. In addition, 200-m cell size was selected as a critical cell size for peak sediment and CE evaluation criteria. Indeed, 5, 10 and 50 m cell sizes were determined as critical cell sizes in association with RMSE evaluation criterion. In this matter, the maximum frequency of critical scale for all evaluation criteria (i.e., REs for total sediment, peak

Table 2
Results of simulated sedimentgraph components for vector scale of 1:50000 and different cell sizes for Nov. 14, 2012 storm event for the Galazchai Watershed, Iran.

No	Cell size (m)	Total sediment (t)	Peak sediment (gr l^{-1})	Time to peak (h)	Base time (h)
1	**5**	55.21	0.91	2.50	12.00
2	**10**	54.99	0.91	2.50	12.00
3	**20**	55.51	0.92	2.50	12.00
4	**30**	55.15	0.91	2.50	12.00
5	**50**	55.76	0.92	2.50	12.00
6	**100**	55.94	0.93	2.00	12.00
7	**200**	56.42	0.93	2.00	12.00
Maximum		56.42	0.93	2.50	12.00
Minimum		54.99	0.91	2.00	12.00
Mean		55.57	0.92	2.36	12.00
Coefficient of variation (%)		0.91	0.91	10.35	0.00

Table 3
Results of ANOVA for the study components of the direct sediment resulted from optimal clusters for the Galazchai Watershed, Iran.

Variables		Error		F-Value	P-Value
		Mean Square	df		
RE	**Total sediment**	0. 003	636	7408.777	0.00
	Peak sediment	2.017	636	11602.341	0.002
	Time to peak	4.580	636	12234.534	0.003
	Base time	1.953	636	14579.378	0.001
CE		0.014	636	18922.542	0.01
RMSE		0.002	636	8521.180	0.000

Table 4
Results of one-sample *t*-test for critical scales and cell sizes of optimal cluster based on different evaluation criteria for the Galazchai Watershed, Iran.

Variables		Test value (%)	df	Significant level (2-tailed)	Mean difference	95% confidence interval of the difference	
						Lower	Upper
RE	**Peak sediment**	5.08	27	0.00	− 1.50	− 1.78	− 1.23
	Time to peak	3.98	27	0.002	− 0.40	− 0.65	− 0.16
CE		4.40	27	0.001	− 0.82	− 1.01	− 0.64
RMSE		7.37	27	0.001	− 1.85	− 2.37	− 1.34

Note: No critical scale and cell size were determined for total sediment and base time.

Table 5
Characteristics of selected critical scale and cell sizes for the simulated sedimentgraphs resulted from optimal clusters based on evaluation criterion for the Galazchai Watershed, Iran.

Evaluation criteria		Critical scale (m)	Critical cell size (m)	Optimal TC (h)	Error (%)
Relative Error (RE)	**Total sediment**	Whole	whole	2.5–4	− 8.74
	Peak sediment	Whole	200	2.5	− 7.53
	Time to peak	Whole	5, 20, 30, 50, 100	2.5–4	− 3.54
	Base time	Whole	whole	2.5–4	+ 6.24
Coefficient of Efficiency (CE)		Whole	200	2.5	63
Root Mean Squared Error (RMSE)		1:50000 1:100000	50 5 10	4	4.67

sediment, time to peak, base time, CE and RMSE) was found to be in associated with 1:50000 and 1:100000 and the critical cell sizes of 5, 50 and 200 m were also the most frequent ones. All the vector scales played important roles in estimation of total sediment, peak sediment, time to peak and base time as well as CE evaluation criterion. These findings verified that a particular scale and cell size cannot be necessarily determined as a critical scale and cell size for the entire study variables. In sediment simulation process there were two effective factors including IUH and DSG. The IUH was produced based on TAHs but DSG was developed based on effective rainfall. The former is directly influenced by scale and cell size but the latter is based on characteristics of input variable of rainfall which is not directly controlled by changes in scales and cell sizes. Because effective rainfall each storm event (extracted from rainguage station without depending to maps scales and cell sizes) were used to produce total sediment and DSG. On the other hands, effective runoff and other parameters (depending to maps scales and cell sizes) were used as inputs of Clark's IUH model for simulating runoff. Therefore, it can be implied that change in rainfall properties has more controlling role than change in vector scales in total sediment, peak sediment, time to peak, base time and the whole shape of the DSG represented by CE. In contrary, the implication is different for evaluation criteria of RMSE, since vector scales of 1:50000 and 1:100000 vector scales were denoted as critical scales. These findings clearly verified the high sensitivity of some shape components of simulated sedimentgraph to scales and cell sizes and TC of the watershed. It can be further said that total sediment and base time as two elementary characteristics of sediment yields estimation in the watershed scale are less depending upon hydrological features such as TAHs and TC. Even though time to peak also had similar behavior with base time and total sediment because all scales and a large number of cell sizes (i.e., 5, 20, 30, 50 and 100 m) were selected as critical sizes. In this context, Ahmad, Ghumman, and Ahmad (2009) confirmed complexity of effects of rainfall on the simulation of different components of hydrograph. It can be said that RMSE is the most sensitive evaluation criterion to changes in vector scales with 1:50000 and 1:100000. The highest sensitivity of evaluation criteria to changes in cell sizes was also attributed to peak sediment (200 m), CE (200 m) and RMSE (5, 10, 50 m). Although, Vaze, Teng, and Spencer (2010) and Charrier and Li (2012) confirmed that DEMs with higher resolution had better accuracy in the hydrologically important spatial indices, stream network and floodplain boundaries. Herein, although evaluation criteria of peak sediment and CE have the highest sensitivity to cell sizes but they have the lowest sensitivity to vector scales. The result shows vector scales compared to cell sizes play weak role in controlling estimation accuracy of total sediment, peak sediment, time to peak and base time as well as CE criterion. This is more obvious in case of peak sediment and CE criteria respectively, since cell size of 200 m was lonely selected as critical cell size. Likewise, Silakhori and Ownegh (2012) have also showed that 1:25000 vector scale had no acceptable efficiency to distinct geomorphological units. In fact, changes in measures and rates of information related to vector scales were not able to change simulation results. In the event that different cell sizes had different effects upon accuracy of estimation of sedimentgraph components. The results were verified by Zhang et al. (2009) who reported that different topographic maps represented various levels of simulation results. Azizian and Shokoohi (2014) similarly showed that DEMs with different resolutions had different effects on performance of the hydrological models.

In addition, the estimated TC for the best simulated sedimentgraphs in optimal clusters based on REs for total sediment, time to peak and base time were 2.5–4 h. Whereas, the TC resulted from simulated sedimentgraphs in optimal cluster based on REs for the peak sediment and CE was 2.5 h. While, RMSE based TCs

were estimated 4.0 h in the best simulated sedimentgraphs. Das, Patel, and Sengupta (2016) verified the effects of different cell sizes on physiographic and morphometric parameters of the watersheds. The mean and standard deviation of TC of 23 observed storm events were about 4 ± 1.81 h. It can be concluded that different vector scales and cell sizes led to the different number of isochrones and TCs as an important factor in the Clark's IUH model and finally, difference in the accuracy of simulated sedimentgraphs components. Olivera (2001) showed that different digital spatial data based on DEMs with different cell sizes had different effects on accuracy of the hydrological models outputs.

Indeed, mean REs for total sediment, peak sediment, time to peak and base time in each optimal cluster were calculated (Table 5). Accordingly, REs for total sediment, peak sediment, time to peak and base time components in critical scales and cell sizes were estimated − 8.74, − 7.53, − 3.54 and + 6.24%, respectively. The mean values of CE and RMSE were also acceptably estimated 63% and 4.67%, respectively. In addition, as shown in Table 3, total sediment volume, peak sediment and time to peak were underestimated, while, the base time was overestimated. Likewise, the time to peak and total sediment had the respective lowest and highest errors of 3.54, 8.74%. In this matter, Saeidi et al. (2016) confirmed that time to peak of the sedimentgraph had the highest accuracy compared to other simulated sedimentgraph components. Further, RE for base time (6.24%) was less than that of time to peak (7.53%). The result showed that estimation errors of non-sensitive sedimentgraph components to critical scales and cell sizes were high due to more effectability from highly changeable rainfall and sediment concentration characteristics. Similar findings have been reported by Usul (2002) and Mostafazadeh et al. (2015) in developing storm-wise sedimentgraphs at Watershed scales. Rovira and Batalla (2006) and Sadeghi et al. (2008) confirmed the meaningful effects of rainfall variable on sedimentgraph components. Indeed, the values of CE and RMSE resulted from simulated sedimentgraphs of optimal clusters were estimated 63% and 4.67%, respectively. However, the overall applicability of the simulated sediment was proved for the small study watershed as already confirmed by Zhang, Chang, and Wu (2008) and Lu et al. (2017). On the other hand, the CEs resulted from optimal clusters for estimation of sediment properties showed that the CE has not been influenced by different vector scales but it depended on cell sizes. So that, 200-m cell size showed the best performance of CE. Besides, RMSE had the highest sensitivity to different vector scales. This difference in quiddity of CE and RMSE led to their different performances as mentioned by Ritter and Muñoz-Carpena (2013).

3.5. Results of factor analysis of the study variables

The six optimal clusters with the highest accuracy of evaluation criteria including REs for total sediment, peak sediment, time to peak, base time and also, CE and RMSE resulted from critical scales and cell sizes were reduced to two factors (Table 6) using Principal Component Analysis (PCA) (Suganyadevi & Savitha, 2016). The factors showed correlation rate of evaluation criterion and also of the most effective clusters (Noori, Khakpour, Omidvar, & Farokhnia, 2010; Westra, Brown, Lall, & Sharma, 2007). In addition,

Table 6
Factor analysis of the study DSGs resulted from optimal cluster based on different evaluation criteria for the Galazchai Watershed, Iran.

Factor	Total	Partial Variance (%)	Cumulative (%)
1	2.85	47.63	47.63
2	1.36	22.67	70.30

Table 7
Correlation coefficients of the study DSGs resulted from optimal cluster based on different evaluation criteria for the Galazchai Watershed, Iran.

Sedimentgraph variables		Factor	
		1	**2**
RE	Total sediment	0.86*	− 0.16
	Peak sediment	0.85*	− 0.27
	Time to peak	0.17	0.83*
	Base time	− 0.84*	− 0.07
CE		− 0.08	0.68*
RMSE		− 0.79*	− 0.28

the best simulated sedimentgraphs resulted from critical scales and cell sizes determined both accuracy and correlation. In this matter, Hu, Wu, and Zhang (2007) verified applying PCA in results of rainfall–runoff components. Indeed, Nagel, Rieckermann, and Sudret (2017) showed successful performance of PCA led to acceptable sensitivity analysis of simulated hydrological components. Considering Table 6, PCA divided principal parameters (six optimal clusters) into two factors and also Table 7 showed correlation coefficients of the study DSGs of optimal cluster based on different evaluation criteria.

Based on all the evaluation criteria, clustered simulated sedimentgraphs related to these two evaluation criteria contained the highest correlation coefficient and also defined some 70.30% of variances of all simulated sedimentgraphs (Tables 6, 7). So that, the first factor explained some 47.63% of whole variance of all the simulated sedimentgraphs (Table 6). The first factor included clustered simulated sedimentgraphs based on the least REs for total sediment, peak sediment, base time and RMSE with respective correlation coefficients of 0.86, 0.85, − 0.84 and − 0.79. While, the second factor showed correlation coefficients of simulated sedimentgraphs related to RE for time to peak (0.83) and CE (0.68) with partial contribution in defining some 22.67% of total variance of all simulated sedimentgraphs. It is further implied that, RMSE (belong to the first factor) appropriated higher variance (47.63%) of all the simulated sedimentgraphs and with negative correlation coefficient of 0.79, while CE (belong to second factor) explained lower variance of 22.67% with correlation coefficient of 0.68. The acceptable results of data reduction using PCA for spatial analysis of hydrologic models have also been verified by Moradi Dashtpagerdi et al. (2013). Although RMSE was well-correlated with more number of sedimentgraphs components, but it is very important that the differences be considered in the hydrologists researches and finally represent an indicator among all the evaluation criteria of sediment modeling as representative and reflective all the sedimentgraph components features.

It can be inferred from the results that the RMSE can be supposed as a candidate for evaluation of accuracy of total sediment, peak sediment and base time of the sedimentgraphs. Whereas, the CE evaluation criterion is a suitable criterion for common sense about the accuracy of time to peak of the simulated sedimentgraph. Although both CE and RMSE evaluation criteria together represented all the sedimentgraph components features in sediment simulation. Besides, the variability of sedimentgraph components such as REs for peak sediment, time to peak, RMSE and CE evaluation criteria with different cell sizes were considerable for sediment simulation and the results were verified by Bruneau, Gascuel, Robin, Merot, and Beven (1995) and Chaplot (2005) for runoff simulation. The study findings also agree Zhang et al. (2014) who verified different behaviors of DEMs with different cell sizes on the sediment yield. They proved that DEM with mesh sizes of 30–100 m play role of an optimal sizes for sediment yield. Although, variability of sedimentgraph components such as REs for

peak sediment, time to peak and CE for different vector scales was alike. In other words, results of effect of some vector scales on some sedimentgraph components were similar. This shows different vector scales does not necessarily lead to different results for sedimentgraph components. In fact, in some conditions, different vector scales play same performance. So that the performance of vector scales of 1:25000, 1:50000, 1:100000 and 1:250000 for sedimentgraph components of total sediment, peak sediment, time to peak and base time was completely analogous. In this matter, Moradi Dashtpagerdi, Sadeghi, and Moradi (2017) showed that different topographic maps resulted from different vector scales played concordant performance for determination of some physiographic features in the Galazchai Watershed, Iran. Likewise, vector scales of 1:50000 and 1:100000 had similar performance in viewpoint of RMSE. The same vein, the comparable performance of the entire cell sizes for total sediment and base time components of the simulated sedimentgraph was approved. Whereas less cell sizes for REs for peak sediment, time to peak, RMSE and CE evaluation criteria produced analogous performance. Teegavarapu et al. (2006) and Vazquez and Feyen (2007) verified different effects of cell sizes on the hydrological models through evaluation of effects of DEMs resulted from different cell sizes. The results were confirmed by Zhang et al. (2018) whose findings showed the effects of different scales and cell sizes on estimation of soil organic carbon in eastern China.

4. Conclusion

The effect of vector scales and cell sizes on simulating sedimentgraphs based on IUHs resulted from the Clark's model (dependent to scale and cell size) and also DSGs resulted from input rainfall (independent from scale and cell size) was proved during the current study. So that, different high level of dependency of some components (i.e., sediment peak and time to peak) to different scales and cell sizes such as sediment peak, time to peak and some other sedimentgraphs components (i.e., total sediment and base time) to the effective rainfall were ascertained. It can be concluded from the results that the determination of critical scale and cell size for different sedimentgraph components is complex and depends on different issues. The results of current study further confirmed relationship between some sediment components and changes in DEMs resulted from different vector scales and cell sizes. It can be approved that sedimentgraph components affected by runoff and rainfall charactristics that runoff characteristics were produced based on different scales and cell sizes and but rainfall characteristics were earned based on rainguage station without impact of scale and cell size. Our findings showed that although occurring runoff and sediment are mutually necessary and depends on rainfall but variability of sedimentgraph components influenced by more rainfall charactristics than runoff characteristics. In this regard, to detect complexity of sediment processes and increasing accuracy of sedimentgraph simulated components it is necessary that impacts of various of rainfall, runoff characteristics and also scales and cell sizes role on sediment components were analyzed as well as. Correspondingly, the analysis of critical scale and cell size are necessary enough for hydrologists and soil and water conservationists to identify appropriate resolution for input variables in sediment modeling. Thought, more insight and comprehensive studies under different circumstances with more storm events are needed to prepare appropriate platform for drawing integrated conclusion.

Acknowledgement

The current research has been prepared based on the facilities collaboratively provided by Tarbiat Modares University, Iran, and Wageningen University and Research, the Netherlands, during the En. Mostafa Moradi's sabbatical leave whose valuable supports of both universities are acknowledged. The partial support of the Agrohydrology Research Group of Tarbiat Modares University (grant No. IG-39713), Iran, with regard to the corresponding author is also acknowledged. The constructive and valuable comments of anonymous reviewers and Editor-in-Chief of the Journal are greatly appreciated. The authors also are thankful to Dr. Mostafazadeh and Dr. Saeidi for providing the initial data bank of rainfall storm events. The valuable cooperation of Dr. M. Adhami in helping prepare the first draft of the manuscript is also thanked.

References

Adhami, M., & Sadeghi, S. H. R. (2016). Sub-watershed prioritization based on sediment yield using game theory. *Journal of Hydrology*, *541*, 977–987.
Adhami, M., Sadeghi, S. H. R., & Sheikhmohammady, M. (2018). Making competent land use policy using a co-management framework. *Land Use Policy*, *72*, 171–180.
Agirre, U., Goñi, M., López, J. J., & Gimena, F. N. (2005). Application of a unit hydrograph based on subwatershed division, comparison with Nash's instantaneous unit hydrograph. *Catena*, *64*(2), 321–332.
Ahmad, M. M., Ghumman, A. R., & Ahmad, S. (2009). Estimation of Clark's instantaneous unit hydrograph parameters and development of direct surface runoff hydrograph. *Water Resources Management*, *23*(12), 2417–2435.
Amore, E., Modica, C., Nearing, M. A., & Santoro, V. C. (2004). Scale effect in USLE and WEPP application for soil erosion computation from three Sicilian basins. *Journal of Hydrology*, *293*(1), 100–114.
Ariza-Villaverde, A. B., Jiménez-Hornero, F. J., & de Ravé, E. G. (2015). Influence of DEM resolution on drainage network extraction: A multifractal analysis. *Geomorphology*, *241*, 243–254.
Ayana, V. S., & Vargheese, K. O. (2013). Estimation of flood hydrograph using IUH and GIUH Based Clark Models. Proceedings of International Conference on Materials for the future-Innovative Materials, Processes, Product and Applications, pp. 325-329.
Azizian, A., & Shokoohi, A. (2014). DEM resolution and stream delineation threshold effects on the results of geomorphologic-based rainfall runoff models. *Turkish Journal of Engineering and Environmental Sciences*, *38*(1), 1–15.
Banasik, K., & Walling, D. E. (1996). Predicting sedimentgraphs for a small agricultural watershed. *Nordic Hydrology*, *27*(4), 275–294.
Bro, R., & Smilde, A. K. (2014). Principal component analysis. *Analytical Methods*, *6*(9), 2812–2831.
Bruneau, P., Gascuel, O. C., Robin, P., Merot, P., & Beven, K. (1995). Sensitivity to space and time resolution of a hydrological model using digital elevation data. *Hydrological Processes*, *9*(1), 69–81.
Chaplot, V. (2005). Impact of DEM mesh size and soil map scale on swat runoff, sediment, and NO3-N loads predictions. *Journal of Hydrology*, *312*(1–4), 207–222.
Charrier, R., & Li, Y. (2012). Assessing resolution and source effects of digital elevation models on automated floodplain delineation: A case study from the Camp Creek Watershed, Missouri. *Applied Geography*, *34*, 38–46.
Chow, V. T., Maidment, D. R., & Mays, L. W. (1988). *Applied hydrology* (p. 72) New York: Editions McGraw-Hill.
Clark, C. O., (1945). Storage and the unit hydrograph. In Proceedings of the American Society of Civil Engineers, ASCE, 69(9), pp. 1333-1360.
Cotter, A. S., Chaubey, I., Costello, T. A., Soerens, T. S., & Nelson, M. A. (2003). Water quality model output uncertainty as affected by spatial resolution of input data. *Journal of the American Water Resources Association*, *25*(39), 977–986.
Das, S., Patel, P. P., & Sengupta, S. (2016). Evaluation of different digital elevation models for analyzing drainage morphometric parameters in a mountainous terrain: A case study of the Supin–Upper Tons Basin, Indian Himalayas. *Springer Plus*, *5*(1), 1544.
Dixon, B., & Earls, J. (2009). Resample or not?! Effects of resolution of DEMs in watershed modeling. *Hydrological Processes*, *23*(12), 1714–1724.
Fang, X., Cleveland, T., Garcia, C., Thompson, D., & Malla, R. (2005). *Estimating timing parameters for direct runoff and unit hydrograph for Texas Watersheds* (p. 83) Lamar University (Technical Report 0-4696-1).
Froehlich, D. C. (2011). The Natural Resources Conservation Service (NRCS), overland flow travel time calculation. *Journal of Irrigation and Drainage Engineering*, *137*(4), 258–262.
Geng, X., Burcher, R., Kroetsch, D., & Mitchell, S. (2016). Multi-scale feature data and landscape analysis toolkit for predictive soil mapping. *Computing Ethics: A Multicultural Approach* (p. 271), 271.
Gentine, P., Troy, T. J., Lintner, B. R., & Findell, K. L. (2012). Scaling in surface hydrology: Progress and challenges. *Journal of Contemporary Water Research &*

Education, *147*(1), 28–40.
Ghasemizade, M., & Schirmer, M. (2013). Subsurface flow contribution in the hydrological cycle: Lessons learned and challenges ahead—a review. *Environmental Earth Sciences*, *69*(2), 707–718.
Giuntoli, I., Vidal, J. P., Prudhomme, C., & Hannah, D. M. (2015). Future hydrological extremes: The uncertainty from multiple global climate and global hydrological models. *Earth System Dynamics*, *6*(1), 267.
Goodchild, M. F. (2011). Scale in GIS: An overview. *Geomorphology*, *130*(1), 5–9.
Gurnell, A. M., Rinaldi, M., Belletti, B., Bizzi, S., Blamauer, B., Braca, G., … Demarchi, L. (2016). A multi-scale hierarchical framework for developing understanding of river behavior to support river management. *Aquatic Sciences*, *78*(1), 1–16.
Han, J., Pei, J., & Kamber, M. (2011). *Data mining: Concepts and techniques* (p. 703) Elsevier.
Hu, T., Wu, F., & Zhang, X. (2007). Rainfall–runoff modeling using principal component analysis and neural network. *Hydrology Research*, *38*(3), 235–248.
Huang, J., & Zhang, J. (2011). Fuzzy C-means clustering algorithm with spatial constraints for distributed WSN data stream. *International Journal of Advancements in Computing Technology*, *3*(2), 165–175.
Javernick, L., Brasington, J., & Caruso, B. (2014). Modeling the topography of shallow braided rivers using Structure-from-Motion photogrammetry. *Geomorphology*, *213*, 166–182.
Kauffeldt, A., Wetterhall, F., Pappenberger, F., Salamon, P., & Thielen, J. (2016). Technical review of large-scale hydrological models for implementation in operational flood forecasting schemes on continental level. *Environmental Modelling & Software*, *75*, 68–76.
Kim, M., & Ramakrishna, R. S. (2005). New indices for cluster validity assessment. *Pattern Recognition Letters*, *26*(15), 2353–2363.
Kumar, R., Chatterjee, C., Lohani, A. K., Kumar, S., & Singh, R. D. (2002). Sensitivity analysis of the GIUH based Clark model for a catchment. *Water Resources Management*, *16*(4), 263–278.
Kumar, S., & Rastogi, R. A. (1987). A conceptual catchment model for estimating suspended sediment flow. *Journal of Hydrology*, *95*, 155–163.
Lemma, T. M., Gessesse, G. D., Kassa, A. K., & Edossa, D. C. (2018). Effect of spatial scale on runoff coefficient: Evidence from the Ethiopian highlands. *International Soil and Water Conservation Research*, *6*(4), 289–296.
Lhomme, J., Bouvier, C., & Perrin, J. L. (2004). Applying a GIS-based geomorphological routing model in urban catchments. *Journal of Hydrology*, *299*(3), 203–216.
Liu, J., Liu, T., Bao, A., De Maeyer, P., Kurban, A., & Chen, X. (2016). Response of hydrological processes to input data in high Alpine catchment: An assessment of the Yarkant River Basin in China. *Water*, *8*(5), 181.
Lu, X., Li, Y., Washington-Allen, R. A., Li, Y., Li, H., & Hu, Q. (2017). The effect of grid size on the quantification of erosion, deposition, and rill network. *International Soil and Water Conservation Research*, *5*(3), 241–251.
Lv, L., Liao, K., Zhou, Z., Zhu, Q., & Shen, C. (2019). Determining hot moments, spots of hillslope soil moisture variations based on high-resolution spatiotemporal soil moisture data. *Catena*, *173*, 150–161.
Matei, D. (2012). *Runoff modeling using GIS. Application in torrential basins in the Apuseni Mountains (PhD dissertation)* (p. 2712) Romania: Physical and Technical Geography, University Cluj-Napoca.
Metz, J., & Tielbörger, K. (2016). Spatial and temporal aridity gradients provide poor proxies for plant–plant interactions under climate change: A large scale experiment. *Functional Ecology*, *30*(1), 20–29.
Mishra, S., Dwivedi, V. K., Sarvanan, C., & Pathak, K. K. (2013). Pattern Discovery in hydrological time series data mining during the Monsoon period of the high flood years in Brahmaputra River Basin. *International Journal of Computer Applications*, *67*(6), 7–14.
Moradi Dashtpagerdi, M., Nohegar, A., Vagharfard, H., Honarbakhsh, A., Mahmoodinejad, V., Noroozi, A., & Ghonchehpoor, D. (2013). Application of spatial analysis techniques to select the most suitable areas for flood spreading. *Water Resources Management*, *27*(8), 3071–3084.
Moradi Dashtpagerdi, M., Sadeghi, S. H.R ., & Moradi, H. R., (2017). Role of concordant performance of cell sizes of different scales of topographic maps on analysis of time of concentration estimation in Oshnaveyeh Galazchai Watershed. 2nd National Iranian conference on Hydrology, Iran, Shahrekord University⟨https://www.researchgate.net/publication/318598525⟩ (in Persian).
Morera, S. B., Condom, T., Vauchel, P., Guyot, J. L., Galvez, C., & Crave, A. (2013). Pertinent spatio-temporal scale of observation to understand suspended sediment yield control factors in the Andean region: The case of the Santa River (Peru). *Hydrology and Earth System Sciences*, *17*(11), 4641–4657.
Mostafazadeh, R., Sadeghi, S. H. R., & Sadoddin, A. (2015). Analysis of storm-wise sedimentgraphs and rating loops in Galazchai watershed, West-Azarbaijan. *Journal of Water and Soil Conservation*, *21*(5), 175–191.
Murphy, K. P. (2012). *Machine learning: A probabilistic perspective* (p. 1104) MIT Press (ISBN: 9780262306164).
Nagel, J. B., Rieckermann, J., & Sudret, B. (2017). Uncertainty quantification in urban drainage simulation: fast surrogates for sensitivity analysis and model calibration. arXiv preprint arXiv:1709.03283, pp. 1–37.
Nelson, P. A., Bellugi, D., & Dietrich, W. E. (2014). Delineation of river bed-surface patches by clustering high-resolution spatial grain size data. *Geomorphology*, *205*, 102–119.
Noori, R., Khakpour, A., Omidvar, B., & Farokhnia, A. (2010). Comparison of ANN and principal component analysis-multivariate linear regression models for predicting the river flow based on developed discrepancy ratio statistic. *Expert Systems with Applications*, *37*(8), 5856–5862.
Olivera, F. (2001). Extracting hydrologic information from spatial data for HMS modeling. *Journal of Hydrologic Engineering*, *6*(6), 524–530.
Ouédraogo, M. M., Degré, A., Debouche, C., & Lisein, J. (2014). The evaluation of unmanned aerial system-based photogrammetry and terrestrial laser scanning to generate DEMs of agricultural watersheds. *Geomorphology*, *214*, 339–355.
Overton, D. E., & Meadows, M. E. (2013). *Stormwater modeling* (p. 370) Elsevier, Academic Press (eBook ISBN: 9781483264660).
Pawluszek, K., & Borkowski, A. (2017). Impact of DEM-derived factors and analytical hierarchy process on landslide susceptibility mapping in the region of Rożnów Lake, Poland. *Natural Hazards*, *86*(2), 919–952.
Purviya, R., Tiwari, H. L., & Mishra, S. (2014). Application of clustering data mining techniques in temporal data sets of hydrology: A review. *International Journal of Scientific Engineering and Technology*, *3*(4), 359–363.
Ritter, A., & Muñoz-Carpena, R. (2013). Performance evaluation of hydrological models: Statistical significance for reducing subjectivity in goodness-of-fit assessments. *Journal of Hydrology*, *480*, 33–45.
Rovira, A., & Batalla, R. (2006). Temporal distribution of suspended sediment transport in a Mediterranean basin: The Lower Tordera (NE SPAIN). *Geomorphology*, *79*, 58–71.
Sadeghi, S. H. R., & Asadi, H. (2010). Importance of travel time duration between isochrones in estimation of flood resulting from Clark instantaneous unit hydrograph. *Journal of Water and Soil, Ferdowsi University of Mashhad*, *24*(4), 625–635.
Sadeghi, S. H. R., & Dehghani, M. (2006). Efficacy of estimation methods for storage coefficient of instantaneous unit hydrograph in flood unit hydrograph regeneration. *Journal of Agricultural Sciences and Natural Resources*, *13*(3), 152–160 (In Persian).
Sadeghi, S. H. R., Gholami, L., Sharifi, E., Darvishan, A. K., & Homaee, M. (2015a). Scale effect on runoff and soil loss control using rice straw mulch under laboratory conditions. *Solid Earth*, *6*(1), 1.
Sadeghi, S. H. R., Jalili, K., & Nikkami, D. (2009a). Land use optimization in watershed scale. *Land Use Policy*, *26*(2), 186–193.
Sadeghi, S. H. R., Mizuyama, T., Miyata, S., Gomi, T., Kosugi, K., Fukushima, T., … Onda, Y. (2008). Development, evaluation and interpretation of sediment rating curves for a Japanese small mountainous reforested watershed. *Geoderma*, *144*(1), 198–211.
Sadeghi, S. H. R., Mizuyama, T., Singh, J. K., & Tofighi, B. (2009b). Applicability of instantaneous unit sedimentgraph model in an Iranian large watershed. *International Journal of Ecological Economics and Statistics*, *13*(W09), 30–45.
Sadeghi, S. H. R., Mostafazadeh, R., & Sadoddin, A. (2015b). Changeability of simulated hydrograph from a steep watershed resulted from applying Clark's IUH and different time–area histograms. *Environmental Earth Sciences*, *74*(4), 3629–3643.
Saeidi, P., Sadeghi, S., & Telvari, A. (2016). Simulation of sedimentgraph using hydrograph. *Watershed Engineering and Management*, *8*(1), 28–41 (In Persian).
Saeidi, P., Sadeghi, S. H., & Telvari, A. (2017). Dynamic of sediment hysteresis patterns during storm events. *Journal of Range and Watershed Management (Iranian Journal of Natural Resources)*, *70*(1), 125–138 (In Persian).
Saghafian, B., Julien, P. Y., & Rajaie, H. (2002). Runoff hydrograph simulation based on time variable isochrone technique. *Journal of Hydrology*, *261*(1), 193–203.
Schmalz, B., Zhang, Q., Kuemmerlen, M., Cai, Q., Jähnig, S. C., & Fohrer, N. (2015). Modelling spatial distribution of surface runoff and sediment yield in a Chinese river basin without continuous sediment monitoring. *Hydrological Sciences Journal*, *60*(5), 801–824.
Schneider, D. (2009). *Quantitative Ecology: Measurement, models, and scaling* ((2nd ed.). . Elsevier Inc.
Schoorl, J. M., Sonneveld, M. P. W., & Veldkamp, A. (2000). Three-dimensional landscape process modelling: The effect of DEM resolution. *Earth Surface Processes and Landforms*, *25*, 1025–1034.
Seong, K. W., & Lee, Y. H. (2011). A practical estimation of Clark IUH parameters using root selection and linear programming. *Hydrological Processes*, *25*(23), 3676–3687.
Shaw, J. R. (2015). *Multi-scale drivers of riparian vegetation form and function in ephemeral stream networks of the Sonoran Desert (Doctoral dissertation)* (p. 120) Colorado State University.
Sherriff, S. C., Rowan, J. S., Melland, A. R., Jordan, P., Fenton, O., & OhUallachain, D. O. (2015). Investigating suspended sediment dynamics in contrasting agricultural catchments using ex situ turbidity-based suspended sediment monitoring. *Hydrology and Earth System Sciences*, *19*, 3349–3363.
Shrestha, P., Sulis, M., Simmer, C., & Kollet, S. (2015). Impacts of grid resolution on surface energy fluxes simulated with an integrated surface-groundwater flow model. *Hydrology and Earth System Sciences*, *19*(10), 4317–4326.
Silakhori, I., & Ownegh, M. (2012). Comparing the effect of map scale in separation geomorphological land units of desertification hazard mapping using GIS (case study: Hares-Abad's Sabzevar region). *Journal of Applied RS & GIS Techniques in Natural Resource Science*, *3*(4), 91–105 (in Persian).
Singh, P. K., Kumar, V., Purohit, R. C., Kothari, M., & Dashora, P. K. (2009). Application of principal component analysis in grouping geomorphic parameters for hydrologic modeling. *Water Resources Management*, *23*(2), 325.
Singh, V. P. (1988). *Hydrologic systems. Rainfall–runoff modeling*. 1. New Jersey: Prentice Hall.
Spitzner, D. J., Marron, J. S., & Essick, G. K. (2003). Mixed-model functional ANOVA for studying human tactile perception. *Journal of the American Statistical Association*, *98*(462), 263–272.
Subramanya, K. (2000). *Engineering hydrology* ((2nd ed.). New Delhi: Tata McGraw Hill Publishing Company Limited (Eighth reprint).
Suganyadevi, P., & Savitha, J. (2016). Application of enhanced clustering for different data mining techniques. *International Journal of Emerging Technologies in*

Engineering Research, *4*(1), 81–87.
Tarolli, P. (2014). High-resolution topography for understanding Earth surface processes: Opportunities and challenges. *Geomorphology*, *216*, 295–312.
Teegavarapu, R. S., Viswanathan, C., & Ormsbee, L. (2006). Effect of digital elevation model (DEM) resolution on the hydrological and water quality modeling. In World Environmental and Water Resource Congress, Examining the Confluence of Environmental and Water Concerns. pp. 1–8.
Thirel, G., Andréassian, V., Perrin, C., Audouy, J. N., Berthet, L., Edwards, P., … Lindström, G. (2015). Hydrology under change: An evaluation protocol to investigate how hydrological models deal with changing catchments. *Hydrological Sciences Journal*, *60*(7–8), 1184–1199.
Tripathi, S., & Govindaraju, R. S. (2008). Engaging uncertainty in hydrologic data sets using principal component analysis: BaNPCA algorithm. *Water Resources Research*, *44*(10), 1–12.
Usul, N., & Yilmaz, M. (2002). Estimation of instantaneous unit hydrograph with Clark's Technique in GIS. In Proceedings of 2002 ESRI International User Conference, USA, p 21.
Vaze, J., Teng, J., & Spencer, G. (2010). Impact of DEM accuracy and resolution on topographic indices. *Environmental Modelling & Software*, *25*(10), 1086–1098.
Vazquez, R. F., & Feyen, J. (2007). Assessment of the effects of DEM gridding on the predictions of basin runoff using MIKE SHE and a modeling resolution of 600m. *Journal of Hydrology*, *3*(34), 73–87.
Vijayalakshmi, M., & Devi, M. R. (2012). A survey of different issue of different clustering algorithms used in large data sets. *International Journal of Advanced Research in Computer Science and Software Engineering*, *2*(3), 305–307.
Vlachos, M., Lin, J., Keogh, E., & Gunopulos, D. (2003). A wavelet-based anytime algorithm for k-means clustering of time series. In: Proceedings of Workshop on Clustering High Dimensionality Data and Its Applications, pp. 23–30.
Welle, P. I., & Woodward, D. (1986). *Time of concentration. Hydrology technical note no. N4, USDA, Soil Conservation Service*. Chester, PA: NETC.
Westra, S., Brown, C., Lall, U., & Sharma, A. (2007). Modeling multivariable hydrological series: Principal component analysis or independent component analysis? *Water Resources Research*, *43*(6), 1–11 (W06429).
Wilbanks, T. J. (2006). *How scale matters: Some concepts and findings Millennium Ecosystem Assessment* (pp. 21–35)Island Press.
Williams, J. R. (1975). Sediment routing for agricultural watersheds, Water Resources Bulletin. *American Water Resources Association*, *11*(5), 965–974.
Williams, J. R. (1978). A sedimentgraph model based on an instantaneous unit sedimentgraph. *Water Resources Research*, *14*(4), 659–664.
Wu, J., & Qi, Y. (2000). Dealing with scale in landscape analysis: An overview. *Geographic Information Sciences*, *6*(1), 1–5.
Wu, K. L., & Yang, M. S. (2005). A cluster validity index for fuzzy clustering. *Pattern Recognition Letters*, *26*(9), 1275–1291.
Wu, S., Li, J., & Huang, G. H. (2008). A study on DEM-derived primary topographic attributes for hydrologic applications: Sensitivity to elevation data resolution. *Applied Geography*, *28*(3), 210–223.
Xiong, H., Wu, J., & Chen, J. (2009). K-means clustering versus validation measures: A data-distribution perspective. *IEEE Transactions on Systems, Man, and Cybernetics, Part B (Cybernetics)*, *39*(2), 318–331.
Yao, Y., Liu, Y., Yu, Y., Xu, H., Lv, W., Li, Z., & Chen, X. (2013). K- Support Vector Machine: An effective SVM algorithm based on K-means clustering. *Journal of Computers*, *8*(10), 2632–2639.
Zhang, J. X., Chang, K. T., & Wu, J. Q. (2008). Effects of DEM resolution and source on soil erosion modelling: A case study using the WEPP model. *International Journal of Geographical Information Science*, *22*(8), 925–942.
Zhang, J. X., Wu, J. Q., Chang, K., Elliot, W. J., & Dun, S. (2009). Effects of DEM source and resolution on WEPP hydrologic and erosion simulation: A case study of two forest watersheds in northern Idaho. *Transactions of the ASABE*, *52*(2), 447–457.
Zhang, L., Liu, Y., Li, X., Huang, L., Yu, D., Shi, X., … Xing, S. (2018). Effects of soil map scales on simulating soil organic carbon changes of upland soils in Eastern China. *Geoderma*, *312*, 159–169.
Zhang, P., Liu, R., Bao, Y., Wang, J., Yu, W., & Shen, Z. (2014). Uncertainty of SWAT model at different DEM resolutions in a large mountainous watershed. *Water Research*, *53*, 132–144.
Zong, Y., Jin, P., Xu, D., & Pan, R. (2013). A clustering algorithm based on local accumulative knowledge. *Journal of Computers*, *8*(2), 365–371.

International Soil and Water Conservation Research 7 (2019) 150–157

Contents lists available at ScienceDirect

International Soil and Water Conservation Research

journal homepage: www.elsevier.com/locate/iswcr

Original Research Article

Quantitative analysis of morphometry on Ribb and Gumara watersheds: Implications for soil and water conservation

Daniel Asfaw [a], Getachew Workineh [a,b]

[a] Debre Tabor University Department of Geography and Environmental Studies, Ethiopia
[b] Debre Tabor University Guna Tana Integrated Field Research and Development Center, Ethiopia

ARTICLE INFO

Article history:
Received 18 August 2018
Received in revised form
24 December 2018
Accepted 4 February 2019
Available online 5 February 2019

Keywords:
Morphometric analysis
Drainage density
Guna-Tana watershed
Soil and water conservation

ABSTRACT

Morphometric analysis is a quantitative measurement and mathematical analysis of landforms. It plays a significant role in understanding the geohydrological characteristics of a drainage basin in relation to the terrain feature and its flow patterns. It also helps to estimate the incidence of infiltration and runoff, and other related hydrological character of a watershed like erosion and sediment transport which has a strong implication for natural resource conservation. This study has attempted to quantify the morphometric characteristics of Guna- Tana watershed for proper implementation of soil and water conservation practices. ASTER (DEM) was used for extracting morphometric parameters. The watershed covers a total area of 3601.5 km^2 and it has a basin length of 78.89 km. It has been tried to generate morphometric parameters which account basin drainage network, geometry, drainage texture, and relief characteristics together with hypsometric characteristics. The morphometric analysis of drainage density of the study watershed is 0.49 km/km^2 which indicates the basin is highly permeable and result with better underground water storage capacity. Ruggedness number is 0.02 that implies the area is less prone to soil erosion. In addition, it has stream frequency of 0.32 and form factor 0.57 which indicates slightly elongated basin shape. Comparative analysis of its sub watersheds Gumara and Ribb was also undertaken. Therefore, practicing soil and water conservation in the watershed could enhance/strengthen the water storage capacity, prevent sediment loss and related natural resource from the watershed that rehabilitate its productivity.

1. Introduction

Morphometric analysis is a quantitative measurement and mathematical analysis of landforms (Clarke, 1996; Kaur, Singh, Verma, & Pateriy, 2014; Vaidya, Kuniyal, & Chauhan, 2013). Morphometric study of a basin provides valuable information about the drainage characteristics of a basin (Aparna, Nigee, Shimna, & Drissia, 2015; Dubey, Sharma, & Mundetia, 2015; Strahler et al., 1964). As Horton (1932) and Soni (2017) described, morphometric analysis is an important indicator of landform structure and hydrogeologic processes (Gizachew & Berhan, 2018; Smith, 1958; Miller, 1953), losses of materials from a watershed, soil physical properties, land processes and erosional features (Khare, Mondal, Mishra, Kundu, & Meena, 2014). Morphometric analysis was introduced by Horton (1932, 1945), to study the origin of river networks. Further works were made by Strahler (1952, 1964).

In morphometric analysis linear aspect (basin length, stream order, steam length, mean stream length, bifurcation ratio, mean bifurcation ratio), areal aspect (basin area, drainage density, basin shape, drainage texture, circulatory ratio, stream frequency, elongated ratio) and relief aspect (basin relief, relief ratio, ruggedness number, gradient ratio, basin slope and relative relief) of a watershed is computed to derive the general character of the watershed (Melton, 1958; Miller, 1953; Strahler, 1964). Lithology, relief and climate are the main environmental natures that determine the nature of basin and respective characteristics of running water systems working at the basin level (Rastogi & Sharma, 1976).

Recently with the advancement of remote sensing and spatial technology, computation of various terrain and hydro-morphometric characters of drainage basins was simplified (Aparna et al., 2015; Gizachew & Berhan, 2018; Gutema, Kassa, Sifan, & Koriche, 2017). A number of researchers who have conducted morphometric analysis by implementing geospatial methods confirmed that, detailed and updated information of drainage basin can be

Peer review under responsibility of International Research and Training Center on Erosion and Sedimentation and China Water and Power Press.

https://doi.org/10.1016/j.iswcr.2019.02.003

generated in a systematic way (Aparna et al., 2015; Ayele, Yasuda, Shimizu, Nigussie, & Kifle, 2017; Farhan, Anbar, Al-Shaikh, & Mousa, 2017; Gizachew & Berhan, 2018; Gutema et al., 2017; Javed, Khanday, & Ahmed, 2009; Kulkarni, 2013; Magesh, Chandrasekar, & Soundranayagam, 2012; Pande & Moharir, 2017; Prakash, Singh, & Shukla, 2016; Rai, Mohan, Mishra, Ahmad, & Mishra, 2017; Soni, 2017; Singh, Gupta, & Singh, 2014; Singh, Sarangi, & Sharma, 2008). Their finding showed that, morphometric analysis provides basic information about hydrogeologic, erosion prone areas and characteristics of watershed in terms of ground and surface water potential. As Harinath and Raghu (2013) described, since in-situ method is capital and labor intensive, and time consuming, spatially explicit morphometric analysis is panacea for intended morphometric characterization of the watershed.

Soil and water resource are basic and critical resources for developing countries like Ethiopia, where majority of the society and the overall national economy relied on agricultural production system (Daniel & Mulugeta, 2017; Gezahegn, Anteneh, Solomon, & Reddy, 2018; Sharma, Gajbhiye, Nema, & Tignath, 2014). Therefore, this invaluable natural resource needs protection and conservation before it is exposed to degradation (Morgan, 2005). Watershed level soil and water conservation activities demand a thorough understanding of its physical characteristics (Gezahegn et al., 2018; Gutema et al., 2017; Kaur et al., 2014). Even though this is an established reality, still there is paucity of detailed studies which characterize morphometric characteristics of Guna-Tana watershed. Therefore, the objective of this study was to quantify the hydro-morphometric character of Ribb and Gumara sub watersheds which can serve as a reconnaissance input for soil and water conservation related planning activities.

2. Methods and materials

2.1. Description of the study area

Gumara and Ribb are sub watersheds Guna-Tana watershed, which is found at astronomic location of 11°00'∼12°30' North latitude and 37°30'∼38°30' East longitude. Relatively, Guna-Tana watershed is found in South Gondar Zone, Amhara National Regional State (ANRS) where it extends from the top of Mount Guna towards Lake Tana in north west part of the region. The watershed has an area coverage of 3601.5 km^2 and 401.73 km perimeter with 78.9 km basin length. Topographically, it lies over the area altitudinally ranging from 4104 m to 1755 m above mean sea level. Ribb and Gumara rivers are the main streams which d flows from Mount Guna to Lake Tana. These streams have pivotal role in social and economic contribution for the society. The watershed consists three agroecology. These were *Kola* (Sub tropical), Woina Dega (Sub humid) and *Wunch* (Afro-alpine) ecosystems. Mountain ecosystem at mount Guna and its surrounding is threatened by human encroachment where it is found soil and water conservation hotspot geographic area (Fig. 1).

2.2. Data source and analytical approach

Remotely sensed Surface Radar Topographic Mission (SRTM) Digital Elevation Model (DEM) with 30 m spatial resolution was downloaded from United State Geological Survey (USGS) website (). Since the watershed lies on four different scenes, ERDAS 2015 software was used to mosaic, extract Area of Interest (AOI) (Gumara and Ribb sub watersheds) for the study. From extracted DEM artificial sinks were removed by filling operation. Overall watershed boundary delineation and generation of stream features

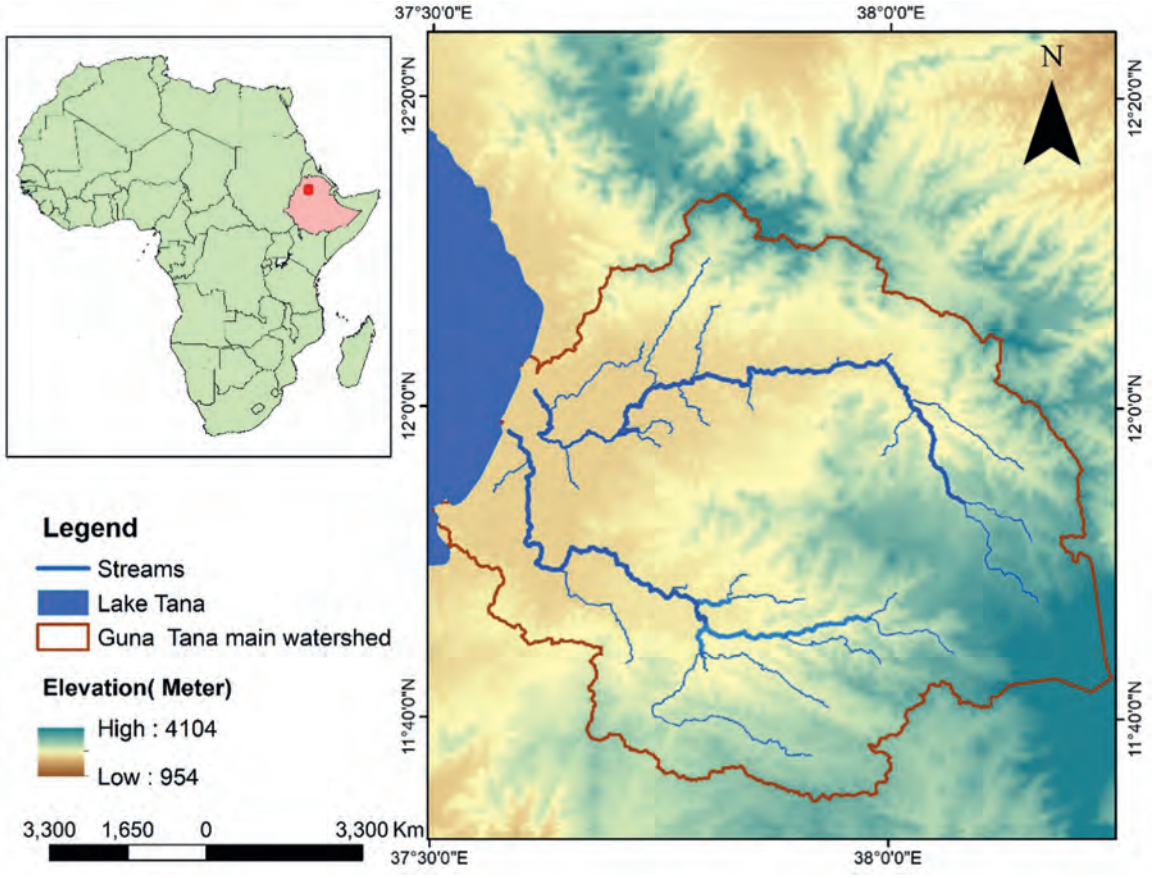

Fig. 1. Location map of Guna-Tana watershed.

Table 1
Selected Morphometric parameters and respective equations.

Category of parameter	Name and Notation of Morphometric Parameters	Given equation	References
Linear parameters	Stream Order	Hierarchical Rank	Strahler (1952)
	Stream number (Nu)	Nu = N1 + N2 + …+Nn	Horton (1945)
	Stream length (LT) (km)	Lt = L1 +L2 + L3 + …+ Ln	Strahler (1964)
	Mean Stream Length (RI)	Lum=Lu / Nu	Strahler (1964)
	Stream length ratio (Lur)	Lur=Lu/(Lu−1)	Strahler (1964)
	Bifurcation ratio (Rb)	Rb=Nu/Nu+ 1	Strahler (1964)
	Mean Bifurcation Ration (Rbm)	Rbm=Average of bifurcation	Strahler (1964)
	Basin length (Km)	Obtained from Arc Map	
	Main stream Length (Km)	Obtained from Arc Map	
Areal parameters	Area of the basin (Km^2)	Obtained from Arc Map	
	Basin Perimeter (Km)	Obtained from Arc Map	
	Form factor Ratio (Rf)	$Rf = A / Lb^2$	Horton (1932)
	Elongation Ratio (Re)	$Re= (2/ Lb)* 2\sqrt{(A/\pi)}$	Schumm (1956)
	Circularity Ration (Rc)	$Rc = 4\pi * A / P^2$	Strahler (1964)
	Drainage Density (Dd) (km/Km^2)	Dd = Lu / A	Horton (1932)
	Drainage Texture (T)	T = Lu / P	Horton (1932)
	Stream Frequency (Fs)	Fs = Nu / A	Horton (1932)
	Compactness coefficient (Cc)	$Cc = 0.2824 * p/ \sqrt{A}$	Gravelius, (1914)
Relief parameters	Maximum Basin Height (m)	GIS software analysis	
	Minimum Basin Height (m)	GIS software analysis	
	Basin Relief (R)(m)	R= Max H – Min H	Strahler (1952)
	Relief Ratio (Rr)	Rr = R / Lb	Schumm (1956)
	Relative Relief Ratio (Rhp)	Rhp = H * 100/P	Melton (1958)
	Ruggedness Number (Rn)	Rn = Dd * (H / 1000)	Patton and Baker (1976)
	Gradient ratio (Rg)	Rg = Es - Em/Lb	Sreedevi, Owais, Khan, and Ahmed (2009)
	Hypsometric curve and	Partial area (a/A) with partial altitude (h/H)	Kouli, Vallianatos, Soupios, and Alexakis (2007)
	HI (Hypsometric Integration)	*Emean* – *Emin* / *Emax* –*Emin*	Pike and Wilson (1971)

and respective spatial computation activities were done by using ArcMap version 10.4. Microsoft excel was also used for derivation some primary and derived morphometric parameters by using basic attributes computed from spatial data (Table 1).

3. Result and discussion

3.1. Linear morphometric parameters of Gumara and Ribb sub watersheds

Linear aspect is a one-dimensional characteristic of morphometric analysis of a basin. Our analysis accounted linear parameters which consists of Stream Order, Number of Stream Order and stream Number ratio. In drainage basin, stream network is a collection of stream segments (Horton, 1945; Leopold, Wolman, & Miller, 1964; Strahler,1957). The position of a stream in the hierarchy has been assigned a sequence of numbers according their position. Even though, there are different methods of assigning number for streams, current study has adopted Strahler (1952) stream order model.

According to the Strahler (1952) ordering, each fingertip channel is assigned as a first order and as two similar orders confluences they form the next higher order and when two different order streams meet together, the order takes the value the higher order stream. Accordingly, both Gumara river and Ribb rivers have 4th level stream orders with a total of 54 and 69 streams (Table 2) and both of them have dendritic drainage pattern. As Gizachew and Berhan (2018) and Soni (2017) stated a basin with such type of pattern developed upon uniform resistant rocks, massive igneous rocks and produces large quantity of streamflow.

Results indicated that total stream length of the basin is inversely proportional to the stream order, in that the lower stream order has shorter length (176,153.11 km) with larger number of streams (39) and in the higher order, a single stream has 50364.73 km length (Table 2 and Fig. 2). Similar results were reported by many empirical studies (Farhan et al., 2017; Gizachew & Berhan, 2018; Gutema et al., 2017; Khare et al., 2014; Singh et al., 2014). This is attributed to variation of slope and physiographic structure in the basin. This further implies the variability of infiltration capacity with level of stream orders across the basin. in addition to

Table 2
Linear morphometric parameters of Gumara and Ribb sub watersheds.

Watershed	Stream order	No of str orders	Total_Str_ Length (km)	Mean Stream length	Stream Length ratio	Bifurcation ratio	Mean bifurcation ratio	Basin Length (km)	Fitness ratio
Gumara Sub watershed	1	39	176153.11	4516.7	–	–	3.75	74.07	0.31
	2	12	139590.84	11632.57	0.79	3.25			
	3	2	42798.13	21399.06	0.31	6.00			
	4	1	50364.73	50364.73	1.18	2.00			
		54	408906.81				3.75	74.07	0.31
Ribb sub watershed	1	51	322040.55	6314.52	–	–	3.77	85.43	0.37
	2	14	82052.82	5860.92	0.25	3.64			
	3	3	39657.64	13219.12	0.48	4.67			
	4	1	64876.08	64876.08	1.64	3.00			
		69	508627				3.77	85.43	0.37

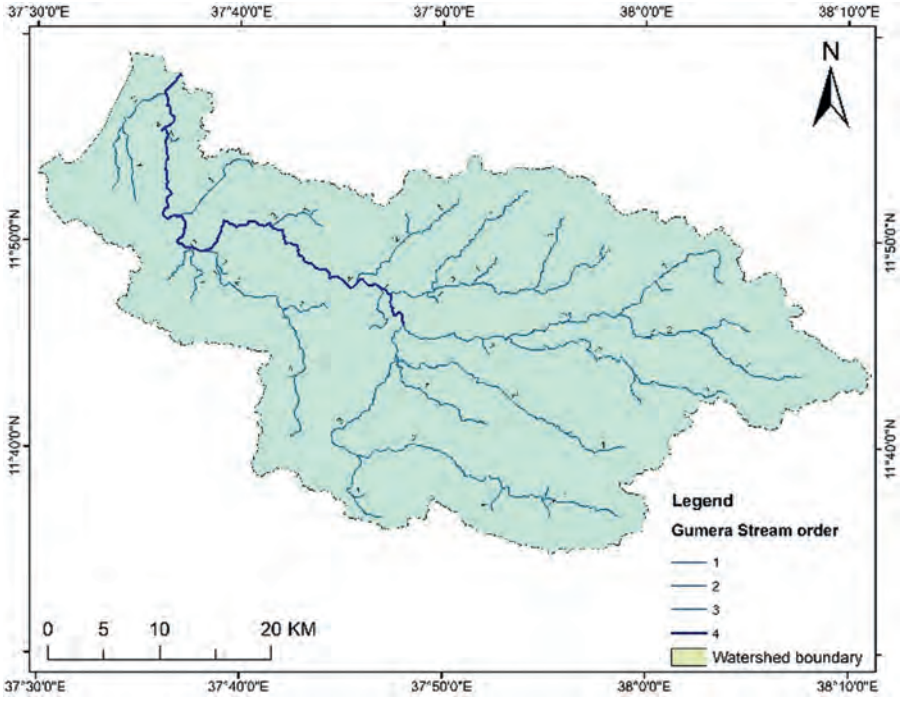

Fig. 2. Gumara stream order.

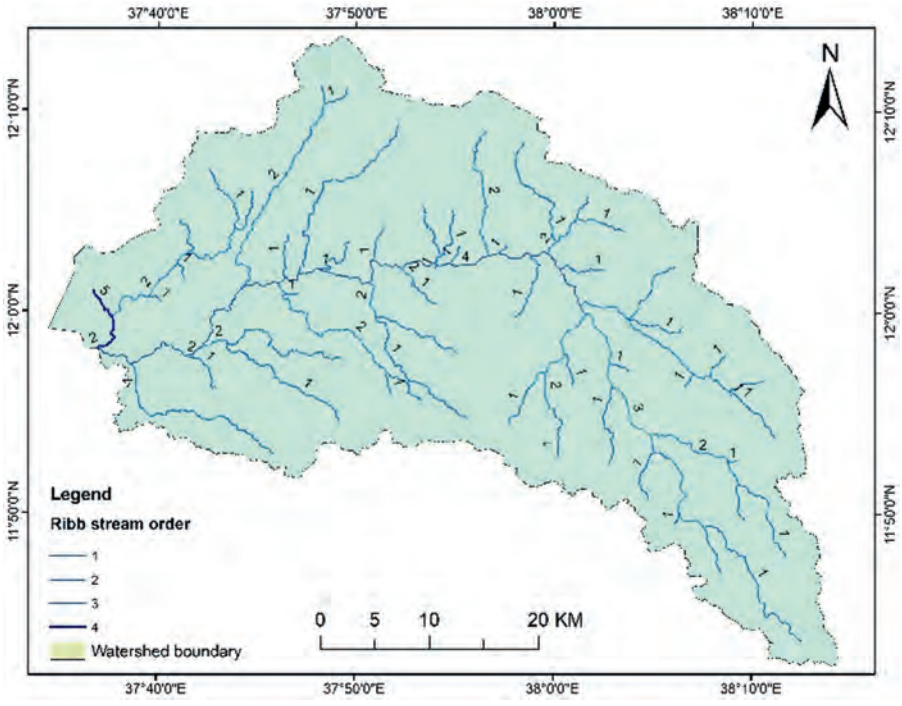

Fig. 3. Ribb stream order.

these, short stream length describes steep slopes while longer lengths indicate relatively flatter gradient (Withanage, Dayawansa, & De Silva, 2014). (Fig. 3)

As indicated on Table 2, the Bifurcation Ratio (*Rb*) for streams in Gumara sub watershed was 3.5, 6.0 and 2.0 for streams with orders of 1, 2 and 3 respectively while for streams in Ribb sub watershed it was found 3.64, 4.67 and 3.0 for stream orders of 1, 2 and 3 respectively. The Mean Bifurcation Ratio (*Rbm*) of Rib sub watershed is greater than Gumara sub watershed (Table 2).

Bifurcation ratio is dimensionless which indicates the degree of integration between streams segments of different orders in drainage basin (Gutema et al., 2017). It has fundamental importance in drainage basin analysis as it is the principal parameter to associate the hydrological character of a basin with the geological structure and climatic conditions (Gizachew & Berhan, 2018; Singh et al., 2014).

If bifurcation ratio ranges between 3.0 and 5.0, the geological structures of the watershed do not affect drainage pattern of streams (Chow, Maidment, & Mays, 1988; Strahler, 1964). Similarly, if the bifurcation ratio is less the 3.0, the geological structure of the

basin is flat and homogenous. In this respect, the bifurcation values of Ribb sub watershed (range from 3.64 to 3.00). This implies that it is developed on almost homogenous topographic structure where the stream network pattern is less affected by the geological structure, whereas bifurcation values of Gumara sub watershed ranges from 2.0 to 6.0. This indicates that some part of the stream network was influenced by the lithology and geological structure of the watershed.

3.2. Areal morphometric parameters of Gumara and Ribb watershed

Analysis results indicates that Gumara sub watershed has relatively lower drainage density than Gumara sub watershed. Accordingly, Gumara has a drainage density of 0.26 km/km^2 and Ribb experienced 0.30 km/km^2. Even though there were little differences, the sub watersheds have almost similar drainage density which is low. This implies that the basin experience with permeable sub surface material, low erosion exposure (Ali, Ali, Ikbal, Bashir, & Fadhl, 2018; Farhan & Anaba, 2016; Farhan et al., 2017; Prasad, Mondal, Banerjee, Nandakumar, & Singh, 2008) and better ground water potential and the length of stream channel is shorter to carry runoff (Ali et al., 2018; Strahler, 1964). Drainage density (Dd) expresses the closeness of spacing of channels, thus providing a quantitative measure of the average length of stream channel for the whole basin (Horton, 1932; Strahler, 1964). It is measured by dividing the total length of the stream to the area of the basin (Guth, 2011). As Moglen, Eltahi, and Bras (1998); Kelson and Wells (2011) described, drainage density is related to landscape dissection, climate and vegetation, soil and rock properties, and landscape evolution processes. In addition, drainage density reflects the infiltration capacity of the land (Yunus, Oguchi, & Hayakawa, 2014) and the output of water and sediment from the catchment area, and erosion susceptibility (Farhan et al., 2016).

Higher drainage density is related to fine texture with impermeable subsurface material, sparse vegetation and high relief of the basin where erosion potential and run off is higher (Farhan & Anaba, 2016; Horton, 1945; Strahler, 1964). On the other hand, low drainage density leads to coarse basin texture with highly permeable sub-soil and relatively better or thick vegetative cover and low relief (Kaur et al., 2014; Nag & Chakraborty, 2003; Prasad et al., 2008; Vaidya et al., 2013). With this regard, relatively Rib watershed is susceptible for soil erosion as it has large stream length and respective density per unit area.

As Schumm (1956) defined elongated ratio is the ratio of diameter of a circle having the same area as of the basin and maximum basin length. It is a measure of the shape of the river basin and it depends on the climatic and geologic types. The elongated ratio of Gumara sub watershed is 0.60 and Ribb sub watershed is 0.55 (Table 3). A circular basin is more efficient in runoff discharge than an elongated basin (Farhan & Anaba, 2016; Singh & Singh, 1997).

As Strahler (1964) stated the value of elongation ratio generally varies from 0.6 to 1.0 over a large variety of climatic condition and geologic structure. The values close to 1.0 characterizes regions with very low relief (Strahler, 1964) and has circular shape (Schumm, 1956), and also characterized by high infiltration capacity and low runoff (Reddy, Maji, & Gajbhiye, 2004; Singh et al., 2014) whereas that of 0.6–0.8 associated with high relief and steep ground slope (Schumm, 1956). Basins with more elongated shapes have lower numeric values of elongation ratio (Farhan & Anaba, 2016). These values can be grouped into 3 categories, namely circular (>0.9), oval (0.9–0.8) and less elongated (<0.7). Form analysis results of Gumara and rib sub watersheds, it can be inferred that, both sub watersheds have elongated basin shape with higher relief and steep slope. These brought watersheds for high susceptibility to erosion resulted from generation and transportation of high amount of sediment load (Reddy, Kumar, Srivastava, & Singh, 2016; Singh & Singh, 1997).

In addition to elongation ratio, basin shapes and related hydrologic characteristics can be understood from form factor. As per Horton (1932) form factor is the ratio of the area of the basin and square of the basin length. The value of form factor would always be greater than 0.78 for perfectly circular basin (Khare et al., 2014; Strahler, 1964). Smaller the value of form factor ($<$ 0.45), the more elongated the basin (Chopra, Dhiman, & Sharma, 2005). Basins with high values of form factors have high peak flows for shorter duration (Farhan & Anaba, 2016; Singh & Singh, 2011). In line with these, results of morphometric analysis showed that the value of from factor for Gumara and Ribb sub watershed was 0.28 and 0.24 respectively. These form factor numbers were under small category (Chopra et al., 2005). Both watersheds have elongated shape, which is consistent with the result of elongated ratio (Table 3). This implies that, both Gumara and Ribb sub watersheds are elongated in their shape and have a low peak flow with longer duration of time. But relatively, Gumara sub watershed has higher numeric values of form factor. This indicates that it is characterized with high peak flows with shorter duration time. This resulted in flash floods at the lower courses of the stream in surrounding community.

The other areal morphometric parameter analyzed was circularity ratio. Circularity ratio is the ratio of the area of the basins to the area of circle having the same circumference as the perimeter of the basin (Miller, 1953; Strahler, 1964). According to Miller (1953) description the value of circulatory ratio is influenced by length and frequency of streams, geological structure, land use and land cover, climate, relief and slope of the basin. The value of circularity ratio varies from 0 to 1.0. Higher the ratio, the more circular shape of the basin and vice-versa (Miller, 1953). Analysis output indicates that, both Gumara and Ribb sub watersheds has lower circularity ratio. Accordingly, Gumara and Ribb sub watersheds is 0.23 and 0.28 respectively. As stated by Ali et al. (2018), Aparna et al. (2015), Soni (2017), the value of circularity ratio is equal to unity when the basin shape is a perfect circle and it ranges from 0.4 to 0.5, when the basin shape is strongly elongated and highly permeable and composed of homogeneous geologic materials. In line to this, computed circularity ratio values were indications as both sub watersheds experience elongated shape. This in turn indicates the geologic strata of the watershed is composed of relatively homogeneous and highly permeable geologic material.

Table 3
Areal aspect of Ribb and Gumara sub watershed.

Watershed	Drainage Perimeter (km)	Drainage Area (km)	Drainage density in (km/ km^2)	Stream frequency (n/ km^2)	Drainage texture	Form Factor	Drainage intensity	Circulatory Ration	Elongated Ration	Compactness Ratio
Gumara sub watershed	291.94	1559.56	0.26	0.03	0.18	0.28	0.13	0.23	0.60	2.10
Ribb sub watershed	2275.63	1716.58	0.30	0.04	0.25	0.24	0.14	0.28	0.55	1.89

Table 4
Relief aspects of Gumara and Ribb watershed.

Watershed	Min elevation	Max elevation	Basin relief	Relief ratio	Gradient Ratio	Ruggedness Number (Rn)	Hypsometric integration (Hi)
Gumara sub watershed	1758	3700	1942	0.026	0.026	0.502	0.5
Ribb watershed	1760	4103	2343	0.027	0.027	0.694	0.5

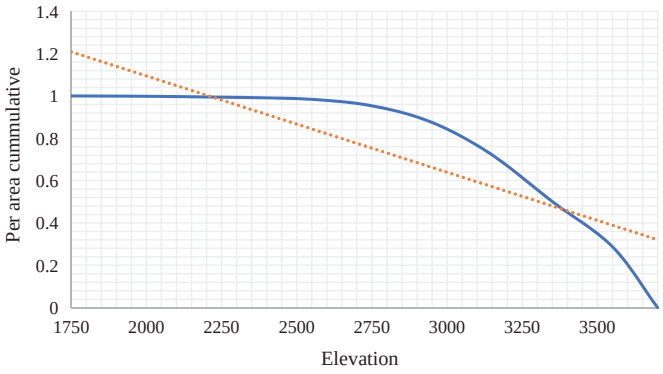

Fig. 4. Hypsometric curve of Gumara sub watershed.

3.3. Relief related morphometric parameters of Gumara and Ribb watershed

As Sahu et al. (2016) stated that relief is a three-dimensional parameter of a drainage basin which expressed in terms of area, volume and altitude of watershed landforms. It measures the vertical fall from the head of each stream segment to the point where it joins the higher order stream (Biswas, Sudhakar, & Desai, 1999; Schumn, 1956).

The study area Guna Tana major watershed, which comprises by Gumara and Ribb sub watersheds is characterized by altitudinal differences of 1755 m above sea level and 4100 m above sea level minimum and maximum elevations. The basin relief ratio of Gumara is 0.026 and Ribb sub watershed is 0.027 (Table 4). Basin relief ratio indicates overall steepness of a drainage basin and the intensity of erosional process operating on the slope of the basin (Schumn, 1956; Chopra et al., 2005; Rudraiah, Govindaiah, & Vittala, 2008) and basin morphological characteristics (Hadley & Schumm, 1961). A study conducted by Kumar and Joshi (2015) came with basin relief ratio indicating steep to moderate slope, where the region is dominated by plateau with undulating landforms.

The other parameter incorporated in analysis was ruggedness number (Rn). It refers to the level of smoothness and roughness of the basin terrain or surface unevenness (Selvan, Ahmad, & Rashid, 2011) and its vulnerability for watershed level soil erosion (Gutema et al., 2017). Ruggedness values range between zero and one., Values nearer to 0 refers to relatively smoother situation and those nearer to 1 shows more rugged terrain characteristics. As Strahler (1956) stated if the values of drainage density and relief are extremely high, the value of ruggedness number becomes higher as a result the slope is not only steep but long. The ruggedness value of Gumara sub watershed is 0.502 and Ribb sub watershed is 0.694 (Table 4), which shows the terrain of the basin is moderately rugged. A study by Gizachew and Berhan (2018) on Dhidhessa river basin of Ethiopia shows a ruggedness number 3.1 which is high indicating the area has a rugged topography and susceptible to soil erosion. Similarly, Kumar and Joshi (2015) on another watershed get Rn 0.78 and interpreted as the area has steep slope and susceptible for soil erosion. Bothe sub watershed experienced moderately rugged terrain characteristics. Relatively, Ribb sub watershed is more rugged and susceptible for soil erosion and high sediment transport.

3.4. Hypsometric curve

Hypsometric analysis is the association of horizontal cross-sectional drainage basin area to elevation. It was introduced by Langbein (1947) to express the overall slope and forms of drainage basin. In other words, Prasannakumar, Vijith, and Geetha (2011) hypsometric curve is related to the volume of the soil mass in the basin and the amount of erosion that had occurred in a basin against the remaining mass. It can also indicate the amount or level of erosion that has taken place over past geological time (Bishop, Shroder, Bonk, & Olsenholler, 2002). More importantly, the graphical shape of hypsometric curve is an indication of watershed age at landscape evolution. Accordingly, a basin with upwards convex hypsometric curve is at its youth stage, S-shaped curve indicates mature stage and upward concave curves shows the basin on peneplain or old age stages of landscape evolution (Strahler, 1952).

As indicated on Figs. 4 and 5, the hypsometric curve of both sub watersheds is convex upward which connotes as the sub watershed were in its youth stage of land evolution. Such kind of watersheds has experienced slight erosion and dissection process (Ritter, Kochel, & Miller, 2002; Strahler, 1952). According to the watershed is slightly eroded and un-dissected. Analyzed hypsometric Index (HI) value for both sub watersheds was found 0.5 (Table 4). HI values within a range of 0.35–0.60 characterizes watersheds at equilibrium or almost on maturity (Kumar & Joshi, 2015; Strahler, 1952). With this regard, both sub watersheds were approaching to maturity stage but still left with surface material to erode and transported to its downstream. Therefore, if conservation activity is concerted, there is probability of halting erosion to create stable landscape.

3.5. Implications for soil and water conservation

Soil erosion is serious environmental problem in Ethiopian highlands (Mulugeta & Stahar, 2010). Identifying the vulnerability and status of a watershed for intervention is a prerequisite. Drainage density, form factors, circulatory ratio, elongated ratio (Gizachew & Berhan, 2018; Sharma et al., 2014) and other relief morphometric parameters, and hypsometric curve are proxies of soil erosion.

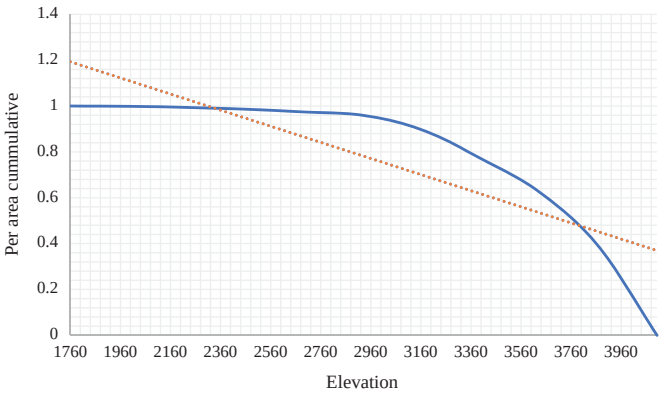

Fig. 5. Hypsometric curve of Ribb sub watershed.

Drainage density of the watersheds implies that experiences high relief and steep slope where generation and transportation of sediment load is higher (Singh & Singh, 1997). Similarly, form factor which show flooding and peak flow duration, and values of ruggedness number implies erosion susceptibility of a watersheds (Chopra et al., 2005; Gutema et al., 2017; Reddy et al., 2016; Ritter et al., 2002). Relatively, Ribb watershed is highly vulnerability for soil erosion as its drainage density, ruggedness number, basin relief and associated parameter values indicted. So, this reconnaissance analysis showed a need to conduct soil and water conservation practices. In addition to which, the watersheds experiences convex upward hypsometric curve where the sub watershed is in its youth stage of land evolution (Bishop et al., 2002) and early stage of loss materials from the watershed. Therefore, early conservation practices will maintain loss of materials and curtails vulnerability of the area.

4. Conclusion

Two major sub watersheds of Gumara and Ribb has very slight differences in both linear, areal, relief morphometric parameters but, relatively Ribb sub watershed is more susceptible for erosion and sediment transport which is evidenced from its drainage density and other areal morphometric parameters like ruggedness number. This indicates that soil and water conservation programs to halt sediment transport, nutrient lose and increasing ground water recharge should prioritize Rib sub watershed. This does not entail Gumara sub watershed is not vulnerable for such kind of surface processes. Both sub watersheds were at its youth age approaching to maturity as evidenced from hypsometric analysis. Such kind of sub basins have profound surface material which is not transported to its outlets that if conservation woks were implemented properly, it can be possible to realize well-functioning hydrogeologic processes.

Acknowledgment

We would like to provide our gratitude for Daniel Ayalew (PhD), whom shares his knowledge and experiences not only in this research issue but also in all GIS and Remote sensing science. Since, without him it couldn't be possible to conduct this research. More than which he was enthusiastic and dedicate to show us the way how to be an expert in our area of specialization. Next to this, our heartfelt goes to Mr. Getu Tessema who were with us by providing documents and ideas for this work. Finally, we thank NASA (USGS open Remote sensing data provider) for providing remote sensing data freely.

References

Ali, U., Ali, S. A., Ikbal, J., Bashir, M., & Fadhl, M. (2018). Soil erosion risk and flood behavior assessment of Sukhnag catchment Kashmir Basin: Using GIS and remote sensing. *Journal of Remote Sensing & GIS*, 7, 230. http://dx.doi.org/10.4172/2469-4134.1000230.

Aparna, P., Nigee, K., Shimna, P., & Drissia, T. K. (2015). Quantitative analysis of geomorphology and flow pattern analysis of Muvattupuzha River Basin using Geographic Information system. *Journal Aquatic Procedia*, *4*, 609–616.

Ayele, A., Yasuda, H., Shimizu, K., Nigussie, H., & Kifle, W. (2017). Quantitative analysis and implications of drainage morphometry of the Agula watershed in the semi-arid northern Ethiopia. *Applied Water Science*, *7*, 3825–3840. http://dx.doi.org/10.1007/s13201-017-0534-4.

Bishop, M. P., Shroder, J. F., Bonk, R., & Olsenholler, J. (2002). Geomorphic change in high mountains: A western Himalayan perspective. *Global and Planetary Change*, *32*, 311–329.

Biswas, S., Sudhakar, S., & Desai, V. R. (1999). Prioritization of sub watersheds based on morphometric analysis of drainage basin: A remote sensing and GIS approach. *Journal of the Indian Society of Remote Sensing*, *27*(3), 155–166.

Clarke, J. I. (1996). *Morphometry from Maps. Essays in geomorphology* (pp. 235–274) New York: Elsevier Publications.

Chopra, R., Dhiman, R. D., & Sharma, P. (2005). Morphometric analysis of sub-watersheds in Gurdaspur district, Punjab using remote sensing and GIStechniques. *Journal of the Indian Society of Remote Sensing*, *33*, 531–539.

Chow, V. T., Maidment, D., & Mays, L. W. (1988). *Applied hydrology*. New York: McGraw Hill.

Daniel, A., & Mulugeta, N. (2017). Factors affecting adoption of soil and water conservation practices: The case of Wereillu Woreda (District), South Wollo Zone, Amhara Region, Ethiopia. *International Soil and Water Conservation Research* (pp. 273–279), 273–279. http://dx.doi.org/10.1016/j.iswcr.2017.10.002.

Dubey, S. K., Sharma, D., & Mundetia, N. (2015). Morphometric analysis of the Banas River Basin using the geographical information system, Rajasthan, India. *Hydrology*, *3*(5), 47–54. http://dx.doi.org/10.11648/j.hyd.20150305.11.

Farhan, Y., & Anaba, O. (2016). Watershed prioritization based on morphometric analysis and soil loss modeling in Wadi Kerak (Southern Jordan) using GIS techniques. *International Journal of Plant & Soil Science*, *10*(6), 1–18. http://dx.doi.org/10.9734/IJPSS/2016/25321.

Farhan, Y., Anbar, A., Al-Shaikh, N., & Mousa, R. (2017). Prioritization of semi-arid agricultural watershed using morphometric and principal component analysis, remote sensing, and GIS techniques, the Zerqa River Watershed, Northern Jordan. *Agricultural Sciences*, *8*, 113–148. http://dx.doi.org/10.4236/as.2017.81009.

Gezahegn, W., Anteneh, D., Solomon, T., & Reddy, R. U. (2018). Spatial modeling of soil erosion risk and its implication for conservation planning: The case of the Gobele watershed, East Hararghe Zone, Ethiopia. *Land*, *7*(25)), http://dx.doi.org/10.3390/land7010025.

Gizachew, K., & Berhan, G. (2018). Hydro-geomorphological characterization of Dhidhessa River Basin, Ethiopia. *International Soil and Water Conservation Research*, *6*, 175–183. http://dx.doi.org/10.1016/j.iswcr.2018.02.003.

Gutema, D., Kassa, T., Sifan, A., & Koriche (2017). Morphometric analysis to identify erosion prone areas on the upper blue Nile using GIS: case study of Didessa and Jema sub- basin, Ethiopia. *International Research Journal of Engineering and Technology*, *04*(08).

Guth, P. L. (2011). Drainage basin morphometry: A global snapshot from the shuttle radar topography mission. *Hydrology and Earth System Sciences*, *15*, 2091–2099. http://dx.doi.org/10.5194/hess-15-2091.

Hadley, R. F., & Schumm, S. A. (1961). Sediment sources and drainage basin characteristics in upper Cheyenne River Basin. USGS Water-Supply Paper. (1531-B, 1-198).

Harinath, V., & Raghu, V. (2013). Morphometric analysis using arc GIStechniques: A case study of Dharurvagu, South Eastern Part of Kurnool district, Andhra Pradesh, India. *International Journal of Science and Research*, *2*(1), 2319–7064.

Horton, R. E. (1932). Drainage basin characteristics. *Transactions of the American Geophysics Union*, *13*, 350–361.

Horton, R. E. (1945). Erosional development of streams and their drainage basins; hydro- physical approach to quantitative morphology. *Bulletin of the Geological Society of America*, *56*, 275–370.

Javed, A., Khanday, M. Y., & Ahmed, R. (2009). Prioritization of sub-watershed based on morphometric and land use analysis using remote sensing and GIS techniques. *Journal of Indian Society Remote Sensing*, *37*, 261–274.

Kaur, M., Singh, S., Verma, V. K., & Pateriy, B., 2014. Quantitative geomorphological analysis & land use/ land cover change detection of two sub-watersheds in ne region of Punjab, India. The International Archives of the Photogrammetry, Remote Sensing and Spatial Information Sciences, Volume XL-8.

Kelson, K. I., & Wells, S. G. (2011). Geologic influences on fluvial hydrology and bedload transport in small mountainous watersheds, northern New Mexico, USA: in drainage basin morphometry for identifying zones for artificial recharge: A case study from Gagas River Basin, India.

Khare, D., Mondal, A., Mishra, P. K., Kundu, S., & Meena, P. K. (2014). Morphometric analysis for prioritization using remote sensing and GIS techniques in a Hilly catchment in the state of Uttarakhand, India. *Indian Journal of Science and Technology*, *7*(10), 1650–1662.

Kouli, M., Vallianatos, F., Soupios, P., & Alexakis, D. (2007). GIS-based morphometric analysis of two major watersheds, western Crete, Greece. *Journal of Environmental Hydrology*, *1*(15).

Kumar, P., & Joshi, V. (2015). Characterization of hydro geological behavior of the upper watershed of River Subarnarekha through morphometric analysis using remote sensing and GIS approach. *International Journal of Environmental Sciences*, *6*(4)), http://dx.doi.org/10.6088/ijes.6049.

Kulkarni, M. D. (2013). The basic concept to study morphometric analysis of river drainage basin: A review. *International Journal of Science and Research*, *4*, 7.

Langbein, W. B. (1947). *Topographic characteristics of drainage basins* (pp. 127–157) (U.S.G.S Water Supply Paper 968C).

Leopold, L. B., Wolman, M. G., & Miller, J. P. (1964). *Fluvial processes in geomorphology*. San Francisco: Free- man.

Magesh, N. S., Chandrasekar, N., & Soundranayagam, J. P. (2012). Delineation of groundwater potential zones in Theni district Tamil Nadu using remote sensing GIS and MIF techniques. *Geoscience Frontiers*, *3*, 189–196.

Melton, M. A. (1958). Correlations structure of morphometric properties of drainage systems and their controlling agents. *Journal of Geology*, *66*, 442–460.

Miller, V. C. (1953). *A quantitative geomorphic study of drainage basin characteristics in the Clinch Mountain area Virginia and Tennessee* (pp. 189–200)Department Geology Columbia University (ONR Project Tech – Report NT 389-042, No. 3).

Morgan, R. P. C. (2005). *Soil erosion and conservation* ((3rd ed.). New York: Blackwell Publishing.
Moglen, G. E., Eltahi, E. A., & Bras, R. L. (1998). On the sensitivity of drainage density to climate change. *Water Resource Research*, *34*, 855–862.
Mulugeta, D., & Stahar, K. (2010). Assessment of integrated soil and water conservation measures on key soil properties in South Gonder, North West highlands of Ethiopia. university of Hohenheim, Stuttgart, Germany. *Journal of Soil Science and Environmental Management*, *1*(7), 164–176.
Nag, S. K., & Chakraborty, S. (2003). Influence of rock types and structures in the development of drainage network in hard rock area. *Journal of Indian Society of Remote Sensing*, *31*(1), 25–35.
Patton, P. C., & Baker, V. R. (1976). Morphometry and floods in small drainage basins subject to diverse hydrogeomorphic controls. *Water Resources Research*, *12*(5), 941–952.
Pande, C. B., & Moharir (2017). KGIS based quantitative morphometric analysis and its consequences: A case study from Shanur River Basin, Maharashtra India. *Applied Water Science*, *7*, 861–871. http://dx.doi.org/10.1007/s13201-015-0298-7.
Pike, R. J., & Wilson, S. E. (1971). Elevation–relief ratio, hypsometric integral and geomorphic area–altitude analysis. *Geological Society of America Bulletin*, *82*, 1079–1084.
Prakash, K., Singh, S., & Shukla, U. K. (2016). Morphometric changes of the Varuna river basin, Varanasi district, Uttar Pradesh. *Journal of Geomatics*, *10*(1).
Prasad, R. K., Mondal, N. C., Banerjee, P., Nandakumar, M. V., & Singh, V. S. (2008). Deciphering potential groundwater zone in hare rock through the application of GIS. *Environmental Geology*, *55*, 467–475.
Prasannakumar, V., Vijith, H., & Geetha, N. (2011). Terrain evaluation through the assessment of geomorphometric parameters using DEM and GIS: Case study of two major sub-watersheds in Attapady, South India. *Arabian Journal of Geoscience*. , http://dx.doi.org/10.1007/s12517-011-0408-2.
Rai, P. K., Mohan, K., Mishra, S., Ahmad, A., & Mishra, V. N. (2017). A GIS-based approach in drainage morphometric analysis of Kanhar river basin, India. *Applied Water Science*, *7*, 217–232. http://dx.doi.org/10.1007/s13201-014-0238-y.
Rastogi, R. A., & Sharma, T. C. (1976). Quantitative analysis of drainage basin characteristics. *Journal of Soil and Water Conservation India*, *26*(1–4), 18–25.
Reddy, O. G. P., Maji, A. K., & Gajbhiye, S. K. (2004). Drainage morphometry and its influence on landform characteristics in a basaltic terrain, Central India—a remote sensing and GIS approach. *International Journal of Applied Earth Observation Geoinformatics*, *6*(1), 1–16.
Reddy, O., Kumar, N., Srivastava, M., & Singh, R. (2016). Morphometric analysis in basaltic Terrain of Central India using GIS techniques: A case study. *Applied Water Science*. , http://dx.doi.org/10.1007/s13201-016-0442-z.
Ritter, D. F., Kochel, R. C., & Miller, J. R. (2002). *Process geomorphology*. Boston: McGraw Hill.
Rudraiah, M., Govindaiah, S., & Vittala, S. S. (2008). Morphometry using remote sensing and GIS techniques in the sub-basins of Kagna river basin, Gulburga Basin district, Karnataka, India. *Journal of the Indian Society of Remote Sensing*, *36*, 351–360.
Sahu, N., Reddy, O., Kumar, N., Nagaraju, M., Srivastava, R., & Singh, K. S. (2016). Morphometric analysis in basaltic terrain of central India using GIS techniques: A case study. *Applied Water Science*. , http://dx.doi.org/10.1007/s13201-016-0442-z.
Schumm, S. A. (1956). Evolution of drainage systems and slopes in badlands at Perth Amboy, New Jersey. *Geological Society of America Bulliten*, *67*, 597–646.
Selvan, M. T., Ahmad, S., & Rashid, S. M. (2011). Analysis of the geomorphometric parameters in high altitude Glacierised terrain using SRTM DEM data in central Himalaya, India. *ARPN Journal of Science and Technology*, *1*(1), 22–27.
Sharma, S. K., Gajbhiye, S., Nema, R. K., & Tignath, S. (2014). Assessing vulnerability to soil erosion of a watershed of Tons River Basin. *International Journal of Environmental Research and Development*, *4*(2), 153–164.
Singh, P., Gupta, A., & Singh, M. (2014). Hydrological inferences from watershed analysis for water resource management using remote sensing and GIS techniques. *Egypt Journal Remote Sensing Space Science*, *17*, 111–121.
Singh, S., & Singh, M. C. (1997). Morphometric analysis of Kanhar River Basin. *National Geographical Journal of India*, *43*, 31–43.
Singh, V., & Singh, U. C. (2011). Basin morphometry of Maingra river, district Gwalior, Madhya Pradesh, India. *International Journal of Geomatics and Geosciences*, *1*(4).
Singh, O., Sarangi, A., & Sharma, M. (2008). Hypsometric integral estimation methods and its relevance on erosion status of North-Western Lesser Himalayan Watersheds. *Water Resource Manage*, *22*, 1545–1560. http://dx.doi.org/10.1007/s11269-008-9242-z.
Soni, S. (2017). Assessment of morphometric characteristics of Chakrar watershed in Madhya Pradesh India using geospatial technique. *Applied Water Science*, *7*, 2089–2102. http://dx.doi.org/10.1007/s13201-016-0395-2.
Sreedevi, P. D., Owais, S., Khan, H. H., & Ahmed, S. (2009). Morphometric analysis of a watershed of South India using SRTM data and GIS. *Journal of the Geological Society of India*, *73*(4), 543–552.
Strahler, A. N. (1952). Hypsometric analysis of erosional topography. *Geological Society of America Bulletin*, *63*, 1117–1142.
Strahler, A. N. (1964). Quantitative geomorphology of drainage basins and channel networks In: V. Chow (Ed.), *Handbook of Applied Hydrology* (pp. 439–476). New York: McGraw Hill.
Vaidya, N., Kuniyal, J. C., & Chauhan, R. (2013). Morphometric analysis using GIS for sustainable development of hydropower projects in the lower Satluj river catchment in Himachal Pradesh, India. *International Journal of Geomatics and Geosciences*, *3*(3).
Withanage, S. N., Dayawansa, K. D. N., & De Silva, P. R. (2014). Morphometric analysis of the Gal Oya River Basin using spatial data derived from GIS. *Tropical Agricultural Research*, *26*(1), 175–188.
Yunus, A. P., Oguchi, T., & Hayakawa, Y. S. (2014). Morphometric analysis of drainage Basins in the Western Arabian Peninsula using multivariate statistics. *International Journal of Geosciences*, *5*, 527–539. http://dx.doi.org/10.4236/ijg.2014.55049.

International Soil and Water Conservation Research 7 (2019) 158–166

Contents lists available at ScienceDirect

International Soil and Water Conservation Research

journal homepage: www.elsevier.com/locate/iswcr

Original Research Article

Land use in agricultural landscapes with chernozems contaminated after Chernobyl accident: Can we be confident in radioecological safety of plant foodstuff?

Olga Komissarova*, Tatiana Paramonova

Radioecology & Ecotoxicology Department, Soil Science Faculty, Lomonosov Moscow State University, Leninskie Gory 1-12, Moscow 119991, Russia

ARTICLE INFO

Article history:
Received 24 January 2019
Received in revised form
20 March 2019
Accepted 20 March 2019
Available online 13 April 2019

Keywords:
Radioactive soil contamination
Caesium-137 ^{137}Cs
Arable soils
"Soil-plant" system
Chernobyl accident
Radioecologically safe land use

ABSTRACT

Agricultural land use in the area of the post-Chernobyl Plavsk radioactive hotspot (Tula region, Central Russia) has raised a problem of radioecological safety of obtained plant foodstuff. Verification of ^{137}Cs activities and inventories in components of "soil-plant" systems of the territory has been conducted in 2014–2017 in 10 agrosystems and 2 semi-natural meadows. It was revealed that density of ^{137}Cs contamination of arable chernozems and alluvial calcareous soils nowadays varies in a range 140–220 kBq/m^2 and exceeds radiation safety standard by~3.5–6 times. Deep plowing of the arable soils up to 30-cm in 1986–1987 resulted in decreasing of ^{137}Cs inventories in rooting zone by ≈ 70% for crops cultivated with shallow disk plowing (wheat, barley), and by ≈ 35% for crops cultivated with middle plowing (buckwheat, amaranth, white mustard). The investigated plants and their compartments can be grouped on the basis of transfer factor values as follows: maize (stems and leaves) > amaranth > bromegrass > vegetation of dry meadow, galega, sunflower (seeds), vegetation of wet meadow > maize (grain), soybean (pods), barley (grain), buckwheat (grain), potatoes (tubers) > white mustard (seeds), wheat (grain). It is noticeable that generative plant compartments are characterized by less ^{137}Cs activities in comparison with stems and leaves; and that ^{137}Cs root uptake is not coincide with total flux of mineral nutrients in "soil-plant" systems. In sum, ^{137}Cs soil-to-plant transfer in the area of the Plavsk radioactive hotspot is characterized by considerable discrimination, so ^{137}Cs activities in plants are completely in accordance with national standards.

1. Introduction

The functioning of nuclear industry is accompanied with risks of uncontrolled and large-scale accidents. In turn, radioactive fallout resulting from nuclear accidents may cordially change land use policy on the affected lands. And agricultural landscapes may be considered as critical lands in terms of radioactive contamination because of soil transformation form a tool of production into the source of ecological hazard to human health; while to guard against radioactive contamination the elaboration of rehabilitative countermeasures is need from choosing of sustainable agricultural crops up to land exclusion from the turnover.

In particular, after the Chernobyl nuclear power plant accident in 1986 2.955 millions ha of agricultural lands have been got a status of radioactively contaminated with a density of ^{137}Cs soil contamination above 37 kBq/m^2 and 17.1 thousand ha was completely abandoned from agriculture as the exclusive zone with a density of ^{137}Cs soil contamination above 1480 kBq/m^2 (Alexakhin et al., 2004, pp. 330–386). Therefore the Chernobyl accident could be classified as a rural one, especially due to agricultural land use was the major segment of the national economy in the affected accidental areas, especially in radioactively contaminated lands within chernozem zone where the share of arable soils in land use structure was build up to >70% (Regions of Russia …, 2016). The necessity of maximal retention of regional economy structure and

* Corresponding author.
E-mail addresses: komissarova-olga93@yandex.ru (O. Komissarova), tparamonova@soil.msu.ru (T. Paramonova).

https://doi.org/10.1016/j.iswcr.2019.03.001

simultaneous need for the protection of residents from additional irradiation owing to radionuclide-containing local plant foodstuffs caused the top priority of comprehensive study of the bioavailability of artificial radionuclides, first of all the most biologically significant ^{137}Cs, in "soil-plant" systems of post-Chernobyl agricultural landscapes. Additional hazardous radionuclides – ^{131}I, ^{95}Sr, ^{241}Am, etc. – belonged to short-lived radioactive isotopes or have been released into the environment in considerably lesser degree then ^{137}Cs, so nowadays radiocaesium is precisely the main one which creates radioecological conditions of affected areas (Alexakhin et al., 2004, pp. 330–386; De Cort et al., 1998, p. 22; Fesenko, Alexakhin, & Balonov, 2007; Puchkov & Bolshov, 2016).

In this connection during 3 decades passed since the contamination event (~the first half-life period of ^{137}Cs) permanent ecological control of obtaining foodstuff and a lot of original scientific studies on ^{137}Cs biogeochemistry were carried out in the area of Chernobyl radioactive fallout. It has been found that as a consequence of the radionuclide ability to specific and irreversible sorption in interpocket spaces and wedge-shaped marginal widenings of crystal lattice of certain clay and mica minerals (Cornell, 1993; Konopleva, 2016; Kruglov, Anisimov, Anisimova, & Aleksakhin, 2008; Staunton & Roubaud, 1997; Wauters et al., 1996; etc.) mobility of ^{137}Cs in contaminated mineral soils is substantially limited both to water transfer and to biological availability. This is especially true for the chernozem soils of the Russian Plain, enriched in clay minerals of the illite and montmorillonite groups, neutral, rich in exchangeable k and organic matter, which properties are responsible for low intensity of ^{137}Cs fluxes in "soil-plant" system (Sanzharova et al., 2006). In parallel with countermeasures which have been applied on agricultural lands of European Russia that is the case of reasonable values of ^{137}Cs activity in agricultural foodstuff obtained from radioactively contaminated chernozem zone's area (Tula and Oryel regions) since 1988; but sporadic non-compliance of ^{137}Cs content with sanitary and veterinary norms for some crops and forage grasses is fixed by national ecological monitoring service in non-chernozem areas (Bryansk and Kaluga regions) till nowadays (Puchkov & Bolshov, 2016).

However, ecological monitoring network currently, in remote period after the Chernobyl accident, do not mean the application of total observations on contaminated lands, so there is no complete evidence of radioecological safety of the whole plant foodstuff from the area. On the other hand, over the course of the past decades primary spatial heterogeneity of ^{137}Cs in soils of agricultural slope landscapes has become even more pronounceable owing erosion transport of radiocaesium-containing top soil layers, by this means ^{137}Cs inventories in soils of foot slopes nowadays can exceed those that were in 1986 (Golosov, Panin, & Markelov, 1999a; Linnik, Saveliev, & Govorun, 2007). And strong fixation of ^{137}Cs by soil clay minerals and relatively long half-life period ($T_{1/2}$ 30.17 years) have determined the situation that the bulk of the radionuclide is still concentrated within the sod horizon A or plough horizon Ap of arable soils (≈rooting layer) (Alexakhin et al., 2004, pp. 330–386; Fesenko et al., 2007; Konoplev & Konopleva, 1999; Paramonova, Belyaev, Komissarova, & Ivanov, 2017; etc.).

Field observations in post-Chernobyl areas contaminated by ^{137}Cs do not lose their relevance in this connection. In a broad sense, close inspection of the radionuclide behaviour in "soil-plant" systems of post-accidental agricultural landscapes allows learning from the past and developing a rapid response measures in the future. The present study was conducted to examine ^{137}Cs bioavailability for main agricultural crops of the European Russia and to make independent assessment of the radioecological safety of plant foodstuff grown on arable chernozems subjected to Chernobyl fallout.

2. Materials and methods

2.1. Study area and experimental plots

Investigation of ^{137}Cs behaviour in "soil-plant" systems of the main agricultural crops was carried out in 2014–2017 period (~25–30 years after Chernobyl accident) in the central part of so-called "Plavsk radioactive hotspot" (≈650 km northeast of Chernobyl, Tula Region) – one of the areas within chernozem zone characterized by the most significant Chernobyl fallout in the European Russia (Fig. 1). Initial soil contamination by ^{137}Cs in the Plavsk radioactive hotspot agricultural landscapes in 1986 was evaluated as 185–555 kBq/m^2, and exceeds of the radionuclide sanitary standard (=37 kBq/m^2) in region are presumed to remain detectable until the end of 21st Century (De Cort et al., 1998, p. 22; Izrael & Bogdevich, 2009).

Soils of the territory are predominantly presented by arable leached Chernozems (WRB – Voronic Chernozems, FAO – Haplic Chernozems) derived from loess calcareous loams which are extensively used in agriculture and are belonging now by an agroholding. Cultivated arable lands dominantly occupy the surfaces of watersheds as well as upper and middle parts of hillslopes. The lower parts of hillslopes and floodplains with semi-natural meadows on native leached Chernozems and alluvial calcareous soils (WRB and FAO – Fluvisols Calcaric) derived from calcareous alluvial loams are used as pastures and hayfields. Chernozems and alluvial soils of the territory are characterized by similar properties – a thick humus layer with high organic carbon content, heavy loamy texture, neutral pH_{H2O} and very well-developed structure of topsoil horizons determining optimal bulk density (Table 1). The important feature of arable soils of the Plavsk radioactive hotspot is rather high thickness of the plowed horizon Ap which clearly reflects that a deep plowing (up to 30 cm) was applied on agricultural lands as a rehabilitating countermeasure after the Chernobyl accident.

Experimental plots were organized in agrosystems of 10 typical crops widely cultivated in moderate climate most: wheat, barley, buckwheat, maize, soybean, potatoes, amaranth, white mustard, sunflower, and cultivated species of cereal-leguminous (bromegrass-galega) mixture; as well as for 2 semi-natural ecosystems of dry and wet meadows (Fig. 2). Basically, the experimental plots were located within the basin of small river Plava and could be considered as catena of the landscape geochemical linking between the interfluve and the floodplain. Several plots were placed some distance apart to include into study agricultural crops of additional plant species and production groups of plants. Total square of the investigated area was about 130 km^2 with the longest distance between plots ≈20 km. It was presumed that primary density of the Chernobyl fallout in these sites was more or less comparable to make possible proper assessment of ^{137}Cs bioavailability from radioactively contaminated chernozem and chernozem-like alluvial soils.

2.2. Sampling procedure

The procedure of soil and plant foodstuff sampling has been conducted uniformly for all of the experimental plots and followed the methods recommended for environmental contaminants and studies of plant traits (International Atomic Energy Agency [IAEA], 2004; Perez-Harguindeguy et al., 2013). For the entire 4-years field campaign of 2014–2017 fieldworks were carried out during the final vegetation period of cultural crops immediately prior to harvesting, in most cases – during a period between August 10th and 25th. Sampling points were selected by the principle of typical (average) plant and soil visible characteristics and were located

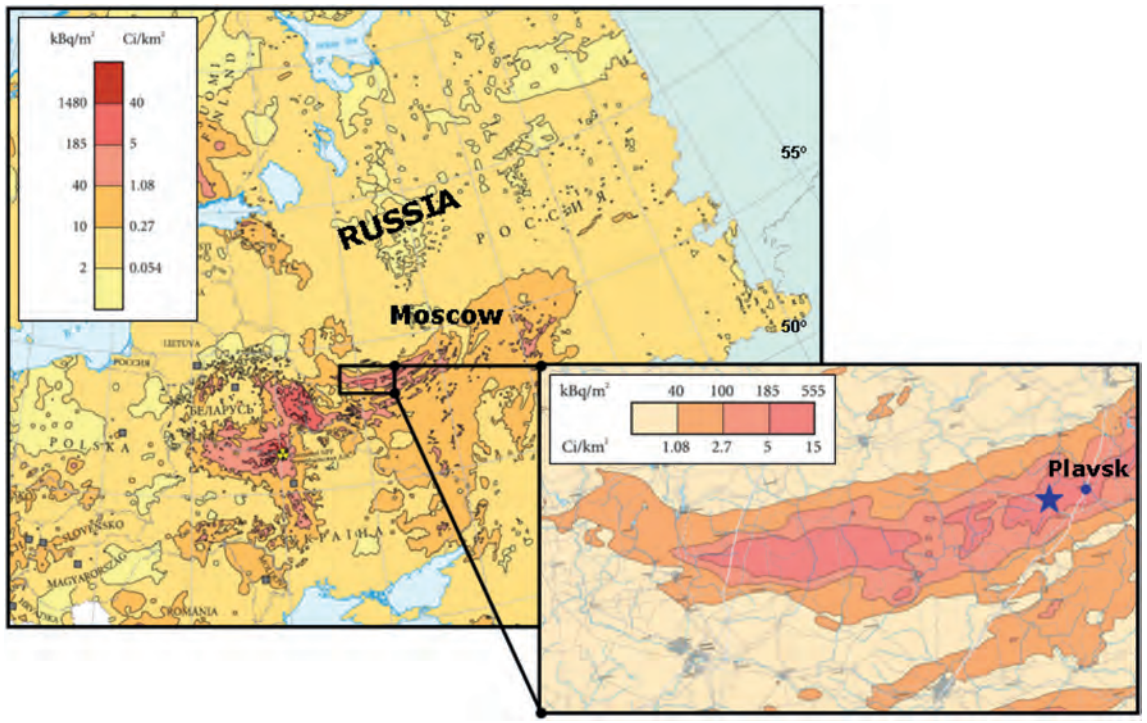

Fig. 1. Location of the Plavsk radioactive hotspot on the map of generalized levels of the ^{137}Cs pollution in European Russia after Chernobyl accident, May 1986 (De Cort et al., 1998, p. 22); the star-sign marks general position of experimental plots.

Table 1
Main properties of arable chernozems and alluvial calcareous soils of the Plavsk radioactive hotspot.

Characteristic	arable Chernozems	Alluvial calcareous soils
Lower boundary depth, cm		
Ap/Ad horizon[a]	30 ± 1[b]	11 ± 3
A horizon	32 ± 3	30 ± 6
A + AB/A + AC horizons	71 ± 6	63 ± 5
Bulk density, g/cm^3		
0–10 cm	0.96 ± 0.04	0.98 ± 0.03
10–20 cm	1.43 ± 0.03	1.17 ± 0.02
20–30 cm	1.36 ± 0.05	1.27 ± 0.03
Physical clay particles (<0.01 mm), %		
0–10 cm	57,9 ± 1.8	54.8 ± 2.6
10–20 cm	56,8 ± 2.1	52.1 ± 1.4
20–30 cm	56,9 ± 1.4	51.6 ± 2.7
C_{org}, %		
0–10 cm	6.8 ± 0.2	7.3 ± 0.1
10–20 cm	6.5 ± 0.2	5.3 ± 0.5
20–30 cm	5.6 ± 0.2	5.2 ± 0.1
pH_{H2O}		
0–10 cm	6.60 ± 0.08	6.22 ± 0.08
10–20 cm	6.52 ± 0.05	6.53 ± 0.04
20–30 cm	6.48 ± 0.06	6.50 ± 0.06

[a] Data for arable chernozems and alluvial soils are given above and under the line, respectively.
[b] Hereafter confidence limits of the mean was calculated as $\pm t_{0.95} \times m$ at n = 10.

randomly within experimental plot at a distance 5–10 m from each other.

Stratified approach has been applied for soil sampling: undisturbed depth-incremental samples were collected from a fixed surface area and depth intervals 0–10, 10–20 and 20–30 cm by steel cylindrical corer sampler (diameter 8.2 cm, volume 425 cm^3). Testing of soil profiles up to depth 30 cm was decided on the basis of previous investigation on the territory of the Plavsk radioactive hotspot which has revealed that more then 90% of ^{137}Cs inventories are accumulated in this top layer (Paramonova et al., 2017).

Plant samples were collected to consider both capacity and intensity of ^{137}Cs biogeochemical cycle parameters. First, aboveground biomass of vegetation was collected from a fixed space (250 cm^2) situated just above the points of the next soil sampling; and then, when needed, divided into stems and leaves, and grain or seeds. Belowground biomass of potatoes was collected from the same fixed space (250 cm^2) of soil surface up to depth 30 cm and subsequently carefully washed it from soil particles with a visual control of the signs of adhesion.

Second, additional amounts of plant foodstuff were gathered, if necessary, without taking account the growing area to provide sufficient dry mass of samples (≈ 100 g) for increasing accuracy of γ-spectrometric analysis.

Replication of soil and plant foodstuff sampling points on each experimental plot was threefold.

Laboratory pretreatment of soil samples involved drying at room temperature, grinding, sieving to particles <2 mm for homogenization of samples before the onset of γ-spectrometric and other assays. Plant compartments were oven-dried at 105 °C and milled by laboratory mill.

2.3. Laboratory analysis

Spectrometric measurements of ^{137}Cs in soils and plant foodstuff were performed using a GR 3818 semiconductor γ-spectrometer with a Canberra high-purity (HPGe) detector (United States) calibrated with standard reference materials. Mass of samples was taken to fill the Russian standard geometry of the 120-ml "Denta" cylindrical plastic vessel. Energy spectra measurements from soil and plant foodstuff samples were accounted for 0.5 h and 24 h, respectively, and ^{137}Cs activities were calculated from the net full energy peak 661.7 keV using the "Progress 5.1" spectrometric analysis software package. The analytical error did not exceed

Fig. 2. Location of the experimental plots with agrosystems of main agricultural crops and semi-natural meadows on the territory of the Plavsk radioactive hotspot: 1 – wheat, 2 – barley, 3 – buckwheat, 4 – maize, 5 – soybean, 6 – potatoes, 7 – amaranth, 8 - white mustard, 9 – sunflower, 10 – grass mixture, 11 – dry meadow, 12 – wet meadow (designed on the basis of Google Earth image).

2–7%.

In turn, main soil properties (soil bulk density, clay content, C_{org}, pH_{H2O}; ash content in plant compartments) were determined by conventional techniques (Arinushkina, 1970).

2.4. Calculations and statistical analysis

The obtained data of ^{137}Cs specific activities in investigated soils and plant foodstuff were recalculated to the date of the latest 2017 field campaign with account of the radionuclide's decay rate, by the following Eq. (1):

$$A^{Cs-137} = A_0^{Cs-137} \times \exp^{(-0.023 \times t)}, \quad (1)$$

where A^{Cs-137} is the required specific activity of ^{137}Cs, A_0^{Cs-137} – specific activity of ^{137}Cs at the initial time, and t – amount of years passed for this period.

To assess intensity of ^{137}Cs transfer from soils into plants and their edible compartments the values of transfer factor (TF (originally F_v)) were calculated based on the Eq. (2) in accordance with IAEA recommendations (2010):

$$TF = \frac{A_{plant}^{Cs-137}}{A_{soil}^{Cs-137}}, \quad (2)$$

where $A^{Cs-137}{}_{plant}$ is specific activity of ^{137}Cs in dry mass of plant or plant compartment, $A^{Cs-137}{}_{soil}$ is specific activity of ^{137}Cs in dry mass of soil in the specified soil layer – 30 cm in the case of the present study.

For the purpose to compare the intensity of ^{137}Cs root uptake by selected crop with the radionuclide root uptake by the referent group of cereals the conversion factor (CF) was estimated on the basis of the following Eq. (3):

$$CF = \frac{TF_{plant}}{TF_{cereals}}, \quad (3)$$

where TF_{plant} is transfer factor of ^{137}Cs for definite plant foodstuff, and $TF_{cereals}$ (TF_{wheat} or TF_{barley}) is transfer factor of ^{137}Cs for grain of cereal crops.

To assess mean values and variability of the data ANOVA (analysis of variance) was performed following at $P \leq 0.05$ using Statistica StatSoft (version 8).

3. Results and discussion

3.1. ^{137}Cs activities and inventories in soils of the Plavsk radioactive hotspot

The area of the Plavsk radioactive hotspot on the eastern track of Chernobyl fallout has been founded after 1986 with the help of airborne γ-spectrometry (De Cort et al., 1998, p. 22), only later *in situ* measurements of γ-dose rates and γ-spectrometric analysis of soils have been done. Towards the end of 20th century considerable spatial heterogeneity of the contaminated area has been revealed by Golosov, Walling & Panin (1999, 2000): even in the very center of the Plavsk radioactive hotspot inventories of ^{137}Cs in arable chernozems of cultivated fields belonging to different local interfluves varied from 368 ± 56 to 559 ± 93 kBq/m^2. Besides, there has been significant decrease in ^{137}Cs content in arable soils of slopes and corresponding increase in ^{137}Cs accumulation in alluvial soils of river valley's bottom.

Nowadays, as shown at the present study, density of ^{137}Cs soil contamination at the central part of the Plavsk radioactive hotspot vary in a range 140–220 kBq/m^2 (Table 2), with variation coefficient for separate experimental plots located at different sites of watershed surface 20% and variation coefficient for catena's geochemically linked experimental plots – 26%. Thus, large variability of ^{137}Cs content characteristics for soils reflects primary small-scale spatial heterogeneity of Chernobyl fallout within the area as well as secondary redistribution of the radionuclide via erosion of cultivated lands. Owing to the last process, ^{137}Cs inventories in meadow soils of the lower parts of slope are ≈40% greater than arable chernozems of elevated positions of relief. In any event, ^{137}Cs inventories in arable and native soils of the territory still exceed the radiation standard by ~3.5–6 times.

Table 2
Accumulation of ^{137}Cs in chernozem and chernozem-like alluvial soils of the Plavsk radioactive hotspot.

Crop/vegetation	Landscape unit, altitude above sea level (m)	Land use and agricultural practice	Soil	^{137}Cs in soil	
				(Bq/kg)	(kBq/m^2)
Wheat	Upper part of slope, 240	Arable land, shallow disk plowing	Arable Chernozem	435 ± 32	161 ± 13
Barley	Upper part of slope, 237	Arable land, shallow disk plowing	Arable Chernozem	363 ± 68	150 ± 28
Buckwheat	Watershed, 231	Arable land, middle plowing	Arable Chernozem	647 ± 90	217 ± 39
Maize	Watershed, 252	Arable land, deep plowing	Arable Chernozem	338 ± 77	129 ± 28
Soybean	Watershed, 242	Arable land, deep plowing	Arable Chernozem	434 ± 47	160 ± 25
Potatoes	Upper part of slope, 241	Arable land, deep plowing	Arable Chernozem	389 ± 18	147 ± 29
Amaranth	Watershed, 244	Arable land, middle plowing	Arable Chernozem	541 ± 148	187 ± 48
White mustard	Watershed, 229	Arable land, middle plowing	Arable Chernozem	522 ± 54	201 ± 31
Sunflower	Watershed, 245	Arable land, deep plowing	Arable Chernozem	356 ± 54	139 ± 11
Grass mixture	Upper part of slope, 238	No annual tillage	Arable Chernozem	418 ± 77	145 ± 18
Dry meadow	Bottom part of slope, 203	Pasture, native vegetation	Chernozem	650 ± 71	223 ± 24
Wet meadow	Floodplain, 194	Hayfield, native vegetation	Alluvial calcareous soils	685 ± 55	216 ± 11

Vertical distribution of the ^{137}Cs activities in 0–30 cm top layer of arable chernozems of the Plavsk radioactive hotspot exhibits reasonably homogeneous penetration of the radionuclide up to this depth, whereas in native chernozem and chernozem-like alluvial soil of meadows drastic decreasing of ^{137}Cs content is noticeable with depth (Fig. 3). Such difference in ^{137}Cs distribution in cultivated and native soils clearly demonstrates governing factor of agrogenic turbation (rotational plowing, disking, harrowing, shelling and other cultivation activities) in the process of the radionuclide penetration up to lower frontier of plowed layer. ^{137}Cs is thus seen to be an effective tracer in diverse processes of soil mass redistribution and turbation, as predicted by different researchers (Guidelines for using …, 2014; Impact of Soil Conservation …, 2011; etc.). Moreover, since current depth of chernozems tilling in the area of Plavsk radioactive hotspot not exceeds 10–25 cm, the detection of considerable ^{137}Cs activity beneath actual Ap horizon has revealed application of the deep plowing (up to 30 cm) contaminated fields after the event of Chernobyl radioactive fallout in 1986–1987.

Deep plowing is presumed as one of the most effective measure to reduce an emergency of ^{137}Cs soil-to-plant transfer after radioactive contamination of agricultural lands. It was established for arable mineral soils of European Russia that such countermeasures as liming of acidic soils, NPK and manure application, zeolites input can decrease intensity of ^{137}Cs root uptake by 1.5–3 times, whereas ordinary plowing (up to 20–25 cm) or, especially, deep plowing (up to 30–50 cm) can provide a 8–12-fold decrease in the radionuclide concentration in plant foodstuff; just as radical improvement of meadow soils can provide a 1.5–9-fold decrease of the ^{137}Cs bioavailability (Sanzharova, Fesenko, Kotik, & Spiridonov, 1996). As for the investigated agrosystems of the Plavsk radioactive hotspot, main rooting biomass of crops cultivated with shallow disk plowing (wheat, barley) or without annual tillage (perennial grass mixture) are in contact engagement only with 32–33% of total ^{137}Cs inventory in arable chernozems; crops cultivated with middle plowing (buckwheat, amaranth, white mustard) – in contact with 65–66% of total ^{137}Cs inventory; and only crops cultivated with deep rotational plowing (maize, soybean, potatoes) uptake the radionuclide from the all thickness of radiocaesium-containing soil layer. Semi-natural meadow ecosystems of the territory, as observed from ^{137}Cs distribution via profiles of native chernozem and alluvial calcareous soil, obviously have been not subjected to agrotechnical improvement, so 60–65% of ^{137}Cs total inventory in soils is concentrated till now within the top 0–10 cm layer, which is

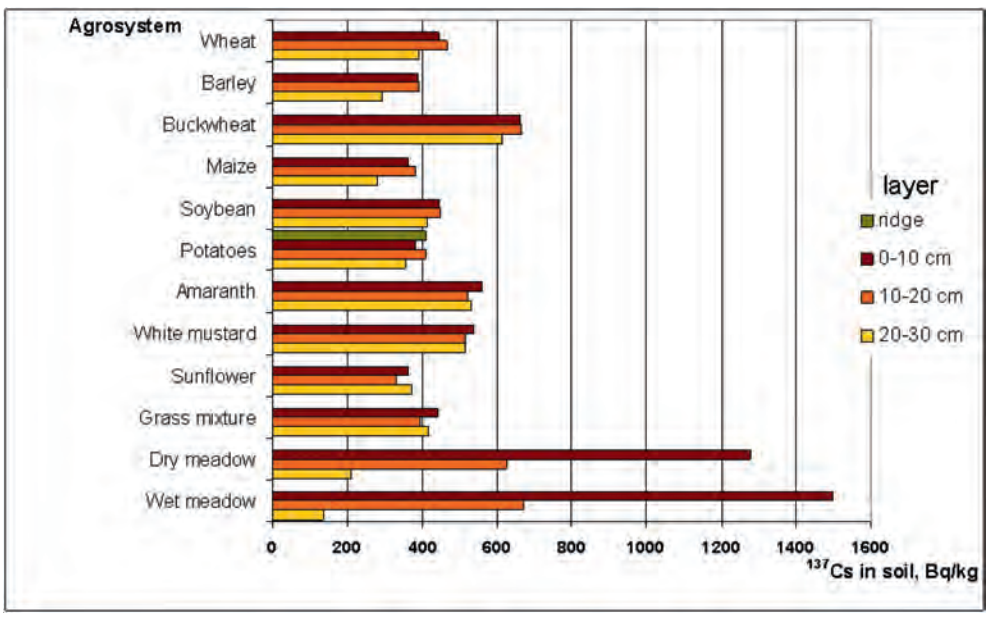

Fig. 3. The depth distribution of ^{137}Cs activities (Bq/kg) in 0–30 cm top layer of arable and native chernozems and chernozem-like alluvial soils of the Plavsk radioactive hotspot.

coincidentally the main rooting layer of meadow vegetation. In parallel with elevated density of ^{137}Cs accumulation in soils of geochemically subordinate landscapes this fact is the reason for considering meadow ecosystems as critical unit for ^{137}Cs behaviour in "soil-plant" systems of radioactively contaminated lands.

3.2. ^{137}Cs activities in plant foodstuff obtained in the area of the Plavsk radioactive hotspot

Despite of the retained severe radioactive contamination of cultivated and pasture lands of the Plavsk radioactive hotspot a strong irreversible fixation of ^{137}Cs by clay minerals of chernozems together with discrimination of the process of ^{137}Cs uptake by plant roots define relatively low bioavailability of the radionuclide in "soil-plant" system. Calculated soil-to-plant TF values for foodstuff of main crops cultivated on the territory are predominantly $n \cdot 10^{-2}$ – $n \cdot 10^{-3}$ (Table 3), and generally they not exceed or are less than recommended by IAEA tentative TF values for agricultural crops growing in temperate climate conditions (2010). As a result, ^{137}Cs activities in obtained foodstuff are completely in accordance with national standards of sanitary rules and norms: 60 Bq/kg for cereals and maize grain, 80 Bq/kg for potatoes and vegetables, 400 Bq/kg for forage grass (Hygienic requirements …, 2011).

It's notable that accumulation of the radionuclide in potatoes tubers is negligible despite of their close contact with surrounding soil material containing ^{137}Cs two orders of magnitude more. Similar results have been detected by Popplewell, Ham, Johnson, Stahner, and Sumner (1984) in long-term model experiment with extremely high activities of ^{137}Cs in soil. Thus, potatoes roots are able to exhibit effective protective barrier property against ^{137}Cs, while diffusion of the radionuclide into plant tissues is minor.

One more distinctive feature of obtained TFs data is that intensity of ^{137}Cs translocation into aboveground parts of perennial plant species (vegetation of meadows and forage grass mixture cultivated without tillage for 6–8 years) is similar to the radionuclide fluxes into annual agricultural crops. Notwithstanding the fact of elevated density of radioactive contamination specified for the native soils, root systems of meadow vegetation suppress successfully ^{137}Cs transfer into green parts, and capacity for discrimination of the radionuclide penetration into biological cycle of elements appears as basic peculiarity of grassy agrosystems and semi-natural ecosystems.

Close inspection of TF values for different crops and foodstuff obtained in the area of the Plavsk radioactive hotspot has revealed rather wide variability of the indexes. In order of decreasing TFs the investigated plants and their compartments can be grouped such manner: maize (stems and leaves) > amaranth > bromegrass of grass mixture > vegetation of dry meadow, galega of grass mixture, sunflower (seeds), vegetation of wet meadow > maize (grain), soybean (pods), barley (grain), buckwheat (grain), potatoes

Table 3
^{137}Cs root uptake and transfer into plant compartments of main crops cultivated on the territory of the Plavsk radioactive hotspot.

Plant group	Plant family (*in Latin*)	Crop/vegetation	Plant compartment	Biomass (kg/m^2)	Ash content (%)	^{137}Cs in plant (Bq/kg)	TF	
							Calculated	Recommended[a]
Cereals	Gramineae	Wheat	Grain	0.94 ± 0.31	4.1 ± 0.4	3.1 ± 1.7	7.1×10^{-3}	1.1×10^{-2} – 4.3×10^{-2}
			Stems and leaves		5.5 ± 0.6	22.1 ± 7.3	5.1×10^{-2}	5.6×10^{-2} – 1.1×10^{-1}
		Barley	Grain	0.57 ± 0.04	4.5 ± 0.3	6.1 ± 2.3	1.7×10^{-2}	1.1×10^{-2} – 4.3×10^{-2}
			Stems and leaves		6.2 ± 0.7	31.5 ± 18.7	8.7×10^{-2}	5.6×10^{-2} – 1.1×10^{-1}
	Polygonaceae	Buckwheat	Grain	0.43 ± 0.05	5.3 ± 0.4	9.5 ± 4.5	1.5×10^{-2}	1.1×10^{-2} – 4.3×10^{-2}
			Stems and leaves		6.8 ± 0.7	24.3 ± 4.6	3.8×10^{-2}	5.6×10^{-2} – 1.1×10^{-1}
Maize	Gramineae	Maize	Grain	2.02 ± 0.27	5.8 ± 0.6	6.3 ± 1.7	1.9×10^{-2}	1.2×10^{-2} – 1.6×10^{-2}
			Stems and leaves		8.0 ± 1.4	38.4 ± 6.1	1.1×10^{-1}	1.5×10^{-2} – 2.2×10^{-2}
Leguminous vegetables	*Fabaceae*	Soybean	Pods	0.74 ± 0.15	10.4 ± 0.9	7.4 ± 1.3	1.7×10^{-2}	1.3×10^{-2} – 2.0×10^{-2}
			Stems and leaves		8.0 ± 0.4	24.9 ± 10.4	5.7×10^{-2}	no data
Tubers	Solanaceae	Potatoes	Tubers	0.14 ± 0.05	5.4 ± 1.0	5.0 ± 0.4	1.3×10^{-2}	2.5×10^{-2} – 5.8×10^{-2}
Non-Leafy vegetables	*Amaranthaceae*	Amaranth	Stems and leaves	0.48 ± 0.07	19.1 ± 2.5	46.8 ± 14.2	8.6×10^{-2}	no data
Herbs	Brassicaceae	White mustard	Seeds	0.50 ± 0.24	5.6 ± 0.7	4.1 ± 2.4	7.8×10^{-3}	no data
			Stems and leaves		6.3 ± 1.5	32.3 ± 9.8	6.2×10^{-2}	6.6×10^{-2}
Other crops	Asteraceae	Sunflower	Seeds	1.68 ± 0.32	4.1 ± 0.8	9.7 ± 3.8	2.7×10^{-2}	no data
			Stems and leaves		13.1 ± 1.5	20.6 ± 0.4	5.8×10^{-2}	no data
Grasses + Leguminous (cultivated species)	Gramineae	Bromegrass	Stems and leaves	0.21 ± 0.07	8.6 ± 1.8	19.4 ± 4.1	6.0×10^{-2}	4.6×10^{-2} – 1.5×10^{-1}
	Fabaceae	Galega	Stems and leaves	0.13 ± 0.05	10.6 ± 2.7	20.6 ± 5.0	3.5×10^{-2}	1.2×10^{-2} – 4.8×10^{-2}
Pasture (natural species)	Gramineae+ others	Dry meadow	Stems and leaves	0.10 ± 0.03	7.9 ± 0.9	23.2 ± 6.1	3.6×10^{-2}	1.8×10^{-2} – 1.9×10^{-2}
	Gramineae (mainly)	Wet meadow (Bromegrass)	Stems and leaves	0.50 ± 0.20	6.5 ± 0.8	18.2 ± 6.7	2.7×10^{-2}	1.2×10^{-2} – 2.8×10^{-1}

[a] Recommended values of TF for agro-productive group of plants growing in temperate environment on loamy and clay soil texture (Handbook of Parameter Values …, 2010).

(tubers) > white mustard (seeds), wheat (grain). Taking into account single scenario of primary land contamination, common climatic conditions, and similar properties of soils, the principal causes responsible for TFs differences are biological features of agricultural crops and plant communities. For comparison, total aboveground biomass of wet meadow vegetation, almost completely represented by wild bromegrass (*Bromus inermis*), is characterized by minimum TF 0.027, whereas aerial part of maize agrosystem is characterized by maximum TF 0.103 (a single value that exceeds TF recommended by IAEA). For a first glance, intensity of ^{137}Cs transfer into aerial compartments of plants can depend on biomass productivity and the growth rate, but the relationship between these parameters is rather weak and statistically not significant (Fig. 4A). In particular, sunflower having high aboveground biomass is characterized by only moderate TF value, while white mustard having aboveground biomass 3 times less exhibits ~ equal TF. The relationship between TFs and ash content in aerial parts of the investigated crops/vegetation is expressed even worse (Fig. 4B), so there in no correlation in ^{137}Cs accumulation and distribution of majority of mineral nutrients in plants.

Generative plant compartments (grain, seeds, and pods) are characterized by less ^{137}Cs activities and TF values for all investigated crops in comparison with stems and leaves (Fig. 5), but there is unavailable to fix correlation between TFs for generative and vegetative plant compartments correspondingly ($r = 0.23$). Therefore, there are specific biological barriers immediately within plants to protect progeny against radioactive influence. The most pronounced difference has been established for white mustard (with a factor 8); TFs for grain of cereals are 5–7 times less than for green parts; difference for soybean, buckwheat, and sunflower are relatively less (with a factor 2–3).

Total amount of ash nutrients in plant compartments varies in a range 4–8% with exception of 10% for pods of soybean and of 13% for stems and leaves of sunflower. As a whole ash content in generative organs 0.5–1.5% less than in vegetative aerial parts – the same commonly can be noticed for TF values, – but trends in traits variations are unlike. In this connection, transfer of ^{137}Cs from shoots into grain, seeds, and pods of plants, as well as transfer of ^{137}Cs from soil to roots, and from roots to green parts of biomass, apparently proceeds not as indifferent participation of the radionuclide in total flux of nutrients, but under the effect of protective biological peculiarities of plants.

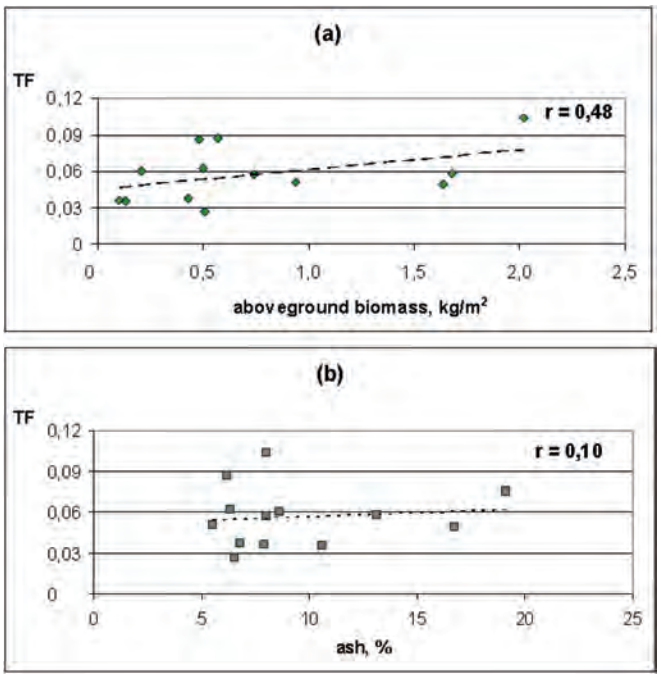

Fig. 4. The relationship between transfer factor (TF) values (dimensionless unit) for aerial parts of the investigated crops/vegetation and (a) – aboveground biomass productivity (kg/m^2), and (b) – ash content (%) in the area of the Plavsk radioactive hotspot.

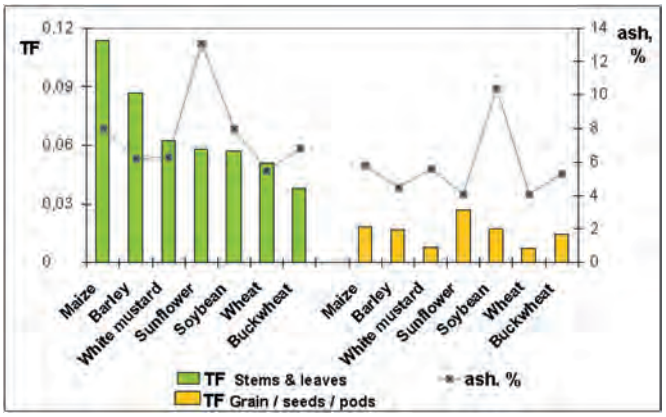

Fig. 5. Transfer factor (TF) values (dimensionless unit) for the pairs "stems & leaves – grain/seeds/pods" and the relationship between TFs and ash content (%) for the investigated crops/vegetation of the Plavsk radioactive hotspot.

3.3. Conversion factors for selected crops cultivated in the area of the Plavsk radioactive hotspot

One of the notable lessons obtained from nuclear accidents could be revealing the general features of ^{137}Cs root uptake by agricultural crops for prediction the radionuclide accumulation in plant foodstuff and its further distribution via food chains. For the sake of simplicity such forecast the concept of conversion factor (CF) was proposed by Frissel et al. (2002), and later CF has been accepted by IAEA (Classification of soil systems …, 2006, pp. 1–19) to obtain generic value of unknown TF of selected crop from the TF of the reference crop cultivated on the same lands. Cereals were selected like reference group of agricultural crops with conventional TF for grain equal 1; and TFs of other plant groups can be calculated by multiplying values for cereals with a CF. It should be remembered that CF as well as TF values are not true constants and can considerably vary in a range of soil and other environmental conditions (Centofanti et al., 2005; Ehlken & Kirchner, 2002; Nisbet & Woodman, 2000; etc.). Nonetheless the approach of the CF concept looks considerably promising for express radioecological assessment of agricultural land use and planning of crop rotation on the fields.

To establish CFs values for plant foodstuff obtained in agricultural landscapes of the Plavsk radioactive hotspot wheat and barley (both from Gramineae family) have been chosen separately as reference crops of cereals group because there is no concrete instruction of IAEA for referent plant species. Calculated in such manner CF_{wheat} and CF_{barley} are distinctly differ due to TF_{barley} is twice as much as TF_{wheat}. However, the data not exactly, but satisfactory agree with IAEA recommendations and reveal the similar order of CFs for plant groups (Table 4).

CF for grain of buckwheat (belonging to agro-productive group of cereals) and CF for maize (belonging to Gramineae plant family), as are CF for green mass of bromegrass of cultivated grass mixture (also belonging to Gramineae plant family), more adequately agree with recommended CF_{barley}; CF for aerial parts of galega of

Table 4
Average values of 137Cs conversion factors for calculation of transfer factors for the investigated plant foodstuff to transfer factors for grain of wheat and barley in the area of the Plavsk radioactive hotspot.

Plant group	Plant family (*in Latin*)	Crop/vegetation	Plant compartment	CF calculated		CF recommended[a]
				CF_{wheat}	CF_{barley}	
Cereals	Gramineae	Wheat	Grain	–	0,4	1
		Barley	Grain	2,4	–	1
	Polygonaceae	Buckwheat	Grain	2,1	0,9	1
Maize	Gramineae	Maize	Grain	2,6	1,1	1
			Stems and leaves	16,0	6,8	no data
Leguminous vegetables	Fabaceae	Soybean	Pods	2,4	1,0	5
Tubers	Solanaceae	Potatoes	Tubers	1,8	0,8	4
Non-Leafy vegetables	Amaranthaceae	Amaranth	Stems and leaves	12,2	5,2	no data
Herbs	Brassicaceae	White mustard	Seeds	1,1	0,5	no data
Other crops	Asteraceae	Sunflower	Seeds	3,8	1,6	no data
			Stems and leaves	8,2	3,5	no data
Grasses + Leguminous (cultivated species)	Gramineae	Bromegrass	Stems and leaves	8,4	3,6	4
	Fabaceae	Galega	Stems and leaves	5,0	2,1	4
Pasture (natural species)	Gramineae+ others	Dry meadow	Stems and leaves	5,0	2,1	4.5
	Gramineae (mainly)	Wet meadow (Bromegrass)	Stems and leaves	3,8	1,6	4

[a] CF recommended by IAEA (Classification of soil systems …, 2006, pp. 1–19).

cultivated grass mixture and vegetation communities of dry and wet meadows give better fit to CF_{wheat}. In regard to obtained CF for potatoes tubers and soybean pods, they present twice less than predicted, when generally recognized data of CF for the other investigated foodstuff (stems and leaves of maize and amaranth, seeds of white mustard, stems, leaves, and seeds of sunflower) are not available.

As a whole, the concept of conversion factors and reference crops for the prediction of ^{137}Cs transfer into plants have considerable promise, but invites further investigation and precise observing environmental conditions.

4. Conclusions

Radioactive pollution of agricultural lands after large man-induced incidents is characterized by long-term occurrence: even 3 decades after Chernobyl accident current density of ^{137}Cs soil contamination in the area of the Plavsk radioactive hotspot in Tula region of Russia varies in a range 140–220 kBq/m^2 and exceeds radiation safety standard by~3.5–6 times. Spatial ^{137}Cs distribution in contaminated lands highly varies due to primary heterogeneity of Chernobyl fallout and secondary redistribution of the radionuclide via erosion of cultivated lands leading to ≈40% growing of ^{137}Cs inventories in meadow soils of the lower parts of slope in comparison with ^{137}Cs content in arable chernozems of elevated positions of relief.

Deep plowing of arable chernozems of the territory obviously has been applied in 1986–1987 to reduce an emergency of ^{137}Cs soil-to-plant transfer, which resulted in relatively uniform vertical distribution of the radionuclide within top 0–30 cm soil layer. Hence, main rooting biomass of crops cultivated with shallow disk plowing (wheat, barley) or without annual tillage (perennial grass mixture) are in contact only with 32–33% of total ^{137}Cs inventory in arable chernozems; crops cultivated with middle plowing (buckwheat, amaranth, white mustard) – contact with 65–66% of total ^{137}Cs inventory; crops cultivated with deep rotational plowing (maize, soybean, potatoes) uptake the radionuclide from the all thickness of radiocaesium-containing soil layer. Native chernozems and alluvial calcareous soils contain 60–65% of ^{137}Cs total inventory within the top 0–10 cm layer, which is coincidentally the main rooting layer of meadow vegetation. In this connection meadow ecosystems can be considered as critical unit for ^{137}Cs behaviour in "soil-plant" systems of radioactively contaminated lands.

Bioavailability of ^{137}Cs in "soil-plant" systems of the Plavsk radioactive hotspot is rather low. Calculated soil-to-plant TF values for foodstuff of main crops cultivated on the territory are predominantly $n \cdot 10^{-2} - n \cdot 10^{-3}$, generally they not exceed or are less than recommended by IAEA tentative TF values of ^{137}Cs for agricultural crops growing in temperate climate conditions. The investigated plants and their compartments can be grouped on the basis of transfer factor values as follows: maize (stems and leaves) > amaranth > bromegrass of grass mixture > vegetation of dry meadow, galega of grass mixture, sunflower (seeds), vegetation of wet meadow > maize (grain), soybean (pods), barley (grain), buckwheat (grain), potatoes (tubers) > white mustard (seeds), wheat (grain). Principal cause responsible for radiocaesium TFs differences are biological features of agricultural crops and plant communities, but ^{137}Cs root uptake is not coincide with total flux of mineral nutrients in the investigated "soil-plant" systems.

Generative plant compartments (grain, seeds, and pods) are characterized by less ^{137}Cs activities and TF values in comparison with stems and leaves. Therefore, there are specific biological barriers to protect progeny against radioactive influence. The most pronounced difference has been established for white mustard (with a factor 8); TFs for grain of cereals are 5–7 times less than for green parts; difference for soybean, buckwheat, and sunflower are relatively less (with a factor 2–3).

To simplify a forecast of ^{137}Cs soil-to-plant the calculation of specific CF of unknown TF of selected crop from the TF of the reference cereals (wheat, barley) seems promising. Values of CF obtained for the investigated agrosystems and meadow ecosystems not exactly, but satisfactory agree with CFs recommended by IAEA. Some CF values (for stems and leaves of maize and amaranth, seeds of white mustard, stems, leaves, and seeds of sunflower) have been proposed at the present study, which call for further investigation.

In sum, ^{137}Cs bioavailability from radioactively contaminated chernozem and chernozem-like alluvial soils of the Plavsk radioactive hotspot is considerably limited by strong irreversible fixation of the radionuclide by soil clay minerals and biological properties of agricultural crops and meadow grasses. As a result, ^{137}Cs activities in plants are completely in accordance with national standards and we can be confident in radioecological safety of obtained foodstuff.

Acknowledgements

The study was supported by the Russian Foundation for Basic Research (14-05-00903).

References

Alexakhin, R. M., Buldakov, L. A., Gubanov, V. A., Drozhko, Y. G., Ilyin, L. A., Kryshev, I. I., et al. (2004). *Large radiation accidents: Consequences and protective countermeasures*. Moscow, Russia: IzdAT Publisher.

Arinushkina, E. V. (1970). *Guidelines for the chemical analysis of soils*. Moscow: Moscow State University Publ (In Russian).

Centofanti, T., Penfield, R., Albrecht, A., Pellerin, S., Flühler, H., & Frossard, E. (2005). Is the transfer factor a relevant tool to assess the soil-to-plant transfer of radionuclides under field conditions? *Journal of Environmental Quality, 34*(6), 1972–1979.

Classification of soil systems on the basis of transfer factors of radionuclides from soil to reference plants. (2006). Vienna, Austria: IAEA. IAEA-TECDOC-1497.

Cornell, R. M. (1993). Adsorption of cesium on minerals: A review. *Journal of Radioanalytical and Nuclear Chemistry, 171*, 483–500.

De Cort, M., Dubois, G., Fridman, Sh., Germenchuk, M., Izrael, Yu., Janssens, A., et al. (1998). *Atlas of caesium deposition on Europe after the Chernobyl accident. EUR report 16733*. Brussels, Luxembourg: Office for Off. Publ. of E.C.

Ehlken, S., & Kirchner, G. (2002). Environmental processes affecting plant root uptake of radioactive trace elements and variability of transfer factor data: A review. *Journal of Environmental Radioactivity, 58*(2–3), 97–112.

Fesenko, S. V., Alexakhin, R. M., & Balonov, M. I. (2007). An extended critical review of twenty years of countermeasures used in agriculture after the Chernobyl accident. *The Science of the Total Environment, 383*(1–3), 1–24.

Frissel, M. J., Deb, D. L., Fathony, M., Lin, Y. M., Mollah, A. S., Ngo, N. T., et al. (2002). Generic values for soil-to-plant transfer factors of radiocesium. *Journal of Environmental Radioactivity, 58*, 113–128.

Golosov, V. N., Panin, A. V., & Markelov, M. V. (1999). Chernobyl ^{137}Cs redistribution in the small basin of the Lokna river, Central Russia. *Physics and Chemistry of the Earth, 24*(10), 881–885.

Golosov, V. N., Walling, D. E., Panin, A. V., Stukin, E. D., Kvasnikova, E. V., & Ivanova, N. N. (1999). The spatial variability of Chernobyl-derived ^{137}Cs inventories in a small agricultural drainage basin in Central Russia. *Applied Radiation and Isotopes, 51*, 341–352.

Golosov, V. N., Walling, D. E., Kvasnikova, E. V., Stukin, E. D., Nikolaev, A. N., & Panin, A. V. (2000). Application of a field-portable scintillation detector for studying the distribution of Cs-137 inventories in a small basin in Central Russia. *Journal of Environmental Radioactivity, 48*(4), 79–94.

Guidelines for using fallout radionuclides to assess erosion and effectiveness of soil conservation strategies. (2014). Austria, Vienna: IAEA. IAEA-TECDOC-1741.

Handbook of parameter values for the prediction of radionuclide transfer in terrestrial and freshwater environments (pp. 39–81). (2010). Austria, Vienna: IAEA. IAEA-TECDOC-472.

Hygienic requirements for the safety and nutritional value of food (2001, renewed 2011). Sanitary rules and norms 2.3.2.1078-01. Registered in the Ministry of Justice Russian Federation on 22 March 2002, N 3326.(2011). Retrieved from http://docs.cntd.ru/document/901806306 (In Russian).

Impact of Soil Conservation Measures on Erosion Control and Soil Quality. (2011). Austria, Vienna: IAEA. IAEA-TECDOC-1665.

Izrael, Y. A., & Bogdevich, I. M. (Eds.). (2009). *Atlas of modern and forward-looking aspects of the consequences of the Chernobyl accident in the affected areas of Belarus and Russia* (pp. 49–54). Moscow-Minsk: Fund "Infosphere"-NIA-Nature (In Russian).

Konopleva, I. V. (2016). Selective sorption of radiocaesium by sorbents based on natural clays. *Sorption Chromatography Procdure, 16*(4), 280–290 (in Russian).

Konoplev, A. V., & Konopleva, I. V. (1999). Parameterisation of Cs-137 soil-plant transfer through key soil characteristics. *Radiation Biology. Radioecology, 39*(4), 455–461 (In Russian).

Kruglov, S. V., Anisimov, V. S., Anisimova, L. N., & Aleksakhin, R. M. (2008). Specific ^{137}Cs-sorption capacity parameters of soils and mineral sorbents. *Eurasian Soil Science, 41*(6), 608–617.

Linnik, V. G., Saveliev, A. A., & Govorun, A. P. (2007). Spatial variability and topographic factors of Cs-137 soil contamination at a field scale. *International Journal of Ecology & Development, 8*(7), 8–25.

Nisbet, A. F., & Woodman, R. F. M. (2000). Soil-to-plant transfer factors for radiocesium and radiostrontium in agricultural systems. *Health Physics, 78*(3), 279–288.

Paramonova, T., Belyaev, V., Komissarova, O., & Ivanov, M. (2017). Homo/heterogeneity of Cs-137 distribution within ploughed horizon of arable chernozems, 30 years after Chernobyl accident. *Radiation and Applications, 2*(3), 192–199.

Perez-Harguindeguy, N., Diaz, S., Garnier, E., Lavorel, S., Poorter, H., Jaureguiberry, P., et al. (2013). New handbook for standardized measurement of plant functional traits worldwide. *Australian Journal of Botany, 61*, 167–234.

Popplewell, D. S., Ham, G. J., Johnson, T. E., Stahner, J. W., & Sumner, S. A. (1984). The uptake of plutonium-238, 239, 240, americium-241, strontium-90 and caesium-137 into potatoes. *The Science of the Total Environment, 38*, 173–181.

Puchkov, V. A., & Bolshov, L. A. (Eds.). (2016). *Russian national report 30 Years of the Chernobyl accident: Results and prospects for overcoming its consequences in Russia. 1986-2016* (pp. 113–137) (In Russian).

Regions of Russia. (2016). *Socio-economic indicators. Statistical compilation*. Moscow, Russia: Rosstat (in Russian).

Sanzharova, N. I., Fesenko, S. V., Kotik, V. A., & Spiridonov, S. I. (1996). Behavior of radionuclides in meadows and efficiency of countermeasures. *Radiation Protection Dosimetry, 64*(1/2), 43–48.

Sanzharova, N., Spiridonov, S., Kuznetzov, V., Isamov, N., Fesenko, S., & Belova, N. (2006). The classification of Russian soil systems on the basis of transfer factors of radionuclides from soil to reference plants. In *Classification of soil systems on the basis of transfer factors of radionuclides from soil to reference plants. IAEA-TECDOC-1497* (pp. 113–137). Vienna, Austria: IAEA.

Soil sampling for environmental contaminants (pp. 7–38). (2004). Austria, Vienna: IAEA. IAEA-TECDOC-1415.

Staunton, S., & Roubaud, M. (1997). Adsorption of ^{137}Cs on montmorillonite and illite: Effect of charge compensating cation, ionic strength, concentration of Cs, K and fulvic acid. *Clays and Clay Minerals, 45*(2), 251–260.

Wauters, J., Elsen, A., Cremers, A., Konoplev, A. V., Bulgakov, A. A., & Comans, R. N. J. (1996). Prediction of solid/liquid distribution coefficients of radiocaesium in soils and sediments. Part one: A simplified procedure for the solid phase characterization. *Applied Geochemistry, 11*(4), 589–594.

International Soil and Water Conservation Research 7 (2019) 167–175

Contents lists available at ScienceDirect

International Soil and Water Conservation Research

journal homepage: www.elsevier.com/locate/iswcr

Original Research Article

Dynamic study of infiltration rate for soils with varying degrees of degradation by water erosion

Yujie Wei, Xinliang Wu, Jinwen Xia, Rubing Zeng, Chongfa Cai*, Tianwei Wang

Key Laboratory of Arable Land Conservation (Middle and Lower Reaches of Yangtze River) of the Ministry of Agriculture, Soil and Water Conservation Research Centre, College of Resources and Environment, Huazhong Agricultural University, Wuhan 430070, China

ARTICLE INFO

Article history:
Received 4 September 2018
Received in revised form
27 December 2018
Accepted 28 December 2018

Keywords:
Soil infiltration
Rainfall simulation
Erosional degradation
Soil texture
Water erosion

ABSTRACT

Ultisols, widely distributed in tropical and subtropical areas of south China, are suffering from serious water erosion, however, slope hydrological process for Ultisols under different erosional degradation levels in field condition has been scarcely investigated. Field rainfall simulation at two rainfall intensities (120 and 60 mm/h) were performed on pre-wetted Ultisols with four erosion degrees (non, moderate, severe and very-severe), and the hydrological processes of these soils were determined. The variation of soil infiltration was contributed by the interaction of erosion degree and rainfall intensity ($p < 0.05$). In most cases, time to incipient runoff, the decay coefficient, steady state infiltration rate, and their variability were larger at the high rainfall intensity, accelerating by the increasing erosion severity. Despite rainfall intensity, the infiltration process of Ultisols was also significantly influenced by mean weight diameter of aggregates at the field moisture content, soil organic carbon and particle size distribution ($R^2 > 30\%$, $p < 0.05$). The temporal erodibility of surface soil and soil detachment rate were significantly and negatively correlated with infiltration rate ($r < -0.32$, $p < 0.05$), but less significant correlation was observed between sediment concentration and infiltration rate for most soils, especially at the high rainfall intensity. The variation of surface texture and soil compactness generated by erosion degradation was the intrinsic predominant factors for the change of infiltration process of Ultisols. The obtained results will facilitate the understanding of hydrological process for degraded lands, and provide useful knowledge in managing crop irrigation and soil erosion.

1. Introduction

Rainfall infiltration is a process that water runs into the soil and leads to an increased total moisture content, contributing to the variation of water partitioning and hydrologic response, and changes the development and recurrence frequency of erosion process (Lu, Zheng, Li, Bian, & An, 2016; Shakesby, Doerr, & Walsh, 2000; Walker, Walter, & Parlange, 2007). To better understand the hydrological and erosion mechanism in tropical and subtropical areas, rainfall infiltration pattern and process should gain more consideration in those regions where precipitation is the dominant source for soil erosion.

The process of rainfall infiltration is controlled by several factors, including geomorphology, rainfall or climatic properties, surface roughness, soil porosity or density, organic carbon content, size and stability level of the aggregates, and soil hydraulic properties (Mohamadi & Kavian, 2015; Morbidelli, Saltalippi, Flammini, & Govindaraju, 2018). These factors consequently interfere on runoff. Prior research generally confirmed that land cover significantly affects infiltration, reducing the direct impact of raindrops on the soil (Almeida et al., 2018). Soil surface roughness, porosity and infiltration decrease due to the limited plant canopy or residue cover for bare soils, causing the increase of runoff and intensification of the erosion process. Widely accepted that, the formation of surface crust is the predominant process influencing soil infiltration during the rainfall, especially for bare lands (e.g., Assouline, 2004; Durán Zuazo & Rodríguez Pleguezuelo, 2008; Le Bissonnais et al., 2005; Podwojewski et al., 2011). Soils with low aggregate stability but high dispersivity form a surface crust much more readily, resulting in the development of a dense, thick and less permeable surface structure (Le Bissonnais, 1996; Rodrigo Comino et al., 2016).

A consensus on an explanation for the influence of rainfall intensity on infiltration rate could be hardly obtained in literatures,

* Corresponding author.
E-mail address: hzaucfcai@163.com (C. Cai).

Peer review under responsibility of International Research and Training Center on Erosion and Sedimentation and China Water and Power Press.

https://doi.org/10.1016/j.iswcr.2018.12.005

and reversed results have been reported in prior publications (e.g., Assouline & Ben-Hur, 2006; Liu, Lei, Zhao, & Yuan, 2011). High rainfall intensity accelerates the dispersion and breakdown of aggregate, facilitating the formation of surface seal. However, an increase in rain intensity lead to a higher transportability of flow, enhancing the mobility the detached particles carried away out of the test area. Briefly, the variation of land surface condition generating the change of infiltration pattern and process should be controlled by the comprehensive effects of rainfall character and the stability of soil structure.

Water erosion, as the most predominant erosion type in tropic and sub-tropic areas, encompasses infiltration, percolation and retention under rainfall (Bossio, Geheb, & Critchley, 2010). Bare lands resulted from erosional degradation are widely distributed around the world, creating severe limitations to the sustainability of natural ecosystems and agricultural activities (García-Ruiz, Beguería, Lana-Renault, Nadal-Romero, & Cerdà, 2017; Gonzalez, 2018; Podwojewski et al., 2011). Land degradation results in the reduction of water productivity, availability, quality and storage at field and landscape scales (Lal, 2001), and caused the deterioration of soil physical, chemical and hydrological process (Bhan, 2013; Le Bissonnais et al., 2005). The reduction of water productivity, availability, quality and storage, the deterioration of soil physical, chemical and hydrological process generated by land degradation are the chronic problems particular for the tropic and sub-tropic areas. Soil thickness declines in various degrees and even has the parent material horizons exposed during the intensification of soil erosion process (Zhang, Yang, & Zepp, 2004). It is traditionally recognized that pedogenic differentiation, including aggregate stability, porosity, density and organic matter et al., leads to the heterogeneity of soil properties in different horizons (e.g., Rejman, Turski, & Paluszek, 1998; Wu, Cai, Wang, Wei, & Wang, 2016). The variability of soil properties resulted from degradation would definitely in turn alters the soil infiltration process (e.g., Assouline, 2004; Carmi & Berliner, 2008; Malvar, Martins, Nunes, Robichaud, & Keizer, 2013).

Most of the existing studies about the correlation between infiltration, soil loss, and surface condition have been performed on small plots with rainfall simulation in laboratory (Cerdà, 1999; Huang, Wu, & Zhao, 2013), but crust formation generated by raindrop impact under natural field conditions is significantly different from crusting in disturbed soil samples in laboratory (Abudi, Carmi, & Berliner, 2012). Ultisols, as the representative quaternary red clay soils in subtropical and tropical regions of central-south China, suffer from serious water erosion. However, few research has been conducted to investigate the infiltration process of Ultisols under different erosion-induced degradation degrees, particular at the field condition.

In accordance with the aforementioned background, this study aims at (i) characterizing the temporal variation of rainfall infiltration process under various erosion-induced degradation degrees at two contrasting rainfall intensities, and (ii) identifying the key physicochemical parameters that account for the dynamic infiltration response indexes. To end this, field plot rainfall simulation experiments were conducted on bare Ultisols with four erosion degrees (non, moderately, severely and very severely eroded) pursuant to the outcrop of eluvium, illuvium and parent material horizons. The obtained results will supplement the knowledge of soil hydrological process of the degraded lands in water erosion dominated regions.

2. Materials and methods

2.1. Experimental sites and soils

Ultisols, derived from quaternary red clay, are the representative soils in subtropical and tropical regions, which occupies 16% of the total areas in China (Fig. S1) (Gao, Li, & Zhou, 1998). East Asian Monsoon climate with the rainy season coinciding with high temperature dominates the climate in these regions. Hilly land with a relative elevation of 10–60 m and a gentle slope ($< 15°$) is the main farmland resource in these areas, and the intensive cultivation makes the soils here are prone to erosion. Water erosion has been a great threat to land productivity and environment protection.

In accordance with the principle of typicality of soil types and accessibility of field rainfall simulation, Ultisols were selected from the north of Changsha city (28°30′N, 112°54′E), Hunan Province, China (Fig. 1-a). The mean annual precipitation and temperature in this area is 1422 mm and 17 °C, respectively. Field plots suffering from different water erosion degrees were selected according to the outcrop the pedogenic horizons (Rejman, Turski, & Paluszek, 1998): soil profile with the intact eluvial horizon (A) was in a non-erosion degree (E0); soil profile with the outcrop of illuvial horizons, B1 and B2, was in the moderate (E1) and severe (E2) erosion degree, respectively; soil profile with the outcrop of parent material horizon (C) was very severely eroded (E3) (Fig. S2). Characteristics of each horizon were summarized in Table 1. Before the installment of field plot, top soil layers (about 1–3 cm thickness) with roots and organic residues were removed to avoid the interference of vegetation impacts. The basic information of Ultisols with different erosion degrees was summarized in Table 2.

2.2. Measurement of rainfall infiltration

Soil infiltration generated by rainfall was determined by field plot rainfall simulation experiments. Field plots for rainfall simulation were equally in an area of 2.40 m^2 (length 3.00 m × width 0.80 m) and at a slope of 10° (the representative slope gradient in this region) (Fig. 1-b). Two repetitions were performed due to the intensive labor and the capture area of the portable rainfall simulator. Big clods (< 3 cm) in the surface layer (< 5 cm) were crushed to simulate the cropland condition. Besides, the plots were presaturated for the consistency of the antecedent water condition, and the raindrop energy was retard with a 2-mm wire screen suspended 0.10 m above the soil surface. The rainfall experiment was conducted after 12 h of the runoff generation.

Rainfall simulator with a SPRACO cone jet nozzle was installed at a height of 5.0 m above the center of the plots to obtained a natural raindrop energy when rain drops approached soil surface (Luk, Abrahams, & Parsons, 1986). In accordance with the representative and common rainstorms in study area, two rainfall intensities (60 and 120 mm/h) were designed. Rainfall simulation was continued for 1 h after runoff initiation. Runoff and sediment were collected at 3-min intervals after runoff generation for measurement of runoff volume (L) and soil loss (g). Infiltration was determined by difference from runoff and rainfall intensity.

Infiltration rate (f) was calculated by difference between rainfall intensity and runoff rate. The infiltration curves were fitted by the Horton (1941):

$$f = \begin{cases} f_0 & T < T_r \\ f_c + \left(f_0 - f_c\right)e^{-k(T-T_r)} & T \geq T_r \end{cases} \quad (1)$$

where, f_0 and f_c are the initial and steady state infiltration rate, respectively (mm/min); k is the Horton's decay coefficient; T_r is the time to incipient runoff (min); T is the rainfall duration (min).

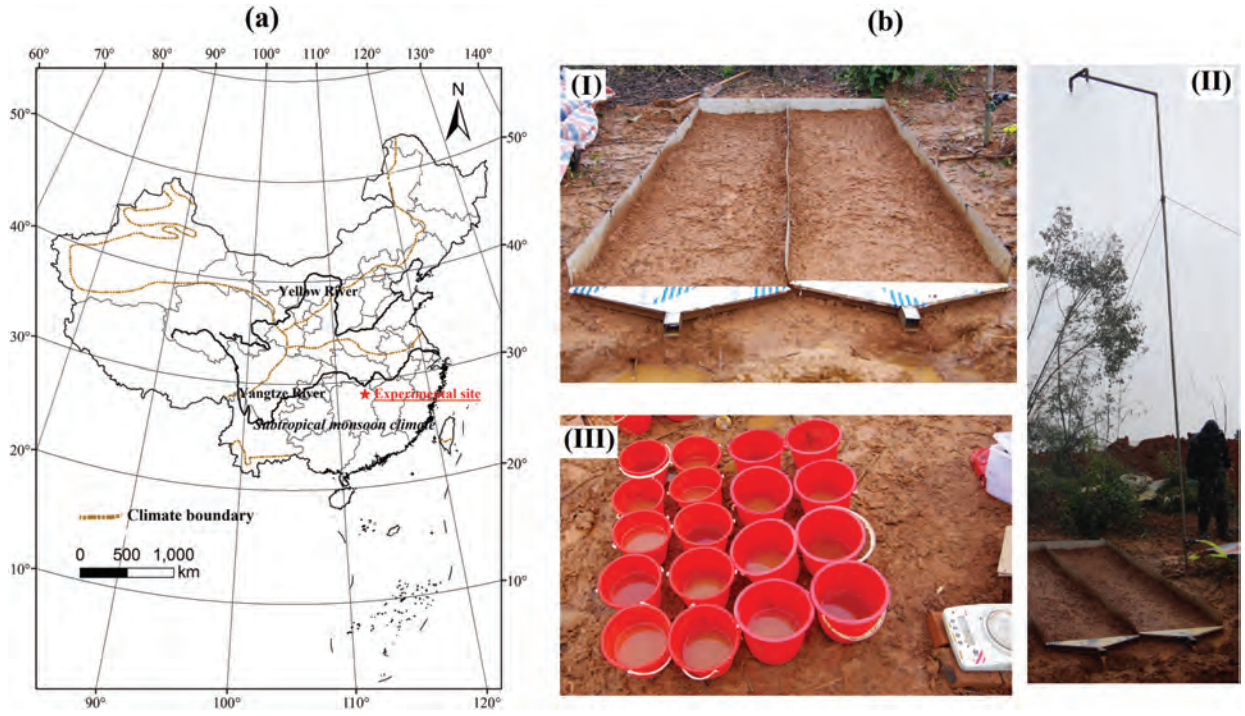

Fig. 1. Location of experimental sites (a), and field experiment components (b).

Table 1
Basic information of the selected Ultisols.

ED	Horizon	Dry color	Land use	Soil structure	Soil description
E0	A	7.5YR 6/6	forest land	granular, loose-well aggregated	high organic matter content and biological activity with a large amount of roots and plant residues
E1	B1	7.5YR 6/6	grassland	tight blocky structure	high contents of iron-manganese cutans and concretions; large amount of roots and plant residues
E2	B2		wasteland		without root and biological activity
E3	C	7.5YR6/8–5YR 4/6	bare land	tight-massive clod structure	red-white reticulated mottling horizon and heavy texture

Note: ED, erosion degree; E0, E1, E2 and E3 denote no, moderate, severe and very severe erosion degrees, respectively.

Table 2
Soil physicochemical properties in different erosion degrees (mean ± standard deviation).

ED	ρ	SOC (%)	γ (g/cm^3)	w_o (g/g)	NP (cm^3/cm^3)	CP	Sand (%)	Silt	Clay	MWD_{FM} (mm)
E0	2.70 ± 0.00	2.59 ± 0.01	1.13 ± 0.06	0.34 ± 0.03	0.16 ± 0.03	0.43 ± 0.02	7 ± 1	42 ± 1	51 ± 0	2.80 ± 0.34
E1	2.72 ± 0.01	0.28 ± 0.01	1.31 ± 0.02	0.30 ± 0.01	0.10 ± 0.02	0.42 ± 0.01	5 ± 0	44 ± 0	52 ± 0	3.50 ± 0.39
E2	2.73 ± 0.01	0.18 ± 0.02	1.31 ± 0.02	0.30 ± 0.00	0.09 ± 0.01	0.42 ± 0.01	5 ± 0	42 ± 0	53 ± 0	2.60 ± 0.14
E3	2.74 ± 0.01	0.06 ± 0.00	1.56 ± 0.01	0.23 ± 0.01	0.05 ± 0.02	0.38 ± 0.01	6 ± 0	39 ± 3	55 ± 3	4.43 ± 0.51

Note: ED, erosion degree; E0, E1, E2 and E3 denote no, moderate, severe and very severe erosion degrees, respectively; ρ, particle density; SOC, soil organic carbon; γ, bulk density; w_o, field moisture content; NP and CP, non-capillary and capillary porosity; Sand, 2–0.05 mm; Silt, 0.05–0.002 mm; Clay, < 0.002 mm; MWD_{FM}, mean weight diameter of aggregates at the field moisture content.

2.3. Data analysis

Statistical tests and figures were performed using the software of SPSS 20.0 (SPSS Inc, Chicago, IL, USA) and OriginPro 2016, respectively. The differences in soil infiltration among different treatments (erosion degree, and rainfall intensity) were analyzed at $p < 0.05$. Shapiro-Wilk statistics were conducted for the normality tests of all dependent and independent variables. Normality tests were carried out for all dependent and independent variables using Shapiro–Wilk statistics. The variables not conforming to normal distribution were transformed by natural logarithmic treatment. Soil properties accounting for the majority of soil infiltration responses were selected by stepwise multiple linear regression analysis (Xue, 2013).

3. Results

3.1. Rainfall infiltration process

The temporal variations in rainfall infiltration rate for Ultisols under different erosion degrees and rainfall intensities were depicted in Fig. 2. Time to incipient runoff (T_r) was evidently larger at the low (8.68–15.13 min) than at the high rainfall intensity (0.78–6.84 min),

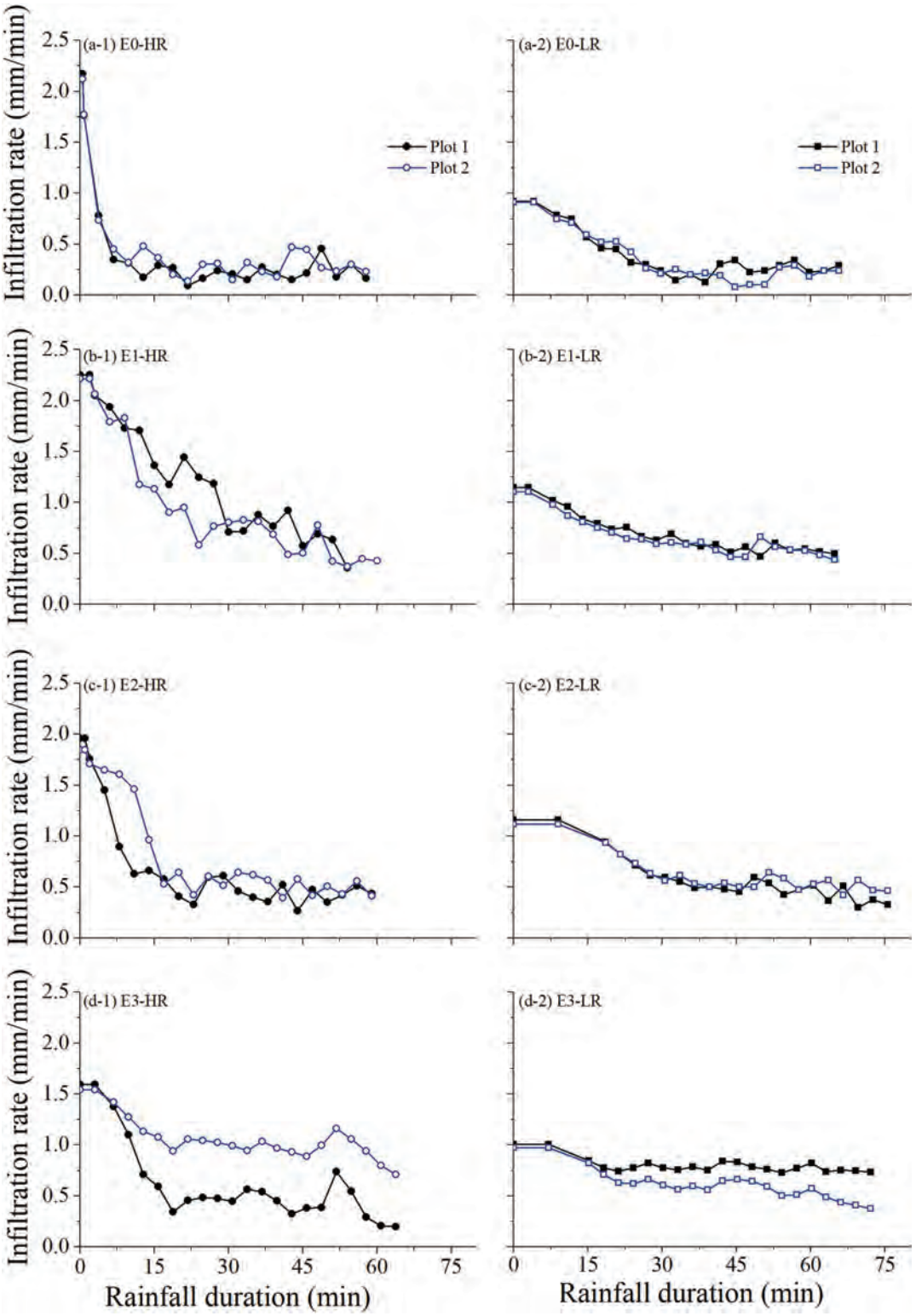

Fig. 2. Temporal variations of soil infiltration rate in different erosion classes (no (E1), moderate (E2) and very-severe (E3)) and at two rainfall intensities (60 mm/h (LR) and 120 mm/h (HR)).

and Tr at the low was around 11 times of that at the high rainfall intensity for noneroded soils (E0) (Fig. 4-a). Additionally, time to incipient runoff generally increased with the increased erosion severity especially at the high rainfall intensity. The difference of Tr between two filed plots seems to be increased with erosion severity, despite the non-eroded soils. Statistically, time to incipient runoff varied significantly with soil erosion degree and rainfall intensity ($p < 0.01$).

After runoff generation, soil infiltration rate decreased sharply after runoff generation, followed by a steady state with continuing rainfall duration. However, infiltration rate at the steady state showed apparent fluctuations, particular for soils at the high rainfall intensity. The temporal variations of infiltration rate were generally gentler at the low than at the high rainfall intensity. Similarly, the difference of temporal rainfall infiltration rate in two

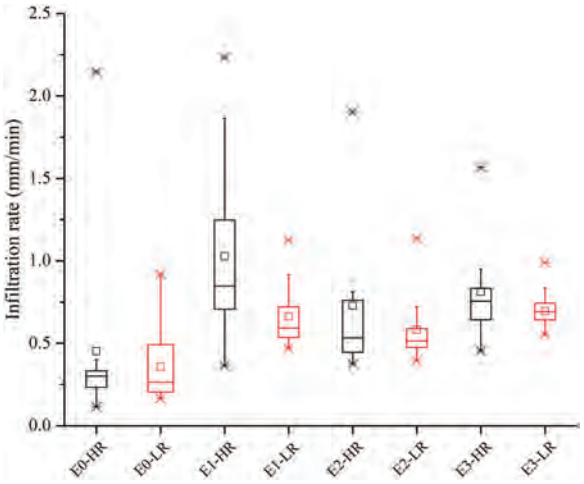

Fig. 3. Boxplots of soil infiltration rate during the rainfall for different types of soils. HR, high rainfall intensity (120 mm/h); LR, low rainfall intensity (60 mm/h); E0 = no erosion; E1 = moderate erosion; E2 = very severe erosion; E3 = very severe erosion. The boxes indicate the 25th and 75th percentiles; the line in the box indicates the median (50th percentile); "×" indicates outlier values; "□" indicates average value.

field plots was evidently larger for soils with the very severe erosion degree (E3).

The effect of erosion severity on the temporal infiltration rate varied with rainfall intensity (Fig. 3). The rainfall infiltration rate showed a relatively larger variability at the high than at the low rainfall intensity, e. g., infiltration rate of the non-eroded soils (E0) at the high and low rainfall intensity was 2.03 and 0.75 mm/min, respectively. Besides, at the high rainfall intensity, the variability of rainfall infiltration rate generally increased with increasing erosion severity, but an opposite trend was observed at the low rainfall intensity. Throughout the rainfall duration, the non-eroded soils (E0) possessed a relatively lower infiltration rate among all the tested soils, especially at the low rainfall intensity.

Infiltration process for most soil types was fitted well with Horton's equation (Adj-R^2 > 0.60, $p < 0.05$), and less satisfied fitting results were observed for the very sever eroded soils. As shown in Fig. 4-b, the decay coefficient *k* ranged between 0.03 and 1.17 for all the tested soils. Apart from the very severely eroded soils (E3), decay coefficient was generally larger at the high than at the low rainfall intensity. However, the difference of decay coefficient between two parallel field plots was significant larger at the low than at the high rainfall intensity, especially for the very severely eroded soils (1.17–0.01). Collectively, the impact of land degradation on the unsteady infiltration process varied with rainfall intensity.

The infiltration rate at the steady state averagely increased with increasing erosion severity, especially for field plot 1 at the high rainfall intensity and field plot 2 at the low rainfall intensity (Fig. 4-c). The difference of the steady state infiltration rate between the parallel treatments was obviously larger at the low rainfall intensity, besides, the infiltration rate at the steady state showed the maximum and minimum variability at field plots with moderate (E1) and very sever (E3) erosion degree, respectively.

3.2. Identification of soil properties influencing rainfall infiltration processes

Multiple stepwise regression results (Fig. 5) indicated that rainfall infiltration process of Ultisols was significantly influenced by rainfall intensity, mean weight diameter of aggregates at the field moisture content, soil organic carbon and particle size distribution ($p < 0.05$). Specifically, rainfall intensity and clay content

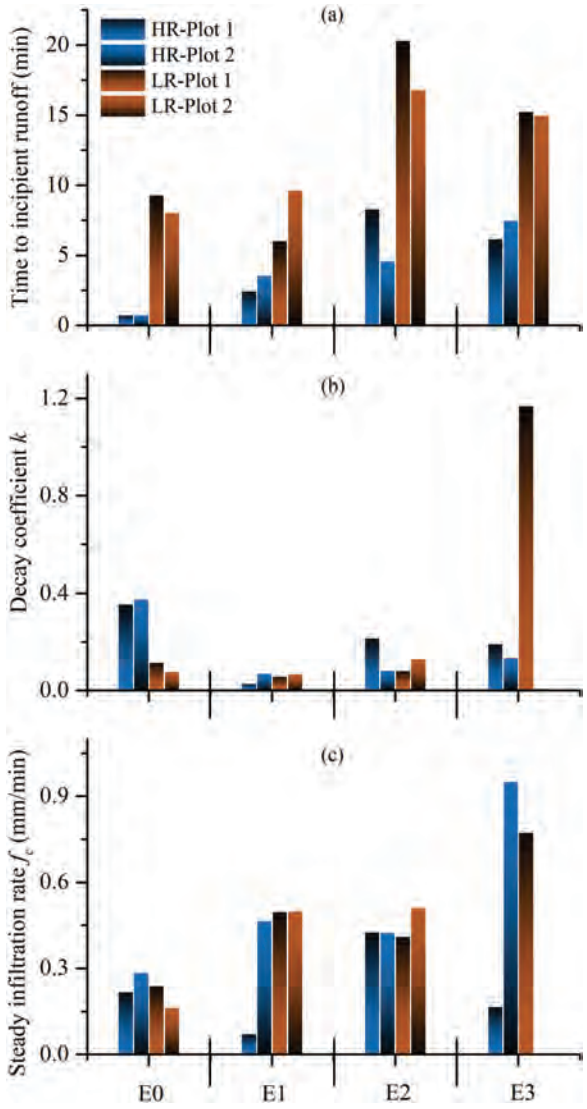

Fig. 4. Parameters of Horton models including (a) Time to incipient runoff (T_r), (b) decay coefficient *k* and (c) steady state infiltration rate (f_c) in different erosion classes (no (E1), moderate (E2) and very-severe (E3)) and at two rainfall intensities (60 mm/h (LR) and 120 mm/h (HR)).

with negative and positive effects on time to incipient runoff (Tr), respectively, explained more than 80% of variance in Tr (Adj-R^2 = 75%, $p < 0.05$). However, the variability of the time to incipient runoff was largely depended on the sand content ($p < 0.01$). The decay coefficient (*k*) with its variability determined by clay content (R^2 = 75%, $p < 0.01$) was decreased by the increasing silt content (R^2 = 56%, $p < 0.01$). The content of soil organic carbon and clay fraction contributed to variation of the infiltration rate at the steady state (f_c) (Adj-R^2 = 79%, $p < 0.01$), besides, the variability of f_c was influenced by mean weight diameter of aggregates at the field moisture content (R^2 = 82%, $p < 0.01$). Generally, the final infiltration rate was determined by soil cement content and aggregate stability.

Considering the significant effects of rainfall intensity on soil infiltration rate, the relationships between rainfall infiltration processes and the influencing factors were analyzed separately under different rainfall intensities (Fig. 5-b and -c). At the high rainfall intensity, clay content facilitated the increasing of the time to incipient runoff (R^2 = 72%, $p < 0.01$) with its variability increased by the interaction of sand content and aggregate stability index (Adj-R^2 = 81%, $p < 0.05$); the variation of decay coefficient

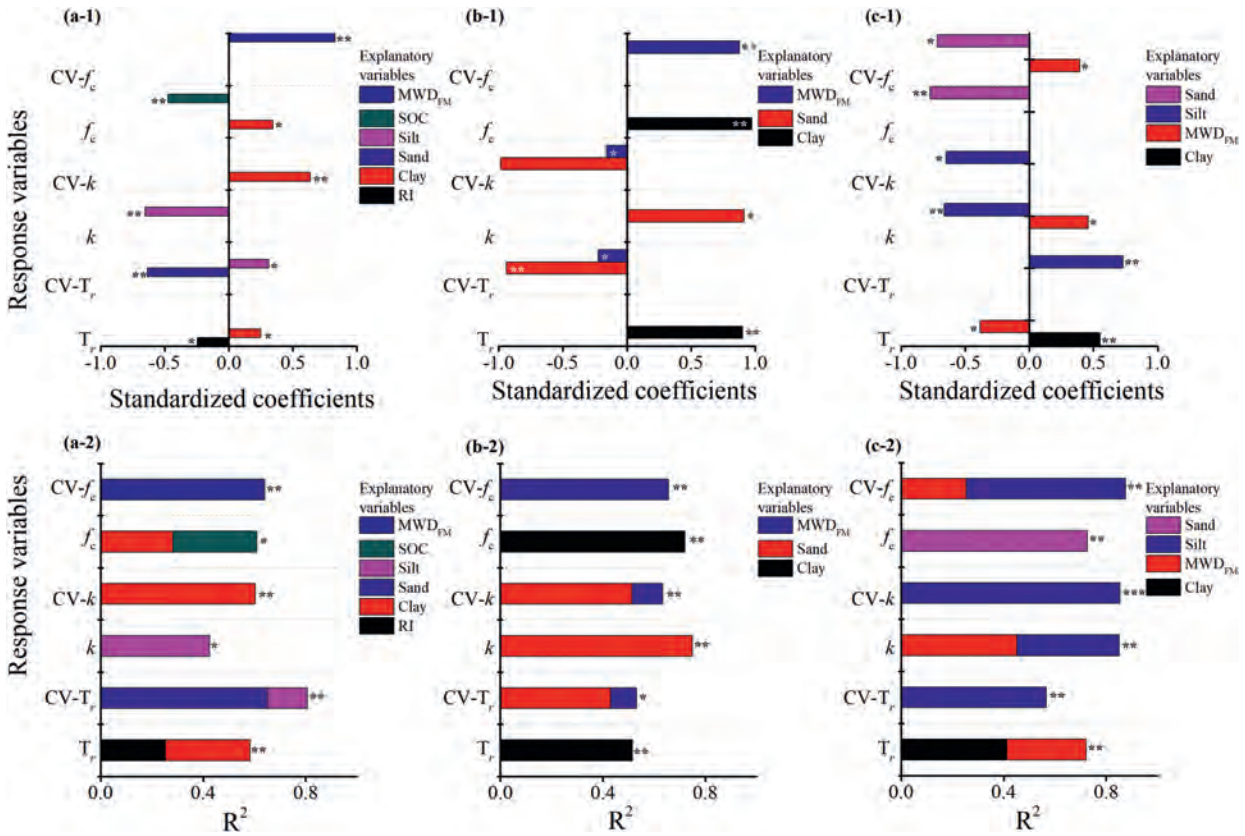

Fig. 5. Standardized coefficients and R square of selected variables accounting for the Horton model parameters based on the all data (a), at the high rainfall intensity (b) and at the low rainfall intensity (c).

(k) was dominated by sand content ($R^2 = 0.62\%$, $p < 0.001$); clay content ($R^2 = 0.82\%$, $p < 0.01$) and mean weight diameter of aggregates at the field moisture level ($R^2 = 0.79\%$, $p < 0.01$) generated the variation and variability of the steady state infiltration rate, respectively. At the low rainfall intensity, time to incipient runoff was influenced by the interaction of clay content and mean weight diameter of aggregates at the field moisture level (Adj-$R^2 = 81\%$, $p < 0.05$), but its variability was generated by silt content ($R^2 = 0.79\%$, $p < 0.01$); silt content ($R^2 = 52\%$, $p < 0.01$) and the mean weight diameter of aggregates at the field moisture level ($R^2 = 0.38\%$, $p < 0.05$) was negatively and positively correlated with the decay coefficient (k), respectively; the variation of steady state infiltration rate was determined by sand content ($R^2 = 83\%$, $p < 0.01$). Collectively, clay and sand content dominated the major variation of rainfall infiltration process at the high rainfall intensity, but silt content contributed to the variation of rainfall infiltration process at the low rainfall intensity.

4. Discussion

According to this study, the variation rainfall infiltration rate was generally changed into three parts: (i) keeping constantly before runoff generation; (ii) declining sharply with rainfall duration; (iii) obtaining a steady state finally. The rainfall infiltration process for bare soils was predominated by the variation of surface soil properties and structures (Assouline, 2004; Carmi & Berliner, 2008), which was intrinsically determined by the extent of the breakdown and dispersion of soil aggregates under the interacts of rainfall (intensity and duration) and surface structure stability (Ran, Su, Li, & He, 2012). Ultisols suffering from different land degradation degrees showed different infiltration processes, altering the sediment transportability and concentration, and hence, influencing the erosion process.

4.1. Effects of rainfall characteristics on rainfall infiltration process

During rainfall, the temporal infiltration process could be reduced by the formation and evolution of surface crusts (Carmi & Berliner, 2008; Ran, Su, Li, & He, 2012). At the initial stage of rainfall, soils possessed a high infiltration capacity, delaying the time to incipient runoff; as rainfall continued, surface structure was gradually compacted by the raindrop impact, especially at the high rainfall intensity and high kinetic energy, and thus facilitated the runoff generation but declined the infiltration (Shi, Yan, Li, Li, & Cai, 2010), as the variation of time to incipient runoff showed in Fig. 4-a. Simultaneously, high rainfall intensity usually contributed to the breakdown of more aggregates and facilitated surface crust formation and pore clogging (Lu, Zheng, Li, Bian, & An, 2016) (Fig. S3), which could also explain the negative effects of rainfall intensity on runoff generation (Fig. 5-a) and the decreased infiltration rate with rainfall duration (Fig. 2).

Surface crusting was formed by an in situ reorganization of existing aggregates and dispersive fragments or sedimentary crusts generated by particle transport and sorting (Le Bissonnais et al., 2005). However, this process was influenced by the dual contribution of rainfall intensity. High rainfall intensity disrupted more soil aggregates (except the very severely eroded soils), facilitating the formation of surface crusts but it also possessed a high sediment transport capacity. Therefore, different degrees of surface crust formation during the continued rainfall duration generated the various infiltration patterns in Fig. 2. Specifically, the well-developed crusting leaded to a nearly constant infiltration rate at the steady state, e.g., the quasi-steady state of infiltration

rate of non-eroded soils (Fig. 2-a). Yet, the re-disrupted crust could be transported by runoff, particular under the high runoff coefficient condition (Fig. S4). The transportability of runoff and the detachment ability of rain drops collectively affected the variation of surface structure and infiltration fluctuation.

4.2. Effects of soil properties on rainfall infiltration process

The variation of surface structure or crusting generated by the mechanical breakdown and dispersion of aggregates for the pre-wetted soils under the rainfall condition (Le Bissonnais, 1996; Shi, Yan, Li, Li, & Cai, 2010). Apart from the rainfall intensity, soil properties and surface soil conditions also made great contributions to the dynamic infiltration rate during rainfall events (Assouline & Ben-Hur, 2006). Due to the different disruptive forces of rainfall intensities, different soil properties were selected to account for the temporal infiltration rate at the high and low rainfall intensity (Fig. 5). During rainfall, sediment transport by runoff dominated the surface variation, indicated by particle size distribution (Kinnell, 2005). This was supposed to be the reason that the content of clay, silt and sand fraction contributed to the variation of infiltration process for Ultisols. Besides, the loos structure (bulk density was in a range of 1.13–1.31 g/cm^3) (Table 2) of the non-eroded (E0), moderately eroded (E1), and severely eroded soils (E2) soils facilitated the disintegration of soil particles and the formation of structural crust (Le Bissonnais, 1996), and hence, the tight density and low permeability of these crusts generated the sharp decreasing of infiltration rate especially at high rainfall intensity (Fig. 2-a–c). Likewise, the relative tight-blocky structure (bulk density was around 1.56 g/cm^3) and high mechanical strength (mean weight diameter of aggregates at the field moisture content was around 4.43 mm) of the very severely eroded soils (E3), accelerated its resistance to rainfall impact and runoff dispersion, resulting in a less susceptibility to breakdown (Misra & Teixeira, 2001), which leaded to a relatively high infiltration rate and less influence by rainfall duration (Fig. 2d). In addition, the rough surface for the very severely eroded soils would reduce the detachment power and transport capacity of runoff, thus enabling a higher infiltration (Prosdocimi et al., 2017).

4.3. Variation of soil loss influenced by erosion degree and rainfall intensity

The hydrological process during rainfall is composed by infiltration and runoff, and the increased runoff or decreased infiltration contributes to increasing the sediment concentration (e.g., Jin et al., 2008; Tadesse, Suryabhagavan, Sridhar, & Legesse, 2017). Though, most of the obtained results in this study were consistent with this conclusion, the effect of infiltration on sediment concentration varied with erosion degree and rainfall intensity (Fig. S5) (Fig. 6), e.g., sediment concentration was positively correlated with infiltration rate for non (E0) and moderately (E1) eroded soils at the high rainfall intensity, and for the very severely eroded soils (E3) at the high and low rainfall intensity ($p < 0.05$). The positive and non-significant correlations could be ascribed by the variation of sediment transport form during erosion process (Assouline & Ben-Hur, 2006; Kinnell, 2005; Mohamadi & Kavian, 2015). It was speculated that soil loss was predominated by detachment-limited regime for the very severely eroded soils (E3) and transport-limited form for the non (E0) and moderately (E1) eroded soils at the high rainfall intensity (Kukal & Bawa, 2013).

In eroded inferior lands, soil was exposed to erosion once losing the surface cover (Kirchhoff, Rodrigo-Comino, Seeger, & Ries, 2017). Surface crusts formed during rainfall induced erosion made dual effects on soil loss: (1) impeding a further detachment of raindrop and runoff to subsurface aggregate, which reduced infiltration and soil loss; (2) increasing the amount of runoff, which momentarily improved the ability of detachment and transport for overland flow. Widely accepted that, surface crusts facilitate particles compaction and clog soil pores, leading to a much lower permeability of the crusted surface than that of the underlying layers (Assouline, 2004), but crust formation reduces the infiltration rate, which increases runoff and accelerates the soil loss (Durán Zuazo & Rodríguez Pleguezuelo, 2008). However, in this

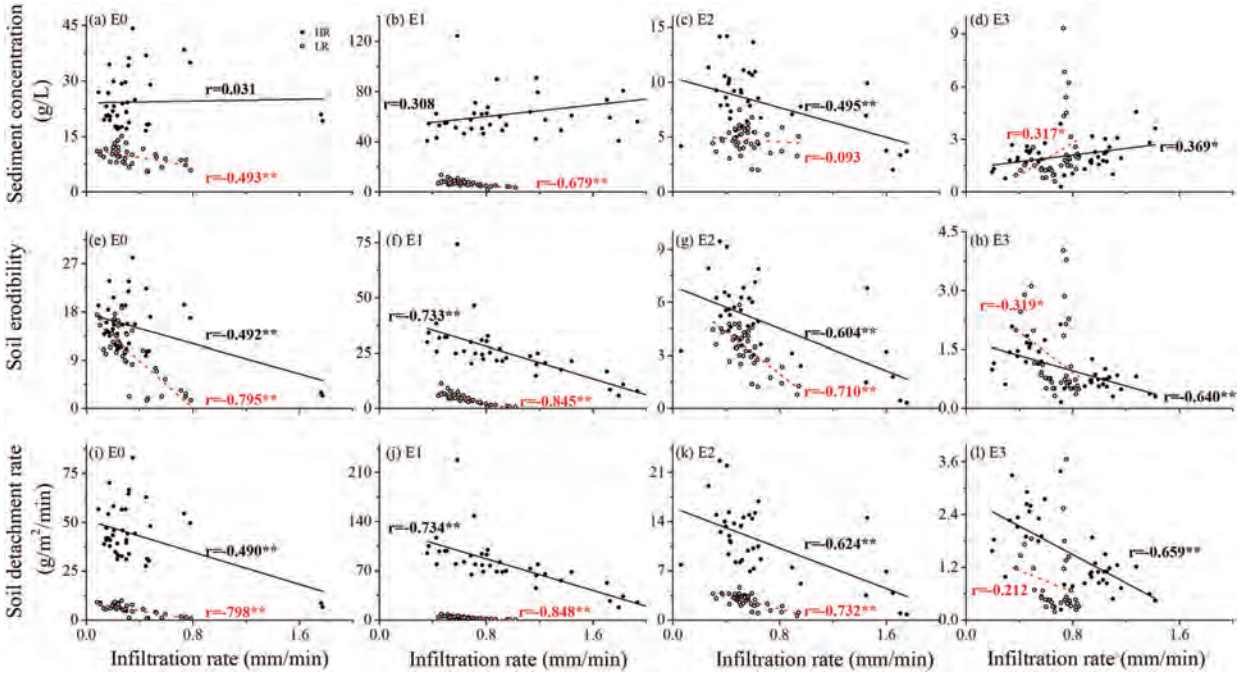

Fig. 6. Relationships of sediment concentration, soil erodibility, and soil detachment rate with infiltration rate. HR and LR indicate high (120 mm/h) and low (60 mm/h) rainfall intensity, respectively. * and ** represent the statistical significance at $p < 0.05$, and 0.01, respectively. The relationship in each treatment was derived from the two plot data rather than their average value ($n = 40$).

study, a significant and negative correlation ($p < 0.01$) has been observed between the temporal soil erodibility and infiltration rate for all the tested soils (Fig. 6). It is noteworthy that, this positive correlation actually reflected the temporal influence of surface crusting to soil erodibility. Surface crusting with high mechanical strength could increase surface shear strength and improve the anti-erodibility of surface soil temporally, compared with the original loss and well aggregated surface structure (Kinnell, 2006; Wei, Wu, & Cai, 2015).

Similar correlation was observed between soil detachment rate and infiltration rate ($r < 0$, $p < 0.01$). The correlation was higher at the low ($r = -0.73$ to -0.89, $p < 0.01$) than at the high rainfall intensity ($r = -0.49$ to -0.73) except for the very severely eroded soils (E3) showing and opposite trend, indicating that soil loess was determined by the transport capacity of runoff, especially at the low rainfall intensity for E0, E1 and E2. Besides, the increased runoff would facilitate the breakdown of the thin crust and then percolated through the subsurface soils, which likely leaded to the fluctuation of rainwater partitioning in the steady state and accelerated erosion on subsurface soils (Ribolzi et al., 2011). Therefore, topsoil was crucial for soil erosion induced by rainfall. Increasing surface cover (such as vegetation and mulch) should be an imperative way to inhibit the formation of soil crust and improve the crop water availability especially for soils in a well aggregate and loose structure (Dlamini et al., 2011; Tadesse, Suryabhagavan, Sridhar, & Legesse, 2017). However, the very severely eroded soils with high infiltration capacity were less productive due to the deficiency of essential elements and structure conditions for crop growth, and hence, different measurements should be considered in practice.

5. Conclusions

In this study, the effects of erosion induced land degradation and rainfall intensity on infiltration process in the Ultisols was investigated by the field plot rainfall simulation experiments. Soil infiltration processes, including time to incipient runoff, the decay coefficient and the steady state infiltration rate, and their variability were generally larger at the high than at the low rainfall intensity, and showed an increasing trend with the increased erosion severity. The dynamic infiltration rate was dominated by rainfall intensity, mean weight diameter of aggregates at the field moisture content, soil organic carbon and particle size distribution, and the specific physicochemical properties that controlling the hydraulic process varied with rainfall intensity. Increasing surface cover should be considered for inhibiting soil erosion for soils with well aggregate and loose structure; but the improvement of soil fertility and structure for the very severely eroded soils is more imperative. The results of this study were obtained based on the hypothesis that soil infiltration differs significantly between land degradation levels and rainfall intensities, and other factors for the field rainfall simulation experiments including slope, bare fallow condition, and antecedent moisture condition of experiment plots kept as consistent as possible. Despite these factors, the hydrological response under the dynamic rainfall intensity also need a further investigation in future studies.

Acknowledgements

This research was supported by the National Key Research and Development Program of China (2017YFC0505401) and the National Natural Science Foundation of China (41807065).

Appendix A. Supplementary material

Supplementary data associated with this article can be found in the online version at https://doi.org/10.1016/j.iswcr.2018.12.005.

References

Assouline, S. (2004). Rainfall-induced soil surface sealing: A critical review of observations, conceptual models, and solutions. *Vadose Zone Journal*, *3*, 570–591.
Abudi, I., Carmi, G., & Berliner, P. (2012). Rainfall simulator for field runoff studies. *Journal of Hydrology*, *454–455*, 76–81.
Almeida, W. S. D., Panachuki, E., Oliveira, P. T. S. D., Menezes, R. D. S., Sobrinho, T. A., & Carvalho, D. F. D. (2018). Effect of soil tillage and vegetal cover on soil water infiltration. *Soil & Tillage Research*, *175*, 130–138.
Assouline, S., & Ben-Hur, M. (2006). Effects of rainfall intensity and slope gradient on the dynamics of the interrill erosion during soil surface sealing. *Catena*, *66*, 211–220.
Bossio, D., Geheb, K., & Critchley, W. (2010). Managing water by managing land: Addressing land degradation to improve water productivity and rural livelihoods. *Agricultural Water Management*, *97*, 536–542.
Bhan, S. (2013). Land degradation and integrated watershed management in India. *International Soil and Water Conservation Research*, *1*(1), 49–57.
Cerdà, A. (1999). Seasonal and spatial variations in filtration rates in badland surfaces under Mediterranean climatic conditions. *Water Resources Research*, *35*(1), 319–328.
Carmi, G., & Berliner, P. (2008). The effect of soil crust on the generation of runoff on small plots in an arid environment. *Catena*, *74*, 37–42.
Durán Zuazo, V. H., & Rodríguez Pleguezuelo, C. R. (2008). Soil-erosion and runoff prevention by plant covers. A review. *Agronomy for Sustainable Development*, *28*, 65–86.
Dlamini, P., Orchard, C., Jewitt, G., Lorentz, S., Titshall, L., & Chaplot, V. (2011). Controlling factors of sheet erosion under degraded grasslands in the sloping lands of KwaZuluNatal. *South Africa Agricultural Water Management*, *98*, 1711–1718.
Gao, Y. X., Li, J., & Zhou, M. C. (1998). *Soil map of China (1:4,000,000)* (pp. 1–6) Beijing: Since Press (In Chinese).
García-Ruiz, J. M., Beguería, S., Lana-Renault, N., Nadal-Romero, E., & Cerdà, A. (2017). Ongoing and emerging questions in water erosion studies. *Land Degradation & Development*, *28*, 5–21.
Gonzalez, J. M. (2018). Runoff and losses of nutrients and herbicides under long-term conservation practices (no-till and crop rotation) in the U.S. Midwest: A variable intensity simulated rainfall approach. *International Soil and Water Conservation Research*, *6*, 265–274.
Horton, R. E. (1941). An approach toward a physical interpretation of infiltration-capacity 1. *Soil Science Society of America Journal*, *5*(C), 399–417.
Huang, J., Wu, P., & Zhao, X. (2013). Effects of rainfall intensity, underlying surface and slope gradient on soil infiltration under simulated rainfall experiments. *Catena*, *104*, 93–102.
Jin, K., Cornelis, W. M., Gabriels, D., Shiettecatte, W., Neve, S. D., Lu, J., & Harmann, R. (2008). Soil management effects on runoff and soil loss from field rainfall simulation. *Catena*, *75*, 191–199.
Kinnell, P. I. A. (2005). Raindrop impact induced erosion processes and prediction: A review. *Hydrological Processes*, *19*, 2815–2844.
Kinnell, P. I. A. (2006). Simulations demonstrating interaction between coarse and fine sediment loads in rain-impacted flow. *Earth Surface Processes and Landforms*, *31*, 355–367.
Kukal, S. S., & Bawa, S. S. (2013). Temporal variations in runoff and soil loss in relation to soil conservation practices in catchments in Shiwaliks of lower Himalayas. *International Soil and Water Conservation Research*, *1*(2), 19–25.
Kirchhoff, M., Rodrigo-Comino, J., Seeger, M., & Ries, J. B. (2017). Soil erosion in sloping vineyards under conventional and organic land use managements (Saar-Mosel Valley, Germany). *Cuadernos Délelőtt Investigación Geográfica*, *43*.
Luk, S., Abrahams, A. D., & Parsons, A. J. (1986). A simple rainfall simulator and trickle system for hydro-geomorphic experiments. *Physical Geography*, *7*(4), 344–356.
Le Bissonnais, Y. (1996). Aggregate stability and assessment of soil crustibility: I. Theory and methodology. *European Journal of Soil Science*, *47*, 425–437.
Lal, R. (2001). Soil degradation by erosion. *Land Degradation & Development*, *12*, 519–539.
Le Bissonnais, Y., Cerdan, O., Lecomte, V., Benkhadra, H., Souchère, V., & Martin, P. (2005). Variability of soil surface characteristics influencing runoff and interrill erosion. *Catena*, *62*, 111–124.
Liu, H., Lei, T. W., Zhao, J., Yuan, C. P., et al. (2011). Effects of rainfall intensity and antecedent soil water content on soil infiltrability under rainfall conditions using the run off-on-out method. *Journal of Hydrology*, *396*, 24–32.
Lu, J., Zheng, F., Li, G., Bian, F., & An, J. (2016). The effects of raindrop impact and runoff detachment on hillslope soil erosion and soil aggregate loss in the Mollisol region of Northeast China. *Soil & Tillage Research*, *161*, 79–85.
Misra, R. K., & Teixeira, P. C. (2001). The sensitivity of erosion and erodibility of forest of soils to structure and strength. *Soil & Tillage Research*, *59*, 81–93.
Malvar, M. C., Martins, M. A., Nunes, J. P., Robichaud, P. R., & Keizer, J. J. (2013). Assessing the role of pre-fire ground preparation operations and soil water

repellency in post-fire runoff and inter-rill erosion by repeated rainfall simulation experiments in Portuguese eucalypt plantations. *Catena*, *108*, 69–83.
Mohamadi, M. A., & Kavian, A. (2015). Effects of rainfall patterns on runoff and soil erosion in field plots. *International Soil and Water Conservation Research*, *3*(4), 273–281.
Morbidelli, R., Saltalippi, C., Flammini, A., & Govindaraju, R. S. (2018). Role of slope on infiltration: A review. *Journal of Hydrology*, *557*, 878–886.
Podwojewski, P., Janeau, J. L., Grellier, S., Valentin, C., Lorentz, S., & Chaplot, V. (2011). Influence of grass soil cover on water runoff and soil detachment under rainfall simulation in a sub-humid South African degraded rangeland. *Earth Surface Processes and Landforms*, *36*, 911–922.
Prosdocimi, M., Burguer, M., Di Prima, S., Sofia, G., Terol, E., Rodrigo Comino, J., … Tarolli, P. (2017). Rainfall simulation and structure-from-motion photogrammetry for the analysis of soil water erosion in Mediterranean vineyards. *Science of the Total Environment*, *574*, 204–215.
Rejman, J., Turski, R., & Paluszek, J. (1998). Spatial and temporal variations in erodibility of loess soil. *Soil & Tillage Research*, *46*, 61–68.
Ribolzi, O., Patin, J., Bresson, L. M., Latsachack, K. O., Mouche, E., Sengtaheuanghoung, O., & Valentin, C. (2011). Impact of slope gradient on soil surface features and infiltration on steep slopes in northern Laos. *Geomorphology*, *127*, 53–63.
Ran, Q., Su, D., Li, P., & He, Z. (2012). Experimental study of the impact of rainfall characteristics on runoff generation and soil erosion. *Journal of Hydrology*, *424*, 99–111.
Rodrigo Comino, J., Iserloh, T., Lassu, T., Cerdà, A., Keestra, S. D., Prosdocimi, M., … Ries, J. B. (2016). Quantitative comparison of initial soil erosion processes and runoff generation in Spanish and German vineyards. *Science of the Total Environment*, *565*, 1165–1174.
Shakesby, R. A., Doerr, S. H., & Walsh, R. P. D. (2000). The erosional impact of soil hydrophobicity: Current problems and future research directions. *Journal of Hydrology*, *231–232*, 178–191.
Shi, Z. H., Yan, F. L., Li, L., Li, Z. X., & Cai, C. F. (2010). Interrill erosion from disturbed and undisturbed samples in relation to topsoil aggregate stability in red soils from subtropical China. *Catena*, *81*, 240–248.
Tadesse, L., Suryabhagavan, K. V., Sridhar, G., & Legesse, G. (2017). Land use and land cover changes and Soil erosion in Yezat Watershed, North Western Ethiopia. *International Soil and Water Conservation Research*, *5*(2), 85–94.
Walker, J. D., Walter, M. D., & Parlange, J. Y. (2007). Reduced raindrop-impact driven soil erosion by infiltration. *Journal of Hydrology*, *342*, 331–335.
Wei, Y., Wu, X., & Cai, C. (2015). Splash erosion of clay-sand mixtures and its relationship with soil physical properties: The effects of particle size distribution on soil structure. *Catena*, *135*, 254–262.
Wu, X., Cai, C., Wang, J., Wei, Y., & Wang, S. (2016). Spatial variations of aggregate stability in relation to sesquioxides for zonal soils, South-central China. *Soil & Tillage Research*, *157*, 11–22.
Xue, W. (2013). *SPSS statistical methods and applications* ((3th ed.). Beijing, China: Publishing House of Electronics Industry (in Chinese).
Zhang, B., Yang, Y., & Zepp, H. (2004). Effect of vegetation restoration on soil and water erosion and nutrient losses of a severely eroded clayey Plinthudult in southeastern China. *Catena*, *57*, 77–90.

International Soil and Water Conservation Research 7 (2019) 176–183

Contents lists available at ScienceDirect

International Soil and Water Conservation Research

journal homepage: www.elsevier.com/locate/iswcr

Original Research Article

Use of a calibrated SWAT model to evaluate the effects of agricultural BMPs on sediments of the Kalaya river basin (North of Morocco)

Hamza Briak [a,b,*], Rachid Mrabet [b], Rachid Moussadek [b], Khadija Aboumaria [a]

[a] Department of Earth Sciences, Faculty of Sciences and Techniques (FST), Abdelmalek Essaadi University, Postal Box 416, 90000 Tangier, Morocco
[b] Department of Environment and Natural Resources, Scientific Division, National Institute for Agricultural Research (INRA), Postal Box 415, 10000 Rabat, Morocco

ARTICLE INFO

Article history:
Received 23 August 2018
Received in revised form
11 December 2018
Accepted 1 February 2019
Available online 18 February 2019

Keywords:
Modeling
Agricultural BMPs
Sediment
SWAT
Kalaya river basin
North Morocco

ABSTRACT

Soil erosion from agricultural fields is a worldwide problem, to influence water quality, soil fertility and reservoir sedimentation especially in Mediterranean countries such as Morocco. In fact, this work assesses the effects of Best Management Practices (BMPs) on sediments using the Soil and Water Assessment Tool (SWAT) model in the Kalaya watershed in Northern Morocco, to recommend the most appropriate practice. This study is based on the use of three most usable practices: contouring, strip-cropping and terracing, by the calibrated SWAT model. The general parameters of the model have been modified to reflect the implementation of different agricultural BMPs used. Resulting sediment yield were compared with the baseline scenario, for validation. However, the effective measures to reduce sediment losses at the watershed level are organized according to their effectiveness, and these are terracing (28% reduction and the value is 15t/ha/yr) followed by strip-cropping (9% reduction and the value is 5t/ha/yr). In contrast, measurements performed by the contouring are inappropriate for the study area because they have contributed to increasing the soil erosion (more than 31% of losses and the value is 17t/ha/yr more than existing conditions). Therefore, the model illustrates that the terrace is effective for reducing sediment losses and limiting soil erosion especially on steep slopes. Thus, the results provide useful information for targeted management in order to implement the most effective agricultural BMPs in the watershed.

1. Introduction

Soil is a natural resource dynamic non-renewable that directly or indirectly affects our daily activities, and which plays a vital role in maintaining life on the planet. The Movements and water quality, land use and vegetation productivity all have relationships with soil (Briak, 2017). In fact, the soil has always faced the phenomena of water erosion, which poses a major problem in the preservation of our environment (Pimentel et al., 1995; Portenga & Bierman, 2011; Wu & Chen, 2012; Yang, Kanae, Oki, Koike, & Musiake, 2003). Soil erosion by water is one of the main factors negatively affecting agricultural productivity (Kefi et al., 2011) and one of the most widely reported forms of land degradation in the world mainly in Mediterranean watersheds (Cosentino, Copani, & Scalici, 2015; Grimm, Jones, & Montanarella, 2002; Hallouz, Meddi, Mahé, Alirahmani, & Keddar, 2018; Hudson, 1991; Lahmar & Ruellan, 2007; Yaalon, 1997), especially since the highest rates are recorded in northern Morocco (Benmansour et al., 2014; Briak, Moussadek, Derradji, Aboumaria, & Mrabet, 2016a; Briak, Moussadek, Aboumaria, & Mrabet, 2016b; El Garouani, Chen, Lewis, Tribak, & Abharour, 2008; Heusch, 1970; Iaaich et al., 2016; Merzouk & Dahman, 1998; Sabir & Roose, 2004). The Mediterranean climate is identified by the seasonal contrast (Aboumaria, 2009), where soil erodibility can be affected by the dry and warm summer climate (Le Bissonnais et al., 2007; Mrabet, Ibn Namr, Bessam, & et Saber, 2001) and where soil erosion can be influenced by the concentration of rainfall, especially in autumn (Moussadek et al., 2011; Ramos & Martínez-Casasnovas, 2009). In addition, the soil sensitivity of northern Morocco to erosion can be explained by *i)* the topography and its great dissection, *ii)* the effects of the rains aggressiveness, *iii)* a much ramified hydrographic network and especially *iv)* a very erodible marl lithology. As well as the high human density promotes this phenomenon following to the degradation of vegetation and poor farming practices. Furthermore; all conditions are met for water and soil

* Corresponding author at: Department of Earth Sciences, Faculty of Sciences and Techniques (FST), Abdelmalek Essaadi University, Postal Box 416, 90000 Tangier, Morocco.
E-mail address: hamza.briak@gmail.com (H. Briak).
Peer review under responsibility of International Research and Training Center on Erosion and Sedimentation and China Water and Power Press.

https://doi.org/10.1016/j.iswcr.2019.02.002

losses reach a significant speed on vulnerable lands, located on the steepest and longest slopes (Panagos et al., 2015; Roose, 1994; Zhou et al., 2016). This erosion problem in Northern Morocco can be mitigated by agricultural conservation practices, which are often referred to as Best Management Practices (BMPs) (Logan, 1993). The BMPs are effective ways not only to improve agricultural productivity, but also to limit soil erosion impacts and to reduce also nutrients, pesticides, animal wastes and other pollutant loads from their source area at the reception of water bodies in the complex process (Dakhlalla & Parajuli, 2016; Wu, Liu, Liu, & Zhu, 2014). However, to reduce the soil erosion intensity, it is required first to determine the sources areas of sediment yield where soil conservation works have to focus on. The environmental effects of BMPs can be evaluated through experimental monitoring and model simulation. Moreover, because the approach of experimental monitoring is time and costs consuming, distributed parameter watershed models are often used for evaluating the effectiveness of various best management practices (BMPs) (Xie, Chen, & Shen, 2015). Among several watershed models that can assess the environmental effectiveness of BMPs in terms of sediment yield reduction, Soil and Water Assessment Tool (SWAT) model (Arnold, Srinivasan, Muttiah, & Williams, 1998) was selected for this study. SWAT has been widely adopted because of its robust algorithms for simulation of the hydrologic system, sediment and pollutant transport, as well as its comprehensive database on agricultural management practices (Arabi, Frankenberger, Engel, & Arnold, 2008; Betrie, Mohamed, Van Griensven, & Srinivasan, 2011; Dechmi & Skhiri, 2013; Ramos, Benito et al., 2015; Yang et al., 2010). In this context, the objective of this work is to evaluate the effects of different agricultural BMPs on sediments using SWAT model in the Kalaya river basin in order to recommend the most appropriate one.

2. Methods

Our study localized on the Kalaya basin (38 km^2) situated in the North of Morocco (Briak, Moussadek, & Derradji et al. 2016a), which is characterized by *i)* sub-humid Mediterranean climate, a wet winter (an average annual rainfall of 667 mm) and a dry summer (an average annual temperature of 18 °C), *ii)* different classes of slopes (50% of the area $<$ 15%, 40% of the area between 15% and 30% and 10% of the area $>$ 30%), *iii)* a varied pedological mosaic (76.86% of the area is occupied by poorly developed soils; 6.30% of vertisoils; 6.02% of paravertisoils; 3.05% of complex colluvial and alluvial soils; 2.36% of complex calcareous brown soils; 1.85% of complex lithosols and fersiallitic soils; 1.62% of complex regosols and poorly developed soils 1.27% of complex calcic brown soils and leached soils and 0.67% of Brown soils) and different classes of land use (74.98% of the surface is occupied by agricultural areas; 10.47% of urban areas; 9.33% of arable land; 3.26% of hardwood forest degraded; 1.62% of highly degraded areas and 0.34% of sclerophyllous vegetation). Therefore, the agriculture is the primary land use of the watershed, accounting for approximately 75% of the available acres. In fact, The Soil and Water Assessment Tool (SWAT, Arnold et al., 1998) coupled with the Geographic Information System (GIS) software was used for this work. This model is based on a semi-distributed conceptual approach seems more suitable and gives its ease of use, and its speed of execution as well (Rollo, 2012). It allows integrating climate data, hydrological and biological as well as complex phenomena such as erosion, infiltration and agricultural practices (Arnold & Fohrer, 2005).

The general approach of the work is presented in the form of a flowchart at Fig. 1, so as to construct a procedure for using this model to allow the reproduction of the modeling approach in

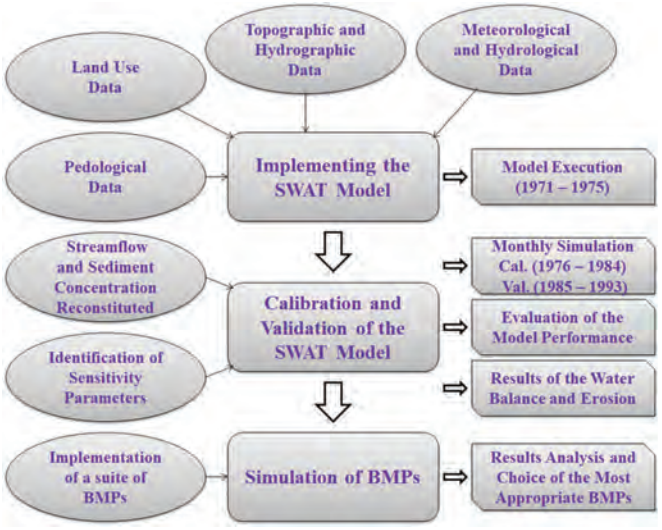

Fig. 1. General Methodology of Using the SWAT Model.

different watersheds. The application of the model is carried out using data spread over 23 years. The periods of the different phases of the implementation of the SWAT model on the Kalaya watershed are then distributed as follows: 5 years for model initialization, 9 years for calibration and 9 years for validation. The SWAT model must first be implemented on the watershed under study and then calibrated and validated. When these steps are completed, the model can be used to perform simulations in Best Management Practices (BMPs). This model works with fin spatial and temporal units. The time step is daily and the spatial resolution is the hydrological response unit (HRU). These geographical units are considered as homogeneous in terms of water, pedoclimatic and land use (Gassman, Reyes, Green, & Arnold, 2007). The HRUs are not spatialized but they are distributed within each own sub-basins. These latter divide the catchment area by stream segments. It is at the scale of these units that the calculations of the model are made which are based on multiple equations from numerous researches (Neitsch, Arnold, Kiniry, & Williams, 2011). From the data its disposal, the model calculates each variable successively.

Indeed, agricultural BMPs implementation and source reduction in various combinations were tested using the SWAT model to investigate different sediment load reduction strategies in the basin. The model was calibrated and validated using observed data; the performance of the model was evaluated using statistical methods and this model estimated the total soil erosion rate in the study area (Briak, Moussadek, Aboumaria et al., 2016b). However, we concentrated on the representation of three interesting and most usable practices by the SWAT model: contouring, strip-cropping and terracing. The simulation of contouring in a field will result in: *i)* reduction of surface runoff by retaining water in small depressions; and *ii)* reduction of sheet and gully erosion by reducing the erosive power of surface runoff and preventing or minimizing channel development. The Implementation of strip-cropping in a field will result in: *i)* reduction of surface runoff by retaining water in small depressions; *ii)* reduction of peak flow rate by increasing surface roughness and slowing surface runoff; and *iii)* reduction of sheet and gully erosion by preventing channel development. The realization of terracing in a field will result in: *i)* reduction of surface runoff by retaining water in small depressions; *ii)* reduction the peak flow rate by reducing the length of the slope; and *iii)* reduction of sheet and gully erosion by an increase the sediments settling in runoff, reducing the erosive power of runoff and preventing the formation of rills and gullies.

Yet, the implementation of the BMPs used was based chiefly on the modification of two main parameters; the first is the curve number (CN), which is a primary parameter used for the calibration of the hydrological components of the SWAT model. Moreover, the second is the USLE Support Practice Factor (USLE_P). Thus, the modification of these parameters was based on previous research and modeling efforts conducted in watersheds and presented in Neitsch, Arnold, Kiniry, and Williams (2005) and Arabi et al. (2008).

3. Results

3.1. Model performance

As a useful means for assessing current processes and possible alternative management scenarios in watersheds, the SWAT model must be calibrated and validated to provide good confidence predictions for its simulation capabilities. In this context, the relative sensitivity values were evaluated in the parameter estimation process. Therefore, sixteen parameters related to streamflow and sediment concentration are considered sensitive to relative sensitivity values. The overall effect of each parameter used was classified using the total sensitivity function in SWAT Calibration and Uncertainty Procedures (SWAT-CUP) using stochastic method Sequential Uncertainty Fitting 2 (SUFI-2). Also, the ability of a hydrological model to adequately simulate streamflow and sediment concentration usually account on accurate calibration of parameters.

However, the monthly calibration and validation efforts allowed us to obtain a good performance of the model for stream flow as well as for sediment concentration whose coefficients of NSE and PBIAS showed optimal values for both simulated variables and on each period. What's more, the sensitivity analysis of parameters that influence the simulation of stream flow and sediment concentration, and the determination of the calibrated value for each parameter were successfully performed. Thus, this model estimated the total soil erosion rate in the study area (Briak, Moussadek, Aboumaria et al., 2016b).

Calibration and validation of the model using the multi-variable approach remains a very complicated method, which is proved by the insufficient of use of this approach since most researchers working with this model use only the uni-variable approach even if these users have observation data of more than one variable. Despite this, the multi-variable approach has allowed us to produce and define more realistic parameters for the model through hydrological processes and geographical areas requiring greater calibration effort (for example, understanding rainfall distribution and the change of soil moisture). As a result, the multi-variable approach can fully use field measurements, and it has been suggested as an effective method for reducing errors of the potential equifinality and uncertainty in the parameter identification; and therefore better represent the various agricultural BMPs of the studied basin (Anderton, Latron, & Gallart, 2002; Bergstrom, Lindstrom, & Pettersson, 2002; Beven, 2006, 2012; Cao, Bowden, Davie, & Fenemor, 2006; Daggupati et al., 2015; Franco & Bonumá, 2017; Molina-Navarro, Andersen, Nielsen, Thodsen, & Trolle, 2017; Santhi, Arnold, Williams, Dugas, & Hauck, 2001; White & Chaubey, 2005). In this sense, Table 1 presents the evaluation of SWAT model performance of different approaches in other basins.

Moreover, from the calibration and validation results, it can be noted that the different steps of the model configuration have been given a high priority to push SWAT to reflect the real conditions (weather, flow, sediment, management of agricultural practices … etc.) as much as possible. This confirms that the model is able to simulate the different BMPs at the watershed Kalaya.

3.2. Best Management Practices (BMPs)

3.2.1. Estimation of the sediment yield of BMPs

Calibrated SWAT model was used to quantify soil loss. Three commonly used practices were used to evaluate soil loss and/soil erosion from different practices. The general parameters of the model have been modified to reflect the implementation of these three different BMPs used. The modification of these parameters was based on previous research and modeling work in watersheds with sufficient data for sediment load calibration, as presented in Bracmort, Arabi, Frankenberger, Engel, and Arnold (2006) and Arbi et al. (2008). The average annual loads of Kalaya watershed sediments were then calculated using the SWAT model. The figures below report the estimated amounts of eroded sediment in each sub-basin after the implementation and simulation of agricultural best management practices. Best practice is determined for recommendation.

3.2.1.1. Terracing. Fig. 2 shows the sediment yield at the Kalaya watershed after terracing simulations. The amount of sediment provided by the different units varies between 10 and 70t/ha/yr, with an average rate about 38 t/ha/yr. The highest sediment levels are observed in sub-basins 17, 21 and 24.

3.2.1.2. Contouring. For contouring simulations, it was found that the sediment yield in Kalaya Basin varies between 20 and 140 t/ha/yr, with an average rate about 70t/ha/yr (Fig. 3). The sub-basins most affected by erosion are 4, 21, 26 and 27.

3.2.1.3. Strip-cropping. Regarding to strip-cropping simulations, Fig. 4 shows that sediment production estimated by the SWAT model varies between 15 and 80t/ha/yr, with an average rate about 49 t/ha/yr. The most degraded sub-basins are 4, 12, 17, 21, 24, 26 and 27.

3.2.2. Impact of agricultural BMPs on the slope

Agricultural BMP sources were tested in various combinations to study implementation characteristics before and after these practices and to evaluate various erosion reduction strategies in the Kalaya watershed. The results of modeling conservation practices (Fig. 5) showed us that there is no effect on agricultural land at slopes between 0% and 5%, as well as between 30% and 50% for the terraces and contours, of which these treatments have remained stable and almost reciprocal with the existing conditions. However, we identified the best reductions at slopes varying between 5% and 30% for terraces. By cons, there was an increase more than the existing conditions when using the contours at the slopes 5–30%. As for the use of strip-cropping, we noticed a significant reduction only in slopes ranging between 0% and 5%. Yet, an increase of the losses was eminent with the increase of the slopes.

3.2.3. Comparison between agricultural BMPs

The results of eroded sediment yield were compared with the simulation result of the baseline scenario (existing conditions) (Fig. 6). In fact, the effective measures to reduce sediment losses at the watershed level are organized according to their effectiveness, and these are terracing (28% reduction and the value is 15t/ha/y) followed by strip-cropping (9% reduction and the value is 5t/ha/y). On the other hand, measurements performed by the contouring are inappropriate for the study area because they have contributed to increasing the soil erosion (more than 31% of losses and the value is 17t/ha/y more than existing conditions). The mean annual values of sediment yields obtained for scenarios with and without BMPs were compared to assess the effectiveness of BMPs. Among all other practices, terracing were the most effective BMPs for

Table 1
SWAT model performance in different regions.

Related studies	Regions	Calibration approach		Time step	Period of calibration / validation	NSE	PBIAS
		Uni-variable	Multi-variable				
Santhi et al. (2001)	South America	–	Q	Monthly	1993–1997 / 1998	0.79 / 0.87	–/ –
			S			0.80 / 0.70	–/ –
White & Chaubey (2005)	South America	–	Q	Monthly	2000 / 2002	0.86 / 0.78	–/ –
			S			0.23 / 0.45	– / –
Galván et al. (2009)	South West Spain	Q	–	Monthly	1990–1999 / 2001–2002	0.83 / 0.7	–/ –
Pisinaras, Petalas, Gikas, Gemitzi, & Tsihrintzis (2010)	North East Greece	Q	–	Daily	2003–2005 / 2005–2006	0.81 / 0.68	–/ –
		NO_3^-				0.90 / 0.73	–/ –
		PO_4^{3-}				0.78 / 0.75	–/ –
Fadil, Rhinane, Kaoukaya, Kharchaf, & Alami Bachir (2011)	North Central Morocco	Q	–	Monthly	1989–1997 / 1998–2005	0.80 / 0.85	-1.01 / 8.69
Fiseha, Setegn, Melesse, Volpi, & Fiori (2013)	Central Italy	Q	–	Monthly	1963–1970 / 1991–1995	0.85 / 0.81	-0.52 / -5.57
Ramos & Martínez-Casasnovas (2015)	North East Spain	–	Q	Daily	2010–2011 / 2011–2012	0.88 / 0.82	-16.3 / -13.8
			S			0.66 / 0.71	-15.8 / 8.6
Serpa et al. (2015)	North Central Portugal	Q	–	Daily	2012–2013 / 2013–2014	0.83 / 0.84	0.44 / -3.34
		S				0.60 / 0.58	46.53 / 35.94
Briak et al. (2016a), Briak et al. (2016b) (***the current study***)	North Morocco	–	Q	Monthly	1976–1984 / 1985–1993	0.76 / 0.67	-11.8 / -14.4
			S			0.69 / 0.70	7.12 / 15.5
Sun et al. (2016)	South West France	Gw	–	Daily	1999–2000 / 2013	0.25 / 0.95	-0.27 / -0.05
Ben Salah & Abida (2016)	Central Tunisia	Q	–	Daily	1987–1988 / 1989–1990	0.52 / 0.61	20.7 / 7.7
				Monthly		0.67 / 0.89	37.7 / 7
Tuo, Duan, Disse, & Chiogna (2016)	North East Italy	Q	–	Monthly	2001–2005 / 2006–2010	0.72 / 0.85	–/ –
Zettam *et al.* (2017)	North West Algeria	Q	–	Monthly	2003–2011 / –	0.75 / –	–/ –
		S		Daily	2003–2006 / –	–/ –	–/ –
Cuceloglu, Abbaspour, & Ozturk (2017)	North West Turkey	Q	–	Monthly	1977–2013	0.61 / 0.81	-4.2 / 4.4
Franco & Bonumá (2017)	South Brazil	–	Q	Monthly	2007–2009 / 2006	0.78 / 0.80	-2.3 / -9.1
			ET			0.63 / 0.39	41.3 / 40.6
Molina-Navarro et al. (2017)	South Denmark	–	NO_3^-	Daily	2000–2005 / –	0.69 / –	-36.9 / –
			PO_4^{3-}			0.51 / –	2.2 / –
Duru, Arabi, & Wohl (2017)	Central Anatolia	Q	–	Daily	1989–1996 / 1982–1984	0.61 / 0.65	–/ –
		S		Monthly		0.81 / 0.77	–/ –
Mtibaa, Hotta, & Irie (2018)	North Tunisia	Q	–	Monthly	1991–2003 / 2004–2012	0.87 / 0.86	1.50 / -18
		S			2002–2012 / –	0.55 / –	-48.76 / –

Q: *Streamflow;*
Gw: *Groundwater;*
S: *sediment concentration;*
NO_3^- : Nitrate loads;
PO_4^{3-} : Phosphate Loads.

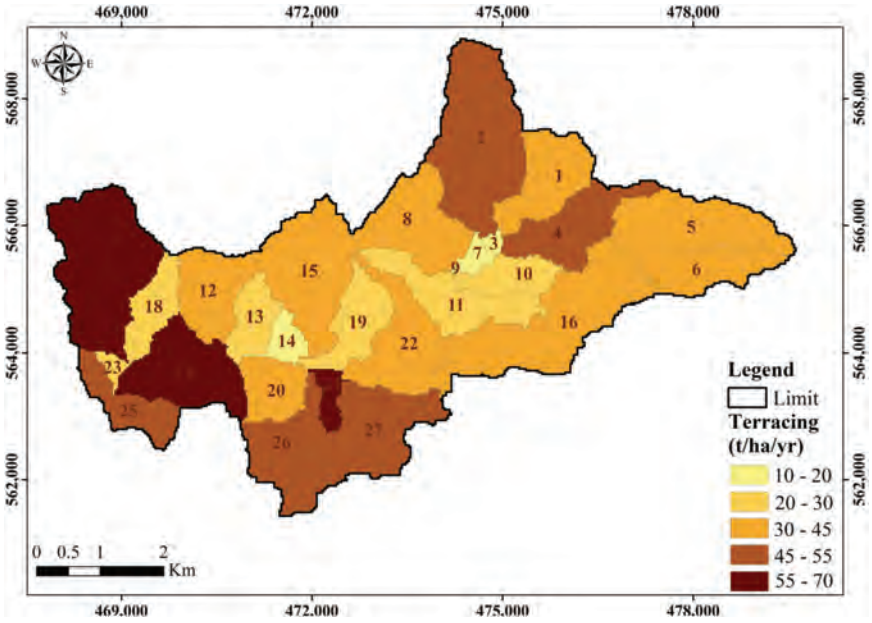

Fig. 2. Sediment yield after terracing simulations at the Kalaya catchment.

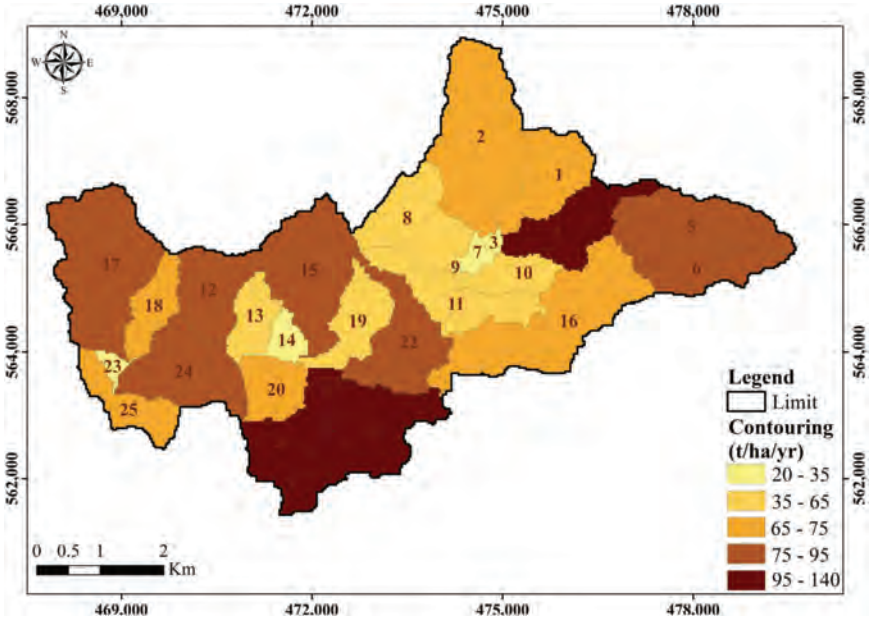

Fig. 3. Sediment yield after contouring simulations at the Kalaya catchment.

reducing sediments. This indicates that the use of terracing on agricultural land can potentially make improvements marked the control and limitation of soil erosion, which is consistent with previous research (Arabi et al., 2008; Bracmort et al., 2006; Daggupati, 2012). These results would provide useful information for targeted management to implement the most effective BMPs within the watershed and/or in other similar watersheds.

4. Discussion

Heavy rainfall, low vegetation cover, topography and intensive farming practices are the main causes of soil erosion (Pimentel & Burgess, 2013). However, the erosion process has many impacts on the site (reduction of soil fertility, crop and nutrient productivity), and off-site (reduction of reservoir storage capacity, increase in risk of flooding and degradation of water quality due to the discharge of sediments and pollutants). These impacts affect the environmental and sustainable development of many developing countries (Ananda & Herath, 2003; Boardman, Shepheard, Walker, & Foster, 2009; Moss, 2008). Abound in this sense, agricultural best management practices (BMPs) have been widely used at the watershed scale to limit the impacts of soil erosion and improve agricultural productivity. These BMPs were modified to further sediment loads reduction exported to the rivers, which is also considered to reduce other types of non-point source pollution, such as N and P exports (Walter, Steenhuis, & Haith, 1979).

In our work, the SWAT model was used after calibration and validation to evaluate the effectiveness of the main BMPs on sediment yield at the Kalaya catchment scale. It is about contouring, terracing and strip-cropping. The simulation results of the conservation practices, proved us that the operation of

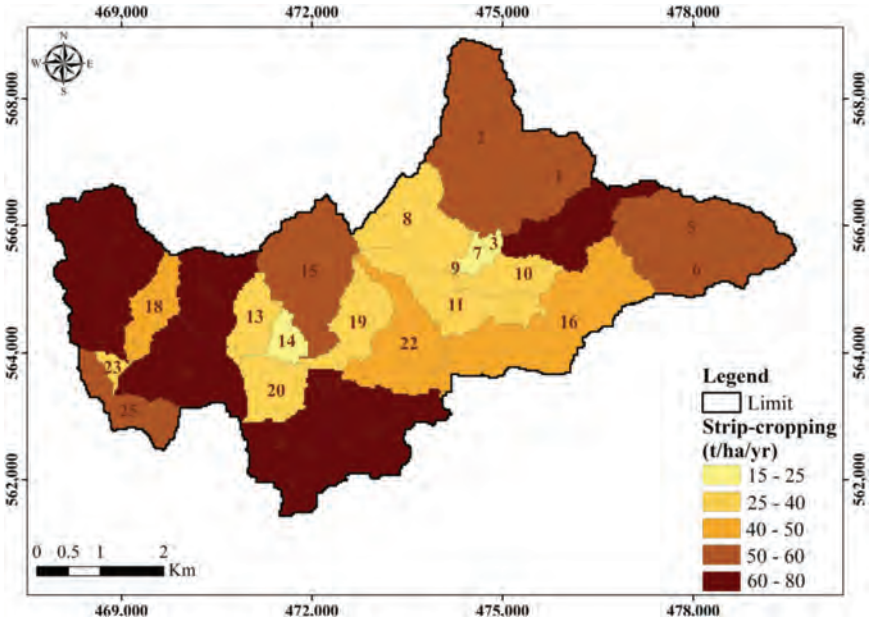

Fig. 4. Sediment yield after strip-cropping simulations at the Kalaya catchment.

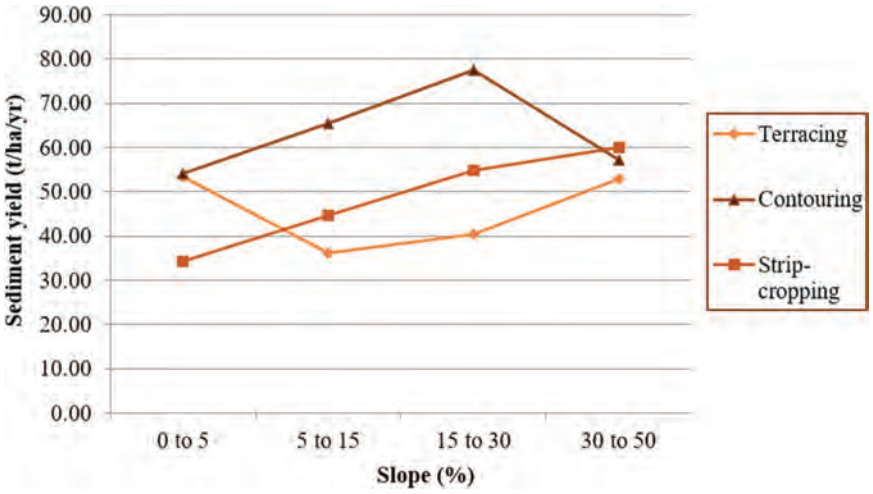

Fig. 5. Impact of agricultural BMPs on the slope.

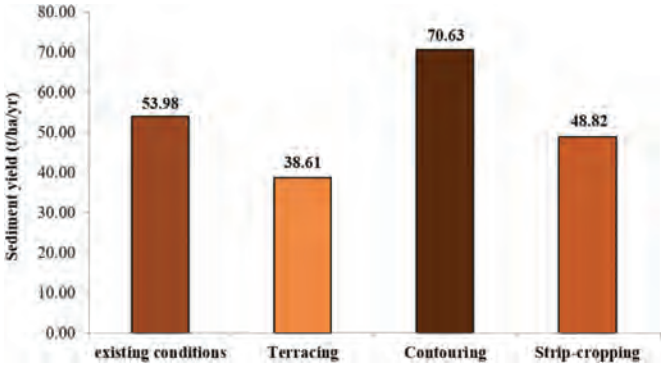

Fig. 6. Average annual sediment yield simulated for each treatment.

terracing is effective to decrease the sediments losses and to limit the soil erosion intensity of the grounds especially at steep slopes. This treatment present a 28% reduction of sediment loss compared to existing conditions. This indicates that the use of parallel terraces on agricultural land can potentially bring significant improvements for the control and limitation of soil erosion.

Moreover, our results corroborate previous similar searches which has been done in different regions of the world by the SWAT model; and who demonstrated that the use of parallel terraces in farmland seems very effective in reducing sediment yield, and therefore, controlling the phenomenon of soil erosion (Arabi et al., 2008; Ayala, Berhanu, & Tolesa, 2017; Betrie et al., 2011; Bracmort et al., 2006; Daggupati, 2012; Mwangi, 2011; Ramos, Benito et al., 2015; Strauch, Lima, Volk, Lorz, & Makeschin, 2013). Other researches showed that the contour significantly reduces sediment loss (Ben Khelifa et al., 2016; Mtibaa et al., 2018; Santhi, Srinivasan, Arnold, & Williams, 2006). In addition to that, this technique was perfectly recommended in the Mediterranean regions in general, to avoid the risk of damage during intense rainfall (Abu Hammad, Borresen, & Haugen, 2006; Durán Zuazo & Rodríguez Pleguezuelo, 2008; Durán Zuazo, Aguilar, Martínez, & Franco, 2005; Roose & Sabir, 2002).

Finally, these techniques allowed us to evaluate the possible management practices most adapted to the actual conditions of

agricultural land in the Kalaya watershed, by aiming simultaneously managing storm water runoff in the basin, trapping eroded land, controlling erosion and sediment reduction, and intensifying agricultural production.

5. Conclusion

In this study, different soil conservation scenarios were simulated and tested with respect to sediment yield using SWAT model. The demonstration study revealed that terracing operation is efficient to decrease soil erosion and the implementation of this soil conservation measures would significantly reduce sediment yields at the outlets of the watershed. Furthermore, the simulation of best management practices (BMPs) by the SWAT model provides us to have an idea on the most effective practice for reducing sediment yield in the watershed. This work will then bring useful information for targeted management and help interested and involved stakeholders in water and soil conservation activities to choose the most appropriate practice for the study area.

References

Aboumaria, K. (2009). Les formations littorales quaternaires de la péninsule de Tanger (Maroc nord occidental): lithostratigraphie, processus sédimentologiques pétrologie et corrélation à l'échelle de la méditerranée centre occidentale. Thèse d'Etat, Université Mohammed V, Rabat, 221 p.

Abu Hammad, H. A., Borresen, T., & Haugen, L. E. (2006). Effect of rain characteristics and terracing on runoff and erosion under the Mediterranean. *Soil and Tillage Research*, *87*, 39–47.

Ananda, J., & Herath, G. (2003). Soil erosion in developing countries: A socio-economic appraisal. *Journal of Environmental Management*, *68*, 343–353.

Anderton, S., Latron, J., & Gallart, F. (2002). Sensitivity analysis and multi-response, multi-criteria evaluation of a physical based distributed model. *Hydrological Processes*, *16*, 333–353.

Arabi, M., Frankenberger, J. R., Engel, B. A., & Arnold, J. G. (2008). Representation of agricultural conservation practices with SWAT. *Hydrological Processes*, *22*(*16*), 3042–3055.

Arnold, J. G., Srinivasan, R., Muttiah, R. S., & Williams, J. R. (1998). Large-area hydrologic modeling and assessment: Part I. Model development. *JAWRA*, *34*(*1*), 73–89.

Arnold, J. G., & Fohrer, N. (2005). SWAT 2000 current capabilities and research opportunities in applied watershed modeling. *Hydrological Processes*, *19*, 563–572.

Ayala, G., Berhanu, S., & Tolesa, O. (2017). Assessing the effect of soil and water conservation practices on runoff and sediment yield on Hunde Lafto watershed of upper Wabi Shebelle Basin. *Civil and Environmental Research*, *9*(*9*), 36–49.

Ben Khelifa, W., Hermassi, T., Strohmeier, S., Zucca, C., Ziadat, F., Boufaroua, M., & Habaieb, H. (2016). Parameterization of the effect of bench terraces on runoff and sediment yield by swat modelling in a small semi-arid watershed in northern Tunisia. *Land Degradation and Development*, *28*(*5*), 1568–1578.

Ben Salah, N. C., & Abida, H. (2016). Runoff and sediment yield modeling using SWAT model: Case of Wadi Hatab basin, central Tunisia. *Arabian Journal of Geosciences*, *9*, 579.

Benmansour, M., Amenzou, N., Zouagui, A., Marah, H., Sabir, M., Nouira, A., … Taous, F. (2014). Assessment of soil erosion and sedimentation rates in My Bouchta watershed in north Morocco using fallout radionuclides and stable isotopes In: L. K. Heng, K. Sakadevan, G. Dercon, & M. L. Nguyen (Eds.), *Managing soils for food security and climate change adaptation and mitigation* (pp. 113–118). Rome: FAO.

Bergstrom, S., Lindstrom, G., & Pettersson, A. (2002). Multi-variable parameter estimation to increase confidence in hydrological modeling. *Hydrological Processes*, *16*, 413–421.

Betrie, G. D., Mohamed, Y. A., Van Griensven, A., & Srinivasan, R. (2011). Sediment management modelling in the Blue Nile Basin using SWAT model. *Hydrology and Earth System Sciences*, *15*, 807–818.

Beven, K. (2006). A manifesto for the equifinality thesis. *Journal of Hydrology*, *320* (1–2), 18–36.

Beven, K. (2012). *Rainfall-runoff modelling: The primer* ((2nd ed.). Chichester: Lancaster University.

Boardman, J., Shepheard, M. L., Walker, E., & Foster, I. D. L. (2009). Soil erosion and riskassessment for on- and off-farm impacts: A test case using the Midhurst area, west Sussex, UK. *Journal of Environmental Management*, *90*, 2578–2588.

Bracmort, K. S., Arabi, M., Frankenberger, J. R., Engel, B. A., & Arnold, J. G. (2006). Modelling long-term water quality impact of structural BMPs. *Transactions of the ASAE*, *49*(*2*), 367–374.

Briak, H., Moussadek, R., Derradji, A., Aboumaria, K., & Mrabet, R. (2016a). Effect of vegetation types on highway erosion in Kalaya basin (North Morocco). *Journal of Materials and Environmental Science*, *7*(*2*), 605–612.

Briak, H., Moussadek, R., Aboumaria, K., & Mrabet, R. (2016b). Assessing sediment yield in Kalaya gauged watershed (Northern Morocco) using GIS and SWAT model. *International Soil and Water Conservation Research*, *4*, 177–185.

Briak, H. (2017). *Estimation de l'Érosion des Sols et Modélisation Hydrologique Spatialisée: Cas d'un Bassin Versant Tangérois au Nord du Maroc (Thèse de doctorat)* (p. 210) Maroc: Université Abdelmalek Essaâdi, Faculté des Sciences et Techniques de Tanger.

Cao, W., Bowden, W. B., Davie, T., & Fenemor, A. (2006). Multi-variable and multi-site calibration and validation of SWAT in a large mountainous catchment with high spatial variability. *Hydrological Processes*, *20*(5), 1057–1073.

Cosentino, S. L., Copani, V., Scalici, G., et al. (2015). Soil erosion mitigation by perennial species under Mediterranean environment. *BioEnergy Research*, *8*, 1538.

Cuceloglu, G., Abbaspour, K. C., & Ozturk, I. (2017). Assessing the water-resources potential of Istanbul by using a soil and water assessment tool (SWAT) hydrological model. *Water*, *9*, 814.

Daggupati, P. (2012). *GIS methods to implement sediment best management practices and locate ephemeral gullies (Ph.D. dissertation)* (p. 161) Manhattan, Kan., USA.: Department of Biological and Agricultural Engineering, Kansas State Univ.

Daggupati, P., Yen, H., White, M. J., Srinivasan, R., Arnold, J. G., Keitzer, C. S., & Sowa, S. P. (2015). Impact of model development, calibration and validation decisions on hydrological simulations in West Lake Erie Basin. *Hydrological Processes*, *29* (26), 5307–5320.

Dakhlalla, A. O., & Parajuli, P. B. (2016). Evaluation of the best management practices at the watershed scale to attenuate peak streamflow under climate change scenarios. *Water Resources Management*, *30*(*3*), 963–982.

Dechmi, F., & Skhiri, A. (2013). Evaluation of best management practices under intensive irrigation using SWAT model. *Agricultural Water Management*, *123*, 55–64.

Durán Zuazo, V. H., Aguilar, R. J., Martínez, R. A., & Franco, D. T. (2005). Impact of erosion in the taluses of subtropical orchard terraces. *Agriculture Ecosystems & Environment*, *107*, 199–210.

Durán Zuazo, V. H., & Rodríguez Pleguezuelo, C. R. (2008). Soil-erosion and runoff prevention by plant covers. A review. *Agronomy for Sustainable Development*, *28*, 65–86.

Duru, U., Arabi, M., & Wohl, E. E. (2017). Modeling stream flow and sediment yield using the SWAT model: A case study of Ankara River basin, Turkey. *Physical Geography*.

El Garouani, A., Chen, H., Lewis, L., Tribak, A., & Abharour, M. (2008). Cartographie de l'utilisation du sol et de l'érosion nette à partir d'images satellitaires et du SIG Idrisi au Nord-Est du Maroc. *Teledetection, Editions Scientifiques GB*, *8*(*3*), 193–201.

Fadil, A., Rhinane, H., Kaoukaya, A., Kharchaf, Y., & Alami Bachir, O. (2011). Hydrologic modeling of the bouregreg watershed (Morocco) using GIS and SWAT model. *Journal of Geographic Information System*, *3*, 279–289.

Fiseha, B. M., Setegn, S. G., Melesse, A. M., Volpi, E., & Fiori, A. (2013). Hydrological analysis of the upper Tiber River Basin, central Italy: A watershed modelling approach. *Hydrological Processes*, *27*, 2339–2351.

Franco, A. C. L., & Bonumá, N. B. (2017). Multi-variable SWAT model calibration with remotely sensed evapotranspiration and observed flow. *RBRH*, *22*, e35.

Galván, L., Olias, M., Fernandez de Villaran, R., Domingo Santos, J. M., Nieto, J. M., Sarmiento, A. M., & Canovas, C. R. (2009). Application of the SWAT model to an AMD-affected river (Meca River, SW Spain) estimation of transported pollutant load. *Journal of Hydrology*, *377*(3–4), 445–454.

Gassman, P. W., Reyes, M. R., Green, C. H., & Arnold, J. G. (2007). The soil and water assessment tool: Historical development, applications, and future research directions. *Transactions of the ASABE*, *50*(4), 1211–1250.

Grimm, M., Jones, R., & Montanarella, L. (2002). *Soil erosion risk in Europe*. Luxembourg: Office for Official Publications of the European Communities.

Hallouz, F., Meddi, M., Mahé, G., Alirahmani, S., & Keddar, A. (2018). Modeling of discharge and sediment transport through the SWAT model in the basin of Harraza (Northwest of Algeria). *Water Science*, *32*, 79–88.

Heusch, B. (1970). L'érosion du pré-Rif, une étude quantitative de l'érosion hydraulique dans les collines marneuses du pré-Rif Occidental. *Annales Recherches Forestières Délután Marocain*, *12*, 1–176.

Hudson, N. W. (1991). A study of the reasons for success or failure of soil conservation projects. *FAO Soils Bulletin*, *64*, 65.

Iaaich, H., Moussadek, R., Baghdad, B., Mrabet, R., Douaik, A., Derradji, A., & Bouabdlid, A. (2016). Soil erodibility mapping using three approaches in the Tangiers province–Northern Morocco. *International Soil and Water Conservation Research*, *4*, 159–167.

Kefi, M., Yoshino, K., Setiawan, Y., Zayani, K., & Boufaroua, M. (2011). Assessment of the effects of vegetation on soil erosion risk by water: a case study of the Batta watershed in Tunisia. *Environmental Earth Sciences*, *64*, 707–719.

Lahmar, R., & Ruellan, A. (2007). Dégradation des sols et stratégies coopératives en Méditerranée: La pression sur les ressources naturelles et les stratégies de développement durable. *Cahiers Agricultures*, *16*(*4*), 318–323.

Le Bissonnais, Y., Blavet, D., Noni, G., Laurent, J., Asseline, J., & Chenu, C. (2007). Erodibility of mediterranean vineyard soils: Relevant aggregate stability methods and significant soil variables. *European Journal of Soil Science*, *58*, 188–195.

Logan, T. J. (1993). Agricultural best management-practices for water-pollution control - Current issues. *Agriculture Ecosystems & Environment*, *46*(1–4), 223–231.

Merzouk, A., & Dahman, H. (1998). Shifting land use and its implication on sediment yields in the Rif Mountains (Morocco). *Advanced in Geoecology*, *31*, 333–340.
Molina-Navarro, E., Andersen, H. E., Nielsen, A., Thodsen, H., & Trolle, D. (2017). The impact of the objective function in multi-site and multi-variable calibration of the SWAT model. *Environmental Modelling & Software*, *93*, 255–267.
Moss, B. (2008). Water pollution by agriculture. *Philosophical Transactions of the Royal Society B*, *363*, 659–666.
Moussadek, R., Mrabet, R., Zante, P., Lamachère, J. M., Pépin, Y., Le Bissonnais, Y., … et Van Ranst, E. (2011). Effets du travail du sol et de la gestion des résidus sur les propriétés du sol et sur l'érosion hydrique d'un Vertisol Méditerranéen. *Canadian Journal of Soil Science*, *91*, 627–635.
Mrabet, R., Ibn Namr, K., Bessam, F., & et Saber, N. (2001). Soil chemical quality changes organic matter and structural stability of a Calcixeroll soil under different wheat rotation and tillage systems in a semiarid area of Morocco. *Land Degradation and Development*, *12*, 505–517.
Mtibaa, S., Hotta, N., & Irie, M. (2018). Analysis of the efficacy and cost-effectiveness of best management practices for controlling sediment yield: A case study of the Joumine watershed, Tunisia. *Science of the Total Environment*, *616–617*, 1–16.
Mwangi, H. (2011). Evaluation of the impacts of soil and water conservation practices in Sasumua services in Sasumua watershed, Kenya, using SWAT model.
Neitsch, S. L., Arnold, J. G., Kiniry, J. R., & Williams, J. R. (2005). *Soil and water assessment tool theoretical documentation, version 2005*. Grassland, Soil and Water Research Laboratory - Agricultural Research Service. Blackland Research Center-Texas Agricultural Experiment Station.
Neitsch, S. L., Arnold, J. G., Kiniry, J. R., & Williams, J. R. (2011). *Soil and water assessment tool theoretical documentation version 2009*. College Station (Texas).: Texas A&M University System, College Station (Texas) (Texas Water Ressources Institute Technical Report 406).
Panagos, P., Borrelli, P., Poesen, J., Ballabio, C., Lugato, E., Meusburger, K., … Alewell, C. (2015). The new assessment of soil loss by water erosion inEurope. *Environmental Science & Policy*, *54*, 438–447.
Pimentel, D., Harvey, C., Resosudarmo, P., Sinclair, K., Kurz, D., McNair, M., et al. (1995). Environmental and economic costs of soil erosion and conservation benefits. *Science*, *267*, 1117–1123.
Pimentel, D., & Burgess, M. (2013). Soil erosion threatens food production. *Agriculture*, *3*, 443–463.
Pisinaras, V., Petalas, C., Gikas, G. D., Gemitzi, A., & Tsihrintzis, V. A. (2010). Hydrological and water quality modeling in a medium-sized basin using the soil and water assessment tool (SWAT). *Desalination*, *250*, 274–286.
Portenga, E. W., & Bierman, P. R. (2011). Understanding earth's eroding surface with 10Be. *GSA Today*, *21*, 4–10.
Ramos, M. C., & Martínez-Casasnovas, J. A. (2009). Impacts of annual precipitation extremes on soil and nutrient losses in vineyards of NE Spain. *Hydrological Processes*, *23*, 224–235.
Ramos, M. C., & Martínez-Casasnovas, J. A. (2015). Soil water content, runoff and soil loss prediction in a small ungauged agricultural basin in the Mediterranean region using the Soil and Water Assessment Tool. *Journal of Agricultural Science*, *153*, 481–496.
Ramos, M. C., Benito, C., & Martínez-Casasnovas, J. A. (2015). Simulating soil conservation measures to control soil and nutrient losses in a small, vineyard dominated, basin. *Agriculture Ecosystems & Environment*, *213*, 194–208.
Rollo, N. (2012). *Modélisation des dynamiques de pollution diffuse dans le bassin versant de la rivière d'Auray (Thèse de doctorat)* (p. 396) France: Université de Nantes.
Roose**,** É. (1994). Introduction à la gestion conservatoire de l'eau, de la biomasse et de la fertilité des sols(GCES). Bulletin pédologique de la FAO n°70, Rome. 420 p.
Roose, É., & Sabir, M. (2002). Strategies traditionnellles de conservation de l'eau et des sols dans le bassin mediterraneen: classification en vue d'un usage renouvelle. *Bulletin Reseau Erosion*, *21*, 33–44.
Sabir, M., & Roose, É. (2004). Influence du couvert végétal et des sols sur le stock de carbone et les risques de ruissellement et d'érosion dans les montagnes méditerranéennes du Rif occidental, Maroc. *Bulletin Délután Réseau Érosion*, *23*, 144–154.
Santhi, C., Arnold, J., Williams, J., Dugas, W., & Hauck, L. (2001). Validation of the SWAT model on a large river basin with point and nonpoint sources. *Journal of the American Water Resources Association*, *37*, 1169–1188.
Santhi, C., Srinivasan, R., Arnold, J. G., & Williams, J. R. (2006). A modeling approach to evaluate the impacts of water quality management plans implemented in a watershed in Texas. *Environmental Modelling & Software*, *21*(*8*), 1141–1157.
Serpa, D., Nunes, J. P., Santos, J., Sampaio, E., Jacinto, R., Veiga, S., … Abrantes, N. (2015). Impacts of climate and land use changes on the hydrological and erosion processes of two contrasting Mediterranean catchments. *Science of the Total Environment*, *538*, 64–77.
Strauch, M., Lima, J. E. F. W., Volk, M., Lorz, C., & Makeschin, F. (2013). The impact of best management practices on simulated streamflow and sediment load in a Central Brazilian catchment. *Journal of Environmental Management*, *127*, S24–S36.
Sun, X., Bernard-Jannin, L., Garneau, C., Volk, M., Arnold, J. G., Srinivasan, R., … Sánchez-Pérez, J. M. (2016). Improved simulation of river water and groundwater exchange in an alluvial plain using the SWAT model. *Hydrological Processes*, *30*, 187–202.
Tuo, Y., Duan, Z., Disse, M., & Chiogna, G. (2016). Evaluation of precipitation input for SWAT modeling in Alpine catchment: A case study in the Adige river basin (Italy). *Science of the Total Environment*, *573*, 66–82.
Walter, M. F., Steenhuis, T. S., & Haith, D. A. (1979). Nonpoint source pollution-control by soil and water conservation practices. *Transactions of the Asae*, *22*(*4*), 834–840.
White, K., & Chaubey, I. (2005). Sensitivity analysis, calibration, and validations for a multisite and multivariable SWAT model. *Journal of the American Water Resources Association*, *41*, 1077–1089.
Wu, Y., & Chen, J. (2012). Modeling of soil erosion and sediment transport in the East River Basin in southern China. *Science of the Total Environment*, *44*, 159–168.
Wu, H., Liu, Y., Liu, J., & Zhu, A. (2014). Representation of agricultural Best management practices in a fully distributed hydrologic model: A case study in the Luoyugou watershed. *Journal of Resources and Ecology*, *5*(*2*), 179–184.
Xie, H., Chen, L., & Shen, Z. (2015). Assessment of agricultural best management practices using models: Current issues and future perspectives. *Water*, *7*, 1088–1108.
Yaalon, D. (1997). Soils in the Mediterranean region: What makes them different? *Catena*, *28*, 157–169.
Yang, D. W., Kanae, S., Oki, T., Koike, T., & Musiake, K. (2003). Global potential soil erosion with reference to land use and climate changes. *Hydrological Processes*, *17*, 2913–2928.
Yang, Q., Zhao, Z., Benoy, G., Chow, T. L., Rees, H. W., Bourque, C. P.-A., & Meng, F.-R. (2010). A watershed-scale assessment of cost-effectiveness of sediment abatement with flow diversion terraces. *Journal of Environmental Quality*, *39*, 220.
Zettam, A., Taleb, A., Sauvage, S., Boithias, L., Belaidi, N., & Sánchez-Pérez, J. (2017). Modelling hydrology and sediment transport in a semi-arid and anthropized catchment using the SWAT model: The case of the Tafna river (northwest Algeria). *Water*, *9*, 216.
Zhou, J., Fu, B., Gao, G., Lü, Y., Liu, Y., Lü, N., & Wang, S. (2016). Effects of precipitation and restoration vegetation on soil erosion in a semi-arid environment in the Loess Plateau, China. *Catena*, *137*, 1–11.

International Soil and Water Conservation Research 7 (2019) 184–195

Contents lists available at ScienceDirect

International Soil and Water Conservation Research

journal homepage: www.elsevier.com/locate/iswcr

Original Research Article

Postglacial incision-infill cycles at the Borisoglebsk Upland: Correlations between interfluve headwaters and fluvial network

Yuliya V. Shishkina [a], Ekaterina V. Garankina [a,*], Vladimir R. Belyaev [a], Ilya G. Shorkunov [b], Pavel V. Andreev [c], Aleksey I. Bondar [a], Viktoria I. Potapova [a], Tatiana A. Verlova [c]

[a] Faculty of Geography, Department of Geomorphology and Palaeogeography and Laboratory for Soil Erosion and Fluvial Processes, Lomonosov Moscow State University, Leninskie Gory, 1, Moscow 119991, Russia
[b] Institute of Geography, Department of Soil Geography and Evolution, Russian Academy of Sciences, Staromonetnyj Lane, 29, Moscow 119017, Russia
[c] Institute of Earth Sciences of Saint-Petersburg State University, St. Petersburg, Universitetskaya nab. 7-9 199034, Russia

ARTICLE INFO

Article history:
Received 24 August 2018
Received in revised form
6 January 2019
Accepted 1 February 2019
Available online 20 February 2019

Keywords:
Interfluve headwaters
Fluvial
Incision-Infill Cycle
Pleistocene

ABSTRACT

The article discusses postglacial landscape transformation in the Northern Hemisphere Middle Pleistocene glaciation area located in the center of the Russian Plain. We attempted to verify the regional paleogeographic model by reconstructing the Late Pleistocene incision-infill cycles at the Eastern Borisoglebsk Upland based on a comparison of inactive interfluves headwaters and actual fluvial network palaeoarchives. The study was also aimed to determine the past extent of fluvial systems. Interdisciplinary research of the actual and buried topography, lithology and pedogenic properties of surface deposits was carrid out with remote sensing data interpretation, DGPS survey, and detailed description of geological cores involved. The study was followed by analysis of grain size, chemical and organic contents, microstructure, and numerical dating. Integrating the available results, we propose a scenario of the fluvial network transformation at the Eastern Borisoglebsk Upland over the last 150 ka. At least four fluvial incision stages were determined while network extent has significantly changed through the Late Pleistocene. Three can be generally associated with the regional base level decrease – Late Moscow, Late Valdai and Late Holocene and accompanying isolation of the Nero Lake terraces of 130 m, 100–105 m and 95–98 m. Incision stages were separated by landscape stability or aggradation periods those were asynchronous at the middle and upper parts of the fluvial network. The main agent of initial valley infill appears to be local lacustrine sedimentation altered by alluvial and colluvial deposition towards the second half of Valdai. Revealed landscape conditions variability emphasize the importance of comprehensive local correlations for regional retrospective models.

1. Introduction

The article concerns one of the numerous uplands of the Northern Hemisphere Pleistocene glaciation area. Postglacial history of its heterogeneous fluvial network reflects specific changes in leading development agents. The latter ones are known to leave many relic features in modern valley systems including excessive width inconsistent with present runoff conditions, highly elevated terraces, and thick bottom sedimentary infills partially incised by modern gullies, headwaters almost infilled and disconnected with the actual fluvial network. Such distinct footprints can be related to much higher intensities of fluvial and associated processes in the past and hold the key to better understanding of the landscape evolution of previously glaciated plains.

Located in the central part of the Russian Plain (Fig. 1A), Borisoglebsk Upland is one of a set of uplands of the Moscow (Saalian) glaciation marginal zone (Semenov, Tsukurova, Kvyatkovskaya, & Kuznetsov, 1972) where the phase of uninterrupted fluvial network evolution is limited to the later glacial-interglacial climatic cycle (Astakhov, Shkatova, Zastrozhnov, & Chuyko, 2016; Hughes, Gyllencreutz, Lohne, Mangerud, & Svendsen, 2016, etc.). Supposedly, erosion network has predominantly inherited widely distributed gently sloped meltwater depressions. The density of the

* Corresponding author.
E-mail addresses: ula.shishkina@mail.ru (Y.V. Shishkina), evgarankina@gmail.com (E.V. Garankina), vladimir.r.belyaev@gmail.com (V.R. Belyaev), shorkunov@gmail.com (I.G. Shorkunov), pavelvandreev86@gmail.com (P.V. Andreev), alekseybondar@outlook.com (A.I. Bondar), V1234567890ika@yandex.ru (V.I. Potapova), tatiana.verlova@gmail.com (T.A. Verlova).
Peer review under responsibility of International Research and Training Center on Erosion and Sedimentation and China Water and Power Press.

https://doi.org/10.1016/j.iswcr.2019.02.001

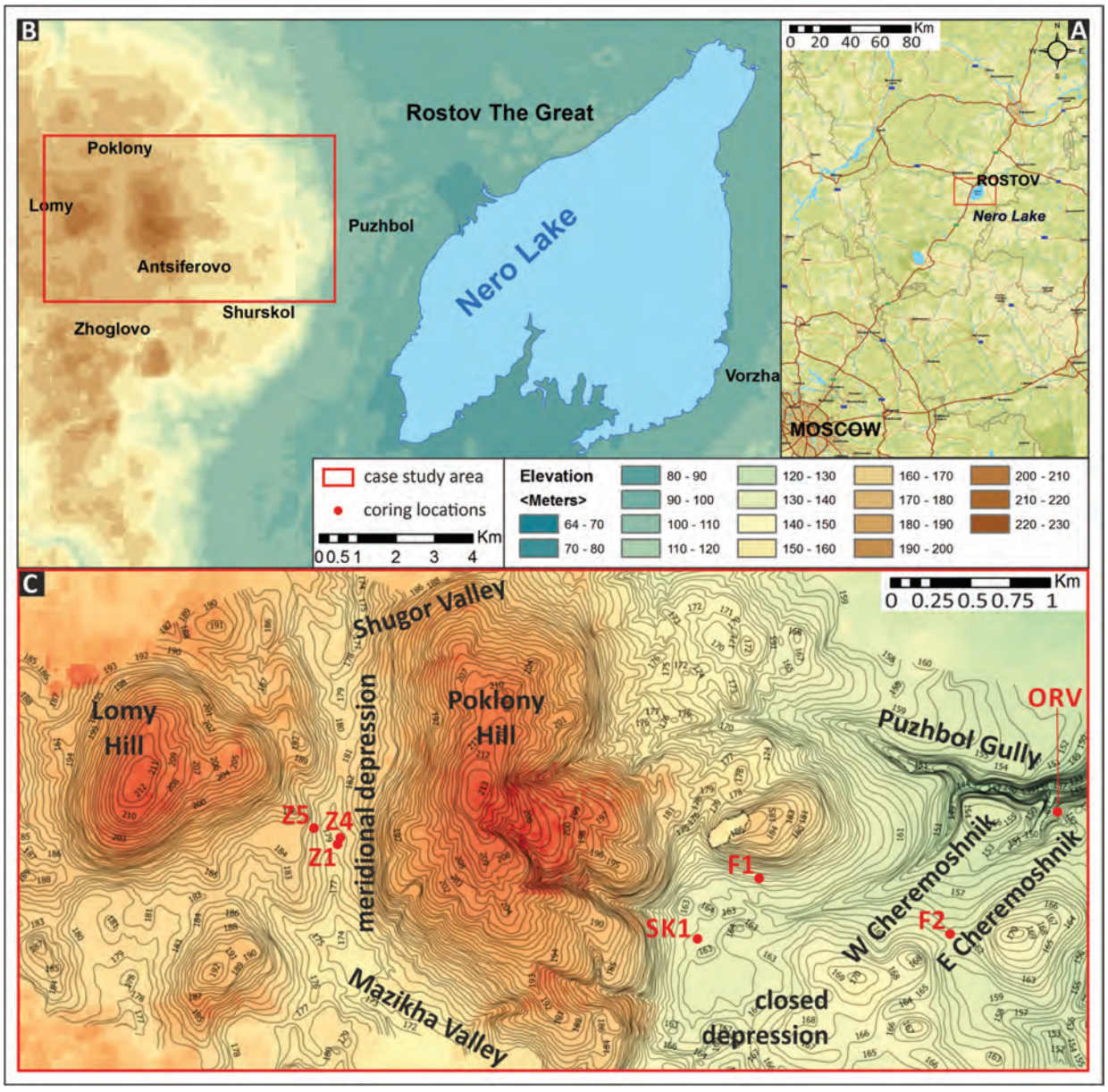

Fig. 1. Position of the case study area: A - at the Central Russian Plain (source: Google global topography, infrastructure and settlements), and B - at the Eastern Borisoglebsk Upland (source: ALOS 3D 30 m); C - its detailed topography based on 1: 10,000 land planning maps (contour interval 1 m).

glaciofluvial network and its penetration into the interfluves significantly exceeded those of modern fluvial systems, as reported for other areas within the marginal zones of the Late Pleistocene glaciations (Belyaev, Grigorieva, Sycheva, & Sheremetskaya, 2008; Belyaev, Panin, & Belyaev, 2003; Eremenko, Panin, & Karevskaya, 2010). However, the relationship and share of both meltwater and fluvial agents in the modern geomorphic structure are unresolved as the role of local and regional base level shifts since the end of the Middle Pleistocene.

It is essential to bear in mind that fluvial responses to climate change may be geographically circumscribed, nondeterministic and nonlinear (Blum & Tornquist, 2000). For example, larger river alluvial sequences of northwestern Europe show significant similarities: main aggradation events correlate with cold periods (Pleniglacial and Lateglacial), whereas erosional phases occurred at the warm-to-cold transitions, and secondarily at the Pleniglacial–Lateglacial transitions, especially since the Upper Saalian (Cordier, Harmand, Frechen, & Beiner, 2006). Footprints of deep incisions at the onset of the Last Glacial are reported for the Dnieper River in the westerly-aligned reach upstream from the Russia/Belarus border. Those are considered to have been caused by valley tilting associated with the growth of glacial forebulge (Panin, Adamiec, & Filippov, 2015). Additional evidence of strikingly different landscape conditions profoundly influencing water runoff formation in periglacial or transitional periods comes from the widespread distribution of enlarged palaeochannels over the Central Russian Plain (Panin et al., 2017; Starkel et al., 2015). Authors suggest that their formation was associated with short-term but dramatic increases of surface runoff during snowmelt periods, especially during rapid degradation of permafrost. At the same time, smaller fluvial systems could show different behaviour, as shown by studies in Poland where the Vistula River tributaries development within the Warsaw Basin was controlled mainly by mutual relation of the ice-dammed lake and ice marginal spillways, both being essential fragments of a widespread drainage network in the Central European Lowland (Marks, 2004; Starkel, 1991).

Although surface water erosion is one of the most well-studied processes, the absolute majority of available data are associated

with soil erosion on cultivated lands. Natural erosion rates have not been investigated in such details. In the areas covered by loesses and loessy-loams drifts, a minimum velocity of the entraining runoff is reported to move silt-clay soil particles (Piest & Spomer, 1968). Soil erosion rates under undisturbed natural forest or even grass cover are reported to be 2–3 order of magnitude lower (e.g., Pederson, Petersen, & Dierker, 2006) than those observed at present on conventionally cultivated lands (Panagos et al., 2015) and are generally negligible for geomorphic landscape modification. Therefore, long-term variability of natural rates of water erosion (as well as mass wasting hillslope processes as creep and solifluction) can be closely related to vegetation successions in general and events such as natural fires in particular (Montgomery, 2007). In order to reconstruct erosion rates variability over timescales of glacial-interglacial cycles as regarded in this study, it is necessary to consider landscape changes from periglacial to non-periglacial environments. Until recently, limited data have been available on natural rates of soil production or long-term geological erosion rates. Progress in dating techniques, however, helped to discover the elevated Late Pleistocene erosion rate in comparison to the Holocene for Mid-European rivers (Schaller et al., 2002), which may be apparently attributed primarily to periglacial – non-periglacial transition.

Regarding gully development, its initial incision can start at any location within a drainageway where gradients or local vegetation disturbances permit sufficient concentration of runoff exceeding the surface critical shear stress (Poesen, Nachtergaele, Verstraeten, & Valentin, 2003; Poesen, Torri, & Vanwalleghem, 2011). Gully growth is then continued by upstream movement of the knickpoint overfall, channel degradation, and its lateral enlargement by eroded bank collapses or slides (Piest & Spomer, 1968). In earlier investigations for the USA loessial region, Thompson (1964) found that the square root of watershed size correlates well with gully growth rate. Beer and Johnson (1963) included an index of surface runoff and the distance from gully head to watershed divide in an equation to estimate areal changes in a gully with time. Leopold, Wolman, and Miller (1964) consider the moisture in the substratum before and during the runoff formation periods. It is evident from the integration of large dataset of long-term studies from practically all over the World (Vanmaercke et al., 2016) that gully head retreat and incision rates are best correlated with headcut-contributing catchment area, gradient and geomorphic position of a gully head (e.g., Vandekerckhove, Poesen, Oostwoud Wijdenes, & Gyssels, 2001; Vandekerckhove, Poesen, & Govers, 2003). However, it is extremely important, in the case of gully erosion as essentially a cycling process, to consider the stage of its development (Sidorchuk, Marker, Moretti, & Rodolfi, 2003). Analyzing a large dataset collected in Russia, it has been found that for different landscape conditions, lithologies and slope gradients critical minimum headcut-contributing catchment areas can be calculated, and that permafrost or at least thick active layer substantially decrease the above threshold value for gully initiation (Panin, Fuzeina, & Belyaev, 2009). It is, however, very difficult to switch from gully initiation thresholds to actual headcut retreat and incision rates, as the latter two are controlled by a number of geomorphic variables discussed above and, also, being subject to strong effects of climatic variability and weather seasonality.

Therefore, for predominantly forested landscapes under undisturbed conditions rates of both sheet and linear erosion are negligible. Specific local catastrophes as forest fires or larger weather extremes such as a 1000-year flood reported in historical documents for July 1342 throughout Central Europe (Dreibrodt, Lubos, Terhorst, Damm, & Bork, 2010) are required to temporarily remove or exceed the vegetation protection threshold in a fluvial system. Over geological timescales, the onset of periglacial conditions was another important trigger of longer-term increase of both erosion and mass wasting rates. We believe that paleoerosional reconstruction as attempted in this study can shed additional light on longer-term landscape drivers of soil and gully erosion, which cannot be fully recognized from the ongoing monitoring programs as some of the paleoenvironments have no present analogues.

Continual slope deposits cover substantial parts of Mid-Latitude landscapes. To explain its diversity and provenance, a concept of Cover Beds was introduced initially for Low Mountain slopes at the Central and Western Europe (Kleber & Terhorst, 2013; Kleber, 1997) and now is successively employing in Europe (Döhler, Terhorst, Frechen, Zhang, & Damm, 2017; Reinhardt-Imjela, Maerker, Schulte, & Kleber, 2018) and even USA Low Mountains regions (Krautz, Gärtner, Hofmann, Linnemann, & Kleber, 2018). The approach presumes gradual slope deposits redeposition downward while admixture of the eolian silty component is significant especially under relict periglacial conditions. Unfortunately, there are no prominent investigations that use the periglacial cover beds concept for extensive plain areas such as the Russian Plain. Nonetheless, there is an interesting attempt to regard specific bipartite sediments forming on top of terraces and some interfluves in the Upper Volga region as a pedocomplex of the basal and upper layer of periglacial cover beds (Makeev et al., 2017).

Most of the landscape development reconstructions at the previously glaciated plains are strongly biased towards understanding fluvial sediment sequences, landforms, and corresponding incision-infill cycles based entirely on a specific type of paleoarchives – various depression infills (Alyoshinskaya & Gunova, 1997; Auslender, 1966; Lowe & Walker, 1998; Velichko et al., 1994; Wohlfarth et al., 2006; Velichko, 2012, etc.). The Upper Volga region has been thoroughly described by more than 20 sections of Quaternary deposits forming a stratigraphic framework for reconstructing postglacial landscape evolution (Aleksandrovskij, 2011; Gey, Saarnisto, Lunkka, & Demidov, 2001; Lavrushin & Chistyakova, 2001; Novskij, 1975; Semenov et al., 1972; Sudakova et al., 2014; Rusakov et al., 2015, 2019, etc.). Nonetheless, they are mainly derived from scattered geological sites exposed in the lower reaches of modern valleys and lake sedimentary sequences while vast adjacent watershed areas remain uninvestigated. However, being initially a part of the fluvial network, the actual interfluves have also undergone some drastic environmental changes, yet in much lower-energy settings. Those alterations are reflected in complex sedimentary sequences unexposed by modern erosion but well preserved in currently dry valley headwaters and closed depressions (Kołodyńska-Gawrysiak & Chabudziński, 2014).

Thus, local retrospective models lacking such a substantial landscape component and source of paleogeographic information are directly extrapolated on a regional scale. That causes inaccuracies in both temporal and spatial frameworks of reconstructed events additionally unsupported by reliable and comparable instrumental dating.

So the primary goal of this research is an attempt to verify the regional paleogeographic model by reconstructing the Late Pleistocene incision-infill cycles at the case study area based on a comparison of both inactive interfluves headwaters and actual fluvial network paleoarchives. Therefore, a thorough investigation of gullies and adjacent dry valley headwaters has been accomplished at the Eastern Borisoglebsk Upland that allowed establishing potential stratigraphic markers for correlating the Late Pleistocene history of different parts of the fluvial network.

2. Materials

Borisoglebsk Upland landscapes are traditionally considered as a glacial plain moderately reworked by superimposed, primarily

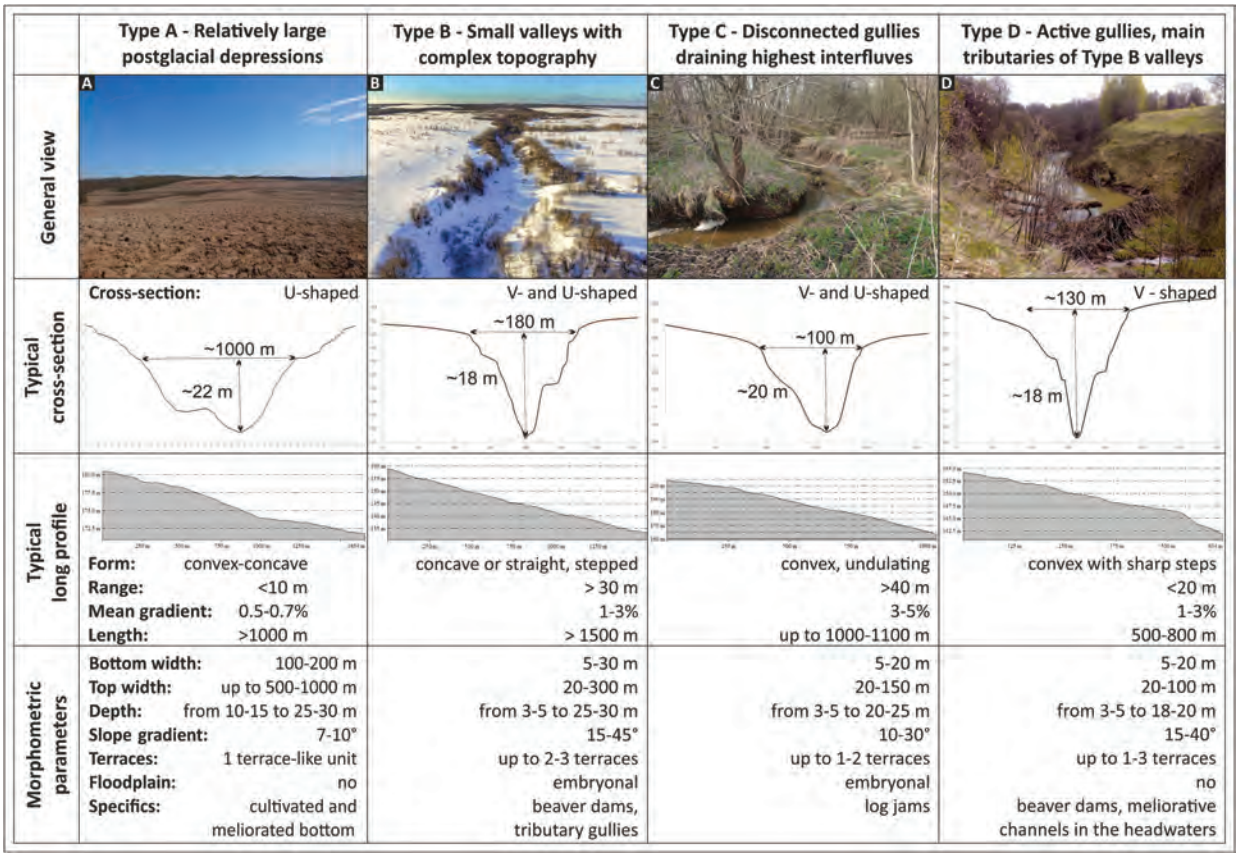

Fig. 2. Types of linear depressions and their morphologic patterns at the Eastern Borisoglebsk Upland. Cross-section and longitudinal profiles are drawn not to scale. *Photos:* A - gently sloped partially infilled meridional depression (by A. Vergun); B - small fluvial Shugor Valley with high accumulative terraces on the sides (by M. Ivanov); C - small actual incisions at the interfluve slopes; D - deeply incised West Cheremoshnik Gully with a fresh beaver dam.

glaciofluvial and erosional, processes (Novskij, 1975; Semenov et al., 1972; Sudakova, Antonov, & Vvedenskaya, 2013). At the case study area (Fig. 1B), most elevated (up to 214 m a.s.l.) interfluves and regional base level (Nero Lake, 93 m a.s.l.) are closely positioned determining a specific structure of the fluvial net (Garankina et al., 2018). Several distinct steps on valley sides (Fig. 2B) indicate potentially multiple incision-infill cycles. Notably, most of them do not respond to regular gully terraces and have a relic, potentially, meltwater origin.

The ORV section at the East Cheremoshnik Gully (Fig. 1C) is one of the main reference sites for general paleogeographic reconstructions in the Upper Volga region, well-studied since 1930-s (Lavrushin & Chistyakova, 2001; Moskvitin, 1976; Rusakov et al., 2015, 2019; Sudakova et al., 1977, etc.). Albeit it reflects confined conditions of partially filled local depression, and genetic and stratigraphic interpretation of the exposed sequences remains questionable.

The modern gully cuts down to the glacial till revealing several overlying layers about 7 m thick on its right side. Main sedimentary units (Fig. 3A) from bottom up are: i) 2.6 m thick gyttja with thin (0.1 m) laminated clays layer at the bottom (Fig. 3J) and peat lenses with well-preserved wooden remnants at the upper part (Fig. 3I) that was commonly attributed to the Early Mikulino (Eemian) interglacial, according to series of palynological investigations (Moskvitin, 1976; Sudakova et al., 1977, etc.); ii) silts and loams with boulders and gravels (up to 1–1.3 m thick) of problematic origin occasionally interpreted either as the Early Valdai (Early Weichselian) glacial till (Moskvitin, 1976; Sudakova, 2008) or slope deposits derived from the older Moscow till (Chebotaryova et al., 1977); iii) gravelly lenses (0.2–0.5 m thick); and iv) loess-like (mantle) loams (1.5 m thick) (Fig. 3H).

Detailed geological structure, pedogenic features, and numerical ^{14}C and U-Th dating of the section have been reported lately by Rusakov et al. (2015), Sedov, Rusakov, Sheinkman, and Korkka (2016), Rusakov et al. (2019). Series of buried organic-rich layers were identified as paleosols. Peat-dark humus paleosol (Fig. 3A) marks incipient subaerial pedogenesis on the erosive upper contact of the Moscow till and is dated to the onset of the Mikulino (MIS5e) by U-Th method (121–144 ka). Peat horizon (Histosol) in the overlying gyttja had supposedly formed later during the Mikulino (114 and 115 ka) while the upper part of gyttja is referred to the Early-Middle Valdai (46 ka cal BP near the upper limit). Within the overlying loamy sequence, paleosols were attributed to the Valdai unit (from bottom to top): i) Reductaquic Cryosols – Bryansk pedocomplex (MIS3, 41.8–27.5 ka cal BP); ii) Gleyic Turbic Cryosol – Trubchevskaya paleosol (MIS2, 19.8 ka cal BP) and iii) pedosediment formed at the end of the BÖlling interstadial (MIS2, 15.0 ka cal BP).

An additional set of geological cores (Fig. 3A) was obtained during the 2016–2017 fieldworks in the dry headwaters of the Mazikha River valley (Z1, Z4, Z5) and several closed (SK1, F1) and open (F2) depressions at the case study area (Fig. 1C). For paleogeographic reconstructions, we consider those sites an informative addition to the previous research data, which were mainly limited to the lower parts of the fluvial network.

3. Methods

In an attempt to reconstruct the past extent, density, and distribution of fluvial systems and to correlate incision-infill cycles in their presently dynamic and inactive parts, interdisciplinary

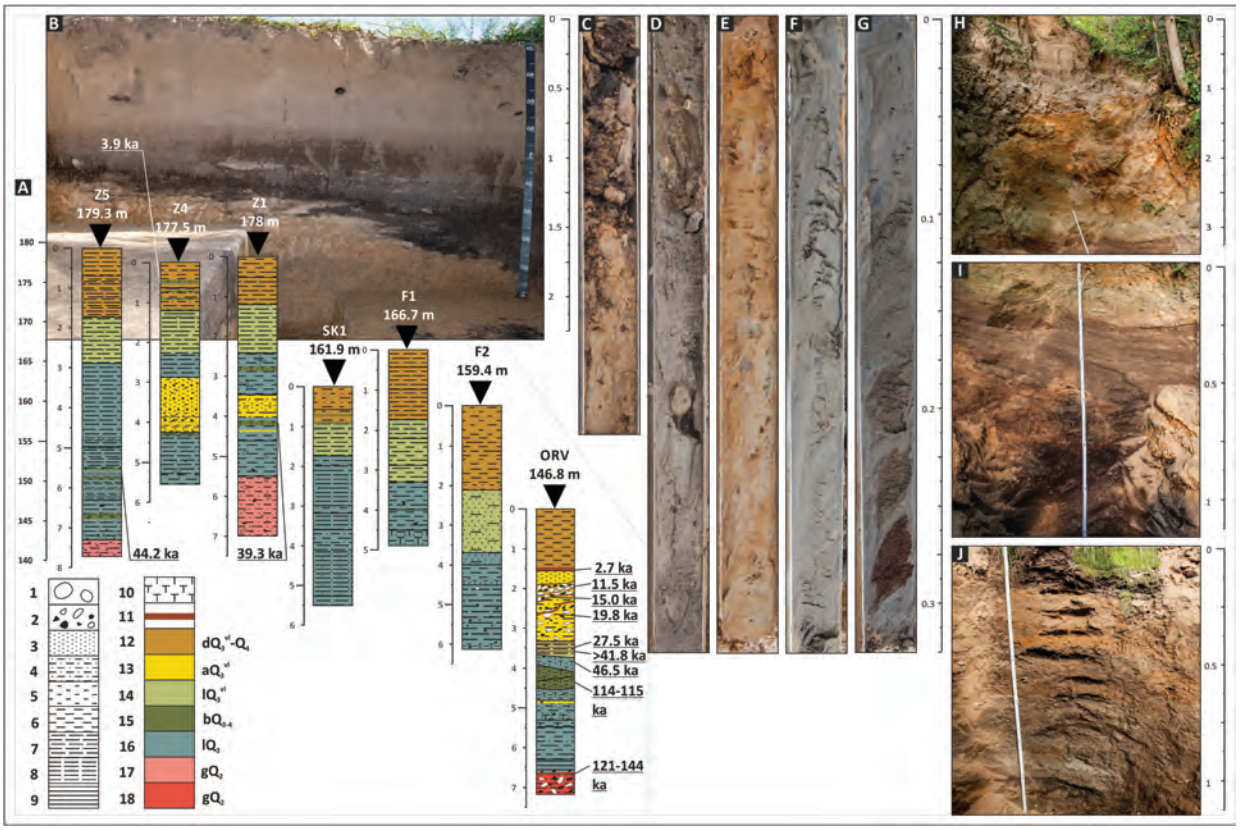

Fig. 3. Sedimentary sequence of valley infills: A - geological scheme of studied cores and cross-section (^{14}C and U-Th dates of the ORV section after Rusakov et al., 2019; also see Table 1); Holocene and Late Valdai cover beds on the side of the Puzhbol Gully (B) and meridional depression (C); D - alluvium (core Z4); Late Valdai (E) and uncertain Middle Valdai-Mikulino (F-G) lacustrine sediments (cores SK1 and Z5); H-J - ORV cross-section (from top to bottom) at the East Cheremoshnik Gully. Vertical scales in meters. *Lithologic features:* 1 – boulders, 2 – angular and rounded gravels and pebbles, 3 – sands, 4 – loamy sands, 5 – sandy loams, 6 – loams, 7 - clayey loams, 8 – silts, 9 – clays, 10 – peat, 11 – paleosols. *Genetic and stratigraphic interpretation:* 12 – Late Valdai - Holocene cover beds (MIS2-MIS1), 13 – Valdai alluvial sediments (MIS3-MIS2), 14 – Late Valdai lacustrine deposits (MIS2), 15 – peat deposits, 16 – Mikulino-Middle Valdai lacustrine sediments (MIS5e-MIS4), 17 – Late Pleistocene glacial tills with texturally differentiated (during MIS5e) paleosol features, 18 – Late Pleistocene glacial till (MIS6).

research of the actual and buried topography of incisive and accumulative units, lithology and pedogenic properties of depression infills has been carried out. Methodologically the research is based on a concept of hierarchical multiscale approach wherein entire set of objects is consistently examined on four general scales: macro- (10^{-1}-10^{3} m), meso- (10^{-4}-10^{-1} m), micro- (10^{-6}-10^{-3} m) and submicro- (10^{-8}-10^{-6} m). The hierarchical approach combines morphological and analytical investigations of a solid phase of sediments and pedofeatures with a specific set of independent methods on each scale. Open-source remote sensing data including satellite imagery DigitalGlobe/GeoEye (Google Earth service), IRS and LANDSAT (Yandex Maps service) and global satellite radar DEMs (SRTM and ALOS 3D), small-scale land planning topographic maps (1: 10,000) and aerial photography obtained by unmanned aerial vehicles DJI Phantom III were used at different scales for the detailed geomorphological evaluation of the area. Remote sensing data interpretation helped to outline the extent of different incision stages of the fluvial network and its inner relationships with locally closed depressions and the main Nero Lake base level. Geological cores (3 cm in diameter) were hand-drilled down to 5–7.5 m from daylight surface. Core positions were obtained by post-processing differential GNSS survey with Leica GX 1200 base-rover complex achieving horizontal error typically $< \pm 2$ cm and vertical $< \pm 10$ cm.

Preliminary textural and structural description of cores' vertical cross-sections was performed in the field supplemented by irregular sampling with 5–10 cm interval, taking into account sedimentary and pedogenic features variability. It was followed by comprehensive lithological and micromorphological analyses. Grain size analysis involved standard sample preparation (Konert & Vandenberghe, 1997; Konstantinov & Eremenko, 2012), dry sieving separation of the coarser fractions (> 100??m) with sieve shaker Fritsch Analysette 3 PRO and laser diffractometry of the finer component (< 100??m) with Fritsch Analysette Nanotek 22 at the Laboratory of Experimental and Dynamic Geomorphology and Paleogeography, MSU, Russia. Organic and chemical contents were estimated by the standard approach of successive weight losses on ignition at 500 °C and 900 °C (Heiri, Lotter, & Lemcke, 2001). Structural organization of sedimentary bodies and pedogenic features were examined using macro photography in reflected light, scanning electron microscopy with JEOL-6610-LV and energy dispersive spectrometry with Oxford INCA Energy at the Laboratory of Radiocarbon Dating and Electronic microscopy, IG RAS, Russia. Additionally, numerical dating of the three organic-rich (with peat lenses and plant detritus) samples from three neighboring cores at the meridional depression was conducted using ^{14}C AMS method at the Laboratory of Radiocarbon Dating and Electronic microscopy, IG RAS, Russia, and Center for Applied Isotope Studies, University of Georgia, USA. Results were calibrated with radiocarbon calibration program CALIB REV7.1.0.

4. Results

General ridge-hilly glacial topography of the Eastern Borisoglebsk Upland is represented by large elevated (214–160 m a.s.l., 25–50 m relative) flat-topped hills with comparatively steep slopes and less prominent but more widespread rounded hills with

relative elevation about 10 m (Fig. 1C) both with thick (4–5 up to 13 m) postglacial sedimentary cover.

Hills are separated by linear and closed depressions with dominant latitudinal orientation. Gently outlined wide (100–300 m) and slightly incised (1–5 m) depressions have length 200–400 m. The largest ones (W-E orientation presenting on both sides of the Shugor Valley and Puzhbol Gully system) has several superimposed depressions more than 10 m in combined depth. There are also fragments of submeridional terrace-like units and shallow kettle holes discordant with the contemporary fluvial network. It is believed that those features are the remnants of the Middle Pleistocene glacial meltwater or dead-ice topography. They can either be drained by modern gullies or disrupt upper and lower fluvial chains. Isometric kettles and hollows 200–600 m in diameter have smooth, but clear rims and often waterlogged flat bottoms at 160–180 m a.s.l.

Consideration of morphologic characteristics including position within the fluvial network, width/depth, longitudinal and cross-section profile shapes, sharpness of the topography breaklines (convex, concave slope breaks and thalweg lines), presence or absence of terraces and bottom morphology allows distinguishing four main types of small linear depressions within the study area (Fig. 2). First type - relatively large postglacial depressions - is represented by the connected headwaters of the two dry valleys separating the two highest hills of the area between the Lomy and Antsiferovo villages (Fig. 1C). Deep (20–25 m) meridional depression is about 2 km long and has relatively steep (7–10°) slopes with several subhorizontal shelves (Fig. 2A). Its wide (100–200 m) slightly undulating bottom is convex in longitudinal profile and opens to small erosional valleys – Shugor and Mazikha – limiting the key area from the North and South respectively. Series of shallow tributary gullies of the main depression are either in agreement with the modern surface runoff system or directed oppositely.

The other three types are represented by the actual fluvial network (Fig. 2B-D) having predominant latitudinal orientation.

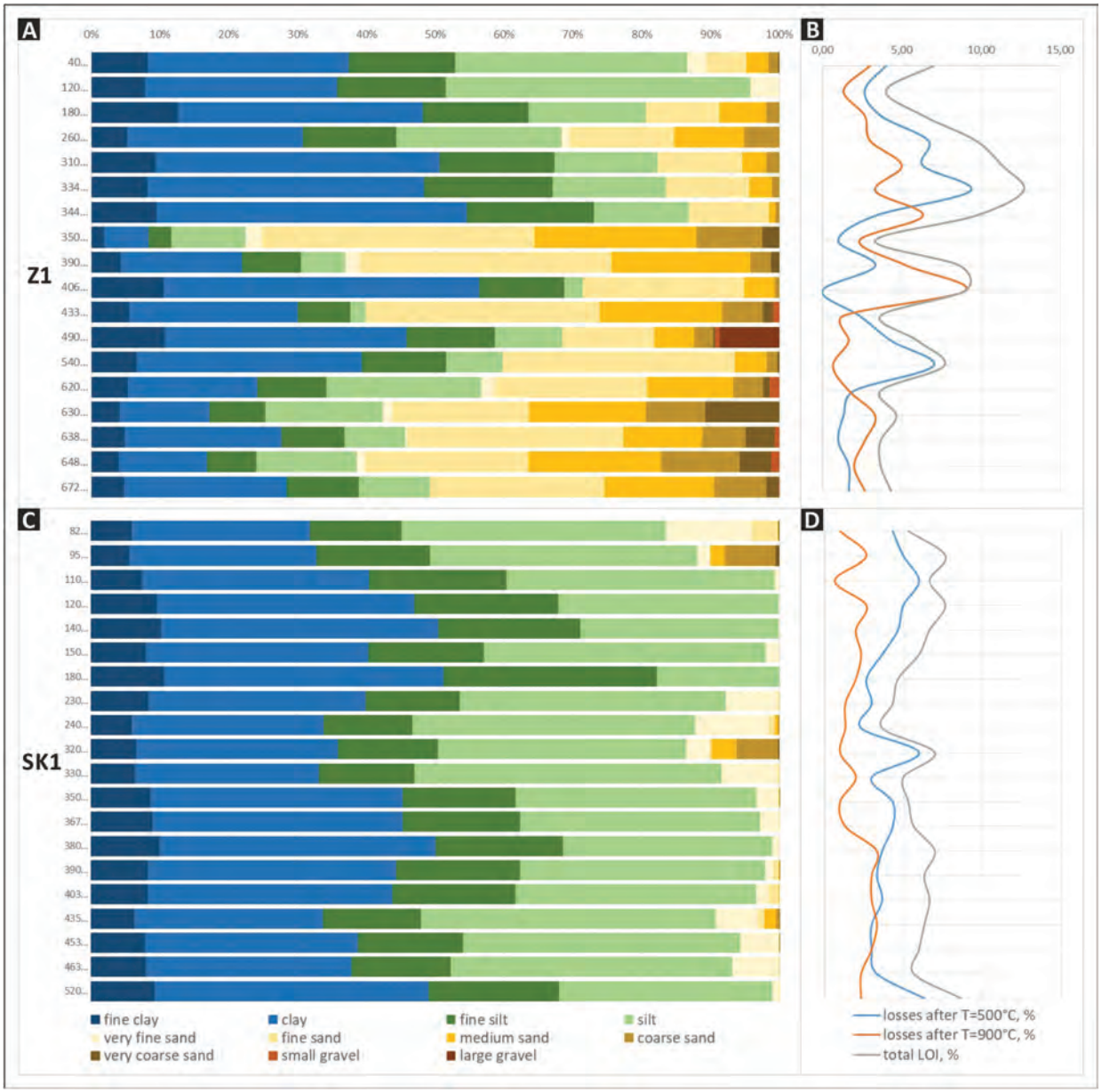

Fig. 4. Grain size (A) and losses on ignition (LOI) (B) charts for the sedimentary infills of depressions (core Z1 - dry valley headwaters of Mazikha River, and core SK1 - closed depression at the headwaters of the West Cheremoshnik Gully).

Small erosional valleys (Fig. 2B) and large gullies (Fig. 2D) are of around 10 and 3 km in length respectively with their heads at 160–175 m a.s.l. Both incise up to 10–20 m in the middle reaches. While small valleys discharge directly into the Nero Lake (base level 93 m a.s.l.), gullies open with large flattened fans to the third lake terrace (110 m a.s.l.). The lower parts of the modern fluvial network at the lower Nero Lake terraces are almost completely transformed due to melioration in 1980-s and, therefore, are excluded from consideration in this work. Smaller gullies on slopes of the higher hills have less than 1 km in length, 5–10 m in depth and either Eastern or meridional direction. Their minor fans are confined to the 160–170 m a.s.l. – bottoms and terrace-like levels on the sides of partially infilled kettle holes. Thus, the fluvial network has a discrete structure where upper erosional chains (Fig. 2C) are completely disjointed from the main fluvial system by locally closed depressions.

A set of three cores (Z1, Z4, Z5) exposes the geological structure of the meridional dry valley headwaters (Fig. 3A). Deep incision into the glacial till is buried at depths of 5.5–7.5 m from the daylight surface (at 172–172.5 m a.s.l.). The upper meter of glacial deposits is greyish brown dense sandy loams with clastic detritus probably reworked by watercourses (Fig. 5A).

The incision is infilled by a polygenic sedimentary sequence. Close to the sides of the depression (at 177 m a.s.l., Z5), 5 m of unclearly laminated blueish-grey loams (Fig. 3F) have well-decomposed peat and darker brownish organic-rich lenses from mm to tens of cm thick (Fig. 3G). Lithologic homogeneity (Fig. 4A) and microlamination of deposits respond to sedimentation in a calm hydrodynamic environment. Thus, a relatively long-lasting lake had existed in the depression with several (at least three) periods of water table drops and waterlogging marked by peat formation.

In the central part of the depression, the lacustrine thickness is interrupted by stratified brownish grey sandy lenses (Fig. 3D) of up to 1.5 m embedded with erosive contact around 173 m a.s.l. Well-sorted coarse to fine-grained sands with gravel (0.5–1.3 m thick) (Fig. 4A) are interpreted as channel facies infilling a secondary incision in the lacustrine sequence.

From the depth of 2.3–2.8 m, both lacustrine and alluvial units are covered by yellowish-light-grey unclearly laminated loams (1–1.25 m thick) (Fig. 3E) followed up to the surface by variegated yellowish-brown loams with series of peat and plant detritus interlayers (2 cm thick) (Fig. 3C). The lower ones could be attributed once again to the lake sedimentary conditions with relatively lower organic content (Fig. 4B) whether the upper ones reflect slope movements intensification with superimposed pedogenesis and cover beds formation. At a depth of 0.4–0.6 m, thin charcoal layers are found in several cores on the interfluve and valley slopes.

Buried organic-rich lenses show the potential as stratigraphic and age indicators of both incision and infill processes and relatively stable periods. For AMS radiocarbon dating, three samples were retrieved (Table 1). Two of them from lacustrine and fluvial facies at the same altitude level (173.8 m a.s.l.) show that the secondary incision occurred no later than the Middle Valdai interglacial being preceded by accumulation of the lower lake stratum.

Quite similar lacustrine sedimentary sequences infill small currently either closed or open depressions at the lower interfluve levels (160–165 m a.s.l., cores SK1, F1, F2, (Fig. 1C). Unclearly laminated heavy loams to silts and sandy silts of more than 4.5 m in thickness (yellowish-light-grey to bluish-grey and brownish-grey downwards) (Fig. 3F) are covered by 1–2 m of variegated slope loamy deposits. Showing no signs of fluvial reworking, the former, though, resemble previously described lacustrine facies (Fig. 4C-D) and incorporate peaty lenses indicating periods of temporary lake water table decreases during the prolonged lacustrine infilling epoch.

Meso- and micromorphological investigation of the underlying glacial till in the core Z1 (Fig. 5A), in first approximation, revealed a set of relic pedofeatures, e.g., fragments of plane pores completely infilled by light brownish clay cutans spreading down strictly from the upper contact of the till (Fig. 5B). Argillaceous cutans those fill in small plane pores have typical thickness 20–70 μm with more than 100 distinct layers and general dense interlayered microstructure (Fig. 5D). The upper layer of cutans has specific microfeatures those are related to post-burial diagenetic superimposed processes. Cutan surface differs from the others by general high inner layer compaction, irregularly perforated (Fig. 5D) and ridge-groove stretched structure (Fig. 5C), which reveal slight shrink-swelling with a short shifting of the groundmass. Specific polygonal microridge structure of the cutan surface (Fig. 5E) relates with post-burial compaction defined by superimposed slight shrink-swell mechanism without groundmass shifting. Complete set of pedofeatures at the upper glacial till contact unveils a fact of long-term pedogenesis in a warm, humid climate that finally formed luvisol-like soil profile. The general stratigraphic position of the unit and required continuous soil formation conditions suggest the Mikulino (Eemian) interglacial as the only possible timeframe of pedogenesis.

Thus, two stages of the dominant incision are found in the valley headwaters. The first could be correlated to the end of the Middle Pleistocene glacial cover degradation (MIS6) followed by a quite prolonged period of the Mikulino (MIS5e) texturally differentiated soil formation; and the second - to the Early-Middle Valdai erosional stage (MIS4-MIS3). Distinct infilling of depressions was predominantly a result of lake environments widespread through the most of Valdai epoch and locally disrupted by the secondary erosion.

5. Discussion

The development history of the fluvial network can be substantially detailed correlating events in the main valley systems with episodes in their upper reaches and watersheds presently non-affected by fluvial processes. Integrating the available results including the examination of previously published data by Rusakov et al. (2015, 2019), we propose a scenario of the fluvial network transformation in the glaciation marginal zone over the last 150 ka, on the example of the Eastern Borisoglebsk Upland.

5.1. Fluvial incisions

5.1.1. The first stage of fluvial incision

The first stage of fluvial incision occurred under still severe periglacial conditions at the end of the Late Moscow. Probably, it

Table 1
AMS ^{14}C dating results from the meridional depression key site and corresponding calibrated ages.

№	Depth / altitude, m	Core	Layer	Material	Laboratory number	^{14}C, yrs BP (± 1σ)	1σ	cal BP yrs 2σ	Median
1	0.54–0.56 / 176.9	Z4	upper layer of cover beds	TOC	$IGAN_{AMS}$ 6289	3630 ± 20	3912–3972	3886–3985	3941
2	4.13–4.22 / 173.8	Z1	base of alluvium	Plant rs.	$IGAN_{AMS}$ 6290	40680 ± 310	43899–44569	43535–44864	44228
3	5.52–5.56 / 173.8	Z5	lower part of lacustrine unit	TOC	$IGAN_{AMS}$ 6288	32450 ± 155	36152–36503	35958–36750	36335

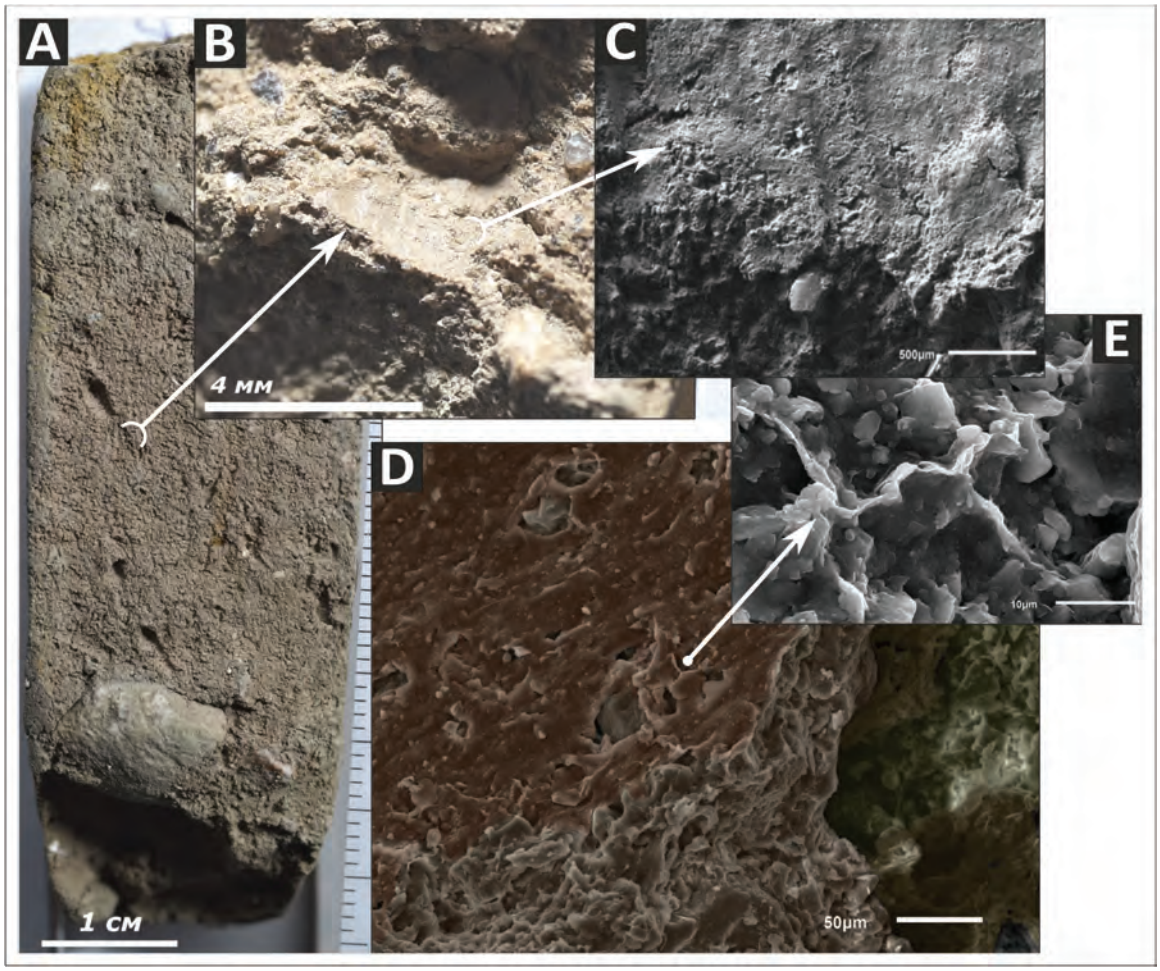

Fig. 5. Relic pedogenic features of the buried Mikulino (Eemian) paleosol in the glacial till (core Z1): A - general structure of the core vertical cross-section; B - fragment of plane pore with dull light yellowish brown argillaceous cutans, mesoscale, fracture section, reflected light image; C - upper plane (surface) of argillaceous clay cutan, mesoscale, fracture section, backscattered electron image; D - microstructure of thin (up to 70 μm) silty clay cutan with dense inner and interlayer compaction, fracture section, colored secondary electron image; E - polygonal microridge structure on the cutan surface, fracture section, secondary electron image.

was triggered by the final degradation of glacial ice in the Nero Lake Basin leading to rapid base-level decrease (Velichko, 2012) and isolation of the high lake terrace (130 m a.s.l.) (Semenov et al., 1972). On the sides of actual valleys, preserved steep (up to 10–15°) fragments 1–4 m high – above the bottom infills and below the rims of much shallower. Thus, wider and more gently sloped depressions of initial glacial topography – indicate Late Moscow incisions. At the actual interfluves, resembling erosive landforms up to 12–20 m deep, partially infilled (8–12 m) and completely inactive, testify to much further propagation of initial incisions than of the modern fluvial network.

Paleopedofeatures discovered at the erosive upper contact of the Middle Pleistocene glacial till in both upper and middle reaches of the Late Moscow fluvial net indicate a definite period of landscape stabilization. At the East Cheremoshnik site, the embryonal paleosol dated 144 and 121 ka is attributed to the Early Mikulino pedogenesis (Rusakov et al., 2019). However, macromorphological investigation reveals definite erosive contact between Crb and Agb horizons indicating *non-in situ* habitus of the palaeosoil body. Thin Agb horizon (1–3 cm), erosive contact inside the profile and absence of well-developed pedofeatures allow assuming only a short period (first years) of soil formation and stable surface existence in the gully bottom environment. That makes non-sufficient supposing an interglacial character of pedogenesis and considering that soil as a stratigraphic unit. At the same time, well-developed textural differentiation of buried soil profile discovered in the dry meridional valley had required relatively warm climatic conditions without permafrost to form. That allows attributing it to the certain Mikulino interglacial pedogenesis and prolonged landscape stabilization at the upper reaches.

5.1.2. The second stage of fluvial incision

The second erosion stage preceded the Middle Valdai. At the interfluve postglacial sequences, that incision reached 3–5 m in depth, which is marked by distinct erosive contact found in two out of three drill cores (Z1 and Z4), and occurred before 44 ka. It could be correlated to one of the stratigraphic unconformities (however, mentioned as clear contacts in the original article by Rusakov et al., 2015) in sedimentary infill exposed in the middle reaches of the Puzhbol Gully system. The upper one lies roughly at 143 m a.s.l. clamped between the layers dated to the Middle Valdai (47–42 ka cal BP) and Mikulino interglacial (114–115 ka). The other erosive contact at 142.5 m a.s.l. underarms the latter represented by a peat lens, which highlights another yet local erosion episode of uncertain (probably Early-Middle Mikulino, according to the U-Th dating) time.

Relationship of those incision events with the Nero Lake base level and isolation of the third (110–107 m a.s.l.) terrace is unclear mainly due to the ongoing debate about the age and possible genesis of corresponding lake level rise and decrease during the Late Pleistocene (Alyoshinskaya & Gunova, 1997; Kvasov, 1975, etc.). It can only be suggested that this incision stage was

associated with profound landscape condition changes, most likely, Early Valdai permafrost degradation. However, more data is undoubtedly needed to clarify the situation.

5.1.3. The third stage of fluvial incision

Third incision stage allocates by numerous morphologic and geologic evidence in the middle reaches of the actual fluvial network and is not to be found in the interfluves postglacial sedimentary cover. The main phase of the incision has determined the general appearance of the actual fluvial network. Resulted in deep erosion cuts it clearly shows in the landscape due to distinct rims and steep ledges of both depositional and erosional terraces 5–6 up to 8–10 m high above the floor of small valleys. Most possibly, these indicate the actual amplitude of the Late Valdai incision probably triggered by drastic water table decrease of the Nero Lake Basin and isolation of the second lake terrace (100–105 m) (Alyoshinskaya & Gunova, 1997). In places, it was re-deepened later during the Holocene.

However, several lower-amplitude incisive episodes could have preceded the main Late Valdai erosive phase. A small V-shaped buried tributary incision (no less than 1.2 m deep) is displayed in the ORV cross-section at the East Cheremoshnik site. A pedosediment on its erosive bottom is dated to the end of the BÖlling interstadial (MIS2, 15.0 ka cal BP) (Rusakov et al., 2019). Although another structural unconformity could be found even below showing remarkable morphologic resemblance to this lens-like erosive structure. It is marked by a slightly darker thin steeply sloping layer that was previously (Rusakov et al., 2015) interpreted as Gleyic Turbic Cryosol – Trubchevskaya paleosol (MIS2, 19.8 ka cal BP). Nonetheless, some pedofeatures interpreted as cryoturbations more likely seem to be a result of desiccation of thin colluvial deposit simultaneously with a short-time (first years) surface stabilization. Therefore, we are prone to advocate for the primary erosive genesis of this inclined surface. Thus, at least two (and probably more) additional local intensifications of erosion are distinguished through the middle of the Late Valdai epoch. Although no signs of such are found in the interfluve areas, those remained relatively stable since then.

5.1.4. The fourth stage of fluvial incision

The latest stage of the major incision is marked by fragments of low (1.5–3 m above the stream) gully terraces and knickpoints in the longitudinal gully profiles (0.5–1.5 m relative height). The probable cause was due to the last significant Nero Lake water table decrease (to 95–98 m) and isolation of the first lake terrace in the Late Holocene (Aleksandrovskij, 2011).

Thus, four successive incision stages are observed in the fluvial network morphology or geological structure: Late Moscow, Early-Middle Valdai, Late Valdai with several substages and Late Holocene. Moreover, only the first two of them reached the Mazikha and Shugor dry valleys headwaters (Fig. 1A).

5.2. Infills

5.2.1. The first infill stage

After a short-time pedogenesis, middle parts of the Late Moscow depressions were gradually infilled by lake and peat deposits. The existence of much greater lake basin is inconsistent with regional paleogeographic reconstructions showing a low level of the receiving Nero Lake during the Mikulino (Alyoshinskaya & Gunova, 1997; Gey, Saarnisto, Lunkka, & Demidov, 2001; Sudakova et al., 1977; Velichko et al., 2001; Velichko, Faustova, Gribchenko, Pisareva, & Sudakova, 2004). Hence, isolated lakes had to appear in the locally dammed Late Moscow incisions probably caused by the increased mass-wasting activity. Later local water table fluctuations led to a low-rate peat accumulation in small drying basins followed by the re-established shallow lake conditions. According to palynological data (Sudakova et al., 1977), ORV reference section represents only the first half of the Mikulino interglacial. New radiocarbon and U-Th dates from peats (Rusakov et al., 2015) suggest a radical shift in sedimentation rates in the second part of the interglacial (115–47 ka BP). However, relatively thin (about 0.5 m) thickness of the dated peat lens and its erosive upper and lower contacts with the accommodating gyttja layers assert for the predominant lacustrine infillings through the entire Mikulino and the first half of the Valdai. Related deposits were removed by several incision episodes, as indicated by long hiatuses in the ORV section sedimentary sequence.

At the upper reaches of the Late Moscow fluvial network, no signs of Mikulino infills have been revealed. Although, a well texturally differentiated soil profile at the erosive contact of the glacial till suggests long-lasting stable conditions during MIS5e. Infilling of the depression with fine lacustrine deposits with organic-rich lenses started afterward. The superimposed Middle Valdai incision allows narrowing the period of this unit formation to the Early Valdai.

5.2.2. The second infill stage

One of the most controversial interpretations of the deposits age and genesis relates to this period of valley infilling. At the East Cheremoshnik site, discussion of the origin of relatively thin (not more than 2 m) loamy layer with rare boulders and gravels is ongoing for the last 70 years. Some researchers (Moskvitin, 1976; Novskij, 1975; Sudakova, Karpukhin, & Altynov, 2014) tend to infer its glacial origin basing on relatively abundant coarse clasts of igneous rocks with increased content of hornblende, dense compaction (comparable to the Moscow till) and supposedly allochthonous character of embedded peaty-lacustrine Mikulino deposits. They propose the Early Valdai glaciation to penetrate the Borisoglebsk Upland and the adjacent Nero Lake depression by marginal valley outlets. Others (Chebotaryova & Makarycheva, 1974; Chebotaryova et al., 1977; Markov, Velichko, Sudakova, Breslav, & Berdnikov, 1969; Rusakov et al., 2015; Sudakova et al., 1977, etc.) suggest that those deposits together with the overlying gravely lenses represent complex slope and fluvial accumulation, based on several specific patterns including rhythmic lamination, grain size differentiation, facial substitution by solifluction deposits. Close mineralogical and petrographic content could be related to the Moscow till as source of local redeposition. Observed distinct "periglacial footprints" – cryogenic structures and chaotic orientation of clasts – could macromorphologically somehow resemble glacial tills. High organic content and even series of embryonal humic layers are also inconsistent with the glacial origin and suggest not Early but Middle-Late Valdai (between 47 and 27 ka cal BP) accumulation (Rusakov et al., 2019; Sedov et al., 2016).

Having considered those opinions, we incline to agree that these units represent interbedded colluvial and alluvial deposits separated by several minor erosion activations and short periods of landscape stabilization that led to an embryonal pedogenesis (see 4.1.3). During the onset of the Late Valdai in severe periglacial environments (Alyoshinskaya & Gunova, 1997) mass-wasting processes (mainly solifluction) cause substantially more active valley infill. The second half of the period was characterized by persistent alteration of erosive and accumulative fluvial phases. Several thin humic horizons at the erosive contacts with underlying slope deposits and overlying alluvial gravel and sand lenses are dated to 19–15 ka cal BP (Rusakov et al., 2015). Coarse layered material presumably is a result of the Middle Pleistocene till erosion and fluvial reworking in the upper reaches followed by short-time slope processes intensification.

At the interfluves, this period could be correlated with accumulation of more than 2.5 m of the channel and lacustrine

sediments. Since the Middle Valdai (44 ka), transportation capacity of the watercourse gradually decreased (from well-sorted coarse sands up to silts and loams with peat lenses) and even shifted once more to a closed basin sedimentation in colder (than at the previous stage - See 4.2.1) conditions of the Late Valdai, according to the low organic content (Fig. 4B, D).

5.2.3. The third infill stage

The end of the Late Valdai - Holocene transition was represented by a significant slope processes activation throughout the entire area and colluvial accumulation on the valley sides and bottoms (Fig. 3B). That phenomena could be correlated to the formation of the intermediate layer of cover beds proposed for Central Europe and North America Mid-latitudes (Döhler et al., 2017; Kleber & Terhorst, 2013; Krautz et al., 2018). Presumably, it was triggered by the predominance of slope processes over linear erosion in degrading periglacial environments. Aggradation was most intensive at the headwaters (up to 2 m of primarily lacustrine turned into colluvium) and less active in the valleys (up to 1.5 m), but generally led to an essential flattening of depressions.

5.3. The latest incision-infill cycle

Thick slope sediments at the top of sedimentary sequences of the Central Russian Plain are typically known to be accumulated during the Late Valdai stage (MIS2) in the region (Velichko et al., 1994, 2001, 2004; Velichko, 2012). However, the radiocarbon dating and increase of organic-rich lenses show, at least, the upper 60 cm to be deposited during the second part of the Holocene. On the background of general erosion network stabilization, *a succession of local incisions and infillings* occurred in the second half of the Holocene. Those possible reasons include natural events such as wildfires and increased number of extreme climatic manifestations (Belyaev et al., 2003) or anthropogenic impact. Partial infilling of small cuts was proposed due to high-rate agro-colluvium accumulation (Rusakov et al., 2015) since the beginning of slash-burn farming (Dreibrodt et al., 2010).

Thus, the main stage of the Late Moscow incision (Fig. 6A) was followed by general landscape stabilization during the Mikulino interglacial. Periods of depressions infilling in locally dammed lakes were uneven in different parts of the area. At the middle reaches of the fluvial net, lacustrine sedimentation started after a short-term pedogenesis at the onset of the Mikulino and continued through the Early-Middle Valdai. At the actual interfluves, prolonged and widespread Mikulino pedogenesis was altered by lake deposition later. During the Late Pleistocene periglacial, only one distinctive incision period was registered there while in the middle reaches deposition was interrupted by at least four probably asynchronous episodes. That allows concluding the Early-Middle Valdai erosion events to have a local signal. So the upper parts of the Late Moscow glaciofluvial depressions and fluvial incisions were predominantly gradually infilled and smoothened by Valdai lacustrine sediments and Late Valdai-Holocene slope deposits. The lower parts of initial fluvial systems experienced additional deep progressive Late Valdai incisions, however, much less extensive (Fig. 6B).

The present-day fluvial network generally inherit Late Moscow incisions not penetrating as far into the most elevated interfluves (Fig. 6B). Infilled headwaters show subdued or no signs of modern (or Late Valdai) fluvial activity except for small gullies on steep hillslopes disconnected from the main network. Buried (Late Moscow and Early-Middle Valdai) incisions testify to a completely different landscape structure and much higher surface runoff discharges during the late glacial and first postglacial stages. It can be explained, respectively, by the Nero Lake level decrease and widespread permafrost causing a substantial increase of surface runoff coefficient. However, while the base level fall can apparently be considered a reason for incision, the permafrost development and degradation can result in diverse effects on fluvial systems from increased upland erosion (Marshall et al., 2015) and associated channel aggradation (Cordier et al., 2006) to episodic extreme river discharges leading to formation and incision of large palaeochannels during rapid degradation of permafrost (Panin et al., 2017; Starkel et al., 2015). Thus, it seems logical for us also to consider the Early-Middle Valdai incision (second stage) as related to permafrost degradation phase during the first half of the Late Pleistocene, although we do not yet have ample direct evidence to support this, except for the stratigraphic position of the associated erosional contacts.

The history of proglacial ice-dammed lakes and its affects on the postglacial landscape transformation, particularly on the fluvial systems development, has been lately extensively studied for the Late Glacial epoch of the Northeastern Europe and Northern Russia (Gorlach, Hang, & Kalm, 2017; Mangerud et al., 2004;

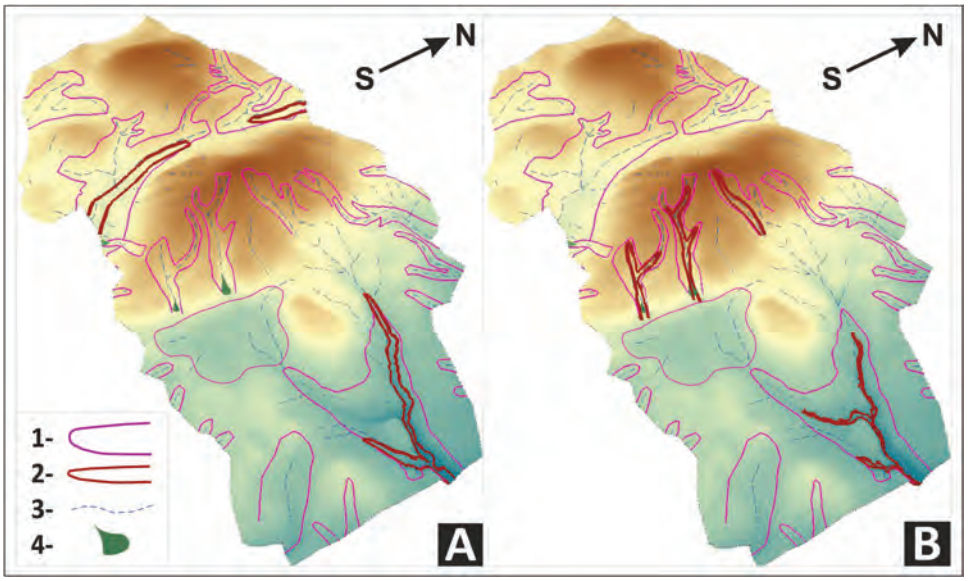

Fig. 6. The fluvial network structure of the Eastern Borisoglebsk Upland for the end of the Late Moscow (A) and the Late Valdai (B) timeslices. 1 – Late Moscow depressions, 2 – incisions, 3 - thalwegs, 4 - fans.

Marks, 2004, etc.), however, its distribution and timing is yet to be established at the Upper Volga region. After the final Middle Pleistocene ice cover degradation, the Nero Lake became local base level for the watercourses of the Eastern Borisoglebsk Upland macro slope. Its fluctuations caused multiple major incision-infill cycles. However, one of the leading regional paleogeographic questions still stands to be the maximum lake level rise during the Late Pleistocene. Often two accumulative lacustrine units are suggested (Alyoshinskaya & Gunova, 1997; Gey et al., 2001) because of well-preserved terraces with the heights 107–110 and 100–105 m a.s.l. Occasionally, extreme water level rise up to 130 (Grosvald & Kotlyakov, 1989; Kvasov, 1975) and even 140–180 m (Auslender, 1966; Chebotaryova et al., 1977; Chizhikov, 1956; Rusakov et al., 2015; Rusakov et al., 2019; Velichko et al., 1994) was proposed due to possible Late Pleistocene glacial dams of the Upper Volga Valley that could have had the opposite runoff direction. Those are potentially marked by the wide distribution of fragments of high terrace-like levels in the region. However, others (Astakhov et al., 2016; Sudakova et al., 2013, 2014) do not support the extent of continental glaciation up to the Plyos area (where the glacial dam is proposed) during the Late Pleistocene. The former hypothesis is also not sustained by either water volume sources or the nature of dams causing such extensive waterbodies to exist in the Postglacial.

6. Conclusions

1. Of the four major incision stages revealed, three can be generally associated with the Nero Lake base level falls (with uncertainties related to hiatuses in the Nero Lake level models itself) - Late Moscow (Saalian), Late Valdai (Late Weichselian) and Late Holocene. Those can be related to the isolation of the Nero Lake terraces of 130 m, 100–105 m and 95–98 m respectively. The Late Moscow and Late Valdai incisions mostly determine general outlines of modern fluvial systems while the former appears to be much more widespread expanding even into the highest interfluves. The Late Valdai gullies cut only their steep slopes and middle reaches of the initial (Late Moscow) fluvial network. The Early-Middle Valdai (Early-Middle Weichselian) incisions have limited distribution, problematic causes and are associated with local transformations of original glacial and glaciofluvial topography.
2. Despite the Holocene stage, another definite period of continuous landscape stabilization indicated by the Mikulino (Eemian) pedofeatures was revealed. It has no local but regional distribution, particularly well preserved in the upper reaches. Broadly discussed sequence of the embryonal Valdai paleosols could not agree with the regional stabilization phase due to their generally *non-in-situ* habitus and short-time development.
3. Lacustrine sedimentation appears to be the most widespread and significant agent of depressions infilling through the Late Pleistocene despite variable appearances and causes of certain lake basins origination. Distinct alluvial and peat accumulations are strongly spatially limited and testify particularly to the local conditions being not responsive to the regional signal.
4. With the regional base level decrease through the Late Pleistocene at the background, active local infilling led to the directive flattening of the case study area. Local lakes caused widespread lacustrine sedimentation predominantly of short-distance transport. Waterlogged environments provoked intensive local landscape transformations those in their turn triggered discrete erosion activations.

Acknowledgments

This work was supported by the Russian Foundation for Basic Research, Russia [projects № 16-35-00605 and № 18-05-01118], the Department of Geomorphology and Paleogeography, Faculty of Geography, Lomonosov MSU, Russia [GM AAAA-A16-11632810089-5] and Department of Soil Geography and Evolution, Institute of Geography, RAS, Russia [GM 0148-2019-0006] in part of field working organization and Russian Science Foundation, Russia [project № 14-27-00133] in part of microscopic and radioisotope research. Authors are grateful to A.P. Vergun and M.M. Ivanov for the provided aerial photo imagery, to Google Earth and Yandex Maps services for remote sensing data and open sources of global satellite radar DEMs (SRTM, ALOS 3D).

References

Aleksandrovskij, A. L. (2011). Soil evolution on the low terraces of Lake Nero. *Eurasian Soil Science*, *44*(10), 1055–1067.
Alyoshinskaya, Z. V., & Gunova, V. S. (1997). Recent deposits and paleogeography of the Nero Lake. *Vestnik of Moscow University, Series 5. Geography*, *1*, 49–52.
Astakhov, V., Shkatova, V., Zastrozhnov, A., & Chuyko, M. (2016). Glaciomorphological map of the Russian Federation. *Quaternary International*, *420*, 4–14.
Auslender, V. G. (1966). Morphological and genetic features of terraced surfaces of the Mologo-Sheksna lowland near Cherepovets In: *Materials on the geology and minerals of the North-West of the RSFSR* (pp. 233–240) (In Russian).
Beer, C. E., & Johnson, H. P. (1963). Factors related to gully growth in the deep loess area of western Iowa. From ARS Misc. Pub. 970, Proceedings of the Federal Interagency Conference.
Belyaev, Yu. R., Panin, A. V., & Belyaev, V. R. (2003). The gullies development history at the Russian Plain Center (on the example of the Cholokhovskaya Gully, MSU Satino polygon). *Vestnik of Moscow University, Series 5. Geography*, *5*, 55–63.
Belyaev, Yu. R., Grigorieva, T. M., Sycheva, S. A., & Sheremetskaya, E. D. (2008). Development of Balka headwaters in the central part of middle-Russian upland during the end of middle-Late Pleistocene. *Geomorfologiya*, *1*, 43–55 (In Russian).
Blum, M. D., & Tornquist, T. E. (2000). Fluvial responses to climate and sea level change: A review and look forward. *Sedimentology*, *47*(Suppl. 1).
Chebotaryova, N. S., Faustova, M. A., Lavrov, A. S., Aboltinsh, O. P., Danilans, I., Ya, … Isachenkov, V. A. (1977). *Structure and dynamics of the last glacial cover of Europe*. Moscow: Nauka Publ (In Russian).
Chebotaryova, N. S., & Makarycheva, T. N. (1974). *The latest European glaciation and its geochronology*. Moscow: Nauka Publ (In Russian).
Chizhikov, N. V. (1956). Geomorphology and soils of the Nero Lake and Ustye-Kotorosl River In: V. N. Sukachev, & N. V. Korde (Eds.), *Materials of the Laboratory of Sapropel Deposits*, 4 (pp. 130–144). Moscow: Academy of Sciences of USSR Publ (In Russian).
Cordier, S., Harmand, D., Frechen, M., & Beiner, M. (2006). Fluvial system response to Middle and Upper Pleistocene climate change in the Meurthe and Moselle valleys (Eastern Paris Basin and Rhenish Massif). *Quaternary Science Reviews*, *25* (13–14), 1460–1474.
Döhler, S., Terhorst, B., Frechen, M., Zhang, J., & Damm, B. (2017). Chronostratigraphic interpretation of intermediate layer formation cycles based on OSL-dates from intercalated slope wash sediments. *Catena*, *162*, http://dx.doi.org/10.1016/j.catena.2017.11.003.
Dreibrodt, S., Lubos, C., Terhorst, B., Damm, B., & Bork, H.-R. (2010). Historical soil erosion by water in Germany: Scales and archives, chronology, research perspectives. *Quaternary International*, *222*, 80–95.
Eremenko, E. A., Panin, A. V., & Karevskaya, I. A. (2010). Postglacial transformation of glaciofluvial channels in the marginal zone of the Moscow (MIS 6) glaciation. *zvestiya of Russian Academy of Sciences, Geography Series*, *5*, 56–70.
Garankina, E. V., Belyaev, V. R., Shorkunov, I. G., Andreev, P. A., Verlova, T. A., Shishkina YuV, Bondar, A. I. (2018). Evolution of Borisoglebsk upland interfluves over the last 150,000 years (marginal zone of Moscow Glaciation, the central part of Russian plain). In Practical Geography and XXI Century Challenges. International Scientific and Practical Conference, 4–6 June 2018, Moscow. Conference Book pp. 197–205. Moscow: Institute of Geography, Russian Academy of Sciences.
Gey, V., Saarnisto, M., Lunkka, J. P., & Demidov, I. (2001). Mikulino and Valdai Palaeoenvironments in the Volga Area, NW Russia. *Global and Planetary Change*, *31*, 347–366.
Gorlach, A., Hang, T., & Kalm, V. (2017). GIS-based reconstruction of Late Weichselian proglacial lakes in northwestern Russia and Belarus. *Boreas*, *46*(3)), http://dx.doi.org/10.1111/bor.12223.
Grosvald, M. G., & Kotlyakov, V. M. (1989). The Great Preglacial drainage system of Northern Eurasia and its significance for interregional correlations. In Quaternary period. Paleogeography and lithology (pp. 5-13). Kishinev. (In Russian).
Heiri, O., Lotter, A. F., & Lemcke, G. (2001). Loss on ignition as a method for estimating organic and carbonate content in sediments: Reproducibility and

comparability of results. *Journal of Paleolimnology*, *25*, 101–110.
Hughes, A. L. C., Gyllencreutz, R., Lohne, Ø. S., Mangerud, J., & Svendsen, J. I. (2016). The last Eurasian ice sheets – a chronological database and time-slice reconstruction, DATED-1. *Boreas*, *45*(1), 1–45.
Kleber, A. (1997). Cover-beds as soil parent materials in midlatitude regions. *Catena*, *30*, 197–213. http://dx.doi.org/10.1016/S0341-8162(97)00018-0.
Kleber, A., & Terhorst, B. (Eds.). (2013). 1st ed. *Mid-Latitude Slope Deposits (Cover Beds). Developments in Sedimentology*, 66). Elsevier Science.
Kołodyńska-Gawrysiak, R., & Chabudziński, L. (2014). The types and function of closed depressions in modern loess landscape of Naleczow Plateau (Lublin upland, E Poland). *Annales Universitatis Mariae Curie-Sklodovska*, *79*(1), 61–77.
Konert, M., & Vandenberghe, J. (1997). Comparison of laser grain size analysis with pipette and sieve analysis: A solution for the underestimation of the clay fraction. *Sedimentology*, *44*, 523–535.
Konstantinov, E. A., & Eremenko, E. A. (2012). Significance of the laser diffraction grain size analysis in the study of loess (for example Melekino section, the Northern Azov sea region). *Otechestvennaya Geologiya*, *3*, 47–54.
Krautz, J., Gärtner, A., Hofmann, M., Linnemann, U., & Kleber, A. (2018). Cover beds older than the mid-pleistocene revolution and the provenance of their eolian components, La Sal Mountains, Utah, USA. *Quaternary Science Reviews*, *185*, 1–8. http://dx.doi.org/10.1016/j.quascirev.2018.01.012.
Kvasov, D. D. (1975). *Late quaternary history of large lakes and inland seas of Eastern Europe*. Leningrad: Nauka Publ (In Russian).
Lavrushin, YuA , Chistyakova, I. A. (Eds.), (2001). Problems in the stratigraphy of quaternary deposits and paleogeography of the Yaroslavl Volga Basin: Proceedings of the International Symposium. GEOS-Press, Moscow. (in Russian).
Leopold, L. B., Wolman, M. G., & Miller, J. P. (1964). *Fluvial processes in geomorphology* (pp. 442–448)W.H. Freeman & Co. P.
Lowe, J. J., & Walker, M. J. C. (1998). *Reconstructing Quaternary environments* ((2nd ed.). England: Longman.
Makeev, A., Kust, P., Lebedeva, M., Rusakov, A., Terhorst, B., & Yakusheva, T. (2017). Soils in the bipartite sediments within the Moscow glacial limits of the Russian Plain: Sedimentary environment, pedogenesis, paleolandscape implication. *Quaternary International* (pp. 1–27), 1–27. http://dx.doi.org/10.1016/j.quaint.2017.09.017.
Mangerud, J., Jakobsson, M., Alexanderson, H., Astakhov, V., Clarke, G. K. C., Henriksen, M., & Svendsen, J. I. (2004). Ice-dammed lakes and rerouting of the drainage of northern Eurasia during the Last Glaciation. *Quaternary Science Reviews*, *23*, 1313–1332.
Markov, K. K., Velichko, A. A., Sudakova, N. G., Breslav, S. L., & Berdnikov, V. V. (1969). Guidebook for field excursions Moscow – Upper Volga. Materials of the Symposium Paleogeography and Pleistocene Periglacial Phenomena. Moscow. (In Russian).
Marks, L. (2004). Middle and Late Pleistocene fluvial systems in central Poland. *Proceedings of the Geologists' Association*, *115*(2), 175–182. http://dx.doi.org/10.1016/S0016-7878(04)80025-7.
Marshall, J. A., Roering, J. J., Bartlein, P. J., Gavin, D. G., Granger, D. E., Rempel, A. W., … Hales, T. C. (2015). Frost for the trees: Did climate increase erosion in unglaciated landscapes during the late Pleistocene? *Science Advances*, *1*(10)), http://dx.doi.org/10.1126/sciadv.1500715.
Montgomery, D. R. (2007). Soil erosion and agricultural sustainability. *Proceedings of the National Academy of Sciences of the United States of America*, *104*(33), 13268–13272.
Moskvitin, A. I. (1976). *Pleistocene reference sections of Russian Plain*. Moscow: Nauka Publ (In Russian).
Novskij, V. A. (1975). *Pleistocene of Yaroslavl Volga region*. Moscow: Nauka Publ (In Russian).
Panagos, P., Borrelli, P., Poesen, J., Ballabio, C., Lugato, E., Meusburger, K., … Alewell, C. (2015). The new assessment of soil loss by water erosion in Europe. *Environmental Science & Policy*, *54*, 438–447.
Panin, A., Adamiec, G., Buylaert, J. P., Matlakhova, E., Moska, P., & Novenko, E. (2017). Two Late Pleistocene climate-driven incision/aggradation rhythms in the middle Dnieper River basin, west-central Russian Plain. *Quaternary Science Reviews*, *166*, 266–288.
Panin, A., Adamiec, G., & Filippov, V. (2015). Fluvial response to proglacial effects and climate in the Upper Dnieper valley (western Russia) during the late Weichselian and the Holocene. *Quaternaire*, *26*(1), 27–48.
Panin, A. V., Fuzeina, J. N., & Belyaev, V. R. (2009). Long-term development of Holocene and Pleistocene gullies in the Protva River basin, Central Russia. *Geomorphology*, *108*, 71–91.
Pederson, J. L., Petersen, P. A., & Dierker, J. L. (2006). Gullying and erosion control at archaeological sites in Grand Canyon, Arizona. *Earth Surface Processes and Landforms*, *31*, 507–525.
Piest, R. F., & Spomer, R. G. (1968). Sheet and gully erosion in the Missouri valley Loessial region. *Transactions of the ASAE*, *11*(6), 850–853.
Poesen, J., Nachtergaele, J., Verstraeten, G., & Valentin, C. (2003). Gully erosion and environmental change: Importance and research needs. *Catena*, *91*, 91–133.
Poesen, J., Torri, D., & Vanwalleghem, T. (2011). Gully erosion: Procedures to adopt when modelling soil erosion in landscapes affected by gullying In: R. Morgan, & M. Nearing (Eds.), *Handbook of Erosion Modelling* (pp. 360–386). Blackwell Publ. Ltd..
Reinhardt-Imjela, C., Maerker, K., Schulte, A., & Kleber, A. (2018). Implications of hydraulic anisotropy in periglacial cover beds for flood simulation in low mountain ranges (Ore Mountains, Germany). *Die Erde*, *149*(2–3), 86–101. http://dx.doi.org/10.12854/erde-2018-374.
Rusakov, A., Nikonov, A., Savelieva, L., Simakova, A., Sedov, S., Maksimov, F., & Titova, D. (2015). Landscape evolution in the periglacial zone of Eastern Europe since MIS5: Proxies from paleosols and sediments of the Cheremoshnik key site (Upper Volga, Russia). *Quaternary International*, *365*, 26–41.
Rusakov, A., Sedov, S., Sheinkman, V., Dobrynin, D., Zinovyev, E., Trofimova, S., & Korkka, M. (2019). Late Pleistocene paleosols in the extra-glacial regions of Northwestern Eurasia: Pedogenesis, post-pedogenic transformation, paleoenvironmental inferences. *Quaternary International*. 1-19 https://doi.org/10.1016/j.quaint.2018.03.020.
Schaller, M., von Blanckenburg, F., Veldkamp, A., Tebbens, L. A., Hovius, N., & Kubik, P. W. (2002). A 30000 yr record of erosion rates from cosmogenic ^{10}Be in Middle European river terraces. *Earth and Planetary Science Letters*, *204*, 307–320.
Sedov, S., Rusakov, A., Sheinkman, V., & Korkka, M. (2016). MIS3 paleosols in the center-north of Eastern Europe and Western Siberia: Reductomorphic pedogenesis conditioned by permafrost. *Catena*, *146*, 38–47.
Semenov, A. A., Tsukurova, A. M., Kvyatkovskaya, G. N., Kuznetsov, V. K. (1972). Geological map of Quaternary deposits. Scale 1:200000. Moscow series. Sheet O-37-XXVIII. Explanatory text. VSEGEI Publ. (In Russian).
Sidorchuk, A., Marker, M., Moretti, S., & Rodolfi, G. (2003). Gully erosion modelling and landscape response in the Mbuluzi River catchment of Swaziland. *Catena*, *50*, 507–525.
Starkel, L. (1991). Long-distance correlation of fluvial events in the temperate zone In: L. Starkel, K. J. Gregory, & J. B. Thornes (Eds.), *Temperate Palaeohydrology* (pp. 473–495). Chichester: John Wiley.
Starkel, L., Michczyńska, D. J., Gębica, P., Kiss, T., Panin, A., & Perşoiu, I. (2015). Climatic fluctuations reflected in the evolution of fluvial systems of central-eastern europe (60–80 ka cal BP). *Quaternary International*, *388*, 97–118.
Sudakova, N. G. (2008). Actual issues of inter-regional correlation of glacial horizons. Lithological concept. *Bulletin of the Quaternary Commission*, *68*, 51–58 (In Russian).
Sudakova, N. G., Agadzhanyan, A. K., Alyoshinskaya, Z. V., Bazilevskaya, L. I., Bolikhovskiy, V. F., Bolikhovskaya, N. S., & Vvedenskaya, A. I. (1977). *Sedimentary sections at glacial regions of the Russian Plain Center*. Moscow: MSU Publ (In Russian).
Sudakova, N. G., Antonov, S. I., & Vvedenskaya, A. I. (2013). Structure of glacial marginal zones in the center of the East European Plain. *Vestnik of Moscow University, Series 5. Geography*, *66*, 55–61 (In Russian).
Sudakova, N. G., Karpukhin, S. S., & Altynov, A.Ye (2014). Reconstruction of radial-marginal pattern and dynamic of glacial marginal zone of Yaroslavl Volga region with the use of satellite data. *Bulletin of the Quaternary Commission*, *73*, 87–98 (In Russian).
Thompson, J. R. (1964). Quantitative effect of watershed variables on the rate of gully head advancement. *Transactions of the ASAE*, *7*(1), 54–55.
Vandekerckhove, L., Poesen, J., & Govers, G. (2003). Medium-term gully headcut retreat rates in Southeast Spain determined from aerial photographs and ground measurements. *Catena*, *50*, 329–352.
Vandekerckhove, L., Poesen, J., Oostwoud Wijdenes, D., & Gyssels, G. (2001). Short-term bank gully retreat rates in Mediterranean environments. *Catena*, *44*, 133–161.
Vanmaercke, M., Poesen, J., Van Mele, B., Demuzere, M., Bruynseels, A., Golosov, V., & Yermolaev, O. (2016). How fast do gully headcuts retreat? *Earth-Science Reviews*, *154*, 336–355.
Velichko, A. A. (2012). *Evolutionary geography: Problems and solutions*. Moscow: GEOS Publ (In Russian).
Velichko, A. A., Faustova, M. A., Gribchenko, Yu. N., Pisareva, V. V., & Sudakova, N. G. (2004). Glaciations of the East European Plain – distribution and chronology In: J. Ehlers, & P. L. Gibbard (Eds.), *Quaternary glaciations – extent and chronology* (pp. 337–354). Elsevier Science.
Velichko, A. A., Shik, S. M., Faustova, M. A., Pisareva, V. V., Sudakova, N. G., Andreicheva, L. N., & Duryagina, N. A. (2001). *Middle Pleistocene glaciations of Eastern Europe*. Moscow: GEOS Publ (In Russian).
Velichko, A. A., Starkel, L., Borisova, O. K., Faustova, M. A., Valchik, M. A., Makkaveev, A. N., & Faustova, M. A. (1994). *The paleogeographical basis of modern landscapes*. Moscow: Nauka Publ (In Russian).
Wohlfarth, B., Tarasov, P., Bennike, O., Lacourse, T., Subetto, D., Torssander, P., & Romanenko, F. (2006). Late Glacial and Holocene Palaeoenvironmental Changes in the Rostov-Yaroslavl' Area, West Central Russia. *Journal of Paleolimnology*, *35* (3), 543–569.

International Soil and Water Conservation Research 7 (2019) 196–202

Contents lists available at ScienceDirect

International Soil and Water Conservation Research

journal homepage: www.elsevier.com/locate/iswcr

Original Research Article

Trees as large-scale natural phononic crystals: Simulation and experimental verification

Jiankun Huang*, Yifan Liu, Yaguang Li

Key Laboratory of State Forestry Administration on Soil and Water Conservation, School of Soil and Water Conservation, Beijing Forestry University, Beijing, China

ARTICLE INFO

Article history:
Received 25 August 2018
Received in revised form
23 February 2019
Accepted 1 March 2019
Available online 6 April 2019

Keywords:
Urban trees
Phononic crystal
Dispersion curve
Band gap
Rayleigh wave

ABSTRACT

Urban trees are usually planted on a periodic layout in the spatial configuration. We regard urban trees as large-scale natural phononic crystals. The entire forest is reduced to a reasonable "tree-soil" unit cell based on the phononic crystal theory and finite element method by COMSOL software is used to obtain the dispersion curves. The Rayleigh wave band gaps of phononic trees are distinguished by the sound cone method. The influences of soil elastic modulus and tree height on band gaps are investigated. A three-dimensional simulation model and experiment test are applied to validate the effect of phononic trees on vibration control. The numerical frequency reduction zones coincide exactly with the theoretical band gaps. Increasing soil stiffness results in a higher-frequency and wider band gap. An increasing tree height is beneficial to obtain low-frequency band gaps. A periodically arranged plantation that Rayleigh wave band gaps at frequency ≤60 Hz could be designed. This study opens up a new theoretical basis for the quantitative analyses of urban trees to the ground vibration mitigation at a certain frequency range.

1. Introduction

With the rapid development of traffic, vibration and chaos are typical environment problems, causing high-precision system to malfunction and extending noise pollution. Some engineering measures for vibration and noise mitigation have a certain effect (Huang, Liu, & Shi, 2017; Pu & Shi, 2018); however, they act against the ecological conception and have a high cost. Controlling the propagation of waves to protect critical infrastructure via a large-scale phononic crystal is of topical interest. The artificially engineered materials with dispersion properties, e.g., periodic pile barriers (Huang & Shi, 2015), are now being transplanted into other wave systems. Locally resonant structures, in this case trees, i.e. forests, interact with Rayleigh waves in surprising ways, are observed as large-scale natural phononic crystals. Forests can improve the ecological environment along the traffic lines and conserve soil and water (Baig, Shahid, & Straquadine, 2013; Blinkov, Kostadinov, & Marinov, 2013; Golosov & Belyaev, 2013). Urban forests not only can be used as wind barriers (Liu, Wagner, Ning, & Qu, 2017), but also have a favorable vibration and chaos reduction effect (i.e, as sound barriers). It is an effective, ecological, and economic method to reduce vibration and control noise.

Since the jungle was found to own sound attenuation feature (Eyring, 1946), research has been extended to choose vegetation to solve environmental vibration and noise problems. Some fascinating design problems, including the effect of urban trees on vibration and chaos mitigation, have been widespread in recent research. Noise attenuation within the low frequency range is caused by the indirect interaction between plant and ground reflections (Fricke, 1984). The noise reduction effect of plant communities is closely related to plant morphology including foliage area, foliage fresh weight, and leaf shape (Fan, Zhiyi, Zhujun, & Jiani, 2010). The influence of geometrical parameters such as different lengths, thickness, and layout of green belts on chaos reduction was also qualitatively studied (Renterghem, Botteldooren, & Verheyen, 2012). However, the previous research on urban forests is mainly qualitative and lack of an exactly physical model and experimental verification to illustrate how urban forests depress vibration and noise.

The research on phononic crystal arose in 90 s. Its unique wave-forbidding characteristic opens up new perspectives for clarifying the mechanism of urban vegetation reducing vibration and noise.

* Corresponding author.
E-mail addresses: jiankunhuang@bjfu.edu.cn (J. Huang), 1378419948@qq.com (Y. Liu), yiaguang@bjfu.edu.cn (Y. Li).

https://doi.org/10.1016/j.iswcr.2019.03.004

Although elastic waves are different from electromagnetic waves, it has been shown that Rayleigh waves have common features with electromagnetic symmetries when they propagate on elastic crystals, due to the existence of elastic wave bandgaps (Achaoui, Khelif, Benchabane, Robert, & Laude, 2011). Regularly arranged green belts can be regarded as phononic crystals and have a better attenuation effect on low-frequency noise than irregularly arranged green belts (Martínez-Sala et al., 2006). The entire forest can convert partial-frequency seismic surface wave modes into harmless downward propagating bulk shear waves (Maurel, Marigo, Pham, & Guenneau, 2018). Certain frequency bands strongly attenuated in the forest validated by field experiments, and this attenuation is caused by the resonant coupling of Rayleigh waves with the trees in the forest (Andrea, Philippe, Sebastien, Philippe, & Craster, 2016).

The previous research demonstrated the feasibility of applying the phononic crystal theory to microphysics realm and the observed frequencies are in the kHz to GHz regime. Forest was represented with a natural phononic crystal and regarded as a seismic cloak. However, the calculation model is simplified as a two-dimensional (2D) system, which has only two degrees in this system. Vibrations can only exist in the in-plane, hence some important information on the out-of-plane was lost (Liu, Shi, & Mo, 2015). This paper regarded the periodically arranged plantation as a large-scale natural phononic crystal and controls the band gap within 60 Hz, which is concerned in the traffic vibration control. In addition, three-dimensional (3D) models were applied to obtain the dispersion relationships and simulate the wave field, which can accurately demonstrate the Rayleigh wave propagation in the natural phononic crystal.

This paper details an investigation of the urban forest to reduce the ground vibration in specific frequency ranges. First, a feasible "tree-soil" unit cell was used to study the features of Rayleigh-wave dispersion relationships by finite element method; then, the influence of soil modulus and tree height on band gaps were investigated. Moreover, a finite phononic-tree model with a designed configuration was applied to numerically verify the band gap in terms of vibration reduction, and the vibration modes were calculated to illustrate generation mechanism. Finally, experiment test was conducted to indicate the effectiveness of phononic trees.

2. Materials and methods

2.1. Research object

This paper presents new perspectives for analyzing the ground traffic vibration mitigation by urban forests. Since urban trees are planted on a periodic layout in the spatial configuration, as shown in Fig. 1(a). We regard such arrangement of trees as a large-scale natural phononic crystal. Under the excitation of elastic waves at a specific frequency, the phononic trees generate resonances and interact with Rayleigh waves in the soil, thus preventing Rayleigh wave propagation at the corresponding frequencies. This attenuation behavior is described as band gap in phononic crystal.

Based on Bloch's theory, it is allowed to select a minimal repeated cell as the unit cell to replace the infinite phononic crystal via the periodic boundary conditions. A "tree-soil" unit cell, as shown in Fig. 1(b), is chosen to represent the entire urban forest. The dispersion curves of the "tree-soil" system can be obtained with the advantage of Bloch's theory. In theory, the urban forests with a periodic arrangement can suppress the propagation of elastic waves in the bandgap frequency range.

2.2. Model parameters

The "tree-soil" system composes a locally resonant phononic crystal. The locally resonant phononic crystal can be simplified as a bending beam system. From the perspective of tree biomass composition, the trunk accounts for 80% of the total mass of the upper part, whereas the remaining branches and crown parts occupy about 20%. Under the observed wavelength (λ up to 10 m), phononic trees were approximated as vertical resonators. Therefore, the effect of branches and crowns can be neglected when establishing the numerical model. The effect of tree roots is ignored, because the scattering effect has a lower order compared to the trunk. In this paper, under considering of the tree growth in urban, e.g., Ginkgo (*Ginkgo biloba* L.) and Metasequoia (*Metasequoia glyptostroboides*), the tree is approximated as a circular-truncated cone. The tree space and height are $a = 2$ m and $b = 10$ m, respectively. The radii of the truck bottom and top are r (=0.3 m) and $0.5r$, respectively. The motion of surface waves decays exponentially with the depth of the media while the energy of surface-wave mainly concentrates in a certain wavelength. According to this characteristic, we need an enough soil depth to decouple surface waves from body waves (Badreddine & Oudich, 2011). Compared with tree space, the soil depth h should be large enough (Oudich & Badreddine, 2012; Xu & Peng, 2015). Thus, the unit cell herein with a height of 30 m (i.e., $h = 10$-$15a$) is sufficient for the theoretical calculation. The 3D unit cell model is plotted in Fig. 1(b). In the calculation, the material is assumed to be continuous, elastic, and undamped. The parameters of the materials used in the following analyses are listed in Table 1.

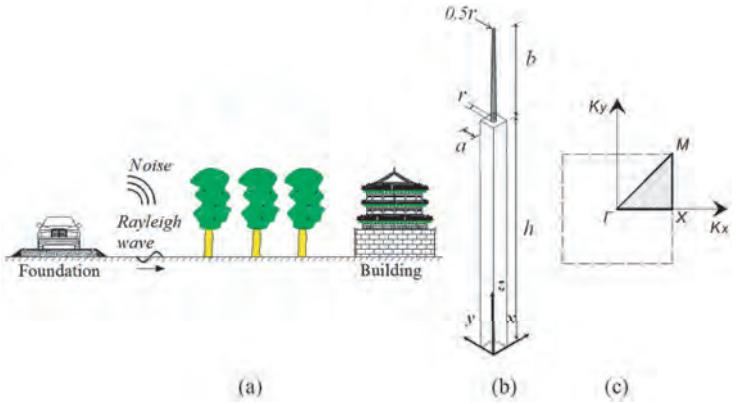

Fig. 1. (a) Rayleigh wave caused by traffic vibration and urban trees with a periodic arrangement, (b) unit cell, (c) first Brillouin zone (meaning as dashed line) and first irreducible Brillouin zone (meaning as solid line).

Table 1
Material properties (Density ρ, Elastic modulus E, and Poisson ratio υ).

Model	ρ(kg/m^3)	E (GPa)	υ
Soil	1700	0.167	0.35
Tree	700	1.67	0.3

2.3. Calculation method

Ignoring the body force, the motion of a 3D unit cell under harmonic excitations can be drawn as follows:

$$\nabla\cdot(\mathrm{C}(\mathrm{r}):\nabla\mathrm{u}(\mathrm{r}))+\rho(\mathrm{r})\omega^2\mathrm{u}(\mathrm{r})=\mathbf{0} \tag{1}$$

where ∇ is a differential operator; $\mathbf{C}(\mathbf{r})$ and $\boldsymbol{\rho}$ $(\mathbf{r})$ are the position-dependent elastic stiffness tensor and mass density; $\mathbf{u}(\mathbf{r})$ is the displacement vector; ω is the circular frequency; $\mathbf{r}=(x, y, z)$ is the position vector.

Based on the Bloch theory, the unit cell should satisfy the periodic boundary conditions:

$$\mathbf{u}(\mathbf{r}+a)=e^{i\mathbf{K}\cdot a}\mathbf{u}(\mathbf{r}) \tag{2}$$

According to the above formula, the phononic structure can be simplified as a unit cell. The four sides on the cell should satisfy the periodic boundary conditions as Eq. (2). Then, the dispersion curve calculation of the unit cell is transformed into an eigenvalue problem:

$$(\boldsymbol{\Omega}(\mathbf{K})-\omega^2\mathbf{M})\cdot\mathbf{u}=0 \tag{3}$$

where $\boldsymbol{\Omega}$ is the stiffness matrix, which is a function of the wave vector; $\mathbf{M}$ is the mass matrix. As shown in Fig. 1(c), the wave vector just needs to be defined in the first Brillouin zone, owing to the symmetry of the Brillouin zone. Actually, only sweeping on the edges "Γ(0,0)-X(π/a, 0)-M(π/a, π/a)" is considered in Fig. 1(c). The dispersion curves of the unit cell are solved via the finite element software COMSOL 5.3a. The periodic boundary conditions are added on the side surfaces (i.e. Eq.[2]) and the fixed boundary condition is added on the bottom (i.e. $\mathbf{u}=0$).

2.3.1. Post-processing methods

The dispersion curves of the 3D model include both Rayleigh-wave modes and other modes. Considering the special feature of the Rayleigh wave propagation, the sound cone method is applied to distinguish pure Rayleigh wave modes (Khelif, Achaoui, Benchabane, Laude, & Aoubiza, 2010). The Rayleigh wave velocity is about 90% of the shear wave velocity propagating in the soil. Meanwhile, the longitude velocity is larger than the shear wave velocity. The sound line corresponds to the minimum phase velocity of the substrate, and were calculated along different directions of the first Brillouin zone and to form a sound cone as Eqs. (4) and (5).

$$\omega=\mathbf{K}\cdot c_s \tag{4}$$

$$c_s=\sqrt{\mu_s/\rho_s} \tag{5}$$

where c_s is the shear wave velocity of the soil; μ_s and ρ_s are the soil shear modulus and density, respectively.

The dispersion curves under the shear wave velocity of the soil only comprise Rayleigh wave modes. Therefore, the Rayleigh modes were distinguished from the entire dispersion curves by the sound cone as shown in Fig. 2. The sound line is marked as a black thick line, and the bands below the sound line is the Rayleigh-wave

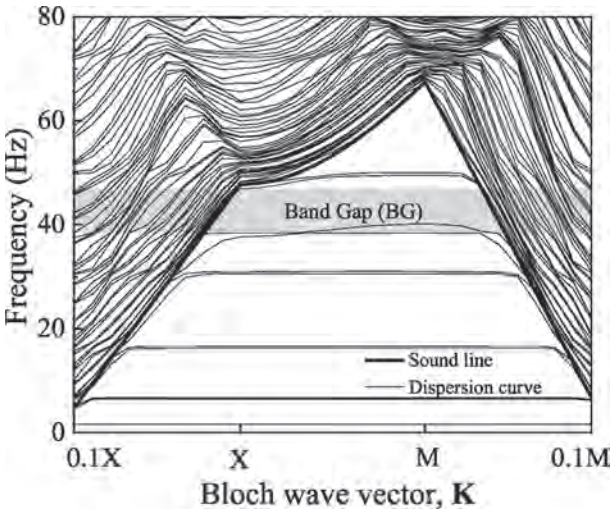

Fig. 2. Dispersion curves of phononic trees.

dispersion curves. Indeed, the bands beyond the sound line denote all possible modes of bulk waves. In this paper, it is sufficient to calculate the first 100 bands.

2.3.2. Comparison and verification

Research on phononic crystals with locally resonant cores primarily focused on microscopic domains such as physics and materials, which are similar with the large-scale natural phononic trees. This paper extended the research method from the microphysics realm to the macroscale field. To validate the present method, the previous model was calculated again compared with the present method. Fig. 3 shows the dispersion curves of a 2D phononic crystal of pillars on a surface (Badreddine & Oudich, 2011). The materials used for the substrate and scatterers are silicon and aluminum, respectively. The results were shown in Fig. 3,

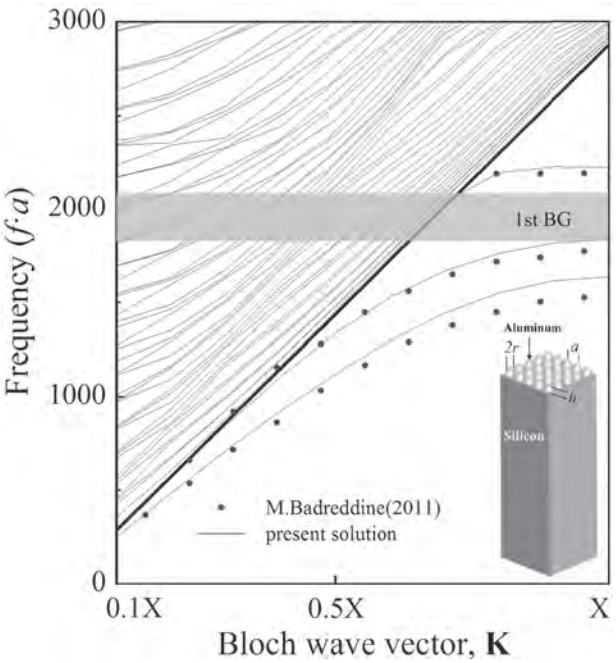

Fig. 3. Dispersion curves of a 2D phononic crystal with pillars on the surface.

and the present calculation results of the band structure (i.e., thin lines) were in agreement with previous research results (i.e., dots), which validated the accuracy of the present method. In Fig. 3, a "ΓX" directional band gap can be found, which indicated that the wave forbidding characteristic of the phononic system.

2.4. Simulation and experiment methods

Dispersion curves were calculated using a representative unit cell and perfect wave-forbidding characteristic existed in an infinite periodic tree. However, periodic trees should be arranged with a finite number in practical applications. To validate the effectiveness of a forest with a periodic arrangement, 3D simulation models with or without multiple (two, four or eight) rows of trees were established in this paper. The dynamic responses of models were calculated based on the finite element software ANSYS17.1. The geometrical sizes of the simulation model are: tree radius $r = 0.3$ m; tree height $b = 12$ m; tree space $a = 2$ m; soil height $h = 30$ m. The excitation and observed line are located at a distance of $2a$ away from the closest unit cell.

The artificial boundaries were introduced to minimizing the wave reflections occurred at the boundaries. The viscous-spring boundary condition as a type of absorbent boundary conditions, has been demonstrated to possess high precision as well as adequate stability (Liu, Du, Du, Wang, & Wu, 2006). The viscous-spring elements were added on the surfaces along the wave propagation and the bottom surface. Meanwhile, symmetrically periodic boundary conditions were imposed on the surface perpendicular to the wave propagation for minimizing the calculations.

Tests were conducted to assess the vibration reduction capabilities of the phononic trees over specific bands. A type of test samples was chosen: Green belt of *Ginkgo biloba* in Beijing as shown in Fig. 4(a). The overall test layout is pictured in Fig. 4(b). The acceleration sensors as the inset were provided perpendicular to tree rows. Acceleration signals were acquired using an eight-channel DEWE-43-A oscilloscope. A personal computer controlled the equipment and facilitated data processing.

3. Results and discussions

The dispersion relationships of phononic crystals are related to the material and geometry properties. To obtain the variation regulations of the band gap in the phononic trees, the two major parameters, including the soil modulus and tree height, were chosen to demonstrate the band gap adjustability in this section.

3.1. Parameter effects

3.1.1. Soil modulus

The soil properties have an important influence on the dispersion curves, which includes three primary parameters: soil modulus, density, and Poisson's ratio. As shown in Eqs. (4) and (5), the sound line corresponds to the smallest phase velocity of the soil along the different directions of propagation. Poisson's ratio and density of the soil cannot commonly varied drastically. Determining the shape of the sound cone, the soil elastic modulus has a more important influence on the band structure. The model in Fig. 1(b) (where $a = 2$ m, $r = 0.3$ m, $b = 10$ m) was used to calculate the effect of soil modulus on the band gap.

In Fig. 5, the width of the second band gap increases from 2.63 Hz at 200 MPa to 7.72 Hz at 250 MPa as the elastic modulus of the soil increases. The lower bound frequency (LBF) of the second band gap and the upper bound frequency (UBF) of the first band gap had a little change. The UBF of the second band gap continuously increases, which results in the increase of the bandgap's width. The first band gap gradually narrows and tends to disappear as the decrease of the soil modulus. As shown in Eqs. (4) and (5), if the elastic modulus of the soil increases, the shear wave velocity of the substrate increases, which results in the sound line cone increases. However, the position of the dispersion curves inside the sound cone, in fact, vary slightly. The total gap width increases with the increase of the soil modulus.

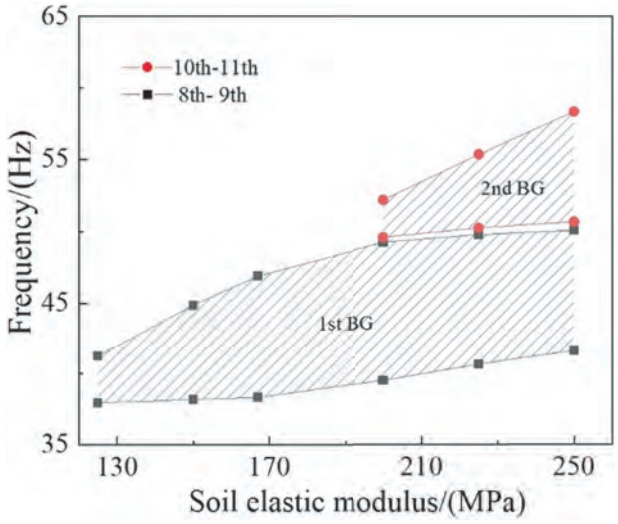

Fig. 5. Influence of soil elastic modulus on band gaps.

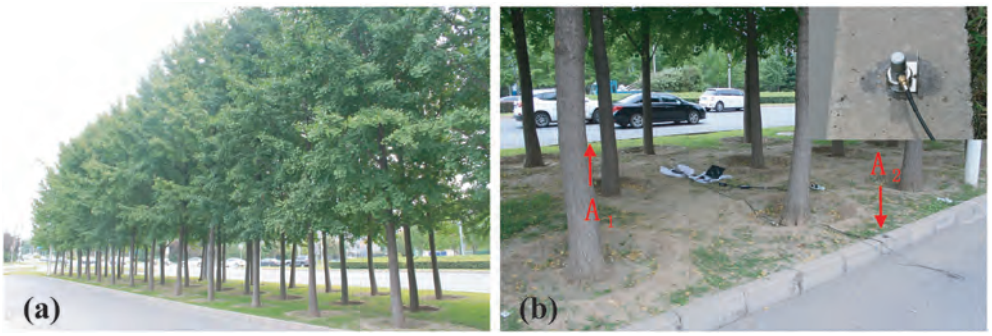

Fig. 4. Vibration experiment of phononic trees. (a) Phononic trees, (b) experimental layout.

3.1.2. Tree height

The influence of the tree height on band gaps is plotted in Fig. 6 (where $a = 2$ m, $r = 0.3$ m). The UBF of band gap varied from slightly along 47 Hz with the increase of tree height varied from 8 m to 12 m, meanwhile the LBF decreases and the total band gap width increases. For the first band gap, the band gap began to appear as the tree height is no less than 8 m. As the tree height increases, the UBF of the first band gap slowly decreases and the LBF of the band gap decreases rapidly. The gap width increases to the peak and then to recede. Meanwhile, the second bandgap began to appear, and occupied the original frequency region of the first bandgap. When the tree height increases to 12 m, the first bandgap almost disappears and the width of the second bandgap arrived at its peak. The total attenuation domain further extended since the tree height increasing. That means as the growth of trees, phononic trees have a better attenuation effect.

3.2. Numerical results

Fig. 7 illustrates the frequency response function (FRF) and dispersion relationships of phononic trees. The calculated band gaps in phononic trees are located at 32.11–32.78 Hz, 34.11–35.26 Hz, and 35.81–47.69 Hz, which matches well with the vibration attenuation region of the FRF. The amplitude attenuates obviously in the band gap range when the row number is up to two. In Fig. 7 (a), the vibration attenuation become more obvious with the increase of row number, especially for the four or eight rows of trees. In engineering applications, the arrangement of eight rows of trees is not common, therefore it is worth considering less rows of trees used in urban forests (e.g., four or two rows), which can obtain similar reduction effects.

The displacement distribution of the simulation model observed at 38 Hz (in the band gap) and 30 Hz (outside the band gap) were shown in Fig. 8. The surface wave feature was simulated as the wave mainly propagates along the ground surface in Fig. 8. In Fig. 8(a), the propagation of the elastic wave is suppressed in the band gap. In Fig. 8(b), the elastic wave passes through the entire model without any disturb if the incident wave is outside the band gap. The results illustrated the wave-forbidding feature of the band gap in phononic trees.

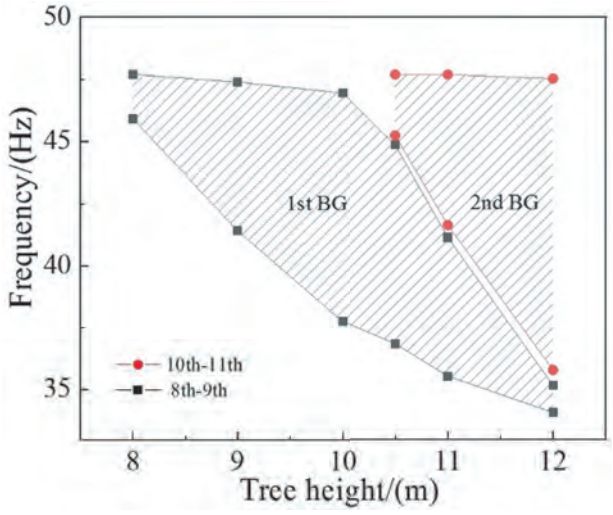

Fig. 6. Influence of tree height on band gaps.

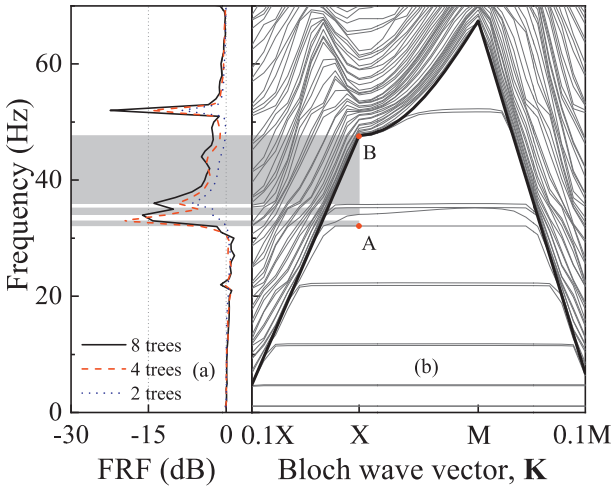

Fig. 7. (a)FRF curves and (b) dispersion curves of phononic trees with multiple rows.

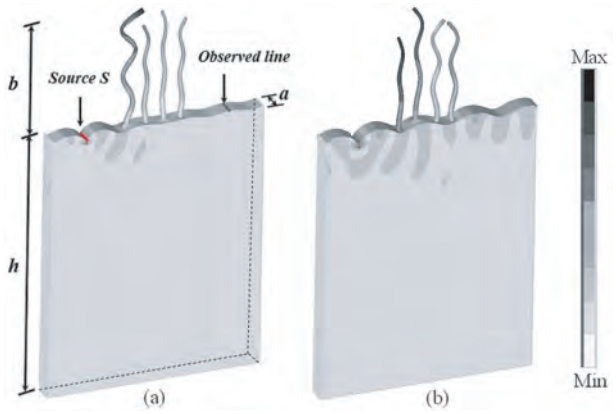

Fig. 8. Displacement distribution in the band gap ($f = 38$ Hz) and outside the band gap ($f = 30$ Hz).

3.3. Bandgap generation mechanism discussions

Vibration modes at the edges of the band gap were calculated to illustrate the band gap generation mechanism. The modes of upper and lower band edges were respectively depicted in Fig. 9. Dark and light grey demonstrate that the maximum and minimum of the mode vibrations. In Fig. 9(a), the vibration of the tree in mode A shown in Fig. 7(b) is a type of longitudinal low-order resonances; meanwhile, the motion of the ground surface was still. In Fig. 9(b), the vibration of the tree in mode B shown in Fig. 7(b) is an obviously flexural motion while the vibration of the soil was concentrated upon the ground surface. We observe the phenomenon that the LBF of the band gap is the result of tree local resonance. The UBF of the band gap is the combination of the trunk flexural resonance and surface wave propagation, which is a hybridization vibration mode. Therefore, the locally resonant band gap is determined by longitudinal resonance and hybridization vibration frequencies.

3.4. Experimental results

Fig. 10 shows the measured responses on different vibration observed points A1 and A2 under the traffic vibrations. The vibration response was reduced up to 60% if the phononic trees existed in Fig. 10(a). Compared to the case of no phononic trees, the vibration had no attenuation in the free field in Fig. 10(b). To

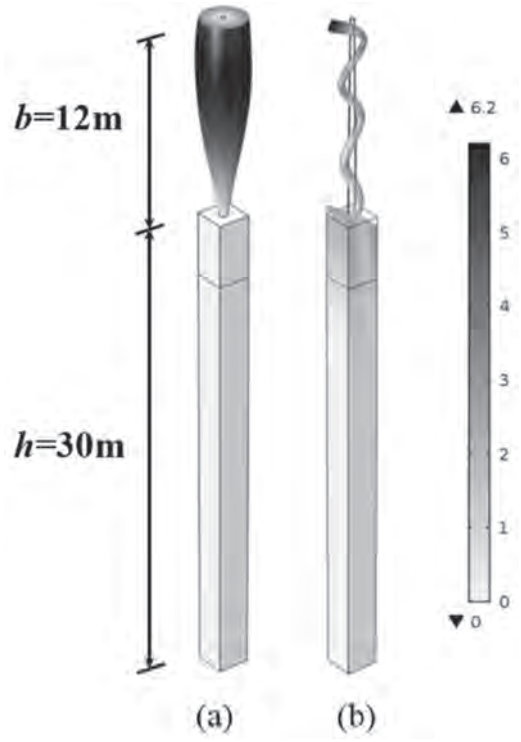

Fig. 9. Vibration modes of phononic trees corresponding to different frequencies. (a) LBF, (b) UBF.

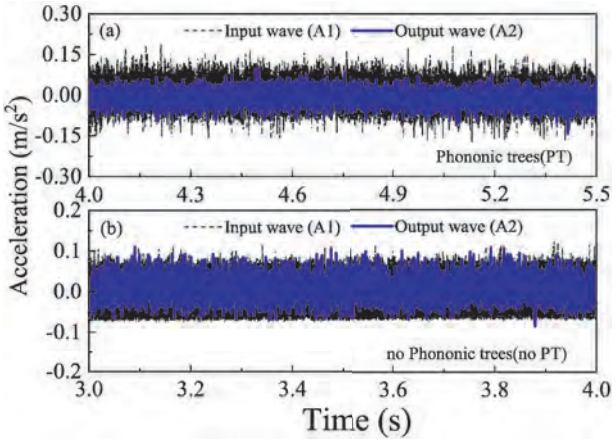

Fig. 10. Vertical acceleration responses to traffic waves with (a) phononic trees and (b) no phononic trees.

demonstrate band gaps' frequency reduction characteristics, the corresponding power spectra of the dynamic responses are displayed in Fig. 11. The power spectrum of the response for the phononic trees was much lower and essentially absent in some specific frequency band compared to the signals taken from the free field.

According to the actual situation of experimental site, the model parameters were set as follows: the elastic modulus of the tree was 3.3 GPa; soil elastic modulus was 250 MPa; tree space was $a = 2.3$ m; trunk radius $r = 0.15$ m. The corresponding periodic boundary conditions and Brillouin zones were based on the triangular lattice to obtain the potential band gap (Huang & Shi, 2013). The reduction phenomenon in the power spectra was consistent with the potential band gap. The attenuation peck showed a

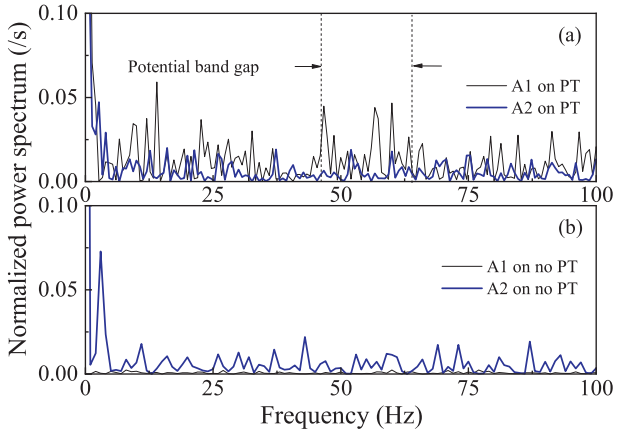

Fig. 11. Power spectra of vertical acceleration responses to traffic waves with (a) phononic trees and (b) no phononic trees.

significant reduction in the phononic trees. Therefore, the use of the phononic trees shows promise for vibration reduction in engineering applications.

4. Conclusions

In this paper, the periodic urban forests were regarded as natural phononic crystals, and the attenuation mechanism of band gap in the phononic trees were analyzed both theoretically and experimentally. All the analyses have confirmed the validity of the bandgap. Conclusions are summarized as follows:

(1) It is difficult to generate band gaps in phononic trees at the soft site with extremely low soil modulus; however, it is benefit to obtaining the low LBF. The more stiffness field can result a higher starting frequency band gap, meanwhile the gap width becomes much larger.
(2) The higher tree height is easier to obtain a wider band gap. Over time, the tree will grow naturally and become taller, which will expand the band gap as the natural succession.
(3) The simulation show that the reduction effectiveness of multiple rows of phononic trees increases with the row number. The experiment results validate the phononic trees can be observed as a large-scale natural phononic crystal.

Acknowledgement

This work was financially supported by the National Natural Science Foundation of China (Grant No. 31700637) and Fundamental Research Funds for the Central Universities of China (Grant Nos. 2015ZCQ-SB-01 and 2017ZY22).

References

Achaoui, Y., Khelif, A., Benchabane, S., Robert, L., & Laude, V. (2011). Experimental observation of locally-resonant and Bragg band gaps for surface guided waves in a phononic crystal of pillars. *Physical Review B: Condensed Matter, 83*(10), 5121–5124.
Colombi, A., Roux, P., Guenneau, S., Gueguen, P., & Craster, R. V. (2016). Forests as a natural seismic metamaterial: Rayleigh wave bandgaps induced by local resonances. *Scientific Reports, 6*, 19238.
Badreddine, A. M., & Oudich, M. (2011). Dispersion curves of surface acoustic waves in a two-dimensional phononic crystal. *Applied Physics Letters, 99*(12), 123505.
Baig, M. B., Shahid, S. A., & Straquadine, G. S. (2013). Making rainfed agriculture sustainable through environmental friendly technologies in Pakistan: A review. *International Soil & Water Conservation Research, 1*(2), 36–52.
Blinkov, I., Kostadinov, S., & Marinov, I. T. (2013). Comparison of erosion and erosion control works in Macedonia, Serbia and Bulgaria. *International Soil & Water*

Conservation Research, 1(3), 15–28.
Eyring, C. F. (1946). Jungle acoustics. *Acoustical Society of America Journal, 18*(2), 257.
Fan, Y., Bao, Z., Zhu, Z., & Liu, J. (2010). The investigation of noise attenuation by plants and the corresponding noise-reducing spectrum. *Journal of Environmental Health, 72*(8), 8.
Fricke, F. (1984). Sound attenuation in forests. *Journal of Sound and Vibration, 92*(1), 149–158.
Golosov, V., & Belyaev, V. (2013). The history and assessment of effectiveness of soil erosion control measures deployed in Russia. *International Soil & Water Conservation Research, 1*(2), 26–35.
Huang, J., Liu, W., & Shi, Z. (2017). Surface-wave attenuation zone of layered periodic structures and feasible application in ground vibration reduction. *Construction and Building Materials, 141*, 1–11.
Huang, J., & Shi, Z. (2013). Attenuation zones of periodic pile barriers and its application in vibration reduction for plane waves. *Journal of Sound and Vibration, 332*(19), 4423–4439.
Huang, J., & Shi, Z. (2015). Vibration reduction of plane waves using periodic infilled pile barriers. *Journal of Geotechnical and Geoenvironmental Engineering, 141*(6), 04015018.
Khelif, A., Achaoui, Y., Benchabane, S., Laude, V., & Aoubiza, B. (2010). Locally resonant surface acoustic wave band gaps in a two-dimensional phononic crystal of pillars on a surface. *Physical Review B: Condensed Matter, 81*(21), 1601–1614.
Liu, J. B., Du, Y. X., Du, X. L., Wang, Z. Y., & Wu, J. (2006). 3D viscous-spring artificial boundary in time domain. *Earthquake Engineering and Engineering Vibration, 5*(1), 93–102.
Liu, X., Shi, Z., & Mo, Y. L. (2015). Comparison of 2D and 3D models for numerical simulation of vibration reduction by periodic pile barriers. *Soil Dynamics and Earthquake Engineering, 79*, 104–107.
Liu, B., Wagner, L. E., Ning, D., & Qu, J. (2017). Estimation of wind erosion from construction of a railway in arid Northwest China. *International Soil & Water Conservation Research, 5*(2), 102–108.
Martínez-Sala, R., Rubio, C., García-Raffi, L. M., Sánchez-Pérez, J. V., Sánchez-Pérez, E. A., & Llinares, J. (2006). Control of noise by trees arranged like sonic crystals. *Journal of Sound and Vibration, 291*(1–2), 100–106.
Maurel, A., Marigo, J. J., Pham, K., & Guenneau, S. (2018). Conversion of Love waves in a forest of trees. *Physical Review B, 98*(13), 134311(14).
Oudich, M., & Badreddine, A. M. (2012). Surface acoustic wave band gaps in a diamond-based two-dimensional locally resonant phononic crystal for high frequency applications. *Journal of Applied Physics, 111*, 014504.
Pu, X., & Shi, Z. (2018). Surface-wave attenuation by periodic pile barriers in layered soils. *Construction and Building Materials, 180*, 177–187.
Renterghem, T. V., Botteldooren, D., & Verheyen, K. (2012). Road traffic noise shielding by vegetation belts of limited depth. *Journal of Sound and Vibration, 331*(10), 2404–2425.
Xu, Y., & Peng, P. (2015). High quality broadband spatial reflections of slow Rayleigh surface acoustic waves modulated by a graded grooved surface. *Journal of Applied Physics, 117*(3), 171911.